Characterization and processability of molecular-based magnetic nanoparticles and 2D crystals by scanning probe microscopy

Instituto de Ciencia Molecular

Universitat de València

. . .

Memoria presentada por Elena Pinilla Cienfuegos para aspirar al grado de Doctor en Nanociencia y Nanotecnología (programa ref. 3045)

. . .

Dirigida por el Dr. Eugenio Coronado Miralles y la Dra. Alicia Forment Aliaga

D. EUGENIO CORONADO MIRALLES, catedrático del Departamento de Química Inorgánica de la Universitat de València y DÑA. ALICIA FORMENT ALIAGA, doctora por la misma universidad y actualmente investigadora Ramón y Cajal en el Instituto de Ciencia Molecular, de la Universitat de València

CERTIFICAN:

Que la memoria presentada por Dña. Elena Pinilla Cienfuegos con título "*Characterization and processability of molecular-based magnetic nanoparticles and 2D crystals by scanning probe microscopy*" corresponde a su Tesis Doctoral y ha sido realizada bajo su dirección en el Instituto de Ciencia Molecular, autorizando mediante este escrito la presentación de la misma para optar al grado de Doctor.
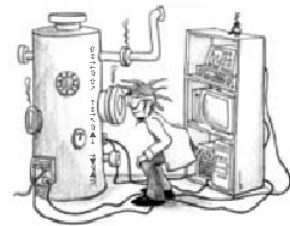

En Paterna, a 6 de febrero de 2014.

Dr. Eugenio Coronado Miralles   Dra. Alicia Forment Aliaga

Elena Pinilla Cienfuegos

The three forces in magnetism: theory, experiment, and simulation.

Agradecimientos

Parece que esta es la parte más fácil de escribir, por lo menos para mí, porque esta tesis no hubiera sido posible sin muchas personas a las que tengo mucho, muchísimo que agradecer. Primero quería agradecer a Eugenio que me ofreciera esta oportunidad, que creyera en mí desde el primer día y que con su peculiar forma de animar, me haya estado apoyando en este proyecto. Aun sufriendo algunos momentos "penosos" creo que ha merecido mucho la pena. Alicia, tú has sido mi referente durante todos estos años, no sólo te admiro como científica, sino también como persona y madre. En este tiempo has sido mi maestra, mi compañera y mi amiga, nunca habría podido imaginar tener una directora mejor. Muchas gracias por todo el esfuerzo y dedicación, esta tesis no es mía, ¡es de las dos!

Este manuscrito no hubiera salido a la luz jamás si no hubiera tenido el apoyo, la ayuda y el empuje final de mis compañeras y amigas Alejandra, Ana y Marian. No encuentro las palabras para agradeceros todo lo que habéis hecho estos últimos días, pero sobre todo, porque desde el principio me habéis acogido como una más, para risas y sustos, para trabajar y para disfrutar, en definitiva hacer que Valencia sea mi sitio. Xelito, no te me pierdas, que tú también formas parte de esta Valencia que me habéis regalado. Moni, que hubiera hecho yo sin tu ayuda con esta plantilla! Gracias de todo corazón, no hay sitio aquí para deciros lo importantes que sois para mí.

Sin lugar a dudas, creo que nadie hace una tesis en ciencia si no está completamente enamorado de esta profesión. Pasárselo bien en el laboratorio es un lujo difícil de explicar a los que no comparten esta pasión, aunque tiene momentos muy duros y es una tarea exigente. Yo he tenido la fortuna de compartir esos momentos con otros "enamorados" como yo, a los que admiro profundamente y con los que he tenido la suerte de crecer por el camino. Efrén, mi media naranja científica, no puedo explicar

lo que he disfrutado trabajando contigo. Eres un gran científico y un amigo, y espero que me sigas enseñando muchas cosas, aunque sea desde lejos. Con Mónica, Mauri, Michele, Salva, Concha y Julia empecé esta aventura y muy pronto llegaron Juan Pablo y Gonzalo. Como ya os he dicho alguna vez, soy mejor científica porque he trabajado con vosotros. ¡Gracias chicos! Después vino Josep. Amigo mío, ya sabes lo contenta que estoy de que trabajemos juntos. Somos todos una panda de cabezotas, ¡donde pensabas que te habías metido!

Pero es mucha la gente que forma este grupo a la que tengo mucho que agradecer. Nunca olvidaré los maravillosos momentos que compartí en la pecera con Mónica, Guille y Santi, o las miles de mudanzas del AFM, gracias a la ayuda de prácticamente todo el grupo. Jose, Ángel, Jorge, Eva, no sé qué hubiera sido de mí en el laboratorio si no hubiera tenido siempre vuestra ayuda incondicional. Jose, con tus espaldas y siempre dispuesto a echarme una mano; Ángel, tus buenas y brillantes ideas me han ayudado en muchas ocasiones; Jorge, gracias por solucionarme las pequeñas cosillas que son tan importantes para trabajar. Eva, de tu dedicación ha dependido gran parte de mi trabajo y siempre con esa sonrisa. ¡Miles de gracias, amiga! Chema, Gloria y Ximo, no sólo sois unos profesionales excelentes, sino que siempre estáis dispuestos a ayudarnos, con tesón y con ganas de que las cosas salgan bien. Somos muchos los afortunados de teneros como compañeros y espero poder seguir aprendiendo de vosotros. Paco y Manuel, ¡qué maravilla de equipo! Sois imprescindibles para nuestro trabajo, y sin embargo, con vuestra sencillez y amabilidad siempre tratáis de pasar desapercibidos. Gracias también a Alex Gómez, siempre tan eficiente en su trabajo. Me reservo unas palabritas especiales para Estela, que desde el primer día nos caímos bien. No has hecho nada más que ayudarme y solucionarme problemas desde el principio, velar por mis "papeles" tan importantes, y yo siempre tan tranquila porque sé que tú siempre estás ahí, cuidando todo con tanto detalle. Te agradezco muchísimo tu trabajo y sobre todo, tu amistad.

Sergio, contigo empecé a trabajar cuando legué al ICMol y aunque te marchaste pronto siempre recordaré los buenos consejos y las primeras lecciones. Muchas

gracias por dedicarme esos y otros muchos ratos más que hemos compartido desde la distancia, trabajando juntos. Eres todo un maestro y me alegro muchísimo de que hayas vuelto. Contigo, Carlos Martí, también he compartido gratas conversaciones de trabajo y de no trabajo. Me gustó mucho trabajar contigo en el laboratorio y espero que lo sigamos haciendo. Con Alex Gaita, Helena Prima, Antonio, Henk, Carlos, Samia y los demás "seniors" aprendo cada día. Me siento realmente afortunada de trabajar con personas a las que admiro y que siempre están dispuestas a echar una mano. Contigo Helena, además disfruto de muchos más ratos aparte, con los nanos y nuestras comidas de chicas, ¡que no se acaben nunca! Con Alex comparto muchas y buenas risas, y conversaciones muy fructíferas. A todo el equipo, en general, del ICMol muchas gracias por ser tan buenos compañeros, sin olvidarme de Amparo y de Paqui, que tan bien nos hacen a todos cuidando de los detalles del día a día.

Hace poco llegó la savia nueva, con Samuel además es "sabia". Chico, ¡tú vales mucho! Espero volver con fuerzas renovadas y seguir trabajando contigo porque es una maravilla ver cómo te empapas cada día de tantas ideas y la ilusión con la que trabajas.

Por otro lado he tenido la suerte de colaborar con el grupo del profesor Nicolás Agraït, en la Universidad Autónoma de Madrid, con el Dr. Andrés Castellanos en Delft, y con el grupo del Dr. Carlos Untiedt de la Universidad de Alicante. A todos ellos les doy las gracias por fructíferas colaboraciones. También quiero agradecer muy en especial la ayuda de Miriam Jaafar, Agustina Asenjo y Julio Gómez en nuestros primeros pasos con el MFM. Sin sus consejos y observaciones no hubiera conseguido avanzar para conseguir la parte de esta tesis de la que me siento especialmente más orgullosa. Y no me quiero olvidar de todo el equipo de Nanotec, con los que me embarqué de nuevo en esta apasionante aventura de la ciencia. Gracias a todo lo que aprendí con ellos he podido hacer este trabajo. Por esto, y por muchos buenos momentos, tengo mucho que agradecerles.

Igualmente quería agradecer a los miembros del tribunal por acceder a formar parte del mismo y a los evaluadores externos por aceptar evaluar esta tesis.

Por último, y no menos importante, quiero dedicar unas palabras a mi familia. Me siento muy afortunada de formar parte de una familia de mujeres inteligentes, trabajadoras, fuertes y tremendamente positivas. Gracias a vosotras creo que he heredado esa fuerza que tanto me ha ayudado en momentos difíciles; gracias a todos por haberme dado una educación excelente. En especial, quiero destacar a mis hermanas M ªPaz y Sole (mi hermana de corazón), a mi abuelita y a mis padres. ¡Ya está hecho! Aún desde lejos, he sentido todo vuestro apoyo.

Y ahora le llega el turno a los que de verdad han "sufrido" conmigo estas últimas semanas, a mi familia valenciana y en especial a mis chicos, Archi y Juan Pablo, que me dan la vida cada día. Gracias por haber sido tan generosos y gracias por regalarme este tiempo tan feliz.

A Lalo

A Archi y Juan Pablo

TITLE

Characterization and processability of molecular-based magnetic nanoparticles and 2D crystals by scanning probe microscopy

MOTIVATION AND ORGANIZATION OF THIS THESIS

The development of new and pioneering multifunctional nanodevices relies on the possibility of the miniaturization and the assembly of nanometric building blocks with specific configurations. The size, shape and properties of these nanocomponents as well as the possibility of their integration and combination are crucial in order to fabricate clever devices that interface small assemblies of nanoobjects with macro(nano)scaled electrodes. The challenge then is twofold: first, the manipulation and characterization of novel materials at the nanoscale and second, their organization onto surfaces and/or their assembly to create heterostructured multifunctional materials.

The two aspects of this challenge will be covered in this thesis by the manipulation, organization and characterization of two types of novel nanomaterials: two-dimensional (2D) atomic crystals and molecular-based nanoparticles.

This manuscript is divided in two main parts:

The first part deals with the manipulation of the two kinds of afore mentioned nanomaterials. The aim of this section is to efficiently produce and transfer onto surfaces these nanoobjects in controllable ways, and one step forward, their manipulation to generate heterostructures. This part comprises three chapters: The first chapter (chapter 1) is a general overview of micro and nanolithography. Three types of *alternative* lithographic methods will be explained as they will be used in chapters 2 and 3: Local oxidation nanolithography (LON) performed with atomic force microscopy (AFM), dip-pen nanolithography (DPN) and soft lithography.

In chapter 2, a feasible route for the creation of heterostructured materials will be proposed which involves an accurate chemical manipulation of atomic monolayers of metallic transition metal dichalcogenides (TMDCs) by means of LON. In this line, a new AFM-LON mode, coined as *static-tip* LON, will be presented that will allow the creation of reproducible oxidation of very low-profile motifs on monolayers of TaS_2. This general method will be also applied to other three types of metallic TMDCs: $TaSe_2$, NbS_2 and $NbSe_2$. A detailed study of the oxidation growth processes on each material will be presented. Besides, a new method for the micromechanical exfoliation of atomically thin layers of 2D layered materials is developed which tries to overcome the limitations of the *Scotch Tape* method for exfoliating metallic TMDCs. This new method it will allow the transference of the delaminated thin patches to a variety of substrates, as well.

In chapter 3, the three lithographic methods introduced in chapter 1, will be used for the accurate and reproducible organization of magnetic Prusian blue analogue nanoparticles (PBA-NPs) which are an important class of molecular-based materials exhibiting tunable magnetic properties. This tunability together with an easy chemical synthesis makes PBA-NPs good candidates for their integration into new electronic or spintronic devices. As a previous step, the development of proper techniques for their structuration on surfaces with control over their positioning, and organization is a crucial issue. This will be achievable by applying hybrid nanoscale patterning strategies to fabricate nanopatterns onto functionalized surfaces combining top down with bottom up approaches. The organization will be performed onto very specific positions of the surface by means of LON and DPN, while large area patterings of several cm^2 will be achieved via soft lithography. Detailed and dedicated studies of the three methods and their results will be presented.

For the proper assembling and integration of these molecular-based NPs on devices, the maintenance and manipulation of their properties once organized onto the surface is crucial. The second part of the thesis is then devoted to the magnetic

characterization and tuning of the above mentioned PBA-NPs by low temperature magnetic force microscopy. This part is also divided in three chapters.

Chapter 4 is a brief introduction of the characterization of magnetic NPs on surfaces in general by means of very different magnetic characterization techniques, and in particular it will be introduced the magnetic force microscopy (MFM) as a powerful tool to characterize the PBA-NPs at low temperature.

In chapter 5, a detailed study of the size-dependence and temperature-dependence of the magnetic properties of single and isolated PBA-NPs will be presented. As well, the different magnetization reversal mechanisms of the NPs derived from the different sizes will be studied by variable field MFM at 4.2 K. The calibration of the magnetic tip as well as other issues related with the measurements at low temperature will be also discussed. The *in-situ* functionalization of the magnetic tip by the attachment of a unique NP onto it will permit the assignment of the magnetization directions of the magnetic moments of individual NPs.

Finally, in chapter 6, it will be presented the magnetic characterization of ordered arrays of PBA-NPs organized by soft lithography. The magnetic interaction between the closed packed NPs and the influence of the organization in the reversibility of the individual NPs inside the patterned lines will be studied. This will be possible by working at low temperatures and with variable applied field.

The list of publications[1] generated during my PhD thesis are listed below:

"Imaging of the magnetization reversal in individual nanoparticles". E. Coronado, A. Forment-Aliaga, E.Pinilla-Cienfuegos. *Submitted*.

"Magnetic Imaging of Molecular-Based Nanoparticles by Low Temperature-MFM". J. Canet-Ferrer, E. Coronado, A. Forment-Aliaga, S. Kumar, S. Mañas-Valero, E. Pinilla-Cienfuegos, L. Catala, T. Mallah. *Submitted*.

"Correction of the Tip Convolution Effects in the Imaging of Nanostructures Studied Through Scanning Force Microscopy". J. Canet-Ferrer, E. Coronado, A. Forment-Aliaga, E. Pinilla-Cienfuegos. *Submitted*.

"Fast and reliable identification of atomically thin layers of $TaSe_2$ crystals." A. Castellanos-Gomez, E. Navarro-Moratalla, G. Mokry, J. Quereda, E. Pinilla-Cienfuegos, N. Agraït, H. S. J. van der Zant, E. Coronado, G. A. Steele, G. Rubio-Bollinger. Nano Research, 6 (3), 191 - 199 (2013).

"Nanofabrication of TaS_2 conducting layers nanopatterned with Ta_2O_5 insulating regions via AFM". E. Coronado, A. Forment-Aliaga, E. Navarro-Moratalla, E. Pinilla-Cienfuegos, A. Castellanos-Gomez. J. Mater. Chem. C, 1, 7692-7694 (2013).

"Nanopatterning of Anionic Nanoparticles based on Magnetic Prussian-Blue Analogues". E. Coronado, A. Forment-Aliaga, E. Pinilla-Cienfuegos, S. Tatay, L.Catala and J. A. Plaza. Adv. Funct. Mater. 22, 3625-3633 (2012).

---

[1] I want to clarify that in papers published by Prof. Eugenio Coronado's group, due to internal policy, authors of the group appear in alphabetic order. If the paper is fruit of collaboration with other groups, authors from the other groups appear afterwards in the order that they decide. Therefore the articles marked in blue are based on my main research results, although in none of them I do not appear as first author.

"Large-scale nanopatterning of single proteins used as carriers of magnetic nanoparticles". R. Garcia, R.V. Martínez, J. Martínez, M. Chiesa, R. Garcia, E. Coronado, E. Pinilla-Cienfuegos, S. Tatay. Adv. Mater. 22, 588 – 591 (2010).

"Tuning Size and Thermal Hysteresis in Bistable Spin Crossover Nanoparticles". J.R.Galan-Mascaros, E. Coronado, A. Forment-Aliaga, M. Monrabal-Capilla, E. Pinilla-Cienfuegos, M. Ceolin. Inorg. Chem. 49, 5706–5714 (2010).

"Hexagonal nanosheets from the exfoliation of Ni^{2+}-Fe^{3+} LDHs: a route towards layered multifunctional materials". G. Abellan, E. Coronado, C. Marti-Gastaldo, E. Pinilla-Cienfuegos, A. Ribera. J. Mat. Chem. 20, 35, 7451-7455 (2010).

Patent: P201300252, "Método y sistema de exfoliación micromecánica por vía seca de materiales laminares bidimensionales."

Abbreviations

2D	two-dimensional
3D	three-dimensional
μCP	microcontact printing
μTM	Microtransfer molding
a	acceleration
AES	Auger electron spectroscopy
AFM	atomic force microscopy
APTES	3 - aminopropyl triethoxysilane
ATR-IRRAS	attenuated total reflection infrared spectroscopy
B	total magnetic field
B_{ext}	external magnetic field
CDW	charge density wave
CNT	carbon nanotube
CVD	chemical vapor deposition
CVT	chemical vapor transport
DLS	dynamic light scattering
DPN	dip-pen nanolithography
d_{ts}	tip-sample distance
EPMA	electron probe microanalysis mapping
EPR	electron paramagnetic resonance
FC	field cooled
FIB	focus ion beam
H_c	magnetic coercive field
HOPG	high oriented pyrolitic graphite
LON	local oxidation nanolithography
l_{coh}	coherent length
l_{ex}	exchange length

LT-MFM	low temperature magnetic force microscopy
l_{SD}	critical single domain size
LWC	lithographically controlled wetting
MExFM	magnetic exchange force microscopy
MFM	magnetic force microscopy
MIMIC	micromolding in capillaries
MOKE	magneto optical Kerr effect
m_{NP}	magnetic moment of a nanoparticle
MNP	magnetic nanoparticle
M_s^{NP}	saturation magnetization of the nanoparticle
M_s^{tip}	saturation magnetization of the tip
NMR	nuclear magnetic resonance
NP	nanoparticle
NIL	nanoimprinting lithography
NV	nitrogen vacancy
OTS	octadecyltrichlorosilane
PBA	Prusian blue analogue
PDMS	polydimethylsiloxane
PLL	phase locked loop
PMMA	polymethyl methacrylate
PVP	polyvinilpirrolidone
REM	reflection electron microscopy
RT	room temperature
SAM	self-assembled monolayer
SAMIM	solvent-assisted micromolding
SET	single electron transistor
SHPM	scanning hall microscopy
SPL	scanning probe lithography

SPM	scanning probe microscopy
STEM	scanning transmission electron microscopy
STM	scanning tunneling microscopy
T_B	blocking temperature
T_c	Curie temperature
TMDC	transition metal dichalcogenide
XMCD	X-ray magnetic circular dichroism
ZFC	zero field cooled
Z_{lift}	lift height

Contents

PART I

PART II

PART I

1

MICRO AND NANOLITHOGRAPHY: A SHORT OVERVIEW

1.1 INTRODUCTION

The ability to generate and manipulate very small structures has been of a great interest in the last decades due to its important application in electronics. The best example is found in microelectronics, where "smaller" has meant better: less expensive, more components per chip, faster operation, higher performance, and lower power consumption, since the invention of transistors in 1947.[1] Microfabrication is based in conventional lithography techniques: optical techniques, (photolithography mainly),[2] electron beam lithography, ion beam lithography, optical projection lithography and X-ray lithography.[3] These techniques rely on both the delivery of energy and destruction of material on a surface to achieve the desired patterning results which are usually cost-intensive. These techniques are also unsuitable to handle a large variety of soft materials (organic and biological systems, soft polymers, molecules or nanoparticles), with are important elements in nanotechnology nowadays. These limitations suggest the need for alternative micro/nano-fabrication techniques capable of generating structures smaller than 100 nm for a wide range of materials.[4] Among the possible alternatives, the so-called *non-conventional, unconventional* or *alternative* approaches emerged around 1990 as low-cost and high resolution techniques (< 100 nm) which applicability covers a broad family of nanomaterials including those that were not compatible with the conventional lithography methods.[5] Some of them can be listed as: nanoimprinting lithography (NIL),[6] soft lithography,[7] and scanning probe lithography (SPL). The last one involves some methods as scanning near-field optical lithography,[8] dip pen nanolithography (DPN)[9] and local oxidation nanolithography (LON) -also called anodic oxidation nanolithography-, nanoshaving, nanografting, and electrochemical and thermal nanolithography.[10]
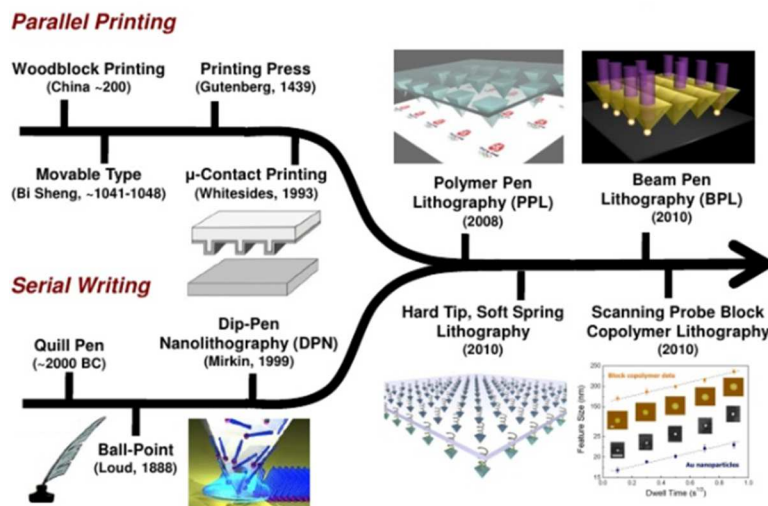
Figure 1. Timeline of two separate paths: serial writing and parallel printing that have recently merged with the invention of polymer pen lithography (PPL) and more recently with the massively multiplexed beam pen lithography (BPL). Image extracted from a personal lecture of Prof. Mirkin, related to ref [14].

In this thesis we will focus on three of the introduced *unconventional* lithography techniques: local oxidation nanolithography (LON), dip pen nanolithography (DPN) and soft lithography. The first two techniques, LON and DPN, are considered as serial methods but the main advantage is their high resolution, as it can pattern features on surfaces with nanometric accuracy (~1 nm height in silicon).[11] Also there are some alternatives for parallel lithography with LON like the multicantilever AFM based Millipede[12] or the local oxidation nanolithography with metallized stamps.[13] Recently parallel approaches have been developed by the group of Prof. Mirkin, for the case of DPN (Figure 1).[14] On the other hand, the main advantage of the soft lithography is that is a parallel nanoprinting technique that provides high-throughput, large-area patterning and the possibility of the fabrication of nanofeatures on planar and nonplanar surfaces. It is also a cheap and reliable nanolithography method that does not need expensive instrumentation and can be performed at any laboratory.

1.1.1 The local oxidation nanolithography

The local oxidation nanolithography (LON) was first performed in 1990 by Dagata and co-workers who locally modified a hydrogen-terminated silicon surface into silicon dioxide by applying a bias voltage to the tip of a scanning tunneling microscope (STM).[10] Only three years after, it was demonstrated the possibility of performing local oxidation experiments with an atomic force microscope (AFM).[15] This method opened the way for applying the technique to a large variety of materials. The first oxidized surfaces were silicon (111) and polycrystalline tantalum although it was rapidly extended to numerous types of materials such as semiconductors,[16] metals,[17] and dielectrics.[18] The main advantage of this technique is the high resolution and alignment accuracy, which could not be achieved by conventional lithographic techniques. Moreover, the LON technique takes advantage of the ability to move a probe over the sample in a controllable way, which allows for the nanopatterning in specific areas of a substrate that is a key requirement for some applications.

The LON is a process where a bias voltage is applied to a conducting or semiconducting AFM tip. The experiment is generally performed in ambient conditions, which imply that the substrate and the tip surface are covered by a water layer (depending on their wettability properties). This voltage produces a water meniscus between the tip and the surface and an electrochemical cell is created (although in some cases the meniscus can also be formed by the mechanical contact between tip and sample surface). The AFM tip is used as a cathode and the water meniscus formed between tip and surface provides the electrolyte (Figure 2). For a generic metallic surface, the following half-cell oxidation reaction (anode) has been proposed [19]

$$M + nH_2O \rightarrow MO_n + 2nH^+ + 2ne^-$$
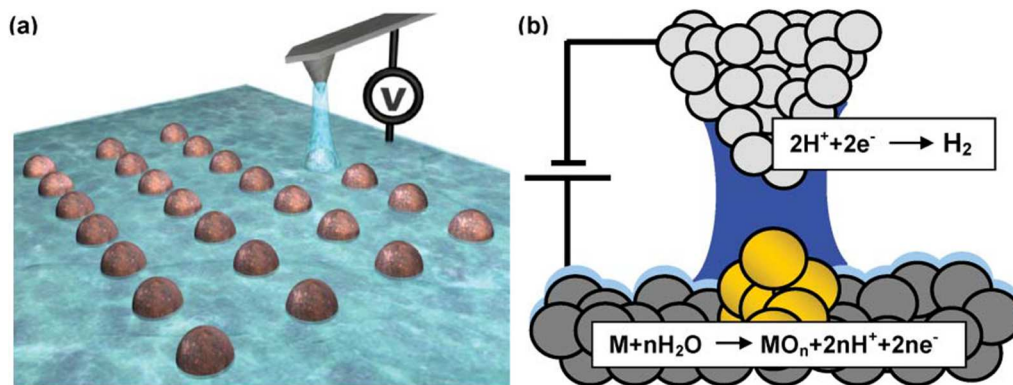<div align="right">Eq. 1.1</div>
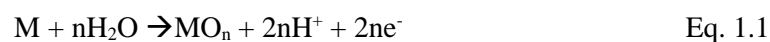
Figure 2. (a) Schematics of a local oxidation nanolithography experiment. The meniscus provides the oxyanions and confines the spatial extent of the reaction. (b) Accepted chemical reactions in the local oxidation of a metallic surface. Figure extracted from reference [19]

LON can be performed in contact and non-contact mode. The non-contact LON mode offers two main advantages with respect to contact SPM oxidation: (1) as the tip lifetime is greatly enhanced due to the absence of contact forces, this increases the reproducibility to pattern surfaces at large scale and (2) the lateral confinement of the oxidation reaction within the limits of the meniscus, whose size can be modified, allows controlling the lateral width of the oxide marks. The evidence of the bridge formation was provided by García et al. analyzing the changes in the oscillation amplitude and in the resonance curves of the cantilever due to the attractive meniscus force. [20]

There are many parameters that influence the oxide formation in LON and all of them have been widely studied mainly focusing on silicon substrates. Dependence of voltage and time pulse,[21] ambient humidity and hydrophobicity of surfaces,[22] curvature tip radius,[20] scanning speeds,[23] voltage modulation studies,[24] voltage polarity[25] and tip-sample distance[26] are important experimental parameters that affect the final shape and size of the oxide patterns. The study of LON on silicon surfaces

has served as a good model to illustrate some of the fundamental aspects involved in the local oxidation process. Regarding the mechanic and kinetic aspects of the oxide growth by LON, a summary can be found in reference [27].

Conveniently, the oxide growth patterns can be chemically etched to discover that the patterns created by LON are three dimensional (3D) features as they grow above and below the surface of the oxidized material. Etching experiments are useful to elucidate the chemical nature of the patterns as well as for some applications. For example, Dorn et al. demonstrated the fabrication of high quality antidot lattices which are particularly appealing for studying quantum signatures in chaotic systems.[28]

Local oxidation processes allow the direct fabrication of dielectric barriers onto metallic materials (heterostructuring), masks for selective etching, and templates. It has been proved to be a versatile lithography technique that enables the fabrication of a wide range of electronic and mechanical devices with nanometer-scale features.[29] Appart from the patterning onto semiconducting or metallic surfaces, LON has shown to be a very suitable technique to selectively deposit nanometric objects onto the fabricated nanopatterns. The method is based on using specific interactions established between functionalized surfaces with SAMs or bare surfaces and target nanoparticles/molecules to anchor the nanoobjets onto the LON patterns. This method has been proved to be quite general and has already been used for the positioning of any kind of nanoparticles and molecules (Figure 3).[30,31,32]

By applying a voltage to the AFM tip, it is also possible to induce electrochemical surface transformations of the head group in SAMs, while fully preserving the overall monolayer structural integrity. Depending on the nature of the transformations, such locally modified monolayer surfaces can be used to induce site-selective self-assembly of a number of different materials (organic, metal, semiconductor), according to a predefined geometric pattern and pre-selected type of chemical modification.[33]
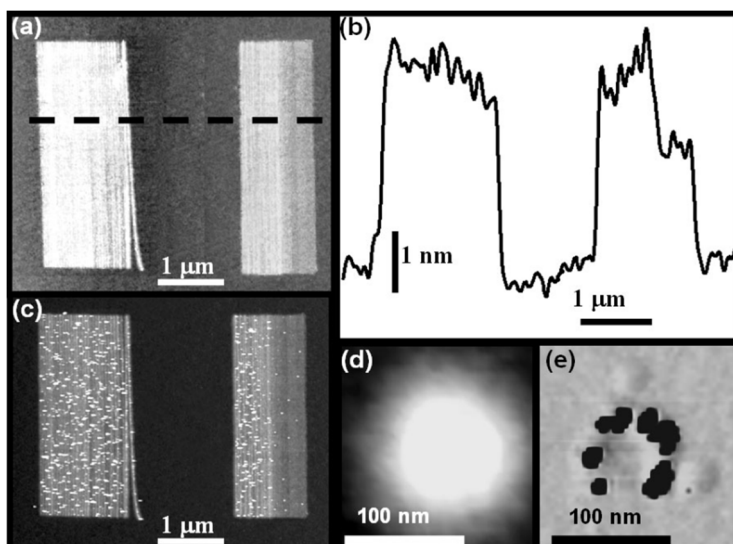
Figure 3. Patterns fabricated by using LON before and after deposition of single molecule magnets (SMMs). a) An AFM image of two parallel stripes. b) A cross section along the line shown in (a). c) A topographic image of the pattern shown in (a) after the deposition of the Mn SMM, $Mn_{12}bet$. The SMMs appear as white dots in the image. d) A topographic image of a local oxide dot 80 nm in diameter. e) The phase image reveals the presence of 16 SMM forming a nanoscale ring around the dot. The phase-shift image reveals the difference in mechanical properties between the molecules and the dot. Figure extracted from reference [30].

In summary, it can be concluded that LON is an effective alternative to conventional lithography techniques for nanofabrication of devices and heterostructures, and offers a low-cost approach for the research of the materials and chemical processes at the nanoscale. LON allows the fabrication of hybrid nanoscale patternings with a strategy that combines the registration and addressability of lithographic techniques with the chemical and physical functionality enabled by intermolecular and/or electrostatic interactions.[34] This combination of top-down (LON) with bottom-up (self-assembly) techniques is the key for the controlled positioning of nanoparticles and molecules in selective areas of a surface. This aspect is not only interesting from the fundamental point of view, but also from the possibility it opens for the integration of these nanoobjects in devices.

1.1.2 Dip pen nanolithography

Dip pen nanolithography (DPN),[9] invented in 1999, is an AFM-based direct-write lithographic technique in which the AFM probe is used as a pen to directly deliver materials (inks) to a nanoscopic region on a target substrate. It has the ability to pattern multiple chemical species with sub-100-nm alignment (Figure 4). In most cases, the transport of ink molecules from the tip to the substrate is mediated by a water meniscus, which is formed through capillary condensation. The transport and deposition of inks depend not only on the formation of the water meniscus but also on the properties of the tip and the substrate, as well as on the ink deposition time and temperature. DPN is compatible with many inks: from small organic molecules to organic and biological polymer, and from colloidal particles to metal ions. It can be used to pattern surfaces ranging from metals to insulators and also to pattern on top of functional monolayers adsorbed on a wide variety of surfaces.[35]
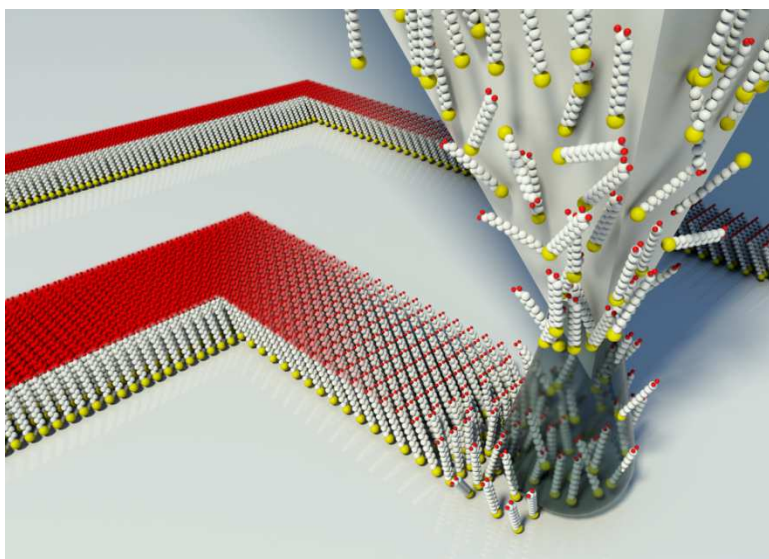

Figure 4. Schematic 3D view of the DPN experiment showing the controlled transport of ink from the AFM tip to the substrate through the water meniscus. Image taken from Prof. Mirkin group webpage.

Since its invention, variations and modifications of the typical DPN experiment have been accomplished by many research groups contributing to its development. The studied topics ranged from the fundamental study of tip-substrate ink transport, to the direct deposition of metallic structures and development of electrochemical DPN, or the deposition of biomolecules and the effects of DPN on the organization of biopolymers. Among these possible variations, the assembly of particles onto surfaces is a powerful and versatile approach. This method implies an indirect patterning developed by the functionalization of the substrate by DPN forming SAMs in specific areas of the surface. Then, the immobilization of particles with diameters ranging from 5 nm to nearly 1 mm is driven by electrostatic interactions between the particles and the functionalized areas.[35] But it is also possible to use DPN to directly place nanoparticles or generate solid nanostructures in specific locations on surfaces. By controlling the contact force between an inked tip with a colloidal suspension of gold nanoparticles (NPs), Ben Ali and coworkers were then able to deposit 5 nm diameter particles in clusters of 50–200 nm in diameter depending on the contact force used.[36] Garno et al. also performed similar experiments to deposit core-shell gold NPs on surfaces modified with SAMs to prevent lateral diffusion.[37] More recently, Bellido and coworkers reported the directly positioning of cobalt NPs on top of graphene by capillary transport without causing any damage.[38]

DPN is now a commercialized process[39] useful for creating functional arrays and nanodevices. For example, the Nscriptor DPN System (NanoInk, Inc., Chicago, IL) is a commercial instrument that allows repeatable and controllable experiments. There are also special probes for the performance of the DPN experiments that are commercially available. Many groups have taken advantage on this instrumentation and this technique is nowadays widely used.

1.1.3 Soft lithography

Among the emerged *unconventional* nanolithographies, soft lithography[40] provides an attractive route for in-situ fabrication soft-matter patterns based on elastomeric stamps, typically poly(dimethylsiloxane) (PDMS).[41] The generated patterns and structures have feature sizes ranging from few nanometers to tens of micrometers. Soft lithography cover several related techniques such as microcontact printing (μCP), replica molding (REM), microtransfer molding (μTM), micromolding in capillaries (MIMIC), and solvent-assisted micromolding (SAMIM).[42]

As an example, the μCP[43] is used to transfer molecules from a patterned PDMS stamp to a substrate by the formation of covalent bonds (nanostructured SAMs). In this process a solution of molecules is inked onto the surface of the PDMS, and this stamp is brought into contact with an appropriate substrate (e.g., a thin gold, silver, or palladium film). The molecules are transferred in a pattern defined by the topography of the stamp (i.e., the regions of atomic-level contact between the stamp and substrate) with a minimum feature size as small as ~30 nm (Figure 5).[44] The flexibility of the PDMS stamp and the ability to achieve conformal, atomic level contact between the stamp and the substrate are both advantageous for printing over large areas (>50 cm^2)[45] and on curved surfaces. [46]

The soft lithography technique has been developed primarily for PDMS stamps although the continuous optimization of this method to match the demands of functional microdevices, has motivated the study of the influence of the stamp material, inks, substrate materials, transfer procedures and further pattern-induced reactions in or after transfer procedure.[47] All these studies give rise to new optimized soft lithography approaches every year. One example of this evolution is the so-called lithographically controlled wetting (LCW).[48] This approach is suitable for large-area

nanopatterning due to its simplicity, speed, and low cost. It yields nanometer-sized structures in a few seconds and a single step.
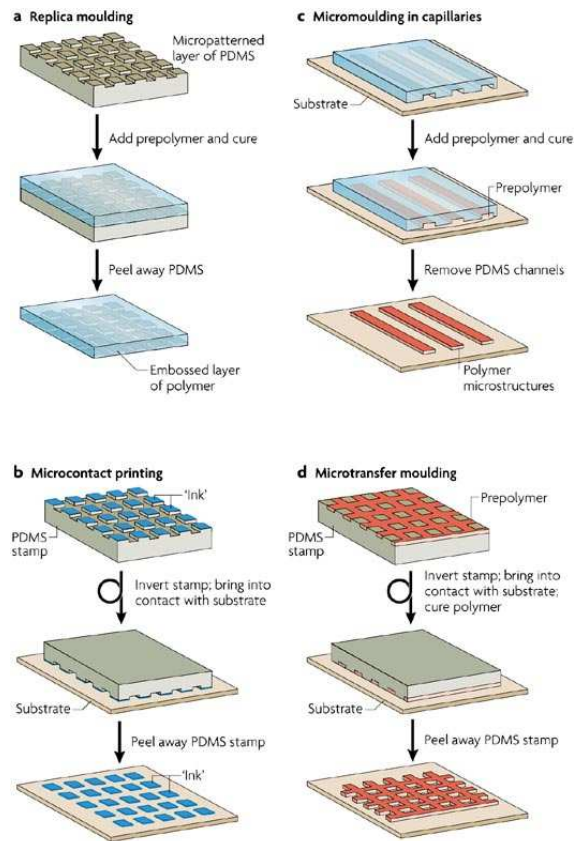
Figure 5. Schemes of several soft lithography processes. Figure adapted from reference [42]

This method is universal for soluble materials as it does not require chemical binding or other specific interactions between the solute and the surface. In LCW, a stamp is placed in contact with a liquid thin film; this way, capillary forces drive the liquid to distribute only under the protrusions of the stamp. As the solvent evaporates, the

deposited solute forms a pattern on the surface with the same length scale of the stamp (Figure 6).
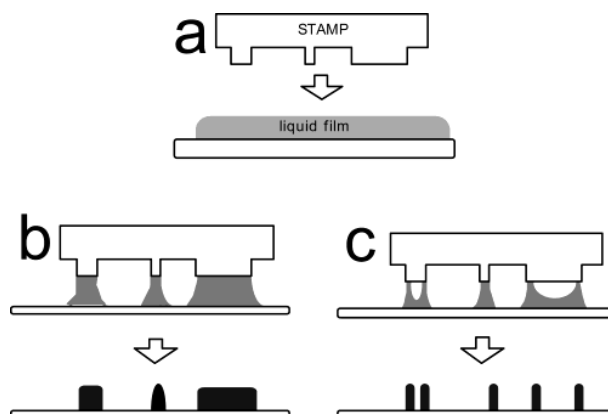
Figure 6. Schematic illustration of printing nanostructures by LCW. (a) A drop of solution is applied to the surface of the substrate, and the stamp is placed on top of it. Process with (b) dilute solution and (c) with extremely dilute solution. Figure extracted from reference [48]

In summary, the lithographic methods reported in this chapter has been shown to be useful for printing nanostructures from solution, or for the controlled deposition of nanometric objects (molecules or nanoparticles) on a surface. They are simple and economic patterning processes and enables the local patterning onto specific areas of the surface (by LON and DPN) as well as the patterning of large areas (by soft lithography).

1.2 BIBLIOGRAPHY

[1] a) Keyes R. W., *Phys. Today* **1992**, 45, *8*, 42. b) Barrett C. R., *MRS Bull.* **1993**, 28, 7, 3. c) Service R. F., *Science* **1996**, *273*, 1834. d) Moore G., *Electrochem. Soc. Interf.* **1997**, 18.

[2] a) Okazaki S., *J. Vac. Sci. Technol. B* **1991**, *9*, 2829. b) Jeong H. J., Markle D. A., Owen G., Pease F., Grenville A., von Bünau R., *Solid State Technol.* **1994**, *37*, 39. c) Levenson M. D., *ibid.* **1995**, *38*, 57. d) Geppert L., *IEEE Spectrum* **1996**, *33*, 4, 33.

[3] Chen Y., Pépin A., *Review. Electrophoresis.* **2001**, *22*, 187.

[4] Xia Y., Whitesides G. M., *Angew. Chem. Int. Ed.* **1998**, *37*, 550.

[5] Gates B. D., Xu Q., Stewart M, Ryan D, Willson C. G., Whitesides G. M., *Chemical Reviews*, **2005**, *105*, 4.

[6] Chou, S.Y.; Krauss, P.R.; Renstrom, P.J. *Science,* **1996**, *272*, 5258, 85.

[7] Xia Y., Whitesides G., *Angew. Chem.* **1998**, *110*, 568; *Angew. Chem. Int. Ed.* **1998**, *37*, 550.

[8] Dunn, R. C. *Chem. Rev.* **1999**, *99*, 2891.

[9] Piner R. D., Zhu J., Xu F., Hong S. H., Mirkin C. A., *Science* **1999**, *283*, 661.

[10] a) Dagata J., Schneir J., Harary H. H., Evans C. J., Postek M. T., Bennett J., *Appl. Phys. Lett.,* **1990**, *56*, 2001. b) Rosa L. G., Liang J., *J. Phys.: Condens. Matter,* **2009**, *21,* 483001.

[11] Tello M., García F., García R., J. *Appl. Phys.,* **2002**, *92*, 7.

[12] Vettiger P., Despont M., Drechsler U., Dürig U., Häberle W., Lutwyche M. I., Rothuizen H. E., Stutz R., Widmer R., Binnig G. K., *IBM J. Res. Develop.*, **2000,** *44*, 323.

[13] Cavallini M, Mei P, Biscarini F, García R. *Appl. Phys. Lett.* **2003,** *83*, 5286

[14] Liao X., Brown K. A., Schmucker A. L., Liu G., He S., Shim W., Mirkin C. A.. *Nature Communications,* **2013**, *4*, 2103.

[15] Day, H. C., Allee, D. R, *Appl. Phys. Lett.* **1993**, *62*, 21, 2691.

16 Heinzel T., Held R., Lüscher S., Vančura T., Ensslin K., Blomqvist T., Zozoulenko I., Wegscheider W. *Advances in Solid State Physics,* **1999,** *39*, 161.

[17] Matsumoto K., Gotoh Y., Maeda T., Dagata J. A., Harris J. S., *Appl. Phys. Lett.* **2000,** *76*, 239.

[18] Gwo S*., J. Phys. Chem. Solids* **2001**, *62*, 1673.

[19] Garcia R., Martinez R. V., Martinez J., *Chem. Soc. Rev.,* **2006**, *35*, 29.

[20] García R., Calleja M., and Rohrer H., *J. Appl. Phys.,* **1999,** *86*, 4.

[21] Calleja M., García R., *Appl. Phys. Lett.* **2000,** *76*, 3427.

[22] Avouris Ph., Martel R., Hertel T., Sandstrom R., *Appl. Phys.* **1998,** *66*, 659.

[23] Minne S.C., Soh H.T., Flueckiger Ph., Quate C.F., *Appl. Phys. Lett.,* **1995**, *66,* 703.

[24] Calleja M, Anguita J, García R, Birkelund K, Pérez-Murano F, Dagata J A. *Nanotechnology* **1999,** *10,* 34.

[25] Martinez R. V., Garcia R., *Nano Lett.*, **2005**, *5*, 6.

[26] Jang J., Schatz G.C., Ratner M.A., *J. Chem. Phys.* **2002**, *116*, 3875.

[27] Xie X.N., Chung H.J., Sow C.H., Wee A.T.S. *Materials Science and Engineering*, **2006**, *54* 1.

[28] Dorn A., Sigrist M., Fuhrer A., Ihn T., Heinzel T., Ensslin K., Wegscheider W., Bichler M., *Appl. Phys. Lett*. **2002**, *80*, 252.

[29] a) Cooper E. B., Manalis S. R., Fang H., Dai H., Matsumoto K., Minne S. C., Hunt T., Quate C. F., *Appl. Phys. Lett.*, **1999,** *75*, 3566. b) Chien F. S., Wu C. L., Chou Y.-C., Chen T. T., Gwo S., Hsieh W.-F., *Appl. Phys. Lett.,* **1999**, *75*, 2429. c) Matsumoto K., Gotoh Y., Maeda T., Dagata J. A., Harris J. S., *Appl. Phys. Lett.,* **2000**, *76*, 239. d) Clement N., Tonneau D., Dallaporta H., Bouchiat V., Fraboulet D., Mariole D., Guatier J., Safarov V., *Physica E* (Amsterdam), **2002**, *13*, 999. f) Villarroya M., Perez-Murano F., Martín C., Davis Z., Boisen A., Esteve J., Figueras E., Montserrat J., Varonil N., *Nanotechnology*, **2004**, *15*, 771. g) Chen C. F., Tzeng S. D., Chen H. Y., Gwo S., *Opt. Lett.,* **2005**, *30*, 652. h) Snow E. S., Campbell P. M., Rendell R. W., Buot F. A., Park D., Marrian C. R. K., Magno R., *Appl. Phys. Lett.,* **1998**, *72*, 3071.

[30] Martínez R. V., García F., García R., Coronado E., Forment-Aliaga A., Romero F. M., Tatay S., *Adv. Mater.* **2007**, *19*, 291.

[31] a) Martínez R. V., Martínez J., Chiesa M., García R., Coronado E., Pinilla-Cienfuegos E., Tatay S., *Adv. Mater.* **2010**, *22*, 588. b) Yoshinobu T., Suzuki J., Kurooka H., Moon W. C., Iwasaki H., *Electrochim. Acta* **2003**, *48*, 3131.

[32] Zheng J., Zhu Z., Chen H., Liu Z., *Langmuir* **2000,** *16,* 4409.

[33] a) Hoeppener S., Maoz R., Coen S. R., Chi L., Fuchs H., Sagiv J. *Adv. Mater.* **2002**, *14*, 1036. b) Liu S., Maoz R., Sagiv J., *Nano Lett.* **2004**, *4*, 845.

[34] Saavedra H. M., Mullen T. J., Zhang P., Dewey D. C., Claridge S. A., Weiss P. S., *Rep. Prog. Phys.* **2010,** *73*, 036501.

[35] Ginger D. S., Zhang H., and Mirkin C. A., *Angew. Chem. Int. Ed.* **2004**, *43*, 30.

[36] Ben Ali M., OndarPuhu T., Brust M., Joachim C., *Langmuir* **2002**, *18,* 872.

[37] Garno J. C., Yang Y. Y., Amro N. A., Cruchon-Dupeyrat S., Chen S. W., Liu G.-Y., *Nano Lett.* **2003**, *3*, 389.

[38] Bellido E., Ojea-Jiménez I., Ghirri A., Alvino C., Candini A., Puntes V., Affronte M., Domingo N., Ruiz-Molina D., *Langmuir* **2012**, *28*, 12400.

[39] a) Nanoink, 1335 W. Randolph St., Chicago, IL 60607, www.nanoink.net. b) Mirkin C.A., Piner R.D., Hong S., US Patent, #6635311, **2003**.

[40] Xia Y., Whitesides G. M., *Annual Review of Materials Science*, **1998**, *28*,153.

[41] Kim H., Jung M., Myung S., Jung D., Lee S. S., Kong K., Lim J., Lee J., Park C. Y., An K. S., *J. Mater. Chem. C,* **2013**, *1,* 1076.

[42] Weibel D. B., DiLuzio W. R., Whitesides G. M., *Nature Reviews Microbiology*, **2007**, *5*, 209.

[43] Rogers, J. A. et al. *Proc. Natl. Acad. Sci.* **2001**, *98*, 4835.

[44] a) Kumar, A., Whitesides, G. M. *Appl. Phys. Lett.* **1993**, *63*, 2002. b) Geissler, M.; Wolf, H.; Stutz, R.; Delamarche, E.; Grummt, U.-W.; Michel, B.; Bietsch, A. *Langmuir* **2003**, *19*, 6301. c) Geissler, M.; Schmid, H.; Bietsch, A.; Michel, B.; Delamarche, E. *Langmuir* **2002**, *18*, 2374. d) Xia, Y.; Whitesides, G. M. *J. Am. Chem. Soc.* **1995**, *117*, 3274. e) Biebuyck, H. A.; Larsen, N. B.; Delamarche, E.; Michel, B. *IBM J. Res. Dev.* **1997**, *41*, 159. f) Li, S. P.; Natali, M.; Lebib, A.; Pepin, A.; Chen, Y.; Xu, Y. B. *J. Magn. Magn. Mater*. **2002**, *241*, 447.

[45] Rogers, J. A.; Baldwin, K.; Bao, Z.; Dodabalapur, A.; Raju, V. R.; Ewing, J.; Amundson, K. *Mater. Res. Soc. Symp. Proc.* **2001**, *660*, JJ7 1/1.

[46] Jackman, R. J., Wilbur, J. L., Whitesides, G. M. *Science,* **1995***, 269*, 664.

[47] Perl, A., Reinhoudt, D. N., Huskens, J., *Adv. Mater.* **2009,** *21*, 2257.

[48] Cavallini M., Biscarini F., *Nano Lett.,* **2003,** *3*, 9.

2

LOCAL OXIDATION NANOLITHOGRAPHY ON 2D CRYSTALS

2.1 INTRODUCTION

The rocketing development of the research devoted to graphene has opened an entire new field that explores the physics underlying atomically thin layers. For a long time, this has left aside a plethora of interesting two-dimensional (2D) layered materials that could match or even outweigh the properties of graphene.[1] Among them, transition metal dichalcogenides (TMDCs) have gained new interest thanks to recent advances in nanoscale materials characterization and fabrication of ultrathin, transparent and flexible electronic devices that have opened up new opportunities for thin 2D layers of TMDCs to be integrated in such devices.[2]

TMDCs have a general formula of MX_2, were M is a transition metal (typically Mo, Ta, W, Nb, Re, Ni, or V) and X is a chalcogenide (typically S, Se, or Te).[3] They consist of a vast family of layered materials (more than 40 different categories) with excellent exfoliation properties and whose electrical, optical and magnetic behaviors drastically vary from one to another depending on the chemical composition. Indeed, materials of this family range from wide band-gap semiconductors as MoS_2, to metallic conductors and superconductors as TaS_2.[4]

TMDCs are layered materials form by the stacking of three atom thick MX_2 layers in the c direction. Inside each MX_2 sheet, there is an hexagonal packing in the ab plane of each metal coordinated by six chalcogen atoms by means of strong covalent bonding. Adjacent sheets are coupled through weak van der Waals forces, leading to hexagonal layers with large c-axis constant and strongly anisotropic properties. This particular structure permits their exfoliation into monolayers or few layer stacks that became a fundamental requirement for their incorporation into nanoscale devices. The order of stacking of the MX_2 sheets originates a wide variety of polytypes. In particular four different layered TMDCs will be studied in this thesis: TaS_2, $TaSe_2$, $NbSe_2$ and NbS_2 (Figure 1).
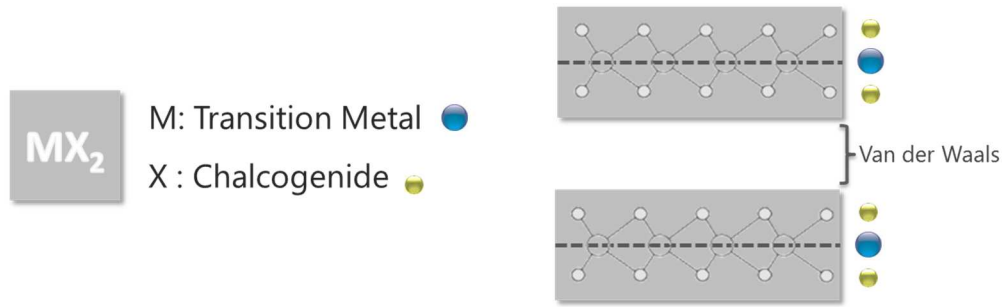
Figure 1. Schematic representation of the TMDC layers. Stack of two TMDC layers made out of chalcogen (X, yellow spheres) and metal (M, grey spheres) sheets. Van der Waals forces are present between the layers.

Among the four chalcogenides under study in this thesis, **TaS₂** is a layered material of the TMDC family that in bulk, exhibits metallic conductivity at ambient conditions and presents a transition to a superconducting state at lower temperatures.[5] The interest on this particular TMDC is based not only on its switchable electronic properties but also in the high crystallinity of its atomically-thin flakes, on their robustness in comparison with other TMDCs and also in the rich, versatile and reproducible polymorphic chemistry exhibited.

As already mentioned, a wide variety of polytypes are originated from the orderly stacking of layers with a certain periodicity, and they are classified in base on the distinct piling orders and identified with a prefix. Different polytypes of the same TMDCs show different properties. For example, the 2H-TaS₂ polytype structure shows a superconducting transition temperature of $T_c = 0.8$ K and presents anisotropic charge-density-wave (CDW) patterns at the surface. These CDW are indeed observable at room temperature for the 1T-TaS₂ polytype. Scanning tunneling microscopy (STM) measurements at ambient conditions were successfully performed onto a 1T-TaS₂ crystal surface and the mentioned CDW were observed (Figure 2).
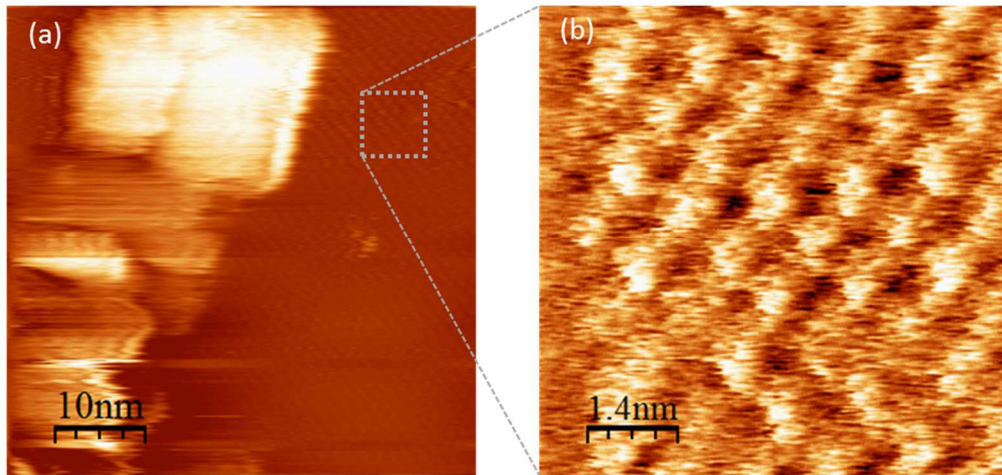
Figure 2. Observation of CDW on a 1T-TaS$_2$ crystal. (a) STM topography image acquired at tunneling current, I$_t$ = 2.2 nA and -100 mV bias. Image size: 50 nm x 50 nm. (b) STM current image of a zoomed area of (a) acquired at tunneling current, I$_t$ = 2.42 nA and -285 mV bias. Image size: 7 nm x 7 nm.

The 2H polymorph of TaS$_2$ was the structure chosen to be studied in this thesis. Its bilayer stack structure is shown in Figure 3a.

Among the systems which exhibits CDW behavior, **TaSe$_2$** is one of the most interesting systems because it shows both incommensurate and commensurate density-wave phases (between 122 K and 90 K) and a superconducting transition temperature, T$_c$, below 0.15 K.[6] In Figure 3b the structure of 2H and 1T polytypes are shown. In this thesis, we will work with the polymorph 2H-TaSe$_2$.

NbSe$_2$ is a layered TMDC and its polytype 2H-NbSe$_2$ exhibits a CDW developed at a temperature, T$_{CDW}$ = 33 K. It also becomes a prototypical anisotropic s-wave superconductor below 7.2 K. The coexistence of the density wave and superconducting phases and the nature of their interplay has been a subject of much recent interest, especially in the context of competing order in strongly correlated systems. [7] 2H-NbSe$_2$ polytype has been used in this thesis.

NbS$_2$ is a metal irrespective of the layer thickness and presents a superconducting transition temperature similar to 2H-NbSe$_2$.[8] The 2H-NbS$_2$ polymorph is the only superconducting 2H-dichalcogenide which does not develop a charge density wave.[9] The 2H-NbS$_2$ will be here studied and its structure is shown in Figure 3c. The niobium atoms are surrounded by sulphur atoms following a trigonal prismatic coordination.
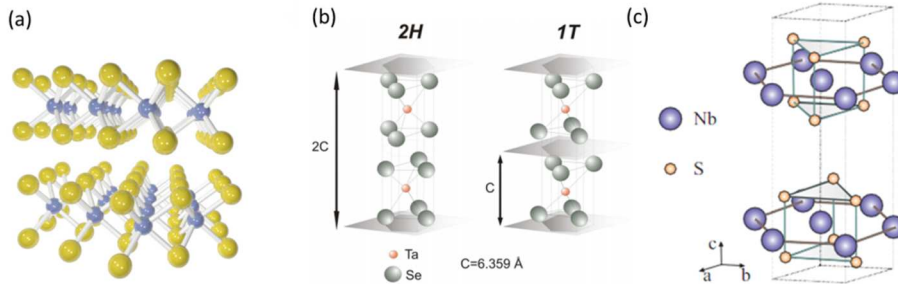

Figure 3. (a) 3D rendered view based on X-Ray crystallography data of 2H-TaS$_2$. Bi-layer stack showing the relative orientation of the two crystallographically non-equivalent TaS$_2$ planes in a 2H crystal. Sulphur atoms are shown as yellow spheres and tantalum atoms as smaller blue spheres (From Dr. Efrén Navarro-Moratalla PhD thesis). (b) TaSe$_2$ layered hexagonal structure. The unit cell consists of two sandwiches of Se-Nb-Se. The two possible polytypes of TaSe$_2$ are shown, the 2H and 1T phases, which consist of two TaSe$_2$ hexagonal prisms rotated with respect to each other, and one trigonal prism. Selenium atoms are shown as gray spheres and tantalum atoms as smaller red spheres. Extracted from reference [6b] (c) Structure of 2H-NbS$_2$. The niobium atoms (blue spheres) are surrounded by sulphur atoms (small orange spheres) following a trigonal prismatic coordination. Extracted from reference [9]

The development of heterostructures and devices by stacking 2D crystals on top of each other (Van der Waals heterostructures) is a new research field, recently emerged, that has gained strength over the past two years as it offers alternative solutions for graphene weaknesses.[10] All the presented TMDCs are good candidates for this new approach where the result is a "multi-sandwich" in which each layer, made of a different component, confers a property giving rise to a multifunctional material (Figure 4). This idea is the dreamscape, but it has some difficulties to overcome as for example, finding a feasible efficient and scalable procedure to isolate and stack up the 2D crystals in perfectly aligned multilayers, or to avoid the interfacial contamination

between the layers. It has been already reported some "bottom-up" examples of graphene, 2D boron nitride (2D hBN) and molybdenum disulfide (2D MoS_2) epitaxially growth on top of each other.[11] However, it is a daunting task to find the right conditions for the so-called Van der Waals epitaxy[12] because the weak interlayer interaction generally favors island growth rather than continuous monolayers. Another scalable approach would be layer-by-layer deposition from 2D-crystal suspensions by using Langmuir–Blodgett or similar techniques.

All in all, the integration and combination of nanocomponents of different nature into novel hybrid systems, opens many possibilities for the design and creation of new multifunctional nanomaterials. In that aspect, another route for the development of multicomponent heterostructured materials is proposed in this thesis. The method consists on a "top-down" approach by the manipulation of the chemical nature of the TMDCs surfaces via Scanning Probe Microscopies (SPMs) to produce two-component surfaces formed by metallic TMDCs and insulating oxide motifs.[13] As introduced in chapter 1, SPM methodologies have been widely used for the creation of oxide patterns onto surfaces and provide a useful lithograph technique at the nanoscale with high accuracy and versatility that has been probed for many materials.[14] In particular, the use of the local oxidation nanolithography with the atomic force microscope (LON-AFM) has been already used on graphene and graphene oxide flakes.[15, 16] Although both STM and AFM have been proposed tools for mechanically processing the surface of some TMDCs bulk crystals,[17, 18] little has been reported regarding the LON on ultrathin flakes.
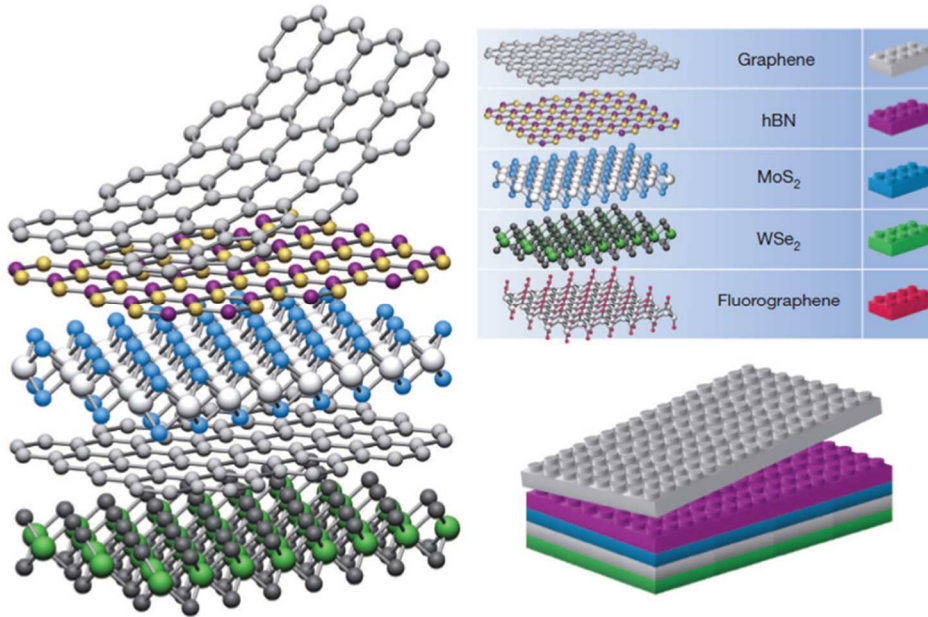
Figure 4. Building van der Waals heterostructures. If one considers 2D crystals to be analogous to Lego blocks (right panel), the construction of a huge variety of layered structures becomes possible. Conceptually, this atomic-scale Lego resembles molecular beam epitaxy but employs different 'construction' rules and a distinct set of materials. Extracted from reference [10]

The experimental design for the LON-AFM on 2D systems requires, as a first step, the isolation and transfer of single or few layers of metallic TMDCs to flat surfaces. In these sense, the four materials introduced in this section TaS_2, $TaSe_2$, $NbSe_2$ and NbS_2, accomplish the requirements because they exhibit metallic behavior at ambient conditions and, as layered materials, they typically cleave due to the weak van der Waals interaction between their coupled neighboring layers.

The pioneering works published by Novoselov et al. gave rise to the isolation of single layers of graphene. They reported the repeated peeling of high oriented pyrolitic graphite (HOPG) on a photoresist layer and the final release of the resulting thin flakes in acetone. This method was later improved and the 'dry' exfoliation of a

manifold of layered materials by simply rubbing the surface of crystalline samples against different surfaces was reported.[19] This basic methodology gave access to large surface area flakes of atomically-thin graphene and also to flakes of certain TMDCs. The technique, soon expanded, was implemented in a variety of different ways under the generic name of micro-mechanical cleavage or exfoliation or, more informally, *Scotch tape* method.

The following decade experienced the development of a great variety of different mechanical cleavage approaches for the clean deposition of extended graphene layers as well as many other layered materials on distinct surfaces. Among them we can highlight micromechanical exfoliation techniques based on the use of silicone stamps[20] and the so-called anodic bonding.[21] At the same time the "bottom-up" approach started attracting big interest. In this way, a lot of research is nowadays being devoted to the growth of large-surface-area graphene films on a variety of surfaces by chemical vapor deposition (CVD) process.[22] But there are many other methods like the dry transfer of epitaxial graphene onto surfaces[23] or the technique based on the laser thinning of TMDC flakes by the use of the laser source used for Raman spectroscopy, recently reported[24] that belong to a wide group of methodologies devoted to the transfer and/or the production of clean and isolated layers of 2D layered materials onto surfaces.

Among the mentioned micromechanical exfoliation methods, the great simplicity together with the relatively high efficiency of the *Scotch-tape* method was the method chosen by us to prepare thin flakes of TMDCs. Unfortunately our first attempts with the TaS$_2$ appeared to be less easily exfoliated by conventional *Scotch tape* procedure than graphene. This fact moved us to develop a new methodology inspired on the original *Scotch tape* but with some modifications to adapt it for the exfoliation of our chosen TMDCs crystals. The new approach named "Nanopress" relies in the same fundation: direct contact physisorption of the 2D crystals with the target surface. However, a few technical upgrades were incorporated in order to improve the control

of the experimental conditions that rule TMDC flake deposition. Finally, the deposition of good quality flakes of any 2D layered material onto an arbitrary substrate turned out to be a sheer question of ameliorating the control over the "drawing by chalk on a blackboard" procedure.

2.2 RESULTS AND DISCUSSION

2.2.1 Design of a new method of exfoliation: the Nanopress

The Nanopress[25] is a device that was assembled due to our need to develop an efficient methodology for the delamination of 2D layered materials in a reproducible way (Figure 5). Its use, enabled us to reach an accurate control at any step of the cleaving process and to fix the proper parameters for the exfoliation of each material in combination to a target substrate. Moreover, it made possible to obtain ultrathin isolated layers of TaS_2 that were not feasible with the *Scotch Tape* method.
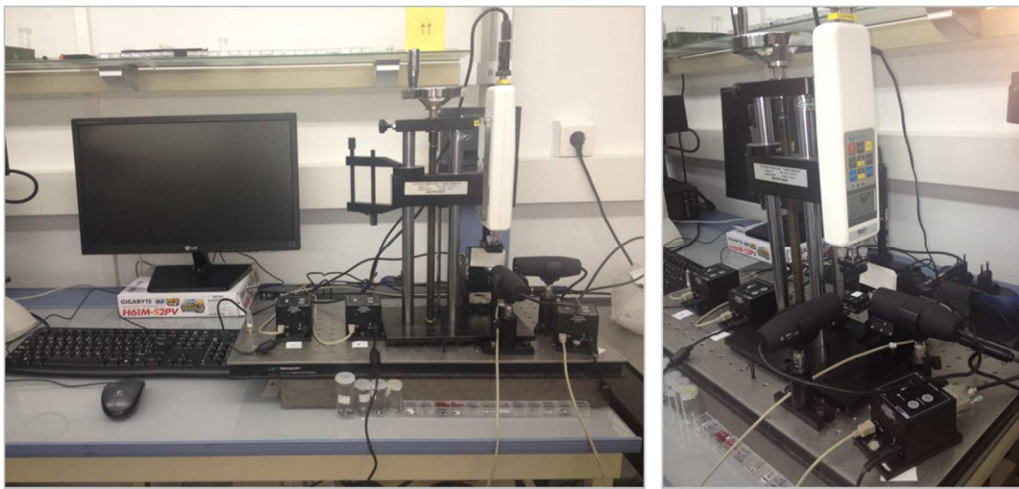

Figure 5. Pictures of the Nanopress device.

The method of exfoliation is based in the principle of a stamp: putting in direct contact the "stamp" (the layered 2D crystal) with a substrate, making a certain pressure over the system and then release it by removing the "stamp". The delivered "ink" would be, in the best case, a single monolayer corresponding to the outermost layer of the crystal

although, it actually uses to be a plethora of stacks with different number of layers and shapes (Figure 6a). We soon discovered that the efficiency improved when the pressure was combined with a lateral movement. This "press and shear" method became the better choice for most of the materials. This way, it was possible to find isolated thin layers of TMDCs spread over the substrate which quantity and quality depended on the experimental conditions (Figure 6b).
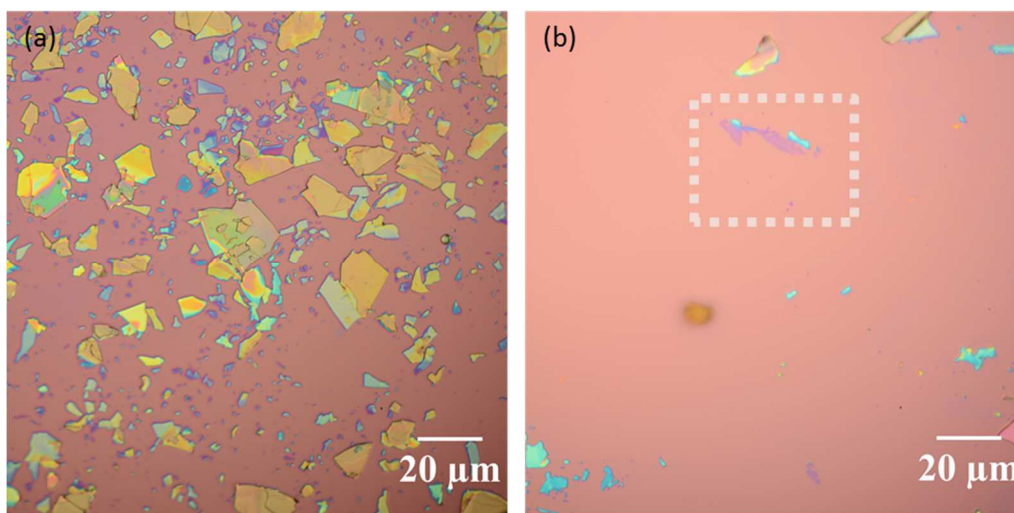

Figure 6. Representing episcopy optical images (100 x) of the results of the exfoliation of TaS_2 onto SiO_2 substrates with the Nanopress. (a) The dispersion of sizes and flake thickness depended on the experimental parameters. (b) The dashed square highlights the presence of isolated of TaS_2 with purpled contrast characteristic of thin layers.

2.2.1.1 Setup design

The 2D crystal is usually glued on a Polydimethylsiloxane (PDMS) block that facilitates the accommodation of the crystal to the substrate when they are put in contact, thanks to its viscoelastic properties. The PDMS/crystal system is mounted onto a glass substrate to be able to assemble it onto a sample holder (Figure 7a).

A schematic view of the experiment is summarized in Figure 7b. First the crystal and substrate are mounted in the holders and alignment of both surfaces is made with tilts adjusters placed on the holders (step i). Then, both surfaces are put in direct contact exerting a certain normal pressure (step ii). At this step, the pressure is kept for some minutes until it stabilizes. Once the system is stable, a lateral movement is applied to the substrate promoting the exfoliation of the crystal (step iii) and finally, the pressure is released as the crystal is detached from the substrate with a vertical movement.
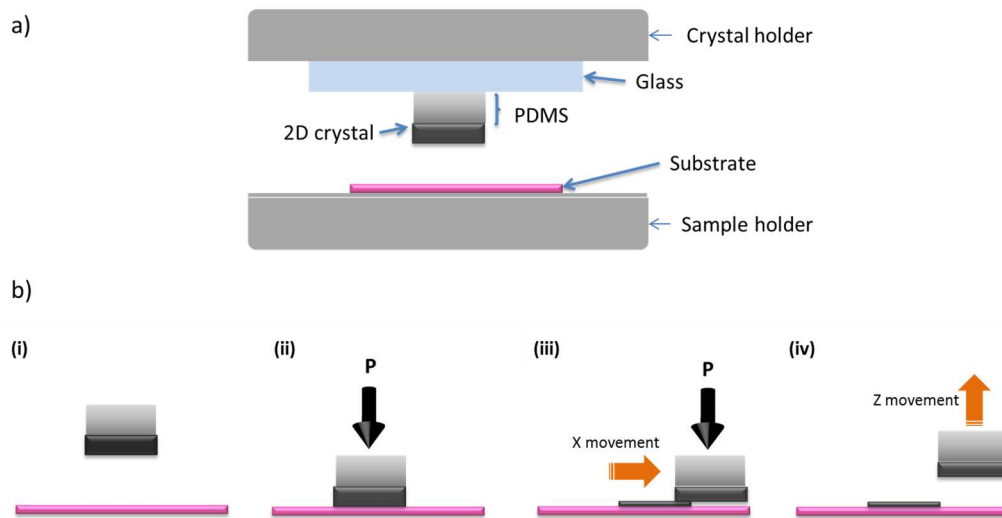

Figure 7. (a) Schematics of the different parts of the Nanopress mounting. (b) Schematic views of the steps of the "press and shear" exfoliation.

Many parameters are involved in this process. Thus, to be able to have access and control over most of them, the device was equipped with several tools. The general design is shown in Figure 8. First, the dynamometer, a digital force gauge with a maximum load of 2 N and a resolution of 0.001 N, is mounted on a test stand equipped with a crank handle to allow the coarse approximation. A second dynamometer with a maximum load of 25 N and resolution of 0,1 N is also available

and compatible with the system. The dynamometer has a LCD display where the real time pressure value was shown. The dynamometer is also connected through a R232 port to a computer where the force data is collected and recorded via software. Kinematic mirror mounts with tilting adjusters have been chosen as holder for both, crystal and substrate, to allow the alignment of the surfaces. The crystal holder is screwed to the dynamometer while the sample holder is screwed to the motorized platform. This XYZ platform is motorized by three independent step-motor actuators that provide a 3D movement to the sample and are connected to the computer via USB. They have a maximum travel of 12 mm and sub-micron resolution, and the speed and acceleration can be set with maximum values of 3 mm/s and 4 mm/s^2, respectively. The movement of the actuators can be controlled manually or by software. The acquisition software permits also to program the experiment and to predefine repetitive movements by controlling time, speed and acceleration. Two optical microscopes mounted on adjustable height posts completed the whole setup. They are connected to the PC via USB and are situated at 90° to facilitate the correct alignment of the system crystal/substrate. They also allow the capture of the image as well as video recording. Finally, all the parts are securely screwed to an optical platform to confer stability.
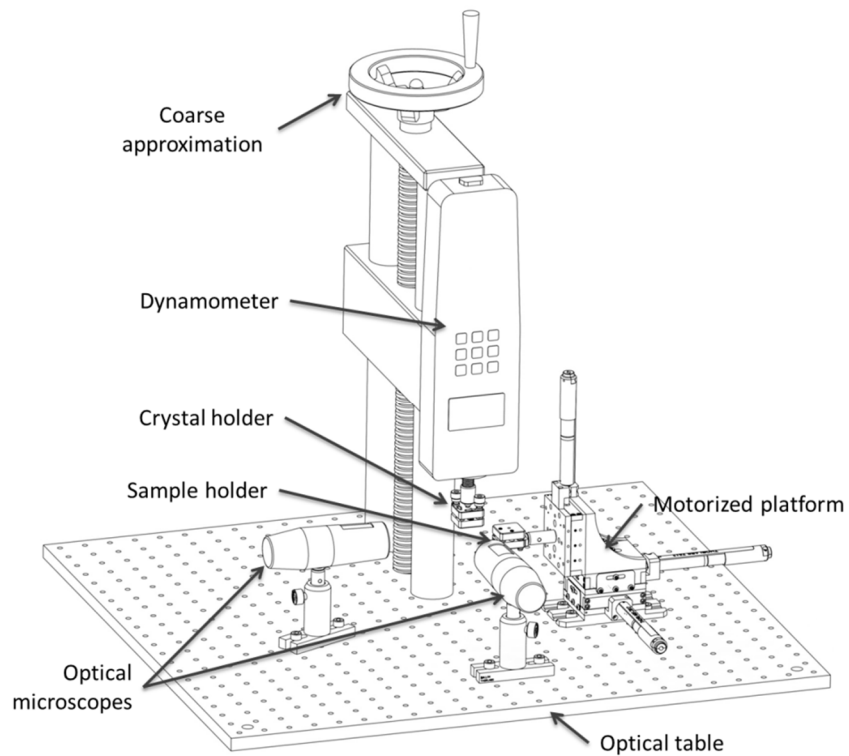
Figure 8. Schematic view of the Nanopress design with the main parts.

The levelling of the surfaces of both, crystal and substrate is one of the keys in the "press and share" experiment. The tilts adjusters of the holders (Figure 9a) combined with the optical access provide by the microscopes allow a rough measure of the real inclinations of the surfaces and thus, this is the less controllable factor involved in the method. When the tilting angles to the X,Y axes are too high, the pressure is not homogeneously applied over the 2D crystal, resulting in an irregular deposition that sometimes produces damages onto the crystal surface (Figure 9b). The PDMS block is used to facilitate the accommodation of the crystal to the substrate and to minimize as much as possible the effects of a non-perfect coplanarity. When the levelling is made,

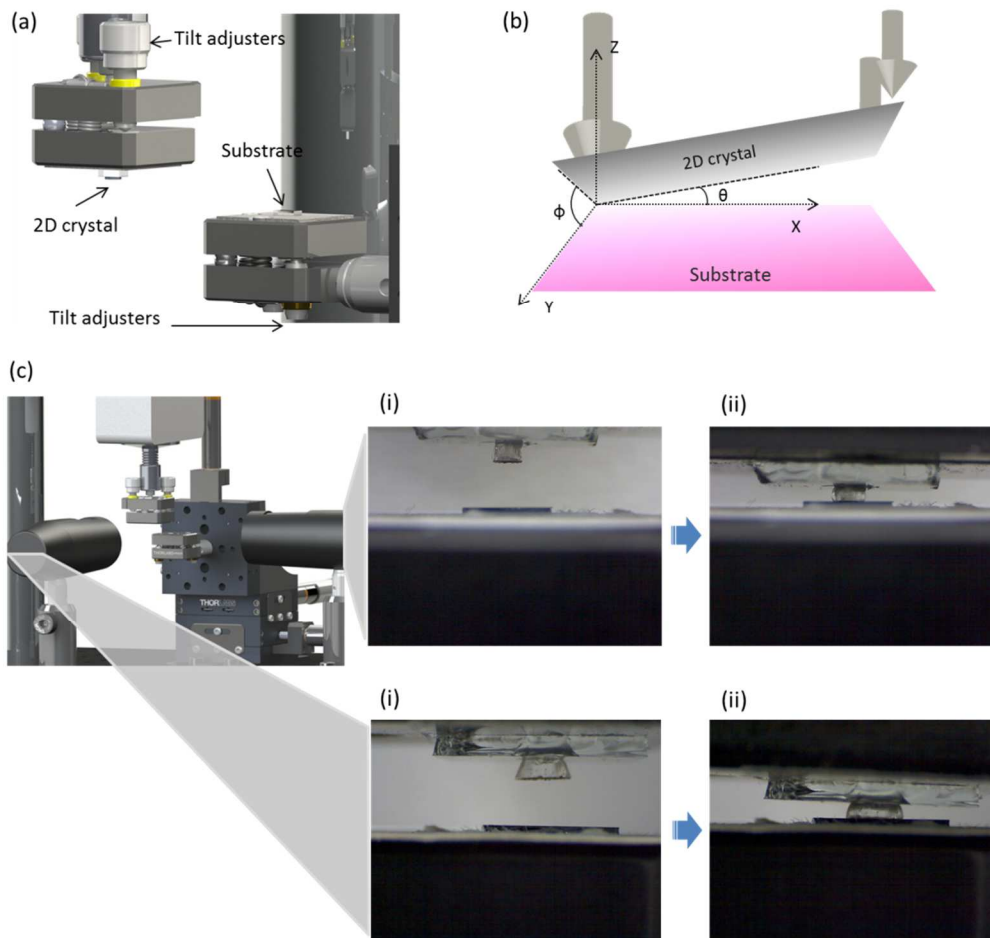the whole process could be seen and recorded by the two optical microscopes situated at 90° (Figure 9c).

Figure 9. (a) 3D rendered view of the position of the holders. (b) Schematic representation of the tilts between the two surfaces. θ is the tilting angle to the X axis and Φ is the tilting angle to the Y axis. The arrows represent the different pressure exerted to the crystal/substrate system due to the tilt between them. (c) 3D rendered view of the optical system situated at 90° to facilitate the surface levelling and to record the experiment. Steps (i) and (ii) are shown with real pictures taken from the two microscopes.

It is important to emphasize that the crystal is always in direct contact with the substrate. In contrast with the *Scotch Tape* method or the silicon stamp assisted

method, our method is clean as no glue or sticky tape are involved. The piece of PDMS used in our method is carefully cut and the crystal stands outs the borders of the PDMS, preventing it to contact the substrate at any moment of the exfoliation process.

2.2.1.2 Experimental results

The first experiments were carried out with TaS_2. The possibility to have TaS_2 donor crystals (grown by chemical vapor transport, CVT) with large surface areas was crucial in order to be able to handle them for their integration in the device. Experiments with thick crystals of few millimeters as well as with thin crystals of several microns were performed. At the very first moment, we thought that thinning the crystals would benefit the deposition of thinner patches but, in turn it was found that the method worked better with thicker crystals.

The TaS_2 donor crystal was conveniently exfoliated, usually by *Scotch tape* to assure a clean surface and then it was glued to a piece of PDMS by a resin epoxy keeping the clean surface face up. The cleaning of the substrate was also very important and depending on the material, a proper cleaning process was chosen (see section 2.3 for details). In particular, the cleaning of silicon substrates (Si or SiO_2)[1] through sonication in basic "piranha" solution also conferred a certain surface passivation which turned out to be benefit for the deposition of thin patches of TaS_2.

As already mentioned, many parameters can influence on the cleaving experiment. Hence, series of tests varying these parameters were carried out to find the best choice to exfoliate the TaS_2 into thin layers. Some of the experiments were *static*, (the crystal was pressed against the substrate without lateral movement) while others were *dynamic* (where the substrate was moved laterally). The movement varied from

---

[1] Due to the working conditions (ambient) the silicon substrates will be always covered by its native oxide (*c.a.* 1-2 nm). When we refer to SiO_2 substrates, we will refer to the substrates with a layer between 200 nm – 285 nm thermally growth onto silicon.

unidirectional movement to back-and-forth movement, and could be continuous or made by steps. So at every experiment, the checked parameters were conveniently recorded and summarized in tables: pressure, time of exerted pressure before applying the lateral movement, speed and acceleration of the movement, movement direction with respect to the crystal (X direction or Y direction), and number and length of steps for the stepping mode.

As an example, we will discuss the experiments performed with TaS_2 thick crystal exfoliated in the following conditions: two consecutive back-and-forth movements, one performed in the X axis and the other in the Y axis in different positions of the substrate, at maximum values of speed and acceleration (3 mm/s and 4 mm/s^2, respectively). The length of the steps was 200 µm in both cases and the applied force was 1.5 N. The crystal was exfoliated onto a SiO_2 substrate (285 nm SiO_2).

The experiment was recorded in a plot of force versus time, shown in Figure 10. Once the two surfaces (TaS_2 crystal/SiO_2 substrate) were situated on top of each other and the tilting correction was adjusted, the manual approach was made by the hand-wheel stage, approaching the crystal to the substrate until a smooth force between crystal and substrate was measured in the dynamometer (in the order of few milinewtons). This instant can be seen in the plot as a step (highlighted by dashed circles). Then, a fine vertical approach was made by moving the substrate against the crystal with the Z motorized actuator by consecutive steps until the target force of 1.5 N was reached. This process is recorded in the plot as small consecutive steps. Then, few seconds were needed until the pressure was stabilized. The back-and-forth movement was then made by the X, Y motorized actuators, while the lecture of the real time value of the pressure was monitored by software. As can be seen in the plot, the back-and-forth steps produce, at each exfoliation experiment, some fluctuations in the applied force. The negative values of the force were due to the pushing, while the positive values were pre-exfoliation experiment, due to the tare of the holder + crystal system.
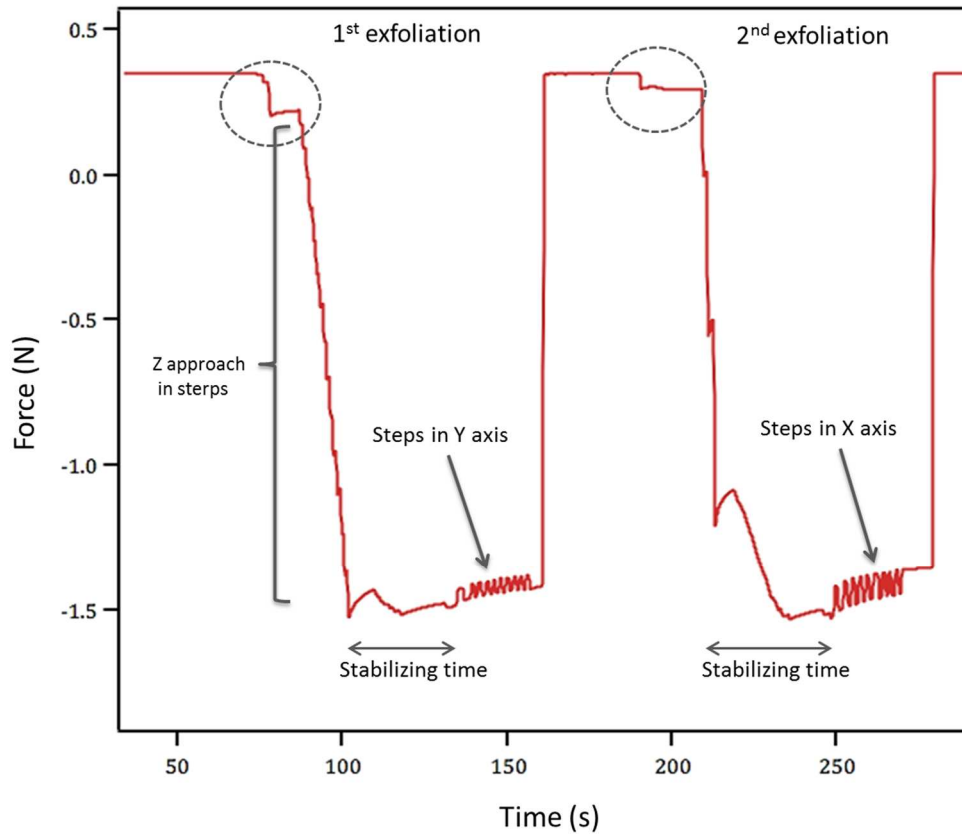
Figure 10. Force versus time plot of two exfoliation experiments on TaS_2. The force negative values denote the pushing force while the positive are due to the tare.

The results of the exfoliation experiments were evaluated by optical microscopy and, when the quality and quantity of exfoliated patches were found acceptable, a detailed characterization of the transferred flakes was made by means of AFM. In this case, series of very thin flakes exhibiting low contrast at the optical microscope were found, typical for thin layers (Figure 11a and Figure 11b). They were inspected by AFM (Figure 11c), and it was confirmed the cleavage and deposition of several isolated

patches with very good quality (smooth and clean surfaces) and with large surface areas. Calculating the probability density distribution of heights, it was found several atomically thin flakes of (1.5 ± 0.5) nm (Figure 11d).
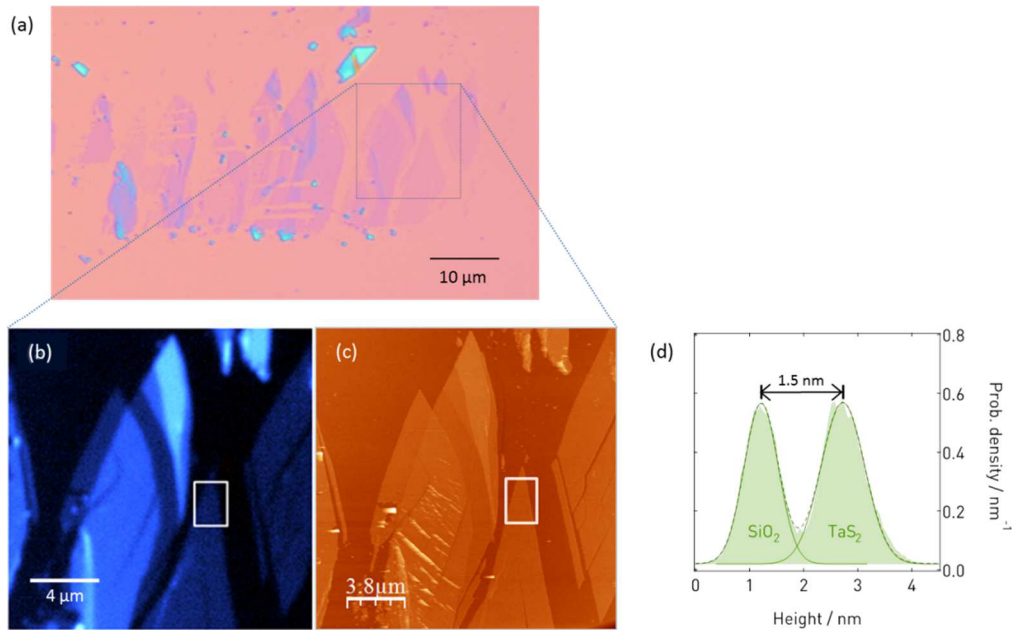

Figure 11. (a) Optical image of atomically thin flakes of TaS_2 deposited on a 285 nm SiO_2 substrate. (a) Optical image acquired with a filter of illumination wavelength of 600 nm. (b) AFM topography image of the same area as (b). (d) Plot of the probability density distribution of heights in the marked area on (b) and (c).

The exfoliation of TaS_2 over different substrates was successfully performed. Some prerequisites have to be accomplished in order to be able to exfoliate atomically thin flakes of 2D layered crystals onto substrates, like flatness and cleanliness. Silicon surfaces created by the selective etching of SiO_2 native oxide of the Si (100) substrates, p-doped Si (100) with 285 nm oxide layer and evaporated gold on silicon substrates are good examples. Results of the exfoliation of TaS_2 onto these substrates are summarized in Figure 12, where optical images as well as AFM images were performed to characterize the exfoliated layers.
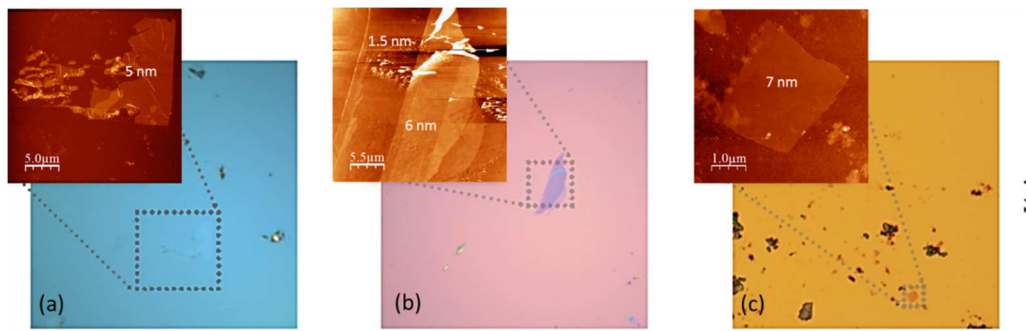
Figure 12. Top: AFM topography images, bottom: optical images. (a) TaS$_2$ flakes onto an etched Si substrate, (b) TaS$_2$ flakes onto a SiO$_2$ substrate and (c) TaS$_2$ flakes onto an Au substrate.

Concerning the contrast formed in the optical images, it is known that the inspection of the samples under an optical microscope enables quick identification of the flakes and their size. In addition, it is possible to get a rough estimation of the thickness of the flakes due to a light interference effect owing to the presence of the thin silicon oxide layer, which makes their color thickness-dependent under white light illumination.[26] The thinnest flakes deposited on Si exhibited a very weak optical contrast (see Figure 12a). It was very difficult to detect very thin layers onto Si substrates (or Si substrates covered with its native oxide) by the optical microscope. On the other hand, if the deposition of the TaS$_2$ flakes were performed onto Si substrates covered with an oxide layer with a thickness larger than 200 nm, the layers exhibit an enhanced optical contrast and were easily detected (Figure 12b).

In summary, the exfoliation of atomically thin layers of TaS$_2$ was only possible by the use of the Nanopress. It could not be achieved by the stamp assisted method of exfoliation, neither by *Scotch Tape*. It can also be highlighted the versatility of the technique, which allowed to fix the experimental parameters for the deposition of TaS$_2$ thin layers on a variety of substrates.

Once probed the viability of the system together with its high efficiency to exfoliate atomically thin layers of TaS_2, this technique was used to exfoliate a wide variety of 2D layered materials. Some examples are shown in the Figure 13.
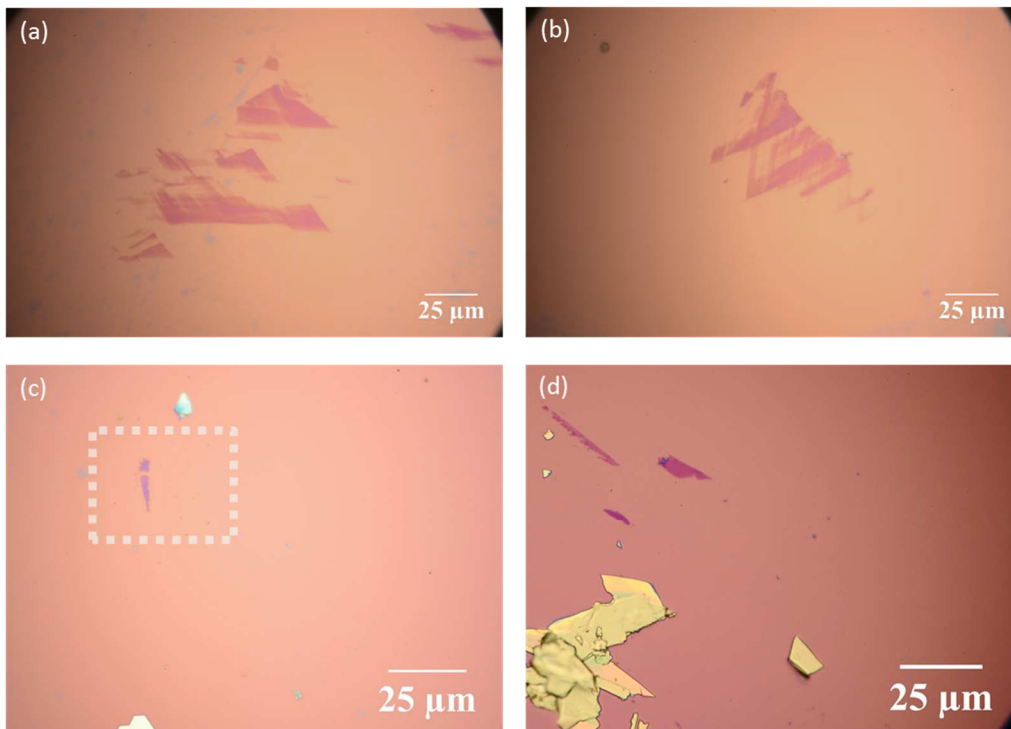

Figure 13. Optical images (100x) of various examples of exfoliation with the Nanopress. (a) and (b) graphene flakes on SiO_2 substrates. (c) MoS_2 single flake on a SiO_2 substrate. (d) NbS_2 flakes on a SiO_2 substrate.

2.2.2 LON on TaS_2

In this section, the manipulation of TaS_2 layers via the AFM-LON technique will be presented. The LON technique was first applied in thick layers of TaS_2 and then, it was extended to atomically thin layers. TaS_2 provided us with a source of room temperature conducting layers, which could be potentially modified at the nanoscale and with a high level of precision by the AFM-LON technique. The oxidation of TaS_2

generates the corresponding metal oxide, Ta_2O_5, which is a high band gap (3.7 eV) insulator widely extended in circuitry and thin-film electronic components.[27]

As mention in chapter 1, LON is a lithography method based on the use of a conductive AFM probe for the fabrication of localized oxide nanostructures. When a voltage pulse is applied through the tip, it induces a water meniscus formed by capillary condensation at the tip-surface interface. This confinement area acts as an electrochemical cell where an oxidation reaction takes place (equation 2.1). In the specific case of the TaS_2, the tip is the cathode, the TaS_2 surface is the anode and the water acts as the electrolyte. A schematic representation of the LON system is shown in Figure 14.
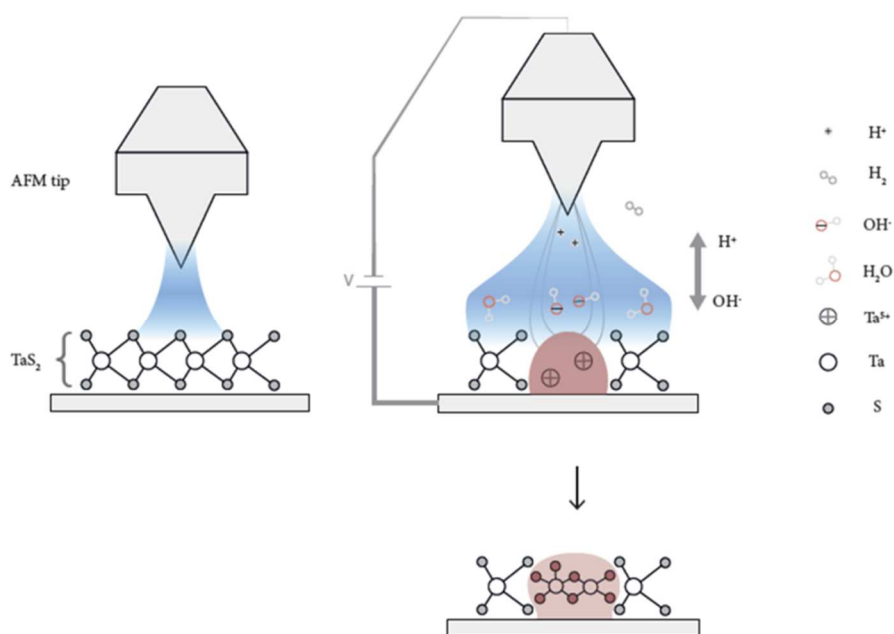
Figure 14. Schematic representation of the electrochemical processes by which LON is ruled: tip approach and meniscus formation on a flake (top left); voltage pulse represented by electric field lines and H^+/OH^- chemical species gradient established along the tip vertical axis (top right). The resulting oxide structure included within the target flake is highlighted in the bottom figure. Notice that the cartoon has been adapted to represent LON on a dichalcogenide TaS_2 single-layer flake.

The specific global equations of the reactions occurring at the cathode (tip) and at the anode (surface) in the specific case of TaS$_2$ could be:

$$2TaS_2 + 5H_2O + 3O_2 \leftrightarrow Ta(OH)_5 + 5/2H_2\uparrow + 2SO_3\uparrow$$

(Eq 2.1)

$$2Ta(OH)_5 \leftrightarrow Ta_2O_5 + 5H_2O$$
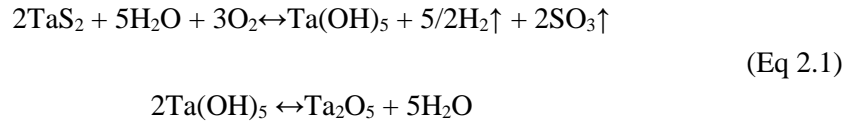
The patterns formed by LON, mainly depend on the relative humidity, the size of the water meniscus, time (t_{ox}) and voltage pulse (V_{ox}) and the scan speed, as well as the nature of the tip and its size. The experiments were carried out at room temperature and the ambient relative humidity of 40-70% by employing a commercial bench-top humidifier. All the LON patterns shown in this thesis are obtained oxidizing at negative tip bias.

The layers of TaS$_2$ were obtained by the press and shear method. As described in section 2.2.1, such methodology required the use of large single crystals of 2H-TaS$_2$ that were grown by CVT (Figure 15a). The Nanopress provided us a plethora of ultra-flat TaS$_2$ patches (RMS = 0.106 nm) within the same substrate (Figure 15b and Figure 15c), being possible to study the LON effects over different samples exhibiting distinct number of layers.
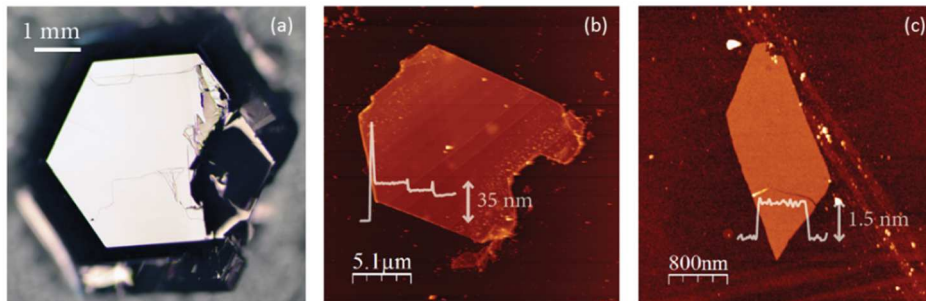

Figure 15. (a) Optical image of a freshly cleaved TaS$_2$ CVT crystal. (b) AFM image and profile of a thick TaS$_2$ flake. (c) AFM image and profile of a TaS$_2$ monolayer.

The sample preparation was always done just before performing the AFM-LON experiment to guarantee a clean surface of the TaS_2 f1akes. Furthermore, water contact angle experiments, that were carried out on freshly cleaved crystals, showed that the exfoliation of the few outermost layers of the single crystal yields a clean surface with remarkable hydrophilicity (Figure 16).
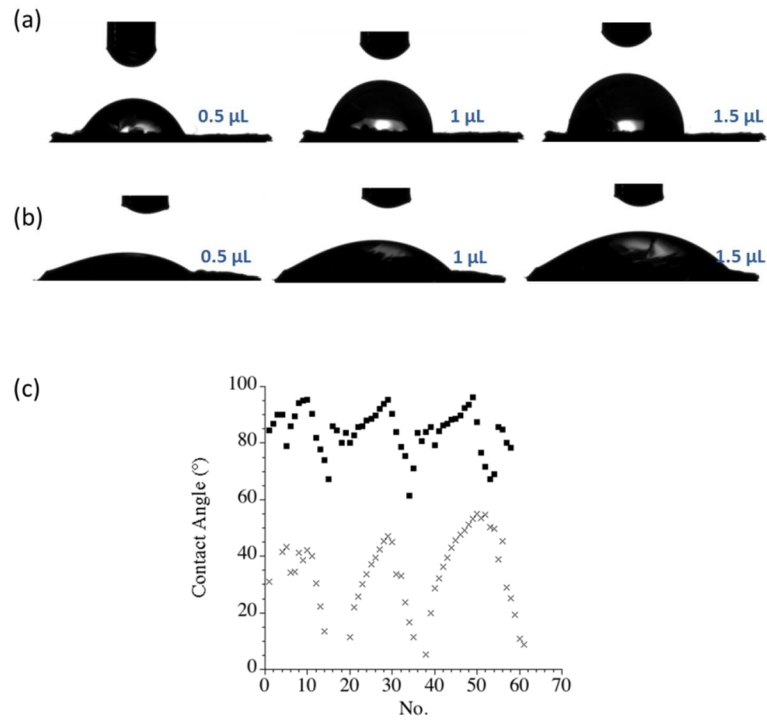

Figure 16. (a) Silhouettes of ultrapure H_2O drops of different volumes laid on the surface of a non-exfoliated large single crystal of TaS_2. (b) Same experiment performed on a freshly cleaved surface of the same TaS_2 crystal. The leading pictures in both cases show the silhouette of the drop at the end of an advancing contact angle run. (c) Advancing/receding contact angle cycles performed on non-cleaved (squares) and on exfoliated TaS_2 surfaces (crosses).

The hydrophilic nature of the sample will influence remarkably the following LON experiments. The structure (height and width) of the oxide patterns is strongly dependent on hydrophobicity, as it influences the spreading of the water on the surface

(thus, influencing in the water meniscus formation). For example, it has been reported that oxide structures formed on hydrophilic functionalized Si surfaces with SAMs tend to be broader. However, hydrophilic surfaces seem to be more suitable for technical applications, as the applied voltage can be reduced and higher tip velocities are possible.[28]

2.2.2.1 LON on thick layers of TaS$_2$

The first experiments were performed on thick layers (> 5 nm). The TaS$_2$ layers were transferred over freshly base-activated Si p-doped substrates. Although single layer crystals on top of native oxide coated Si cannot be detected by the naked eye, flakes as thin as 5 nm may be spotted out by bright-field optical microscope equipped with a DIC prism (as shown in section 2.2.1.2). By scanning of nearby regions via AFM it was revealed the presence of multitude of ultrathin few layer stacks.

The LON experiments on TaS$_2$ thick layers were carried out in ambient conditions using the classical oxidation procedure introduced in chapter 1, in which the tip is oscillating during the process (called from now on: *dynamic-tip* LON). These LON experiments led to massive oxide formations with rippled topographies. These anomalous structures were far from the expected topographies of oxide formations by LON, which usually resemble a homogeneous protrusion whose size depends on the experimental parameters.

The first observation of these similar rippled structures was made by Lyuksyutov et al. in 2003 when they performed LON experiments on n-type silicon surfaces. They observed an anomalously high current during the oxidation process that resulted in the formation of a symmetrical ring around a central spot and suggested that the current involved in the ring formation obeys Ohmic I-V dependence related to an electronic type conductance (unlike the ionic current used in conventional LON). There is then, a threshold bias voltage (V_{th}) at which the breakdown occurs: for $V_{ox} < V_{th}$ only a simple

oxide dot is formed (ionic current) while at $V_{ox} > V_{th}$ the outer ring surrounding the central dot is formed (Ohmic current). The anomalous current is associated with an avalanche breakdown in the part of the space charge layer inside the water meniscus. The authors proposed a possible explanation for the ring formation: the density of electrons inside the meniscus is proportional to the normal component of the electric field, which falls off with the distance from the tip apex. Competition between the recombination of electrons and holes, and the variation in the field-induced hole concentration result in regions of depleted holes and affec the formation of the space charge layer. Hydroxyl ion distribution follows the distribution of the hole concentration, which leads to the oxide growth in the areas where the concentration is maximal (Figure 17).[29]
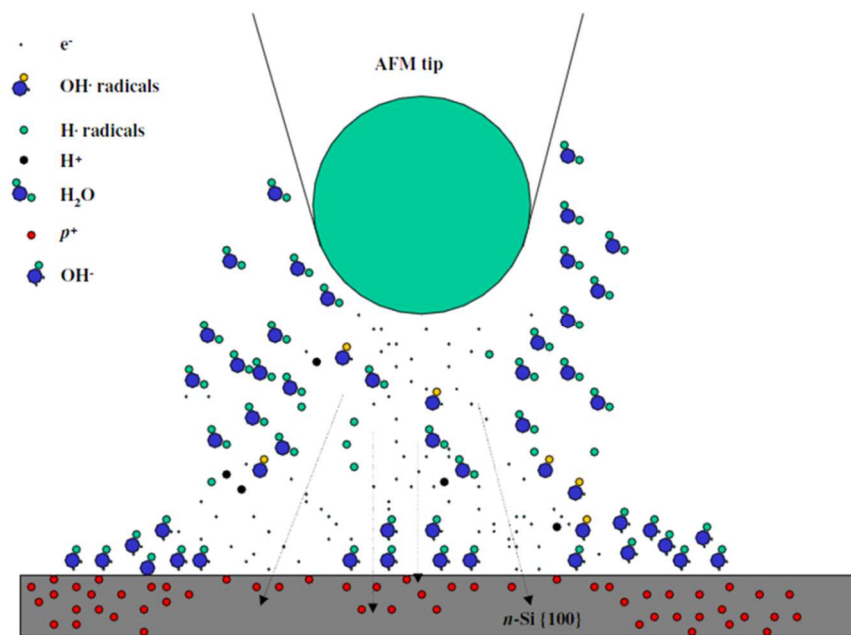

Figure 17. Schematic representation of an AFM tip–surface junction during AFM-assisted oxidation depicting the electrochemical process for the oxide rings formation. Image extracted from reference [29].

Three years later, Xie et al. reported the similar results in Si, polystyrene (PS), and poly(N vinylcarbazole) (PVK). They suggested that the rings are formed by a nanoscale explosion and shock wave generation in a nanometer sized air/water media induced by the biased AFM tip. When the V_{ox} is applied to the tip, the electric field exceeds the breakdown strength of the dielectrics, initiating the explosive discharge of the air/water media in the tip–substrate gap. It was demonstrated that the nanoexplosion is highly localized in the vicinity of the tip apex, and is responsible for the formation of a central structure (dot). Moreover, the nanoexplosion would trigger transient shock waves, generated when large amounts of discharge energy are released to the nanometer sized gap, that propagate parallel to the substrate surface. The propagation of the shock waves helps to significantly expand the trajectory of discharged species out of the explosion zone, thus leading to the formation of an outer ring surrounding the central structure. The occurrence of the stochastic nanoexplosion is highly dependent on the substrate materials and humidity conditions. The substrate-specific surface reactions have a strong impact on the onset voltage of the nanoexplosions. A growth of discharge probability with bias voltage was observed, and was attributed to the enhancement of ionization by higher fields in the Townsend electron avalanche process.[30] High humidity conditions promote the occurrence of nanoexplosions by facilitating secondary avalanches and reducing the degree of electron attachment.[31]

The formation of an outer ring surrounding a central oxide spot is then an anomalous event that has been studied for semiconducting Si substrates and insulating polymers. For LON on metallic TaS_2 surfaces, various concentric symmetrical rings were formed instead of a unique ring. Moreover, the number of rings grew with the lateral size of the oxide motif (Figure 18). Although we still don't have a complete explanation about the formation of various rings instead of only one, the occurrence of the rippled formation resembles the oxide formations mentioned in references [29] and [31]. In

next section (2.2.3) this point will be further discussed in comparison with the LON formations in other TMDC surfaces.
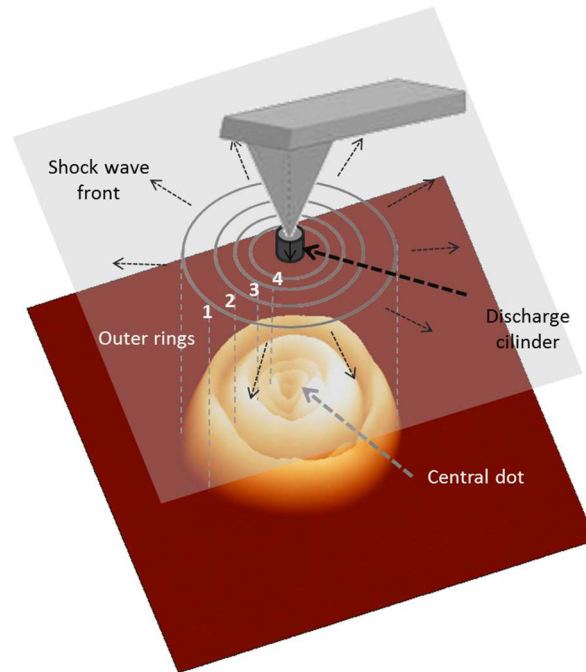

Figure 18. 3D topography image of a d*ynamic-tip* LON performed on the surface of a TaS_2 flake. The oxide exhibits a central dot formation surrounded by 4 concentric rings. The propagation of shock waves is induced by the nanoexplosion.

A systematic study of the ripple oxide formation by *dynamic-tip* LON were done although we found them to be very sensitive to the experimental conditions and little reproducible. In Figure 19a it is shown a set of 5 dots that were consecutive oxidized at the same values of voltage and time pulse, $V_{ox} = -20$ V and $t_{ox} = 35$ ms, on top of a thick flake of TaS_2 (17 nm). It is clear that the dots present not only different topologies (different number of rings) but different heights and widths. It could be explained by considering that the top layer of the cleaved flake is not formed by a continuous layer but formed by few layers with different heights and orientations, and

the chosen sites to perform the oxidation were done onto different layers. When the oxide was formed at the edge of the flake it was always observed that the pattern abruptly interrupted its growth. The experiment was then repeated on top of a thicker flake that presented more homogeneous topography on the outer layer (Figure 19b). Again an array of 5 dots were oxidized with same values of V_{ox} = -16 V and time t_{ox} = 25 ms from left to right with a separation between dots of 200 nm. It resulted again in a non-reproducible pattern, exhibiting different versions of oxide formation at each dot.
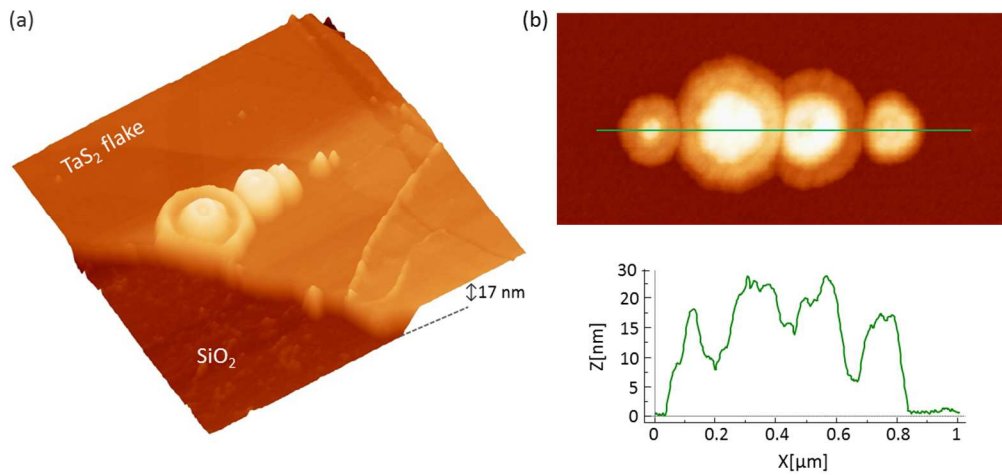

Figure 19. *Dynamic-tip* AFM-LON performed on the surface of TaS$_2$ flakes. (a) 2.5 µm x 2.5 µm 3D topography image of an array of 5 dots oxidized at -20 V and 35 ms on a 17 nm thick flake. (b) Topography image of an array of 5 dots oxidized at -16 V and 25 ms on top of a homogeneous thick layer.

It is known that the size of an oxide pattern by LON depends on the size of the meniscus, and this is dependent on the tip-sample distance (among other parameters). Shorter tip-substrate spacing favors the formation of the water meniscus while an increase in the tip-sample distance leads to a linear decrease in the meniscus width.[32] In our case, the tip-sample distance was found to have a threshold value from which

the size of the pattern grew significantly as can be seen in Figure 20a. The tip-sample distance was checked by recording the so called force-distance curve. This distance can be adjusted by choosing the corresponding amplitude of oscillation and by fitting the set point in dynamic mode. In general, a set point of 1.5 V was initially tuned in order to achieve a reasonable surface proximity for LON purposes. As the tip-sample distance was decreased, the oxide width and height grew. The standard 12-14 nm tip-sample distances led to precise nano-dot writing. As the tip was pushed closer to the surface, uncontrolled massive oxide formations were fabricated. Interestingly, it was also observed that the number of the outer rings of the ripple formations (oxide dots) grew inversely proportional to the tip sample distance: 3 outer rings for d_{ts} =14 nm, 2 outer rings for d_{ts} =15 nm and a single outer ring for d_{ts} =16 nm.

It was also found that there is always a threshold potential from which the oxide started to form. Then, the size of the whole pattern is governed by the pulse time duration (t_{ox}). In Figure 20b it is shown a set of three oxidized dots that were performed at the same tip-sample distance (d_{ts}~ 13 nm) and voltage pulse, V_{ox} = -21 V but increasing the times of oxidation 100 ms, 200 ms, 300 ms, respectively. The formations grew in number of rings, height and width as the pulse time was increased.
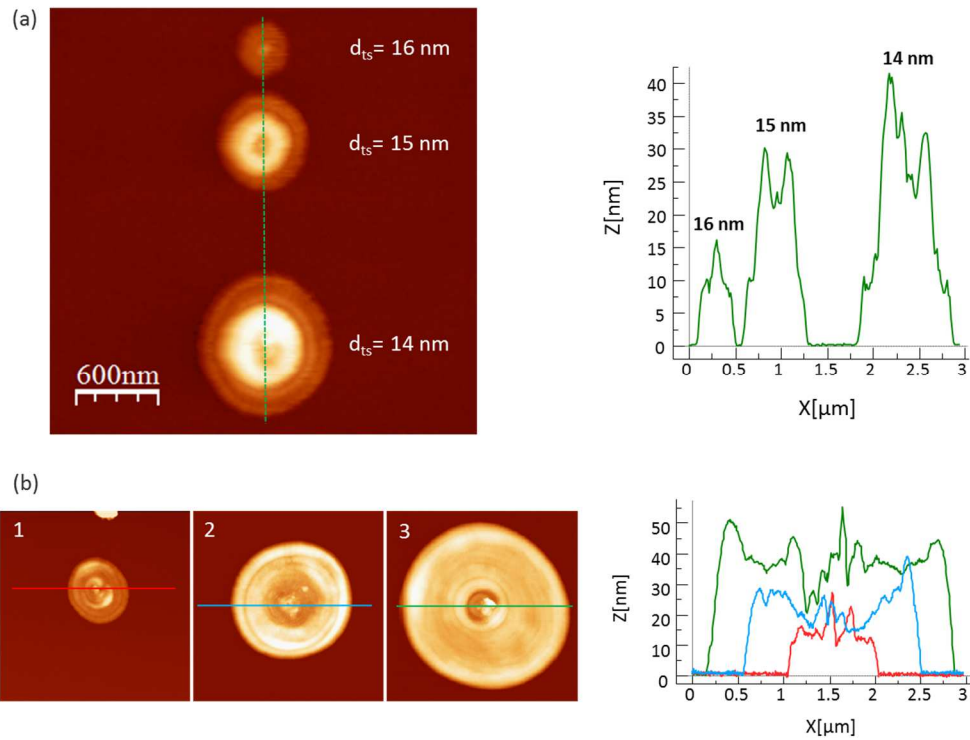
Figure 20. (a) AFM topography image of 3 oxide patterns performed at V_{ox} = -26 V, t_{ox} = 40 ms and different tip-sample distances, from top to down: 16 nm, 15 nm and 14 nm, respectively, and the corresponding height profiles of the oxide patterns. (b) Set of 3 topography images of 3 µm x 3 µm showing dots oxidized at -21 V with an increasing pulse time of (1) 100 ms, (2) 200 ms and (3) 300 ms, respectively, whith their corresponding height profiles on the right side.

Finally, some experiments were performed at a positive bias instead of a negative bias and similar results were obtained. As expected, the polarity of the voltage pulse did not affect the oxidation outcome because we are dealing with metallic conducting flakes.[33]

Summarizing, the size of the oxide motifs on TaS_2 thick flakes performed by *dynamic-tip* LON were found to be extremely sensitive to the experimental conditions as the threshold potential, voltage pulse, time pulse and tip to sample distance, and therefore little reproducible.

In order to overcome this limitation, a modification of the regular *dynamic-tip* LON was introduced. Instead of oxidizing in dynamic mode, it was developed a static oxidation method in which the oscillation amplitude is set to zero just prior and during the application of the voltage pulse (*static-tip* LON). It is noteworthy emphasizing that, in contrast with contact mode AFM (also performed at zero oscillation amplitude),[15(a), 15(f)] the tip here is always freely suspended at a certain distance over the target surface. The performance of the topography images as well as the horizontal tip movement on the oxidation of arrays (or matrices) of dots was made in dynamic mode, maintaining the feedback on the amplitude of oscillation, and correcting the tilt in the XY plane to assure a constant tip-sample distance. Only when the oxidation takes place (the voltage pulse is applied), the tip is not oscillating.

This second oxidation method yielded drastically different results in comparison to the dynamic one. Firstly, the morphology and profiles of the patterned structures were controlled in a much more precise manner by fine-tuning the oxidation conditions on the surface of the TaS_2 thick layers (Figure 21a). Further experiments were directed in order to explore the versatility and precision of the static-tip oxidation in terms of pulse duration and the applied voltage, while maintaining a constant humidity and tip-sample distance. It seems that the height and the final area of the oxidized pattern directly depend on the voltage and time pulse, respectively, while maintaining constant the relative humidity and tip-sample distance. Once again, threshold potentials were found to be very sensitive to experimental instant conditions, varying in the approximately same range as for dynamic-tip oxidation. Once the threshold voltage was established, the resulting oxide sizes could be precisely controlled by adjusting the pulse duration (Figure 21b). In order to assure a precise oxidation of sub-nanometric features on the surface, pulse times within the tens of millisecond time-scale were required.
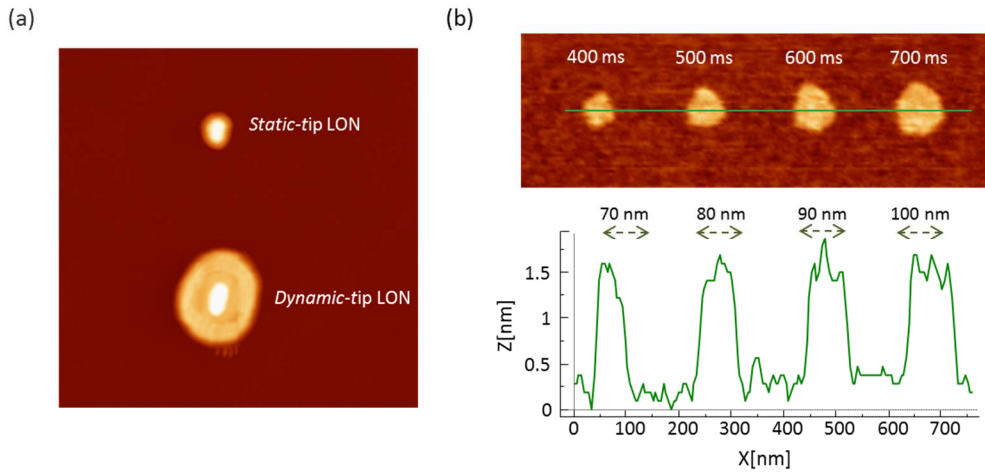
Figure 21. (a) Topography image of 2 dots performed by *static-tip* LON (top) and *dynamic-tip* LON (bottom) at the same oxide conditions: d_{ts} = 15 nm, V_{ox} = -35 V, t_{ox} = 100 ms. Image size: 2.9 µm x 2.9 µm. (b) Topography AFM image of an array of oxide dots performed with *static-tip* LON at a constant voltage value of -42 V and with increasing pulse durations (dwell time step increment is 100 ms). Height profile measured along the line in (b). Image size: 900 nm x 300 nm.

Once the proper working parameters are set, *static-tip* LON enabled the uniform and reproducible patterning of extremely homogeneous oxide motifs on large surface areas of TaS$_2$ thick flakes. Figure 22a shows the high reproducibility reached with the static-tip mode. To illustrate the uniformity reached, the 1040 oxide nanodots reported in Figure 22b, could be fitted to a Gaussian distribution with a standard deviation as small as 0.15 nm. This result is comparable with the precision reached with dynamic-tip LON performed on silicon.[34] All in all, long pulse durations and high values of voltage pulses, gave rise to oxide motifs that exhibit the characteristic rippled structure already observed in *dynamic-tip* LON.
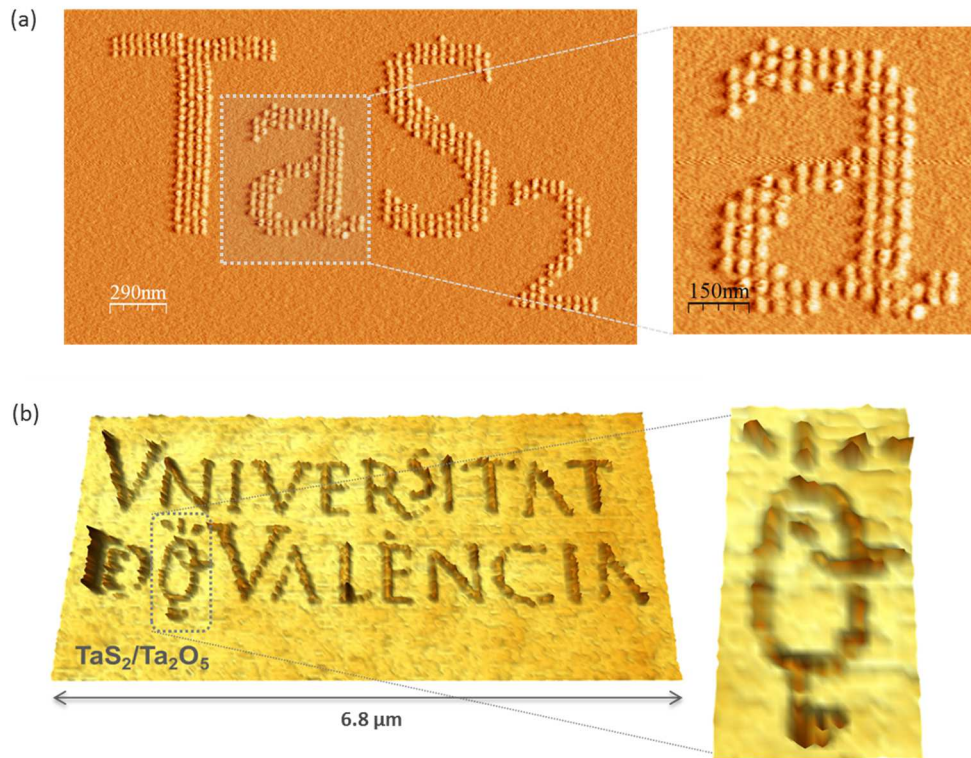
Figure 22. *Static-tip* LON performed on TaS$_2$ thick flakes. (a) AFM image of an oxide pattern performed at a constant voltage value of -34 V and 150 ms. (b) 3D topography image patterned with the university logo made out of 1040 oxide dots, oxidized at -34 V and 150 ms. Average dot heights are 0.58 ± 0.15 nm. (d) Zoom-in image of the region enclosed by the dashed rectangle in (b).

Finally, it was found that the oxidation performed at lower scan speeds produced oxide motifs higher than scanning at faster speeds. For example, Figure 22a, was performed at v = 500 nm/s and the Figure 22b at v = 100 nm/s. A zoom-in of both images shown in the next figure (Figure 23), demonstrates that for the case Figure 23a (lower scan speed) the motifs were higher than in the Figure 23b (faster scan speed).

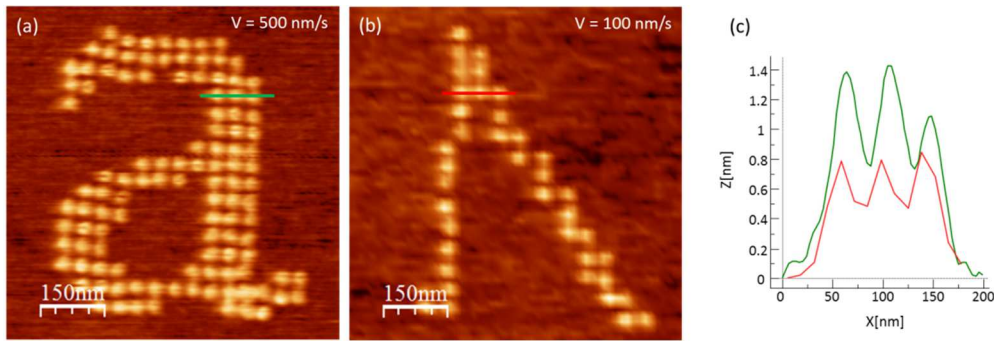Figure 23. Zoom-in of figures 10a and 10b (a) Topography image corresponding to figure 10a. The oxide dots were grown at v = 500 nm/s scan speed. (b) Topography image corresponding to figure 10b. The oxide dots were grown at v = 100 nm/s scan speed. (c) Height profiles of 3 consecutive oxide dots in (a) green line and (b) red line.

2.2.2.2 LON on monolayers of TaS$_2$

The improved control over the patterning technique achieved via *static-tip* LON opened the door to the oxidation of ultrathin few layer TaS$_2$ samples (< 5 nm). Once again, a high reproducibility of low-profile feature fabrication was reached independently on the flake thickness. This is in sharp contrast with previous reports of LON on graphene flakes where the size of the oxide features was dependent on the layer thickness.[15(e)] In an attempt to optimize the response of the TaS$_2$ few layer flakes by varying voltage and pulse lengths, a series of oxidation conditions were explored on ultrathin layers. The proper oxidation parameters in very thin layers were found to be pulses voltages lower than -30 V and time pulses around 50 ms, scan speed v =100 nm/s, tip-sample distance d_{ts} = 11 nm and constant relative humidity around 60%. As can be seen in Figure 24, very precise oxide dots could be created by *static-tip* LON on TaS$_2$ layers of less than 1.9 nm in thickness.
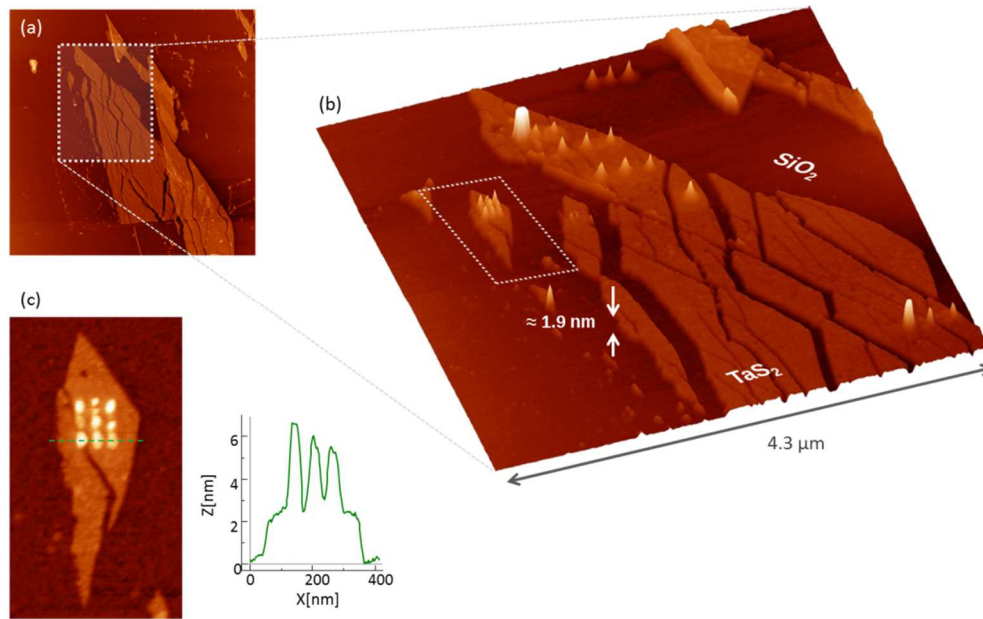
Figure 24. *Static- tip* LON performed on TaS$_2$ thin flakes. (a) Topography image of 1.9 nm thick flake of TaS$_2$ just before the LON experiment. Image size: 10 µm x 10 µm (b) 3D Topography image of the same flake with several oxide nano-dots patterned on the monolayer. Image size: 4.3 µm x 4.3 µm. (c) AFM topography image of a 3 x 3 array of oxide nano-dots patterned on one of the thin flakes, marked with a dashed renctangle in image (b).

Some differences were found in comparison with the LON on thick flakes:

1.- higher voltage pulses resulted in the uncontrolled piercing of the flakes down to the silicon substrate, which makes sense because for the thin layers the quantity of material to be oxidized is much less than for the thicker layers.

2.- usually, the topography characterization as well as the performance of the oxidation experiment is made with the same tip. However, it was found that the thin layers became more instable and sticky to the tip, and during the process of the oxidation the tip was usually damaged. Sometimes it was possible to recover the tip by making some gently indentations on the Si surface or by applying a very high voltage. But most of the cases, for the convenient characterization of the experiment, it was

needed to change the tip right after the LON process, an operation that was not required for the experiments on thick flakes.

3.- It was also found that the roughness of the thinner flakes were higher than the thicker ones. As already mentioned, for the oxidation by LON the use of a humidifier is needed for maintaining a relative humidity of around 60%. This causes that the TaS_2 surface get oxidized with its native oxide and thus, the roughness of the flakes is slightly increased. The surface oxidation happens also for the thick layers. It is well-established how TMDCs tarnish with time, in such a way that it may be observed how nanometer-thick oxide layer generally covers the whole surface of the crystal.[35] However, for the case of the thinner layers of TaS_2 (monolayers or few layers), this process seemed to be faster than for the thicker samples and may be accelerated by the increased relative humidity needed for the LON experiments. Although three-dimensional (3D) crystals may possess thermal and chemical stability, its 2D counterpart can develop more reactivity as they become thinner and they can corrode, decompose, segregate and so forth.[36] It is known, for example, that graphene monolayers are notably more reactive than even graphene bilayers.[37] For the surface of MoS_2 it is known that it starts oxidizing in moist air below 100° C,[38] and even graphene would not survive if the lab were twice as hot, at 600 K.[37a] This third difference may be "linked" to the second one and the oxidation of the thin layers could produce the layers to be more instable and stickier.

2.2.2.3 Etching experiments on LON patterned motifs on thick and thin layers of TaS_2

As occurs for other materials (LON in silicon, for example), the oxide created by LON does not only grow above the surface but also propagates towards the underlying layers of the material creating a 3D pattern. Direct evidence of the bulk characteristics of the oxide motifs created on TaS_2 could be observed by immersing the samples in a HF solution to selectively etch the oxidized motifs (Figure 25). These experiments

confirmed that the wave-like nature of the oxidation mechanism on TaS_2 was transferred into the silicon substrate; this can be clearly observed for the case of the thinner patches (Figure 25b). For the thicker samples we notice that the oxide growth outside the surface is slightly higher than the oxidation inside the sample, in a similar way to what is observed for the LON on Si, where 60% of the oxide is above the substrate baseline.[39]
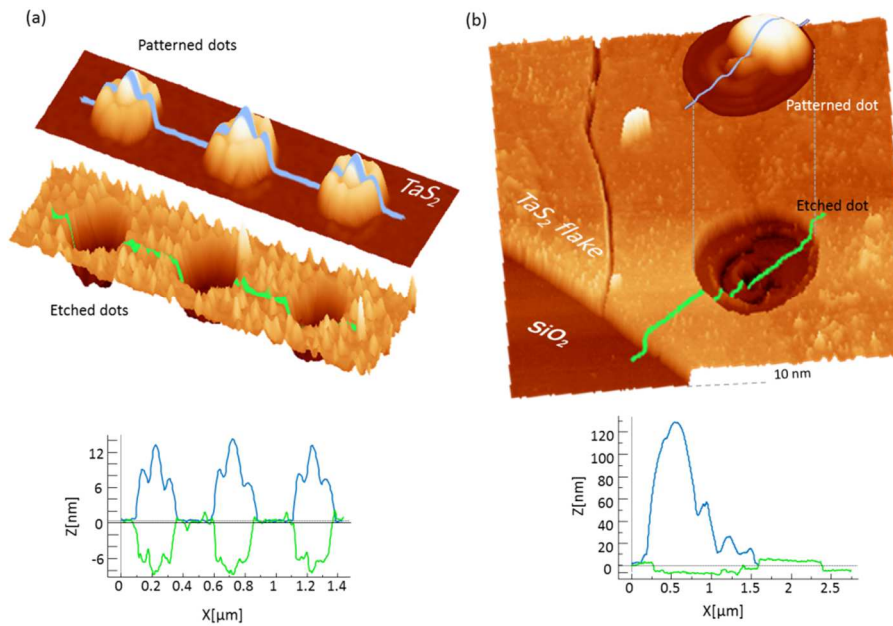
Figure 25. (a) Etching on a thick layer. 3D topography image of an array of three oxide dots created at -22.5 V and 45 ms (top) and the same three HF etched oxide dots (bottom). Below the corresponding profiles for both images pristine (blue) and etched (green) oxide mounds are shown. (b) Etching on a thin layer. 3D topography image of an etched oxide rippled dot on a TaS_2 layer. Inset: AFM topography image of the oxidized dot fabricated at -27 V and 100 ms. Bellow the corresponding profiles for both, oxidized (blue) and etched (green) motifs is shown.

2.2.2.4 Chemical nature of the nanofabricated tantalum oxide

In order to ascertain the actual nature of the oxide motifs produced on the TaS_2 surface, local probe spectroscopies such as electron probe microanalysis (EPMA) or

Photoluminiscence (PL) were employed. A chemical mapping analysis of the surface performed by EPMA clearly showed a high signal of O K_α secondary electrons coming from the oxidized regions (Figure 26).

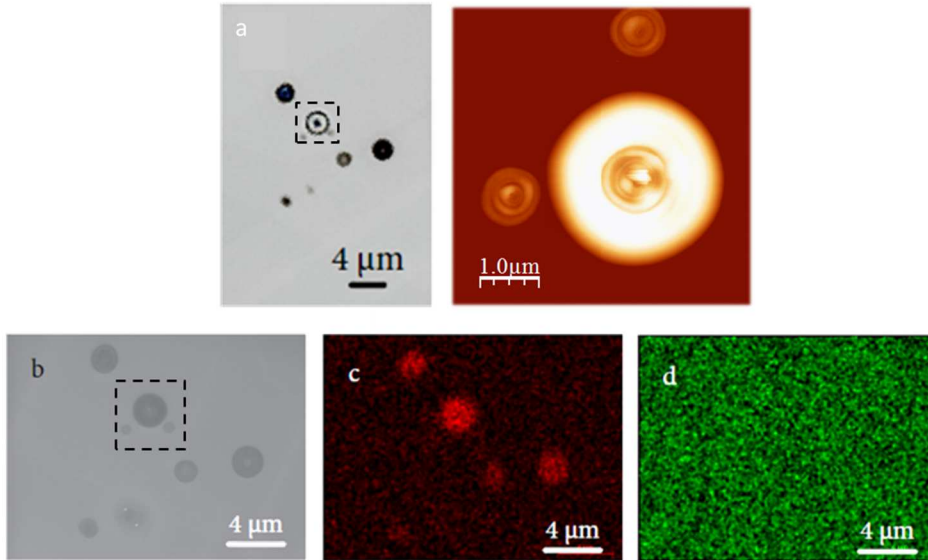Figure 26. SEM-EPMA mapping studies performed on a group of oxide rippled mounds patterned on a thick TaS_2 flake. (a) Optical microscopy image of the group of rippled mounds (left). Highlighted in a dashed square, the three oxide formations shown in the next AFM topography image (right) (b) Secondary electrons (SE) SEM image of the same region. Highlighted in a dashed square same region shown in AFM image. (c) O K-shell SE channel. (d) Ta L-shell SE channel.

PL data were collected from a TaS_2 flake decorated by AFM-LON with a large (2.6 µm in diameter) oxide motif (Figure 27). The results show that before LON, the TaS_2 flakes present a strong featureless background signal in their photoluminescence spectra between 520 nm and 700 nm. The oxide microstructure produced by AFM-LON exhibits a much lower background signal (which indicates a reduction of the optical absorption) together with three narrow peaks at 585 nm, 615 nm and 635 nm. While the peaks at 585 nm and 635 nm are due to the silicon substrate (probably due to excitation of high order phonons), the peak at 615 nm may be associated to the

oxide motif. More precisely, this strong peak is characteristic of the presence of amorphous Ta_2O_5 during the oxidization process.[40] The AFM-LON chemical reaction may therefore be written as displayed in equation 2.1. Noting the chemical transformations involved, it is easy to conceive how the properties of TaS_2 flakes are dramatically altered by means of LON. In this way, AFM provides us with a tool of nanometric precision for the patterning of insulating Ta_2O_5 regions within a metallic conducting TaS_2 flake. A similar scenario has been already described for the local oxidation of graphene or the reduction of graphene oxide flakes.[15] These experiments were conducted in collaboration with Dr. Andres Castellanos-Gomez (Kavli Institute of Nanoscience, Delft University of Technology).
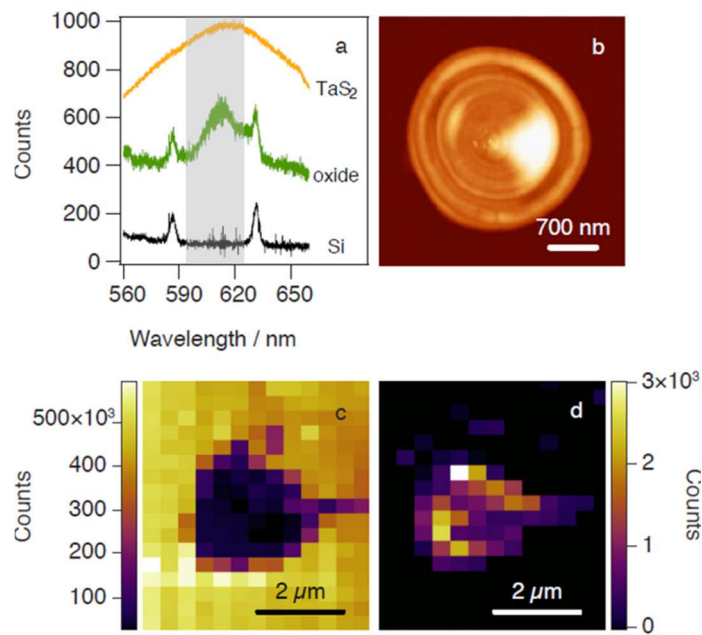
Figure 27. Photoluminescence spectra measured on a TaS_2 flake patterned with a large oxide motif by *dynamic-tip* LON. A comparison between the spectra measured on the pristine flake, the oxidized part and the bare Si substrate is shown in (a). The profile shown for bare TaS_2 has been re-scaled to 1/10 of the raw intensity for comparison. (b) AFM topography images of the oxide motif. Photoluminescence intensity integrated from 600 nm to 625 nm (grey shaded region in (a)) before (c) and (d) after subtracting the baseline.

2.2.2.5 Electrical properties of the ultrathin TaS$_2$ layers

It is known that the conductivity perpendicular to the MX$_2$ planes of TMDCs is at least 100 times lower than the in-plane conductivity and it is also suggested that the movement of the carriers between layers takes place by hopping mechanisms rather than by band-type mechanisms as occurs along the planes.[41] To probe the conducting behavior of the deposited flakes, conducting tip AFM (CT-AFM) was performed onto oxidized and non-oxidized TaS$_2$ flakes. These experiments were conducted in collaboration with Dr. Sergio Tatay (Unité Mixte de Physique CNRS/Thales, France).

First, the resistance map of a flake with different thicknesses deposited on doped silicon was measured. When a 2 V bias was applied between the tip and the surface during contact scanning, a clear contrast in the conductance between TaS$_2$ flakes and the surface was observed (Figure 28). The entire TaS$_2$ surface appeared to have the same conducting behavior and therefore, no effect of the flake thickness was observed (Figure 28b). The electrical properties of the oxide motifs patterned via AFM-LON on top of TaS$_2$ layers were also probed. As expected, a clear contrast was observed between conductive pristine and insulating oxidized regions (Figure 28d). The big difference in conductivity makes these heterostructures TaS$_2$/Ta$_2$O$_5$ surfaces excellent candidates for the fabrication of circuitry at the nanoscale and also for more advanced lower temperature applications profiting from the superconducting properties of TaS$_2$ layers.

Figure 28. (a) AFM topography image measured in contact mode of a TaS_2 flake. (b) CT-AFM resistance mapping of the same flake. (c) AFM topography image of TaS_2 thin flakes. The flake inside the dashed box has been patterned with three round oxidized regions. (d) CT-AFM resistance mapping of the patterned flake highlighted in (c).

An example of the use of AFM-LON for the fabrication of electronic devices is shown in Figure 29. A single-electron tunneling (SET) transistor is based on the Coulomb blockade principle.[42] This phenomenon occurs when a section of conductor called "metal island" is electrically isolated from the rest of the circuit by two tunnel junctions that share a common electrode. A tunnel junction consists of two pieces of metal separated by a very thin (~1 nm) insulator. The only way for electrons in one of the metal electrodes to travel to the other electrode is to tunnel through the insulator. Since tunneling is a discrete process, the electric charge that flows through the tunnel

junction flows in multiples of e, the charge of a single electron. As a preliminary result a pattern of a nanoisland (30 nm in length) was performed on a metallic TaS_2 flake. The island is isolated by lines of 1 nm high of insulating Ta_2O_5 that would act as the tunnel junctions.
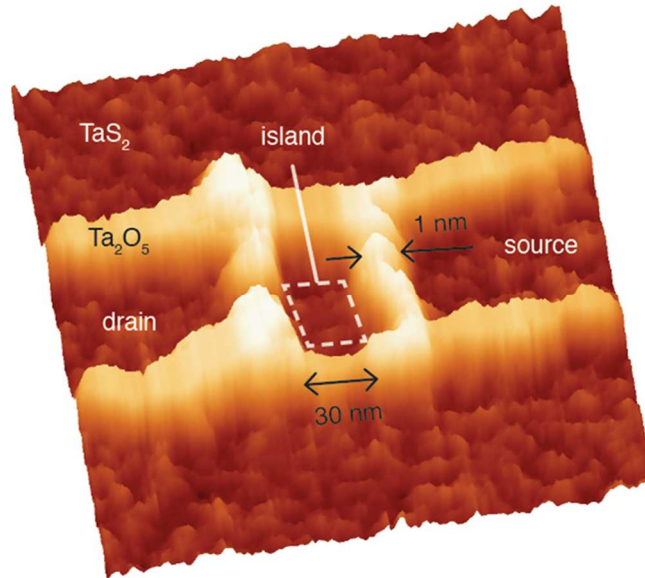
Figure 29. AFM image of a possible design for a SET nanodevice structure. It is patterned via *static-tip* LON on a TaS_2 flake deposited on a Si substrate. The island (nanoscale metal electrode) on the centre of the pattern is isolated by lines of 1 nm of Ta_2O_5 that could act as tunnel junctions.

2.2.3 LON on other TMDCs

The AFM-LON was also performed in other type of TMDCs in order to elucidate the unusual growth mechanism found for the TaS_2 and to extend the method for the fabrication of heterostructures for future applications. The pattering of large areas (μm^2) with nanometric motifs over TMDCs was one of the motivation of this work for its interest in the study of vortices formation and dynamics in 2D superconducting materials. When nanoscopic defects are present in the surface of superconductors, such defects tend to pin the magnetic vortices allowing their study under the

appropriate conditions. Moreover, the possibility of creating these pinning centers by *static-tip* LON with high reproducibility and accuracy in flakes with different thicknesses opens the door for the study of the thickness-dependent vortex dynamics on superconducting TMDC.

The selected TMDCs were: $TaSe_2$, $NbSe_2$ and NbS_2. As well as TaS_2, all of them are layered metallic dichalcogenides at room temperature and superconducting at low temperature. They were conveniently exfoliated from CVT crystals with the Nanopress device (as discussed in section 2.2.1) and transferred over freshly base-activated Si p-doped substrates. Each sample preparation was always done just before performing the AFM-LON experiment following the same procedure used for the TaS_2.

2.2.3.1 LON on $TaSe_2$

The identification of ultrathin flakes of $TaSe_2$ by means of optical microscopy and Raman spectroscopy was recently reported by our group in collaboration with Dr. Andres Castellanos-Gomez (Kavli Institute of Nanoscience, Delft University of Technology) and the group of Prof. Nicolás Agraït (Departamento de Física de la Materia Condensada (C–III). Universidad Autónoma de Madrid).[24] In this work, the $TaSe_2$ flakes were obtained by the stamp assisted exfoliation method. It was also determined the optimal substrates to facilitate the optical identification of atomically thin $TaSe_2$ crystals as well as a monitoring of the possible laser-induced damages caused by the Raman instrument. Although this work will not be discussed in this thesis, it is worthy to emphasize the importance and the difficulty of the exfoliation and identification of defect-free atomically thin two-dimensional $TaSe_2$ crystalline flakes which are crucial steps for further studies of their properties and processability in future applications.

In the experiments discussed in this thesis, the exfoliation and deposition of the $TaSe_2$ layers to the Si substrate were made by the Nanopress device introduced in section

2.2.1. The inspection under the optical microscope enabled the quick identification of some thick flakes that were characterized by dynamic AFM (Figure 30).
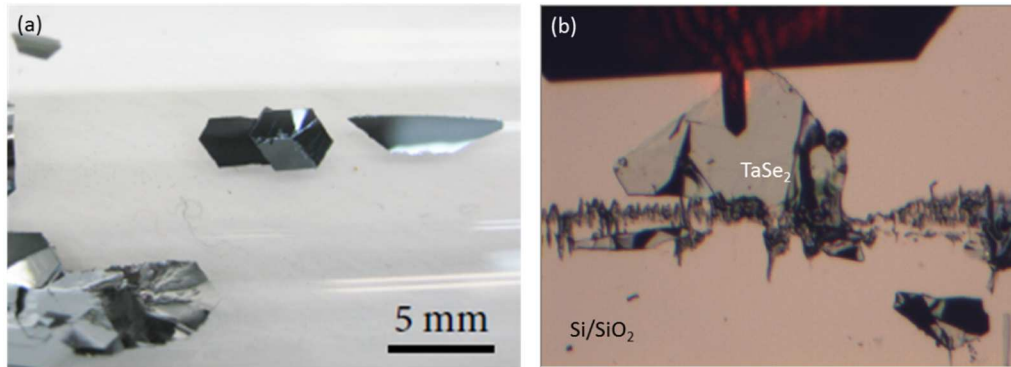

Figure 30. (a) Photograph of TaSe$_2$ crystals growth by CVT. (b) AFM optical image of a TaSe$_2$ flake deposited on a p-doped Si substrate with native SiO$_2$. The cantilever is positioned just above the flake for its AFM characterization.

In this experiment, the AFM characterization and the oxidation lithography were performed one day after the exfoliation. It was found that the flakes presented a surface full of islands with an average height of 1 nm (Figure 31a), that could be due to the oxidation of the surface as observed in the previous section for the case of TaS$_2$.

Concerning to the oxide growth, the unusual behavior of the oxidation by *nanoexplosion* and shock wave propagation on Si, was also found in TaSe$_2$ where one single ring was grown over a central dot oxide formation (Figure 31b). In order to check if the formation of various rings could be possible as happened in TaS$_2$, some experiments applying higher values of time and voltage pulse were performed. By applying more than -24 V and/or 500 ms, the formation of holes into the material was observed. Instead of creating the expected rippled oxide, the nanoexplosion seems to be too strong and thus the material was destroyed just above the tip.
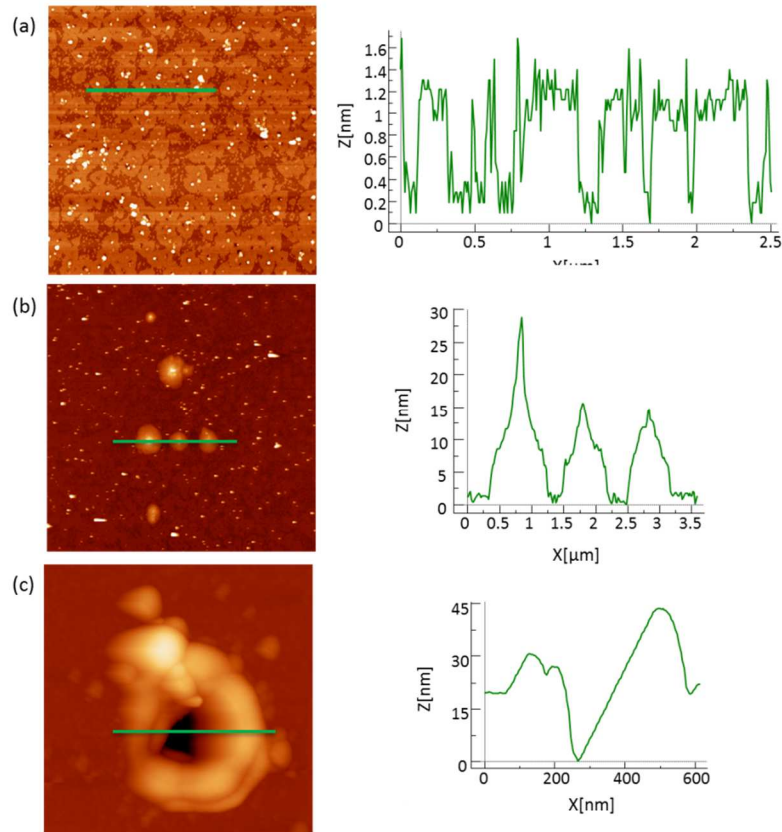
Figure 31. (a) 5 µm x 5 µm topography image of the surface of the exfoliated $TaSe_2$ sample and the corresponding profile of the islands with an average height of 1 nm. (b) 9 µm x 9 µm topography image of $TaSe_2$ surface with some oxide performed by *dynamic-tip* LON. The height profile corresponds to 3 consecutive oxide dots created at -24 V and 200 ms. (c) 900 nm x 900 nm topography image of $TaSe_2$ surface showing a hole created at -24 V and 500 ms, and the corresponding height profile.

2.2.3.2 LON on $NbSe_2$

The LON experiments on $NbSe_2$ were performed following the same procedure as for the TaS_2 and $TaSe_2$. Flakes from CVT crystals were exfoliated with the Nanopress and transferred to a freshly cleaned Si substrate (Figure 32a). For example in Figure 32b, a thick $NbSe_2$ flake was found (~ 160 nm in height) and by scanning the nearby regions few thinner layer stacks were spotted out (Figure 32c).

Figure 32. (a) Photograph of 2H-NbSe$_2$. CVT-grown crystals. (b) 3D topography image of a 160 nm thick flake of NbSe$_2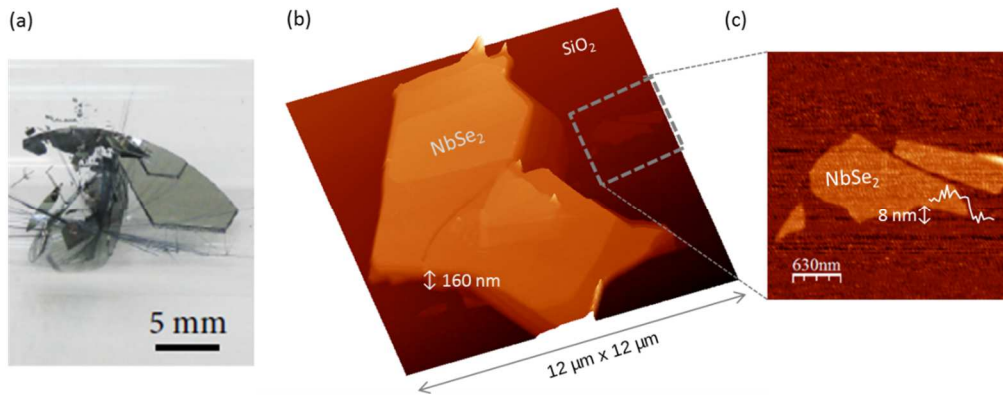$ deposited onto a Si substrate (with its SiO$_2$ native oxide). Nearby, it can be found several thinner patches. A group of them are highlighted with a dashed square and the corresponding topography image of this area is displayed in figure (c). (c) Topography image of a NbSe$_2$ surface of one of the thin flakes. The inset profile shows the heights of the nanometric islands formed onto the surface.

For NbSe$_2$, whenever the exfoliation and the AFM characterization were performed within the same day, a flat surface was detected. However, the characterization by AFM and the LON experiments were done a day after the exfoliation. In this case, the surface of the NbSe$_2$ flakes was full of nanometric islands with average heights of 2 nm as encountered for the TaSe$_2$ samples. It seems then, that the surface of NbSe$_2$ also forms its native oxide by forming islands (Figure 33a).

When performing *dynamic-tip* LON onto one of the flakes, the oxide motifs were formed by a central dot surrounded by one single ring (Figure 33b and Figure 33c), exactly the same patterns were observed in TaSe$_2$. However, if the oxidation was performed at *static-tip* LON, it was possible to create highly reproducible motifs exhibiting only the central spot as probed for the TaS$_2$. Moreover, by the fine adjustment of the LON parameters, we were capable to oxidize a large area of 12.5 µm^2 with a matrix of 20 x 20 dots of average heights of 1 nm (Figure 33e). The

experiment was done on a thick flake exhibiting a smooth surface without islands (Figure 33d).
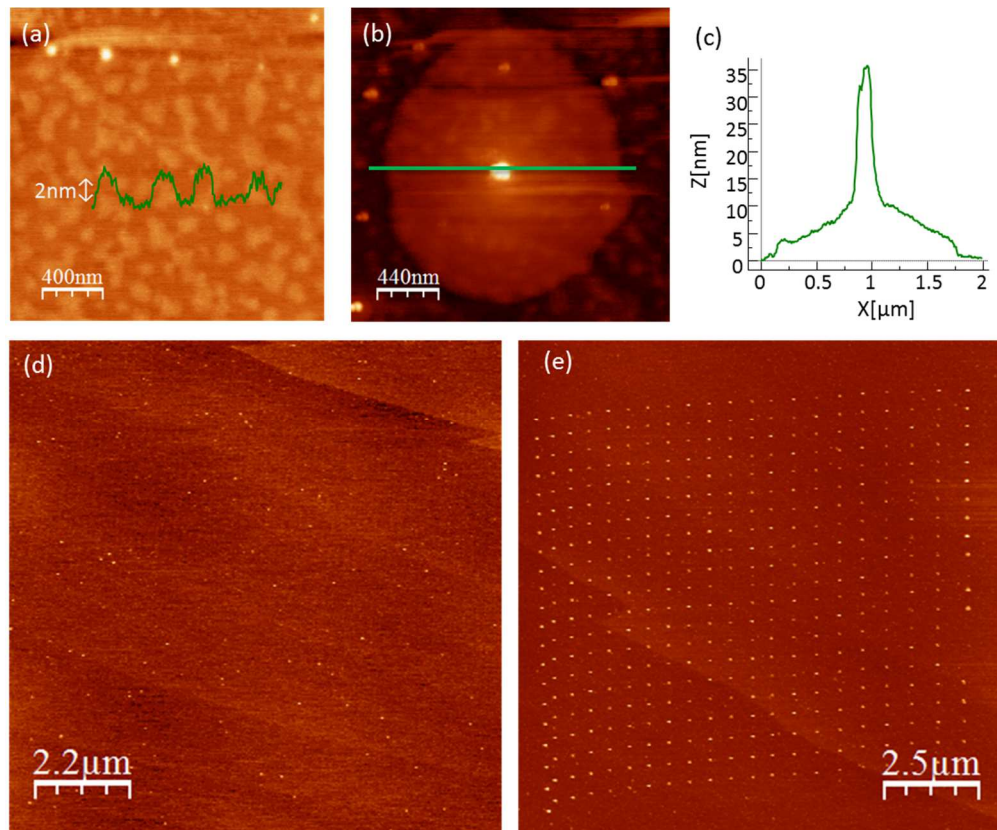
Figure 33. (a) Topography image of a NbSe$_2$ surface of a thin flake. The inset profile shows the heights of the nanometric islands formed onto the surface. (b) Topography image of a LON motif oxidized at -22 V and 150 ms. (c) Topography image of a NbSe$_2$ thick flake just prior the LON experiment. Image size: 11 µm x 11 µm. (b) Topography image of a matrix of 20 x 20 oxide dots onto the NbSe$_2$ surface by *static-tip* LON. Image size : 12.5 µm x 12.5 µm.

2.2.3.3 LON on NbS$_2$

With the CVT growth crystal process, millimeter long hexagonal prisms of 2H-NbS$_2$ were obtained. One of these hexagonal crystals was chosen to be exfoliated with the

Nanopress system (Figure 34a) although two clearly different exfoliated morphologies were obtained: cane- and platelet-like NbS_2 stacks (Figure 34b). The explanation of why these two types of structures were obtained is still under study. Even though they derive from the same crystal, they could be different polymorphic structures of NbS_2. The different stacking sequences of the NbS_2 layers lead to the formation of two polytypes, the hexagonal 2H-NbS_2 with two NbS_2 layers per unit cell, and the rhombohedral 3R-NbS_2 with three layers.
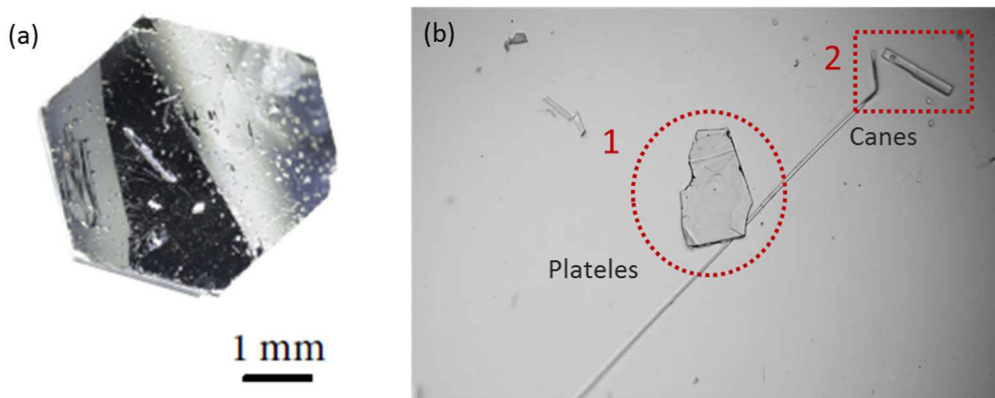
Figure 34. (a) Photograph of 2H-NbS_2 CVT-grown crystal. (b) Optical image showing two different exfoliated morphologies of NbS_2: 1.- Platelets and 2.- Canes.

All in all, AFM-LON experiments were performed in both types of exfoliated morphologies: 1.- platelets and 2.- canes and quite different behaviors were observed after the LON experiments, revealing that the morphology of the surfaces plays a very important role in the oxide growth.

1. LON on platelet-like NbS_2 stacks

The platelet shown in Figure 34b was first characterized by AFM. It was a 400 nm thick stack with a quite smooth surface. *Dynamic-tip* LON experiments were then carried onto the surface and again, it was produced a ripple formation with numerous

rings surrounding a central spot (Figure 35a). Although the LON parameters used were very similar to the oxidation for TaS$_2$ flakes, the number of rings and the size of the oxide motifs were found to be much larger for the NbS$_2$ than for the TaS$_2$ surfaces.
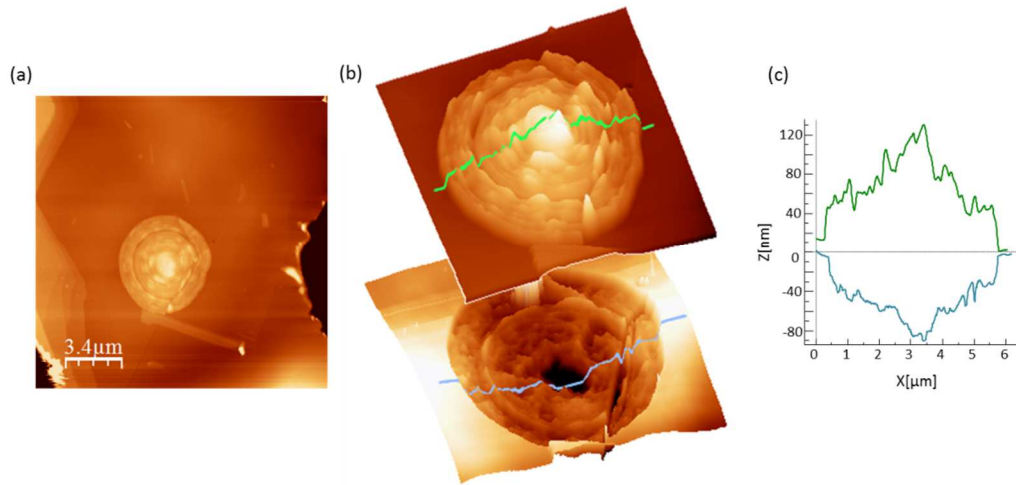
Figure 35. (a) Topography image of a *dynamic-tip* LON motif oxidized at -20 V and 50 ms on a thick flake of NbS$_2$. Image size: 17 µm x 17 µm. (b) 3D topography images of the oxidized (top) and etched (bottom) motif on NbS$_2$. Images size: 7 µm x 7 µm. (c) Corresponding height profiles of the oxidized and etched motifs shown in (b).

Etching experiments were also performed following the same procedure as for the TaS$_2$ (Figure 35b). 3D patterns were created displaying that the oxide grown above the NbS$_2$ surface was higher than the oxidation inside the sample, as encountered for TaS$_2$ (Figure 35c).

2. <u>LON on cane-like NbS$_2$ stacks.</u>

On the other hand, the same exfoliated sample presented a wide variety of sizes of cane-like stacks all around the surface (Figure 36a). Once one of these canes was characterized by AFM, *dynamic-tip* LON experiments were carried out and interestingly, a very distinct oxide growth was encountered for these formations.

Instead of the expected rippled mounds, dendritic shaped oxides were obtained on the canes forming a natural fractal pattern.
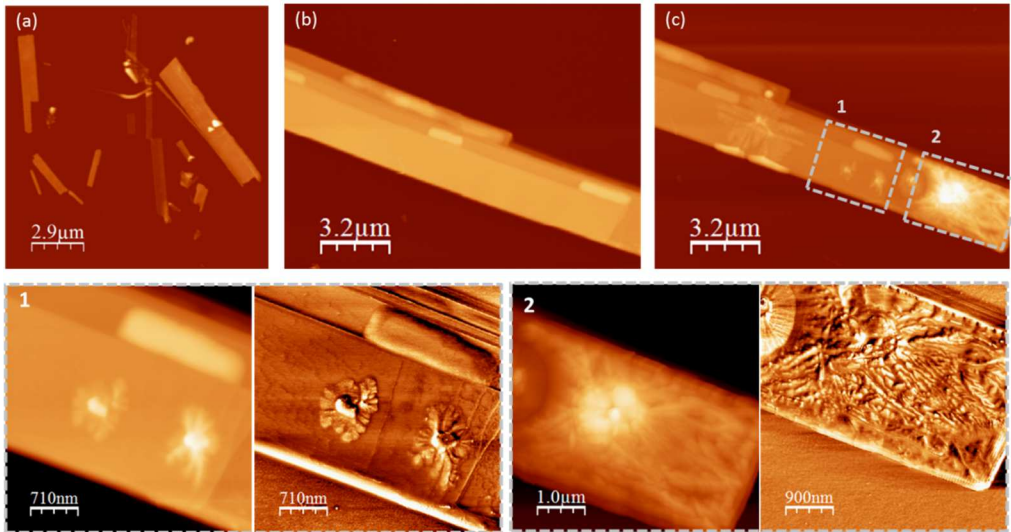
Figure 36. (a) Topography image of various cane-like stacks of NbS_2 onto a Si substrate. (b) Topography image of a cane of NbS_2 previous to its oxidization and (c) same cane oxidized in distinct places employing different oxidation parameters. Two areas are highlighted in dashed squares, (1) topography and phase images of two oxide dendritic growths oxidized at -30 V and 50 ms and (2) topography and phase images of one oxide formation produced at -35 V and 100 ms.

Due to the high accuracy that the AFM provide, it was possible to characterize the cane-like stack right before and after the LON experiment, making oxide patterns in distinct places within the same cane. Various oxidation parameters were utilized to create different sizes although all of them appeared to have the dendritic structure. While applying less voltage and shorter time pulses, the formations obtained were more rounded and smaller in size (Figure 36-1), very high voltages (> 30 V) applied during 100 ms or more derived in a wild oxide branched formation that grew several microns all over the surface until reaching the limits of the cane (Figure 36-2). As observed for the rippling formations, the dendritic oxides always stopped at the edges of the canes. The experiment was repeated in different cane-like stacks of NbS_2 and

always a dendritic growth was obtained (Figure 37). The dendrites have a central circular spot just right below the site were the AFM tip makes the discharge and then, it seems to evolve through avalanches like the ripple formations of the rest of the TMDCs studied in this thesis. Some defects, steps, edges or mismatch between planes on the surface may act as pinning centers and the interactions with these pinning sites would change the evolution of the micro avalanche to produce different oxide dendritic forms.
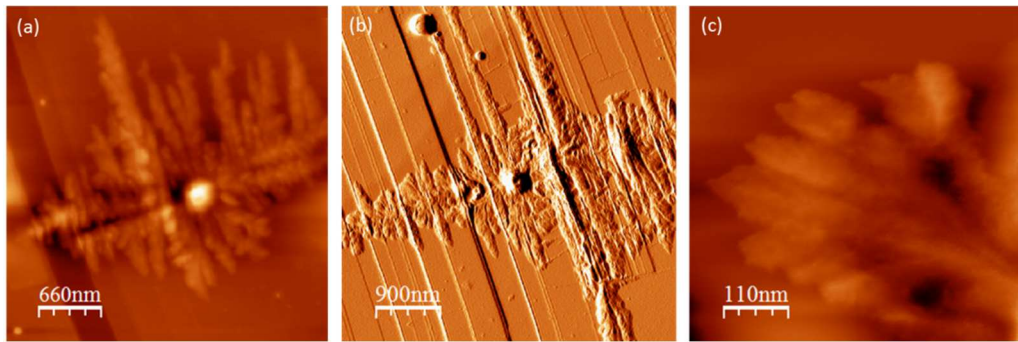
Figure 37. (a) and (b) AFM images of dendrite oxide formations over different cane-like exfoliated NbS_2.(c) Detail of the end of one of the branches of a dendritic oxide formation.

As well as on the previous case (oxidation in platelets), etching experiments were carried out to ascertain the 3D nature of this type of oxide formations. As can be seen in next figure (Figure 38c), the etching reveals a 3D pattern that grew deep inside the NbS_2. The oxide pattern was higher above than below the crystal surface, as observed for etching on TaS_2, and NbS_2 in platelets.
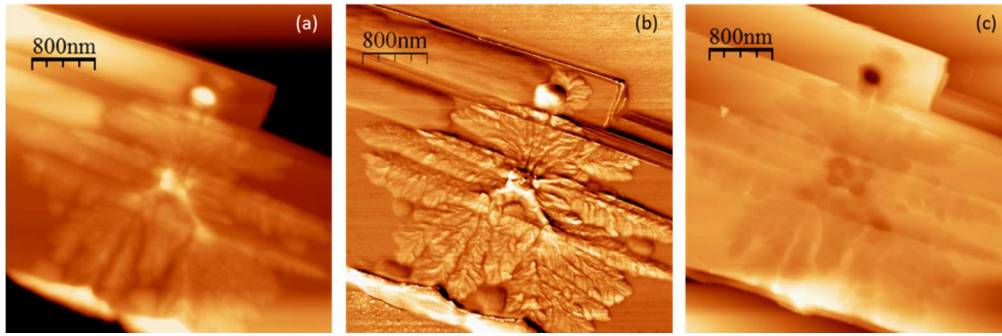
Figure 38. (a) Topography image of a dendrite oxide formation onto a cane of NbS_2 produced at 30 V and 100 ms. (b) phase image corresponding to (a). (c) topography image of the etched oxide shown in figure (a).

Dendrites are branching fern-shaped like structures that can be found in nature in many examples as in the estuary of a river, the shape of neurons or the structure of corals and trees. Dendrite formation has been observed as a growth process of snowflakes, in eumelanin thin films,[43] in the flux branching growth on vortex avalanches formed in superconducting films,[44] and in figures known as "Lichtenberg figures" that are branching electric discharges that sometimes appear on the surface or the interior of insulating materials forming a 3D "electrical tree" (Figure 39).[45]

The dendritic growth mechanism is known in metallurgy were the characteristic tree-like structure of crystals is formed as molten metal freezes. In this case, the dendritic shape is produced by faster growth along energetically favorable crystallographic directions. This growth direction may be due to anisotropy in the surface energy of the solid–liquid interface. In metallic systems, the solid attempts to minimize the area of those surfaces with the highest surface energy. The dendrite thus exhibits a sharper and sharper tip as it grows. The microstructural length scale growth is determined by the interplay or balance between the surface energy and the temperature gradient (which drives the heat/solute diffusion) in the liquid at the interface.
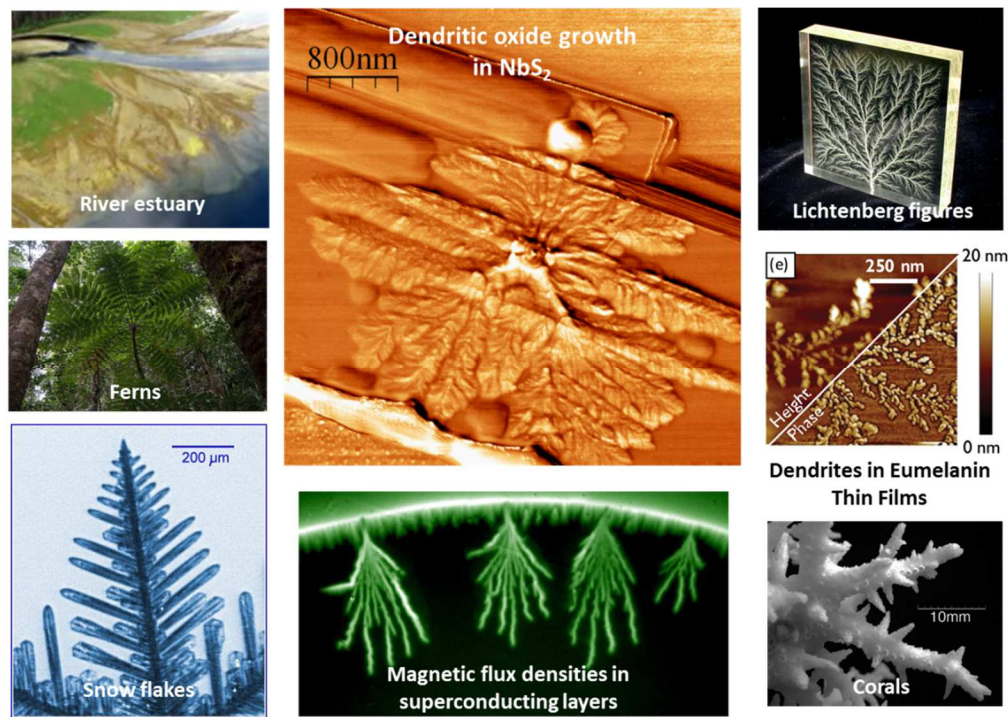
Figure 39. In the center, the AFM image of the dendritic oxide formation of NbS$_2$ is shown surrounded of various examples of dendritic growth in nature.

In a similar manner the growth of the oxide dendrites on NbS$_2$ could be due to its surface anisotropy. It is well known that the layer structure of the NbS$_2$ causes a strong anisotropy in the physical properties e.g. the conductivity and compressibility.[46] The electrical conductivity perpendicular to MX$_2$ planes of a layered TMDC is at least 100 times lower than the in-plane conductivity. And in the same trend, thermal conductivity is lower too when measured perpendicular to the layers. One can suppose then that the cane-like structures may be formed from the same politype compound (2H-NbS$_2$) but exfoliated in a different way. Instead of forming a stack of 2H-NbS$_2$ layers with its basal planes lying parallel to the substrate (platelets), they would be conformed perpendicular to the surface, stacking up orthogonally and thus, forming

the cane-like flakes (see Figure 40). This way, when the tip of the AFM is placed on top of the perpendicular layers and the voltage pulse is applied, the oxide growth would present a dendritic structure that would evolve by micro avalanches triggered by the high voltage pulse. The conductivity anisotropy between the layers would be the responsible of the dendritic form of the oxide growth. Besides, the nanoexplosion produced by the high voltage pulse would also cause a hot spot and the temperature distribution could evolve in a branching manner due to the high anisotropy in the thermal conductivity. This effect has been seen for example in the formation of vortex avalanches in superconductors.[47] Both cases, electric or thermal conductivity anisotropies, seem to be the most plausible explanations for the differences in the oxide growth behaviors between the platelets and the canes. Finally, we cannot forget that the LON process is an electrochemical reaction that takes place with the presence of a water layer absorbed onto the stacks surface. The anisotropy between the layers of the NbS_2 would cause stress in the NbS_2/water interface and therefore, determine the oxide growth through the mentioned micro avalanches.
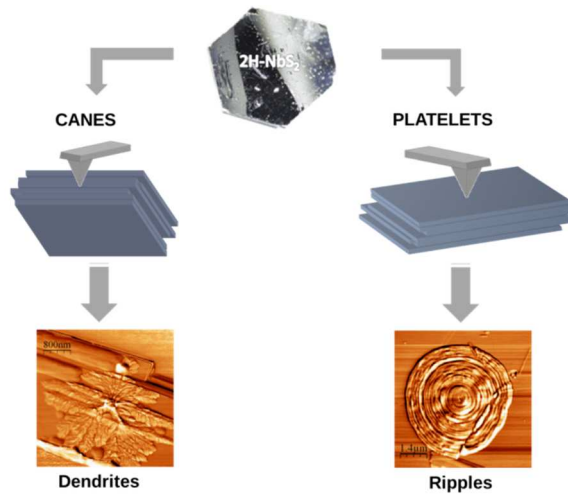

Figure 40. The exfoliation of the NbS_2 rose on two different morphologies: platelets and canes, that could explain different oxide growth behaviors under the application of the voltage pulse: rippled and dendrites, respectively.

All these arguments are just attempts for explanations of the formation of the dendritic growth in NbS_2. However, further analysis like X-ray diffraction or local probe spectroscopies as micro-XPS or micro-Raman are needed in order to ascertain the stoichiometry and polymorphic structure of the cane-like structures.

In addition, it is interesting to see that when the oxide formations are sufficiently large, they can be spotted out by optical microscopy, as it is shown in Figure 41.
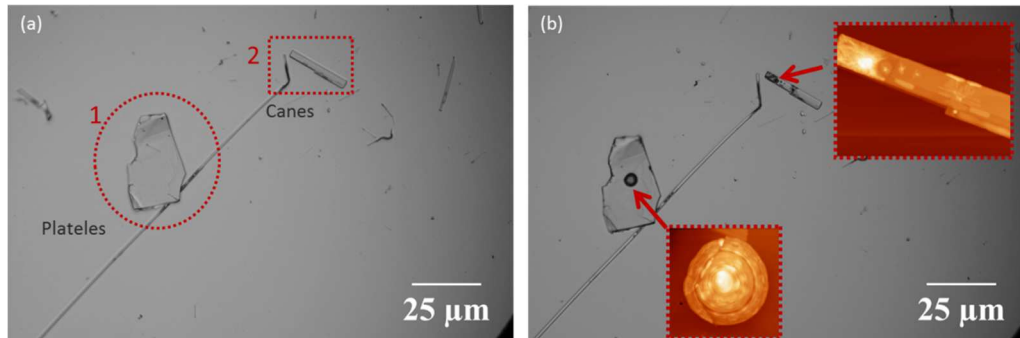
Figure 41. (a) Optical image (100 x) showing two different exfoliated morphologies of NbS_2: 1.- Platelets and 2.- Canes, before the LON experiment. (b) Optical image (100 x) of the same area after the LON experiment. The oxide motifs are pointed out with arrows and the insets show the AFM topographic images of the motifs oxidized on the platelets and on the canes.

Summarizing, the same mechanism of oxidation growth has been observed for the exfoliated layers of $TaSe_2$ and $NbSe_2$. This is very similar to the anomalous oxide growth on silicon and various polymers caused by a *nanoexplosion* followed by a shockwave. These oxide patterns presented morphology of a central spot surrounded by a single ring. However, for the case of sulfides, TaS_2 and NbS_2, the formation of various rings instead of a single one was observed. This particular oxide growth is unprecedented and is still under study. A unique case of dendritic oxide growth has been found for the NbS_2 exfoliated in canes, although the nature of these particular structures has to be confirmed by spectroscopic methods (Figure 42).

On the other hand, although the *static tip* LON experiments were not performed on TaSe$_2$ and NbS$_2$, it has been successfully performed onto TaS$_2$ and NbSe$_2$ demonstrating the possibility of patterning very small oxide motifs with high accuracy and reproducibility. Then, it has been probed that it is a general LON method that could be extended to any TMDCs.
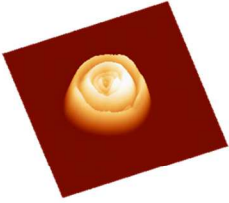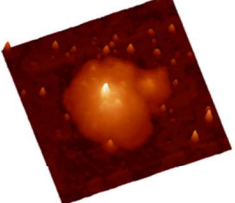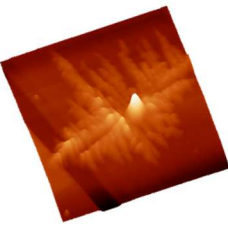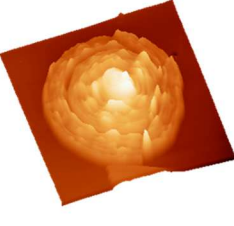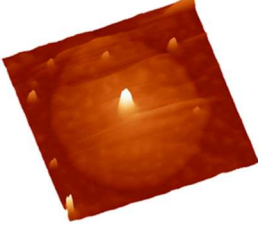
Figure 42. Table for summarizing the oxide growth formations through *dynamic-tip* LON onto the different exfoliates layers of the four types of TMDCs studied: TaS$_2$, TaSe$_2$, NbSe$_2$ and NbS$_2$.

2.3 MATERIALS AND METHODS

Technical specications of the Nanopress

The dynamometer employed was a commercial Sauter FH2 digital force gauge with a maximum load of 2 N and a nominal resolution of 0.001 N. It could be operated in either push or pull modes with a maximum precision of 0.2 % of the load. The maximum frequency data sampling was of 2 Hz.

An MT3-Z8 XYZ motorized stage supplied by Thorlabs was used as the active substrate holder. The triple uniaxial assembly had a maximum horizontal load of 9 kg and a 4.5 kg vertical one. It included three 12 VDC Z812B servo actuators with sub-micron resolution (0.10 μm minimum achievable incremental movement and 0.4 μm minimum repeatable incremental movement, high accuracy (95 μm absolute on-axis accuracy, 0.52% maximum percentage accuracy) and 12 mm maximum travel. In addition, the micrometer head-steppers feature a maximum speed of 3 mm/sec with a maximum acceleration of 4 mm/s^2 ($\pm$ 0.125 mm/s velocity stability, 1.5 μm bidirectional repeatability). Each actuator is operated by its own single-channel TDC001 DC servo motor controller with +15 V & -15 V drive outputs.

Mounted on the Z stage axis was a KMS kinematic mount from Thorlabs. Samples were mounted at the tip of the force gauge spindle on top of another kinematic mount (Thorlabs KMM/S) for tilt control.

Two orthogonally mounted PCE-MM 200 digital microscopes (1280 x 1024 pixels resolution and 10x to 200x magni2cation range) were employed for sample adjustment.

Synthesis of 2H-TaS$_2$ single crystals

The synthesis of the TMDCs crystals was done by Dr. Efren Navarro and it is explained as follows. As an example, the TaS$_2$ crystal growth is explained in detail: TaS$_2$ crystals were synthesized from the elemental components in a two-step process. Firstly, a polycrystalline sample was obtained by ceramic combination of stoichiometric ratios of the metal and chalcogen as described elsewhere. [48] Powdered starting materials were intimately mixed, placed inside an evacuated quartz ampoule and reacted at 900ºC during 9 days. The resulting free-flowing glittery grey microcrystals were then transformed into large single-crystals by the CVT methodology. 1g of TaS$_2$ polycrystalline material together with 275 mg of I2 were loaded into a 500 mm long quartz ampoule (OD: 18 mm, wall-thickness: 1.5 mm). The mixture was thoroughly stashed at one end of the ampoule and the latter was exhaustively evacuated and flame-sealed. The quartz tube was finally placed inside a three-zone split muffle where a gradient of 50ºC was established between the leftmost load (800 ºC) and central growth (750 ºC) zones. A gradient of 25 ºC was also set between the rightmost and central regions. The temperature gradient was maintained constant during 15 days and the muffle was eventually switched off and left to cool down at ambient conditions. Millimetric TaS$_2$ crystals were recovered from the ampoule's central zone, exhaustively rinsed with diethyl ether and stored under a N$_2$ atmosphere.

In the case of NbSe$_2$, TaSe$_2$ and NbS$_2$, large single crystals could also be obtained by using the same procedure as followed for the TaS$_2$. The experimental conditions for each case are described in detail in Dr. Efren Navarro PhD thesis.

Substrate cleanings

Si and Si/SiO$_2$ substrates were cleaned and simultaneously activated by three 10 min sonication cycles in diluted basic piranha solution: NH$_4$OH (conc.) : H$_2$O$_2$: H$_2$O, 1 : 1

: 2 (v/v/v). Between each sonication cycle the substrates were rinsed in water and immersed in a fresh aliquot of piranha solution. 4e substrates were2nally washed by sonication in ultrapure milli-Q water during 10 min. Finally the substrate were thoroughly blow dried before used.

Ultrasonic cleaner: a BRANASONIC MTH-5510 ultrasonic cleaner (power 185 W) was used.

Other substrates with metal coatings, such as Au-coated Si, were more prone to be damaged by the ultrasound treatment. In these cases the substrates were typically cleaned by rinsing thoroughly in iPrOH or EtOH and 2nally blow dried.

Optical microscope

General optical microscopy images were taken using a Nikon D-600 SLR camera mounted on the trinocular stage of a Nikon LV-100 optical microscope. The microscope was equipped with a Nomarski prism for DIC contrast imaging and with 5 Nikon PLAN FLUOR EPI objectives: $5\times$ (numerical aperture, NA = 0.15), $10\times$ (NA = 0.3), $20\times$ (NA = 0.45), $50\times$ (NA = 0.8), $100\times$ (air, NA = 0.9). The calibration of the SLR camera with the $5\times$ and the $10\times$ objective lenses was performed with a reference millimeter reticle, resulting in a lateral space calibration value of 95.3 μm·px-1 and 47.8 μm·px-1. The higher power lenses were calibrated using an AFM calibration grid with a period of 10 μm, resulting in the following values: 238.0 μm·px-1, 95.2 μm·px-1 and 47.4 μm·px-1 for the $20\times$, the $50\times$ and the $100\times$ objectives respectively.

Scanning tunneling microscope (STM)

The STM room temperature measurements were performed with the Cervantes Fullmode SPM (Nanotec Electrónica) using the STM mode. The tips used were obtained from a Pt-Ir wire, mechanically cut.

Atomic force microscopes (AFM) and local oxidation nanolithography (LON) equipment

Two different AFMs were used for the local oxidation nanolithography on TaS_2. One is a Nanoscope IVa (Bruker) interfaced with a home-made voltage amplifier. In this instrument, the nanolithography was made by programming simple patterns (dots, lines and matrices) in C++. The other one is a Cervantes Fullmode SPM (Nanotec Electrónica) using the AFM mode, that provides powerful nanolithography software (WSxM).[49] This software permits to plot customized pre-loaded patterns as well as simple patterns. All experiments were carried out at room temperature and the ambient relative humidity of 40-70% by employing a commercial bench-top humidifier.

In both AFMs, a vertical optical microscope is used to visualize the tip over the surface, being able to position the tip on top of the selected flake. The topographic characterization of the surface is made in dynamic mode, which is a non-invasive mode of operation. The same silicon probes of $f_r \approx 300$ KHz and $k \approx 40$ N/m (PPP-NCH, Nanosensors) were used for the morphological characterization as well as for performing the LON.

Water contact angle measurements

Advancing and receding water contact angle measurements were performed by the "add and remove volume" method in a Ramé-hart Model 200 Standard Goniometer with Dropimage Standard v2.3, equipped with an automated dispensing system. This device includes software as well as a fiber optic illuminator, 3-axis leveling stage, high-speed F4 Series digital camera, microsyringe fixture and assembly for manual dispensing. The system is improved with an automated dispensing system and manual tilting base.

HF selective etching

The etching of oxidized TaS_2 flakes deposited on Si substrates was performed by fast dipping (typically < 1 s inside the etching solution) in an concentrated HF (aq.) solution. The samples were then thoroughly rinsed with milli-Q water and blow dried.

Electron probe microanalysis mapping (EPMA)

EPMA spectra were collected with a 2eld emission gun (FEG) Hitachi S-4800 SEM operated at 20 kV and equipped with a Bruker XR detector. The sample was placed at a working distance of 15 mm and scanned at an approximate count rate of 10 kcps for approximately 15 min. 4e mapping data was collected with Quantax 400 so3ware.

Photoluminesce (PL) measurements

PL measurements have been carried out with a homemade setup that consists of a confocal microscope with a NA = 0.8 objective illuminated by a Z = 532 nm laser beam.254 Typical light intensities of $9.5 \cdot 10\text{-}5$ $\mu W/nm^2$ (75 μW incident power and 500 nm diameter spot) are used. For the scanning PL measurement the diffraction limited spot is scanned using a combination of two galvomirrors and a telecentric lens system while a PL spectrum is acquired in each pixel.

Conducting-tip atomic force microscope (CT-AFM)

CT-AFM was performed under N_2 atmosphere on a Veeco Enviroscope multimode AFM equipped with a Digital Instruments NanoScope IV controller. This apparatus was modified by Houzé *et al.* to perform local resistance measurements in the range of

10^2 to 10^{12} Ohms under a bias voltage ranging from 0.1 to 10 V, with 5% accuracy [50]. In this set-up, the conductive tip is electrically polarized and the current flowing through the sample is amplified, converted in a voltage related to the resistance (V α log(R)) and analysed by the Nanoscope IV's controller. In these experiments samples were contacted to a sample holder with conducting silver paint and bore-doped polycrystalline diamond coated Si_3N_4 tips with spring constant k $\approx$40 N/m (Bruker) were used to scan the sample in contact mode while performing the resistance mapping at an applied bias of 2V.

2.4 CONCLUSIONS

In this chapter, the development of a new device -the Nanopress- and methodology - the "press and shear" method- for the exfoliation of atomically thin layers of 2D crystals has been presented. It has been proved the high efficiency of this system and the versatility of the technique which allows fixing the experimental parameters for the deposition of layered materials onto different substrates. This is clean method which does not use any glue or sticky tape and it is a fast and reliable process that can produce a large number of samples in a short time. The possibility of the optical inspection of the deposited samples facilitated the work of finding the proper experimental conditions for the exfoliation of the different materials. It has been presented in detail the results for the exfoliation of TaS_2, which is layered TMDCs which exfoliation into atomically thin layers has not been feasible by other existing methods like the stamp assisted method or the well-known *Scotch Tape* method. It has been shown as well, the characterization by AFM of the resulted TaS_2 deposited flakes, proving the existence of atomically thin layers created by the Nanopress.

We have performed an exhaustive exploration of AFM-LON on TaS_2 surfaces using thick samples and ultrathin layers. These layered materials have been oxidized using both the conventional *dynamic-tip* mode as much as the new *static-tip* mode herein presented. The most spectacular result in this context has been the demonstration that a *static-tip* LON affords a reproducible oxidation of very low-profile motifs not only on thick TaS_2 flakes (> 5 nm), but also on ultrathin ones (< 5 nm). For the first time, we have shown that these TaS_2 layers may be conveniently oxidized with an unprecedented precision and reproducibility similar to that achieved on silicon, or more recently on graphene surfaces. In fact, the oxide motifs can be conveniently patterned across several square micron areas of TaS_2 conducting flakes, opening the door for the nanofabrication of extended designs with very low profiles (down to 0.58 nm). As these oxide motifs are insulating, one can envision the controlled printing of

nano-circuitry on single TaS_2 conducting layers, which behave as bi-dimensional systems. On the other hand, as TaS_2 exhibits superconducting properties at low temperatures, this methodology could be employed for studying the physical consequences derived from the confinement of this layered superconductor in a nanometric region.

Though the level of precision reached is similar to the one achieved for the oxidation of graphene, the controlled oxidation of TaS_2 opens the door for performing AFM-LON on other TMDC analogues. This offers the possibility of finely tuning the properties of the TMDC/oxide heterostructure depending on the functionality pursued. The oxidation over another three types of TMDCs: $TaSe_2$, $NbSe_2$ and NbS_2, has been also reported in detail.

It has been seen that the growth of the native oxide onto the exfoliated surfaces is enhanced by the high humid ambient conditions needed for the LON experiments. Besides, when the AFM characterization of the exfoliated flakes of $TaSe_2$ and $NbSe_2$ was done one day after their delamination, it was found that the native oxide growth of the two materials formed islands over their surfaces.

Finally, we have found that the mechanism of the oxidation on TaS_2 surfaces as well as the NbS_2 clearly differs from the usual mechanism of oxidation on most surfaces since characteristic rippled mounds were formed. For $TaSe_2$ and $NbSe_2$ the oxide growth behavior resembles to an anomalous LON observed in silicon surfaces as well as in some polymers that it was attributed to the formation of a *nanoexplosion* followed by a shock ware, triggered by the application of a high voltage in a very local site. A theoretical study of the charge propagation mechanism along these TMDCs conducting layers is underway. Besides, some atypical *cane-like* stacks were found for the exfoliation of NbS_2. It has been shown that the local oxidation experiments performed onto the *cane-like* flakes behave completely different from the rest. Dendrite growth has been found in this case. Although the nature of these formations

needs to be confirmed by spectroscopic measurements, one possible explanation of the dendritic growth is that the LON experiment was performed onto the perpendicular side of the stacked layers and the dendritic growth was governed by the high electric and thermal anisotropy characteristic of this material.

2.5 BIBLIOGRAPHY

[1] a) Novoselov, K. S.; Geim, A. K.; Morozov, S. V.; Jiang, D.; Zhang, Y.; Dubonos, S. V.; Grigorieva, I. V.; Firsov, A. A.. *Science* **2004**, *306*, 666–669. (b) Novoselov, K. S.; Geim, A. K.; Morozov, S. V.; Jiang, D.; Katsnelson, M. I.; Grigorieva, I. V.; Dubonos, S. V.; Firsov, A.. *Nature* **2005**, *438*, 197–200. (c) Geim, A. K.; Novoselov, K. S. *Nat. Materials* **2007**, *6*, 183–191. (c) Zhang, Y.; Tan, Y.-W.; Stormer, H. L.; Kim, P. *Nature* **2005**, *438*, 201–204. (d) Li, X.; Cai, W.; An, J.; Kim, S.; Nah, J.; Yang, D.; Piner, R.; Velamakanni, A.; Jung, I.; Tutuc, E.; Banerjee, S.K.; Colombo, L; Ruoff, R.S. *Science* **2009**, *324*, 1312–1314. (e) Castro Neto, A. H.; Peres, N. M. R.; Novoselov, K. S.; Geim, A. K, *Rev. Mod. Phys.* **2009**, *81*, 109–162.

[2] Qing Hua Wang, Kourosh Kalantar-Zadeh, Andras Kis, Jonathan N. Coleman & Michael S. Strano. *Nature Nanotechnology* **2012**, *7*, 699–712.

[3] a) Helveg, S.; Lauritsen, J.; Laegsgaard, E.; Stensgaard, I.; Norskov, J.; Clausen, B.; Topsoe, H.; Besenbacher, F. *Phys. Rev. Lett.* **2000**, *84*, 951–954. (b) Radisavljevic, B.; Radenovic, A.; Brivio, J.; Giacometti, V.; Kis, A. *Nat. Nanotechnology* **2011**, *6*, 147–150. (c). *Nat. Nanotechnology* **2012**, *7*, 683. (d) Wang, Q. H.; Kalantar-Zadeh, K.; Kis, A.; Coleman, J. N.; Strano, M. S.. *Nat. Nanotechnology* **2012**, *7*, 699–712. (e) Yin, Z.; Li, H.; Li, H.; Jiang, L.; Shi, Y.; Sun, Y.; Lu, G.; Zhang, Q.; Chen, X.; Zhang, H.. *ACS Nano* **2012**, *6*, 74–80.

[4] a) Mingsheng Xu, Tao Liang, Minmin Shi, and Hongzheng. *Chen. Chem. Rev.*, **2013**, *5*,113, 3766–3798. b) Wilson, J. A.; Yoffe, A. D. *Adv. Phys.* **1969**, *18*, 193–335.

5 J. A. Wilson and A. D. Yoffe, *Advanced Physics*, **1969**, *18*, 193–335.

[6] a) Leininger, P.; Chernyshov, D.; Bosak, A.; Berger, H.; Inosov,D. S. *Phys. Rev. B*, **2011**, *83*,233101. b) Galvis, J. A.; Rodière, P.; Guillamón, I.; Osorio, M. R.; Rodrigo, J. G.; Cario, L.; Navarro-Moratalla, E.; Coronado, E.; Vieira, S.; Suderow, H. arXiv: 1210. 2659.

[7] Harper, J.; Geballe, T. H.; Di Salvo, F. J.. *Phys. Rev. B* **1977,** *15*, 2943–2951.

[8] (a) Krasowski, R.V. *Phys. Rev. Lett*. **1973**, *37*, 1175-1178. b) A. Kuc, N. Zibouche, T. Heine. *Phys. Rev. B*, **2011,** *83*, 245213.

[9] a) V. G. Tissen, M. R. Osorio, J. P. Brison, N. M. Nemes, M. García-Hernández, L. Cario P. Rodiere, S. Vieira, and H. Suderow. Phys. Rev. B, **2013**, *87*, 134502. b) G.L. Holleck, J.R. Driscoll, *Electrochim. Acta*, **1977**, *22*, 647, 655.

[10] A. K. Geim & I. V. Grigorieva., *Nature*, **2013**,*499*,419.

[11] a) Xu, M., Lian, T., Shi, M.& Chen, H. Chem. Rev. **2013**,*113*, 3766–3798 b) Tanaka, T., Ito, A., Tajiima, A., Rokuta, E. & Oshima, C. *Surf. Rev. Lett.* **2003**,*10*, 721–726.c). Yan, Z. et al. , *ACS Nano*, **2011**, *5*, 8187–8192). d). Liu, Z. et al. *Nano Lett*., **2011**, *11*,2032–2037 e) Garcia, J. M. et al. *Solid State Commun*. **2012**, *152*, 975–978 f). Shi, Y. et al. *Nano Lett*. **2012**, *12*, 2784–2791.

[12] Koma, A. Van der Waals. *Thin Solid Films*, **1992**,*216*, 72–76.

[13] Marian, C.R.K. *Optical Engineering Press*, **1993,** SPIE, IS *10*, SPIE, Bellingham, WA.

[14] Quate, C. F. *Surf. Sci.* **1997**, *386*, 259–264. *A more recent summary may be viewed in*: Garcia; Martinez, R Martinez R.V; *Chem. Soc. Rev.* **2006**, *35*, 29–38.

[15] a) Masubuchi, S.; Arai, M.; Machida, T. *Nano Letters* **2011**, *11*, 4542–4546. (b) Byun, I.-S.; Yoon, D.; Choi, J. S.; Hwang, I.; Lee, D. H.; Lee, M. J.; Kawai, T.; Son, Y.-W.; Jia, Q.; Cheong, H.; et al. *ACS Nano* **2011**, *5*, 6417–6424. (c) Alaboson, J. M. P.; Wang, Q. H.; Kellar, J. A.; Park, J.; Elam, J. W.; Pellin, M. J.; Hersam, M. C.. *Adv. Mater* **2011**, *23*, 2181–2184. (d) Biró, L. P.; Lambin, P. *Carbon* **2010**, *48*, 2677–2689. (e) Masubuchi, S.; Ono, M.; Yoshida, K.; Hirakawa, K.; Machida, T. *Appl. Phys. Lett* **2009**, *94*, 082107. (f) Giesbers, A.; Zeitler, U.; Neubeck, S.; Freitag, F.; Novoselov, K. S.; Maan, J. C. *Sol. State Comm.* **2008**, *147*, 366–369. (g) Weng, L.; Zhang, L.; Chen, Y. P.; Rokhinson, L. P. *Appl. Phys. Lett.* **2008**, *93*, 093107.

[16] a) Wei, Z.; Wang, D.; Kim, S.; Kim, S. Y.; Hu, Y.; Yakes, M. K.; Laracuente, A. R.; Dai, Z.; Marder, S. R.; Berger, C.; et al. *Science* **2010**, *328*, 1373–1376. (b) Mativetsky, J. M.; Treossi, E.; Orgiu, E.; Melucci, M.; Veronese, G. P.; Samorì, P.; Palermo, V. *J. Am. Chem. Soc* **2010**, *132*, 14130–14136. (c) Lu, G.; Zhou, X.; Li, H.; Yin, Z.; Li, B.; Huang, L.; Boey, F.; Zhang, H.. *Langmuir* **2010**, *26*, 6164–6166.

[17] Park, J. B.; Jaeckel, B.; Parkinson, B. A. *Langmuir* **2006**, *22*, 5334–5340.

[18] Wang, C.; Shang, G.; Qiu, X.; Bai, C. *Appl. Phys. A* **1999**, *68*, 181–185.

[19] Novoselov, K. S.; Jiang, D.; Schedin, F.; Booth, T. J.; Khotkevich, V. V.; Morozov, S. V.; Geim, A. K.. *Proc. Natl. Acad. Sci. U.S.A.* **2005**, *102*, 10451–10453.

[20] Meitl, M. A.; Zhu, Z.-T.; Kumar, V.; Lee, K. J.; Feng, X.; Huang, Y. Y.; Adesida, I.; Nuzzo, R. G.; Rogers, J. A. *Nat. Materials* **2005**, *5*, 33–38. Castellanos-Gomez, A.; Wojtaszek, M.; Tombros, N.; Agraït, N.; Van Wees, B. J.; Rubio-Bollinger, G. *Small* **2011**, *7*, 2491–2497.

[21] a) Balan, A.; Kumar, R.; Boukhicha, M.; Beyssac, O.; Bouillard, J.-C.; Taverna, D.; Sacks, W.; Marangolo, M.; Lacaze, E.; Gohler, R.; et al.*Journal of Physics D*: **2010**,*43*,374013. b) Moldt, T.; Eckmann, A.; Klar, P.; Morozov, S. V.; Zhukov, A. A.; Novoselov, K. S.; Casiraghi, C. *ACS Nano*, **2011**, *5*, 7700–7706. c) Gacem, K.; Boukhicha, M.; Chen, Z.; Shukla, A. *Nanotechnology*, **2012**, *23*, 505709.

[22] Jobst, J.; Waldmann, D.; Speck, F.; Hirner, R. arXiv: 0908. 1900.

[23] Caldwell, J. D.; Anderson, T. J.; Culbertson, J. C.; Jernigan, G. G.; Hobart, K. D.; Kub, F. J.; Tadjer, M. J.; Tedesco, J. L.; Hite, J. K.; Mastro, M. A.; Myers-Ward, R.L.; Eddy, C.R.; Campbell, P.M; Gaskill, D.K.. *ACS Nano,* **2010**, *4*, 1108–1114.

[24] Castellanos-Gomez, A.; Barkelid, M.; Goossens, A. M.; Calado, V. E.; van der Zant, H. S. J.; Steele, G. A. *Nano Letters*, **2012**, *12*, 3187–3192.

[25] Patent P201300252. "Método y Sistema de exfoliación micromecánica por vía seca de materiales laminares bidimensionales".

[26] Castellanos-Gomez,A., Navarro-Moratalla,E., Mokry,G., Quereda,J., Pinilla-Cienfuegos E., Agraït,N., Herre van der Zant S. J., Coronado,E., Steele G.A, Rubio-Bollinger,G. *Nano Research*, **2013**, *6(3)*: 191–199.

[27] Nashed, R.; Hassan, W. M. I.; Ismail, Y.; Allam, N. K. *Phys. Chem. Chem. Phys* **2013**, *15*, 1352-1357.

[28] Baumgärtel T., Graaf H.,Von Borczyskowski,C. *Thin Solid Films* ,**2011**,*519*,3443–3447.

[29] Lyuksyutov1 S.F, Paramonov,P.B., Dolog,I, Ralich,R, M. *Nanotechnology* ,**2003**,*14*,716–721.

[30] a) Sigmond, R. S., Goldman, M., Kunhardt, E. E. Luessen, L. H (Eds.). Part B. Macroscopic Processes and Discharge, Plenum Press, New York, **1983**, 1–64. b) Lachaud, S. Loiseau, J. F, *Eur. Phys. J. Appl. Phys.* **2003**, *24*,67.

[31] Xie X.N., Chung H.J., Sow, C. H., Adamiak. K, Shen, A. T., Wee. *Materials Science and Engineering R*, **2006**, *54*, 1–48.

[32] a) Jang, J., Schatz, G. C.,,. Ratner, M.A, *J. Chem. Phys.* **2002**, *11,6*3875. b) Calleja M., Tello, M., Garcıa, R.. *J. Appl. Phys.*, **2002**, *92*, No. 9.

[33] Park, J. B.; Jaeckel, B.; Parkinson, B. A. *Langmuir .***2006**, *22*, 5334–5340.

[34] Tello, M.; García, F; García, R. J. Linewidth. *Appl. Phys.* **2002**, 92, 4075-4079.

[35] Navarro, E. PhD Thesis.

[36] Geim, A. K.. *Rev. Mod. Phys.* **2011**,*83*, 851–862.

[37] a) Liu, L. Ryu,S, Tomasik M,R., Stolyarova,E.,Jung N., Hybertsen M.S., Steigerwald M. L, Brus L. E., Flynn G.W., *Nano Lett.* **2008**. *8*, 1965–1970 ;b) Elias, D:C, Nair R. R., Mohiuddin, T. M. G, Morozov S. V., Blake P, Halsall M. P., Ferrari A. C. Boukhvalov D. W., Katsnelson M. I., Gaim A. K, Novosolov, K.S. *Science*, **2009**, *323*, 610–613.

[38] Ross, S., Sussman, A. *J. Phys. Chem.***1955**, *59*, 889–892.

[39] Garcia R, V. Martineza,R. Martineza, J. *Chem. Soc. Rev.*, **2006**, *35*, 29-38.

[40] Zhu, M.; Zhang, Z.; Miao, W. *Appl. Phys. Lett.* **2006**, *89*, 021915.

[41] a) Bulaevskii, L. N. *Physics-Uspekhi* **1975**, *18*, 514–532. b) Mott, N. F.; Davis, E. A., Oxford University Press, 1979.c) Friend, R.; Yoffe, A. *Adv. Phys.* **1987**, *36*, 1–94. d) Wilson, J. A.; Yoffe, A. D. *Adv. Phys.* **1969**, *18*, 193–335

[42] Goldhaber-Gordon, D, Shtrikman, H. Mahalu, D, Abusch-Magder, D., Meirav, U., Kastner, M. A, *Nature*, **1998**,*391*.

[43] Wünsche J., Cardenas L., Rosei F., Cicoira F., Gauvin R., Graeff C. F.O, Poulin S., Pezzella A., Santato C., *Adv. Funct. Mater.* **2013**, *23*, 5591–5598.

[44] a) Altshuler, E., Johansen, T. H. *Rewies of modern physics*, **2004**, *76*. b) Vestgarden,J. Shantsev, I. D.V, Galperin, Y. M. ,Johansen, T. H. Scientific reports,*2*,886,DOI: 10.1038 /srep 00886

[45] Lichtenberg, G. C (1742-1799). Professor Lichtenberg made this observation in 1777, demonstrating the phenomenon to his physics students and peers. He reported his findings in his memoir (in Latin): De Nova Methodo Naturam Ac Motum Fluidi Electrici Investigandi (Göttinger Novi Commentarii, Göttingen, 1777).

[46] a) Jerome, D.; Berthier, C.; Molinie, P.; Rouxel, *J. J. Phys.* **1976**,*4*, 125-135.;b) Jones, R.E.; Shanks, H.R.; Finnemore, D.K. *Phys. Rev.B* ,**1972**, *6* 835-838.

[47] Aranson, I., A. Gurevich, V. Vinokur, *Phys. Rev. Lett,* **2001**. *87*, 067003.

[48] Gamble,F., DiSalvo,F.,. Klemm,R. A,Geballe T. *Science* **1970**, *168*, 568–570.

[49] Horcas, I., Fernandez, R. Gómez-Rodríguez, J. M, Colchero, J., Gómez-Herrero, J., Baro, A. M. WSXM: *Rev. Sci. Instrum.* **2007**,*78*,013705.

[50] Houzè, F., Meyer, R., Schneegans, O., Boyer, L., *Appl. Phys. Lett*. **1996**, *69*, 1975.

3

ORGANIZATION OF MOLECULAR-BASED MAGNETIC NANOPARTICLES ON SURFACES

3.1 INTRODUCTION

Last years there has seen an enhanced interest in the preparation and processability of magnetic nanoparticles (MNPs) not only for the importance of studying their unusual physical and chemical properties associated to the quantum size effect, but also for their applicability in different fields, from biology to computational science, thanks to properties like giant magnetoresistance or abnormally high magnetocaloric effect.[1] Their appropriate assembling would generate new organized nanostructures which often introduce novel collective physical properties that can be deployed.[2] The processed MNPs are being exploited for their integration in devices such as magnetic recording media,[3] magnetic cellular automata,[4] or magnetoelectronic devices[5] or in more general applications as nanoelectronics, spintronics or biomedicine.[6]

The organization of magnetic nanoparticles is advancing to the forefront of modern research of magnetism and magnetic materials, and many different approaches for the magnetic ordered nanostructure synthesis and processing have been developed until now.[7] The organization strategies can be roughly categorized as either 'top-down' or 'bottom-up'. The adjective 'top-down' is used to describe the breaking down of a system to gain insight into its compositional sub-systems, while 'bottom-up' is used for describing the piecing together of units to give rise to more complex systems. As discussed in chapter 1, many nanolithography methods based in both approaches have been developed to address magnetic molecules and nanoparticles (NPs) offering a wide variety of possibilities.[8]

A close look to Prussian blue analogue nanoparticles

Studies on NPs have been mainly concerned with preparation and characterization of a few number of metallic or metal oxide NPs principally based on Fe or Co.[9] However, the family of molecular-based MNPs[10] opens the way to an almost infinite particle composition with intrinsic properties that come along with their molecular nature like transparency, low density or high tunability, which make them specially interesting in

specific applications. Among them, Prussian blue analogue NPs (PBA-NPs) based on cyanide bridged coordination compounds permit the preparation of a large family of MNPs with similar structure, but showing different physical properties as photomagnetism or superparamagnetism, depending on their composition and size.[11]

In bulk, PBAs can easily be synthesized by the simple reaction of hexacyanometalates $[M'(CN)_6]^{p-}$ with transition metal Lewis acids $[M(H_2O)]^{q+}$ in water to give three-dimensional networks of general formula $A_xM[M'(CN_6)]_z$ nH_2O (where A is an alkali-metal cation and M and M' are transition metal ions connected as M-N≡C-M'). The solids adopt face-centered cubic structures (Figure 1) and whenever z < 1 the presence of vacancies is intrinsic in the structure, (it is not a defect structure). This feature determines some important properties.[12] As molecular-based magnets, PBA are especially interesting because they can be prepared at room temperature from well-characterized and chemically stable building blocks, the metal centers are linked covalently into a 3D network and a wide range of metals with different spin states and oxidation states can be substituted into the structure. Furthermore, the bridging cyanide ligands can promote strong magnetic exchange couplings between paramagnetic centers. These features allow considerable control over the nature and magnitude of the local magnetic exchange interactions and often give rise to structures which magnetism can be tuned by an external stimulus.[13]
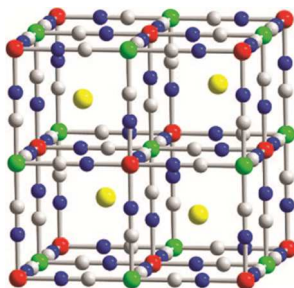

Figure 1. Structures of the Prussian blue analogues, $A_xM[M'(CN_6)]_z$. Yellow, red, green, gray, and blue spheres represent A, M, M', C, and N atoms, respectively. Guest water molecules and hydrogen atoms were omitted for clarity. Figure adapted from reference [12]

Even though the study of PBA have traditionally been limited to bulk compounds, lately they have also been processed onto surfaces as films[14] and more recently into nanoparticles.[11,15] The fact that the NPs properties can be modulated externally deserves special attention thinking in their applicability. For this reason, PBA-NPs can be considered as promising units for processing or storing information, spintronic or even medical applications.[16] However, there are still several limitations to overcome in order to accomplish this objective. For example, in the particular case of NPs, they need not only to be deposited on a controllable way, but also to be positioned on specific regions of the surface. The interest in addressing these MNPs individually have motivated their controlled anchoring and organization onto surfaces following different approaches, for example based on Galvanic displacement,[17] Langmuir Blodgett techniques,[18] or by grafting PBA-NPs on Si(100) by bonding the NPs to a coordination Ni (II) compound previously linked to a self-assembled monolayer on a Si oxide-free surface.[19] In a further step PBA-NPs were patterned over large areas of Si (100) surfaces using Focused Ion Beam lithography (FIB).[20] However, with these reports, yet pioneering, PBA-NPs large patterns are produced by means of usually difficult processes and very poor accuracy. To avoid this limitation, easier protocols, and/or protocols leading to large patterns deposited PBA-NPs at the nanoscale would be desirable.

In this chapter, the family of Ni(II), Cr(III) cyanide-bridged coordination NPs have been chosen for their organization on surfaces. They consist of a three dimensional assembly of structural motifs $-N\equiv C-Cr-C\equiv N-Ni-$ where the Ni^{II} ions are surrounded by six nitrogen atoms and the Cr^{III} ions by six carbon atoms. Both have an octahedral symmetry. Alkaly ions are present in part of the tetrahedral sites of the structure as shown in Figure 1. The three unpaired electrons of Cr^{III} (d^3) and the two unpaired electrons of the Ni^{II} (d^8) through the cyanure bridge give rise to ferromagnetic interacctions. This family of NPs can be synthetized as bare NPs, without the need of

organic capping, and their size (and thus, their magnetic properties) can be tuned at will. [11, 16, 21]

The three different *alternative* lithography techniques mentioned in chapter 1 have been used in this thesis for the controlled positioning of PBA-MNPs: Local Oxidation Nanolithography (LON), Dip-pen Nanolithography (DPN) and Soft lithography. All of them were combined with the formation of specific self-assembled monolayers (SAMs) to functionalize the silicon surfaces where the PBA-MNPs were organized.

3.2 RESULTS AND DISCUSSION

3.2.1 PBA-NPs structural characterization

The Ni(II), Cr(III) cyanide-bridged coordination NPs chosen for this work present a general negative charge that is compensated by the alkaline cations Cs^+ or K^+ ($A_x Ni[Cr(CN)_6]_z$). The Cs based NPs, of general formula $Cs_{0.7}Ni[Cr(CN)_6]_{0.9}$ (CsNiCr NPs), have been deeply studied and there are several publications that describe their structure and magnetic properties.[16,19,21] A scheme of their crystal structure is presented in Figure 2a. The K based NPs were synthetized by the group of Professor Tallal Mallah some years ago and they have been specifically studied in depth for this work, as collaboration between our research groups. Elemental analysis has been performed and reveals that the composition of KNiCr NPs recovered with 20 equivalents of polyvinilpirrolidone (PVP) is $K_{0.22}Ni(Cr(CN)_6)_{0.74}$ $(PVP)_{20}(H_2O)_{36}$ (KNiCr NPs). From the 0.22 K equivalents per unit formula, 0.14 equivalents are inserted within the network.

Both kinds of NPs are cubic shaped. As can be seen by Scanning Transmission Electron Microscopy (STEM) (Figure 2b), KNiCr NPs are almost perfect cubic with an averaged aspect ratio between 1 and 1.1, less pronounced than in the case of CsNiCr NPs that are slighted more elongated, as was reported in refence [21]. They are stable in aqueous solution at pH = 6-7 and below a specific critical size show superparamagnetic behavior with blocking temperatures (T_B) above aprox. 4 K.[16]
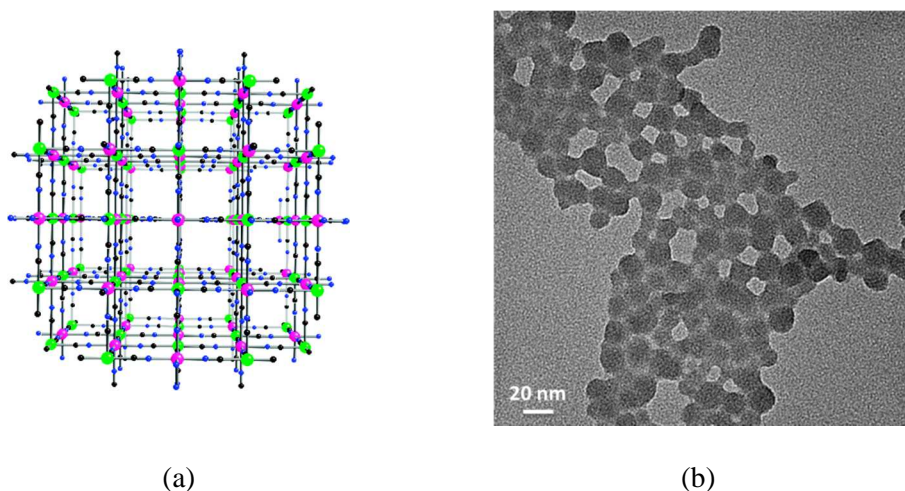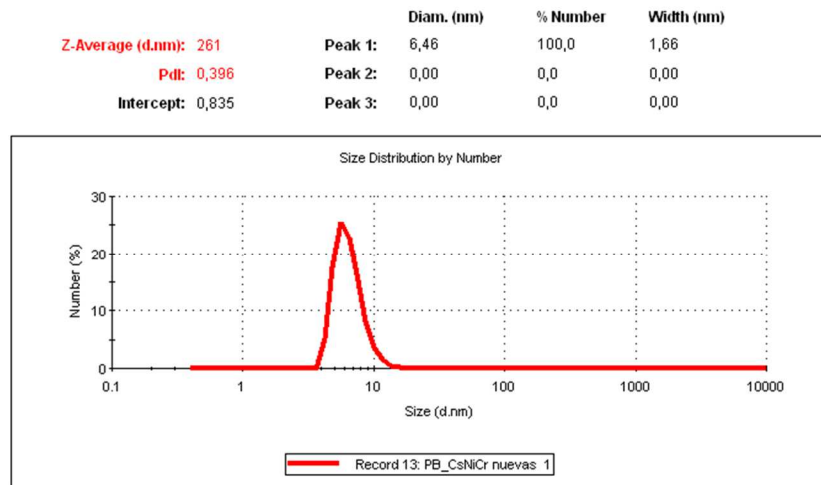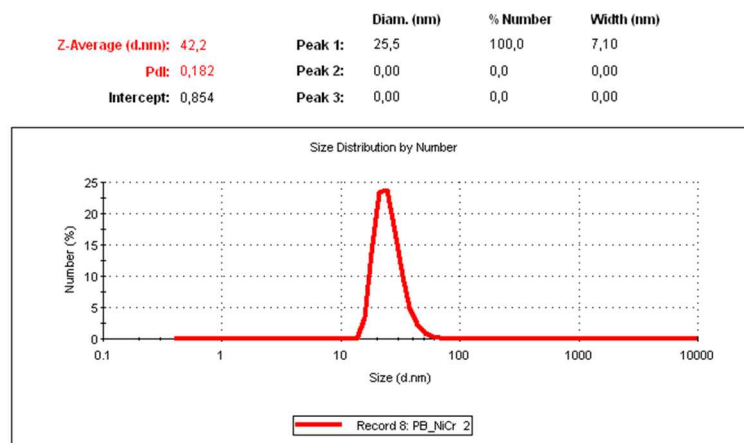
(a)   (b)

Figure 2. (a) crystal structure of the $Cs_{0.7}Ni[Cr(CN)_6]_{0.9}$ PBA-NPs (black:C, blue: N, Green Cr^{III}, pink Ni^{II}). (b) STEM image of the KNiCr-NPs.

When Cs^+ was used as counteranion the size of the CsNiCr NPs was estimated to be approx. 6 nm, as calculated from dynamic light scattering (DLS) (Figure 3a). Whenever Cs^+ is not added to the reaction mixture, higher diameter KNiCr NPs were obtained (approx. 25 nm from DLS (Figure 3b)). Both kinds of particles have the same structure, but as the number of alkaline cations changes, so does the number of $Cr(CN)_6^{3-}$ vacancies, which slightly modifies the anisotropy of the system and the critical temperature. The well-known magnetic characterization of CsNiCr NPs will be briefly discussed later in this chapter to prove the stability of these NPs after surface attachment. A more detailed study about the magnetic properties of KNiCr NPs will be presented in chapter 5 for the interpretations of magnetic force microscopy measurements.

		Diam. (nm)	% Number	Width (nm)
Z-Average (d.nm): 261	Peak 1:	6,46	100,0	1,66
PdI: 0,396	Peak 2:	0,00	0,0	0,00
Intercept: 0,835	Peak 3:	0,00	0,0	0,00

(a)

		Diam. (nm)	% Number	Width (nm)
Z-Average (d.nm): 42,2	Peak 1:	25,5	100,0	7,10
PdI: 0,182	Peak 2:	0,00	0,0	0,00
Intercept: 0,854	Peak 3:	0,00	0,0	0,00

(b)

Figure 3. Dynamic light scattering measurements of 1 mM in Ni PBA-NPs solution:(a) CsNiCr NPs and (b) KNiCr NPs.

3.2.2 PBA-NPs organized by LON

3.2.2.1 Deposition experiments

The approach used to reach the positioning of the PBA-NPs on Si surfaces was done as a combination of self-assembly 'bottom-up' approaches with 'top-down' lithographic techniques that has shown to be very suitable to selectively deposit molecular objects onto the nanopatterns fabricated from LON. [22,23,24,25] The method is based on the electrostatic interactions established between a self-assembled monolayer (SAM) of aminopropyltriethoxysilane (APTES) located on SiO_2 patterned marks and negatively charged nanoparticles. This method is quite general and has already been used for the positioning of any kind of charged nanoparticle (either cationic or anionic) or molecules.

Before performing the LON patterning, an exhaustive study about the affinities of the PBA-NPs was carried out on two types of self-assembled monolayers (SAMs): (APTES and octadecyltrichlorosilane (OTS)) and on two types of surfaces (Si substrate covered with its native SiO_2 and nanolithographically oxidized surfaces (LON-SiO_2 surfaces)) (Figure 4).
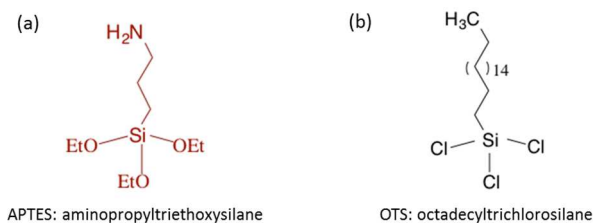

Figure 4. (a) and (b) Schematic structures of SAMs.

The anionic nature of PBA-NPs suggests a preference of the particles by the amino groups in the APTES monolayers, which are known to be easily protonated giving rise to cationic surfaces, while the high hydrophobic surfaces obtained with OTS SAMs imply that the NPs should not get attached onto them. First experiments where

performed by drop casting 50 µL of a freshly prepared solution of CsNiCr NPs (1mM in Ni(II)) for 2 minutes on the different surfaces and rinsing with ultrapure water before NPs solution dried under a N_2 stream (see section 3.3). Regardless of the surface, only few NPs were fixed and high preference needed for the specific deposition on LONs patterns was not reached (Figure 5).
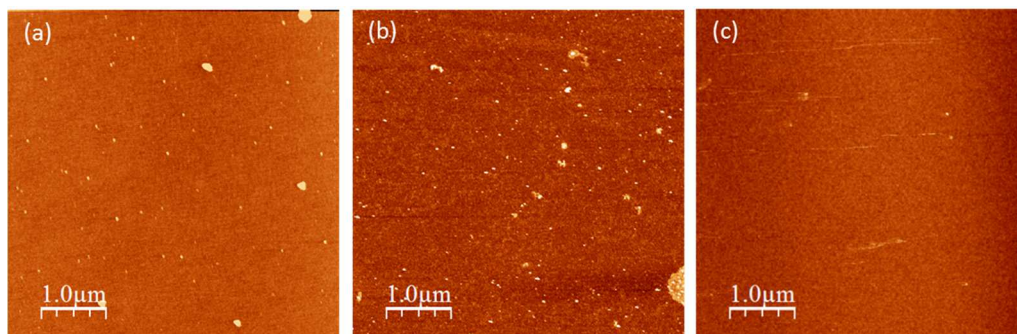

Figure 5. AFM topography images of different surfaces where the CsNiCr NPs has been deposited by drop casting (a) SiO_2 surface. (b) APTES functionalized surface. (c) OTS functionalized surface. No prefferential attachment could be seen.

As a next step, we forced the protonation of the APTES SAM by acid pretreatment and again, all the other surfaces were tested in the same conditions. In a typical experiment the different surfaces were prepared according to the procedure described in section 3.3. Briefly, the substrates were sonicated in a pH = 1 aqueous solution for 7 minutes and dried under N_2 without rinsing. The NPs were then deposited during 1 minute over the substrates by drop casting 50 µL of a freshly prepared 1 mM in Ni aqueous PBA-NPs solution. Next the substrates were rinsed with ultrapure water and dried under a N_2 stream. Finally, the number of deposited nanoparticles was studied by AFM. The obtained results are shown in Figure 6.
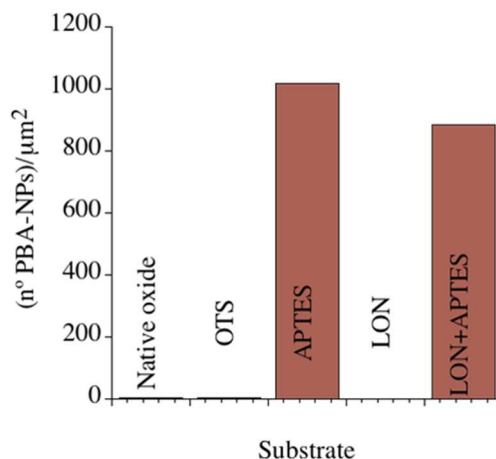
Figure 6. Columns graphic about the number of CsNiCr NPs per square micrometer adhered onto different surfaces: Native oxide (SiO_2), OTS, APTES, LON-SiO_2 mark, and LON-SiO_2+APTES functionalized surface. All the surfaces were treated in diluted HCl solution (7 minutes sonication) before NPs deposition.

It can be observed that PBA-NPs scarcely attach over silicon substrates covered either with native SiO_2, LON-SiO_2 or OTS. However, functionalization of native SiO_2 or LON-SiO_2 marks with APTES largely increases the number of deposited NPs. That can be explained in terms of electrostatic interactions. While in the case of SiO_2 and OTS no protonation is expected at low pH, the -NH_2 group in the APTES SAM at pH = 1 will get protonated, at least to some extent.[26] So, the surface will be positively charged attracting the negatively charged PBA-NPs. These nanoparticles remain attached at the surface even after sonication in water for some minutes. This result shows the strong electrostatic anchoring of the anionic PBA-NPs to the APTES in spite of the lack of covalent bonds. Notice that there is no need of covalent modifications which can be very useful in order to maintain physical properties of the particles unchanged.

In the case of PBA-NPs the strength of the interaction between the surface and the NPs cannot be freely modified by changing the pH of the NPs solution as we did before for the positioning of ferritine biomolecules,[23a] nor it is possible to change drastically their concentration, as this will compromise the integrity of the NPs, which are based on coordination compounds. However, it was possible to modulate the strength of the interaction by controlling the time during which APTES substrates were sonicated in a pH = 1 aqueous solution before getting in contact with the PBA-NPs. In this approach the pH of the PBA-NPs solution was not modified, but the substrates were immersed in acidic aqueous solutions to enhance the protonation of the amino groups of the APTES layer as that maximizes electrostatic interactions during the deposition step.[26] With sonication times equal or higher than 7 minutes, a particle density as high as 940-1100 NP/μm^2 was always obtained, whereas with sonication times below 7 minutes the density of particles decreased and the method became not reproducible (Figure 7.).

The fact that sonication, instead of merely immersion in the acid solution, yielded better results can be explained by the presence of a relatively high amino density in an hydrophobic environment which arises from a disordered structure that exposes methylene groups at the surface, as previously described by others.[27] Once a surface amine group is exposed, it is protonated and its positive charge can suppress the protonation of neighbouring groups. Moreover, poor solvation and bridging between neighbouring charged groups would also suppress further protonation. In this scenario, the sonication will help to overcome the kinetic reorganizations barriers speeding up the protonation process.[26] Together with the sonication effect an increase in temperature during the process could be responsible of the changes observed, however the monitoring of the temperature in the sonication bath indicates that after 7 minutes of sonication, there is no change in temperature. Only after long sonication periods (>15 min., see 3.3 section) the observed increase in sonication bath temperature could contribute to further speed the protonation process.
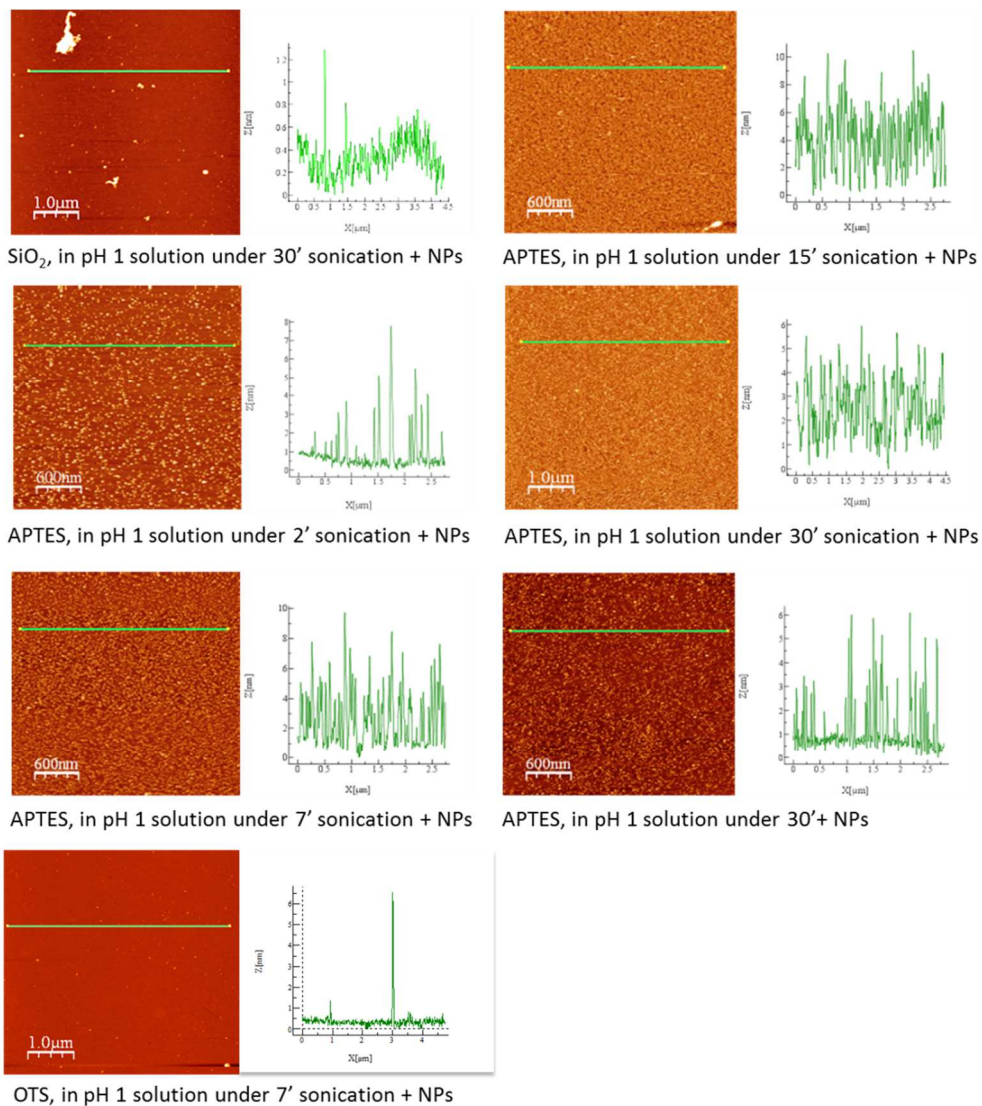
Figure 7. AFM topography images and the corresponding height profiles of protonated APTES functionalized Si surface, showing the CsNiCr NPs preferential deposition with the different times of immersion and/or sonication in HCl solution for the protonation of the SAM.

3.2.2.2 Chemical and magnetic characterization of the grafted PBA-NPs

To prove that the PBA-NPs were not damaged after the anchoring deposition onto the surfaces, we complemented the AFM measurements with spectroscopic and magnetic studies. First, attenuated total reflection infrared spectroscopy (ATR-IRRAS) of the APTES functionalized SiO_2 substrates fully covered with PBA-NPs were carried out to confirm the presence of the NPs. The spectrum shows the characteristic 2171 cm^{-1} peak associated with the existence of bridging CN$^-$ groups in the PBA-NP framework (Figure 8).
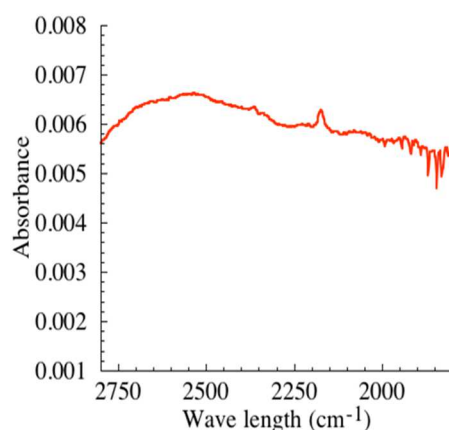
Figure 8. ATR-IRRAS of the CsNiCr NPs grafted on a silicon substrate functionalized with APTES. Substrate was sonicated at pH = 1 before NPs deposition.

For proving the chemical composition of the surfaces, we complementarily performed Auger Electron Spectroscopy (AES) measurements[28] on two kinds of samples: Sample 1 formed by a silicon substrate coated with APTES (Figure 9a), and Sample 2 formed by PBA-NPs grafted on a silicon substrate coated with APTES (Figure 9b). Measurements performed on Sample 1 indicate the presence of the SAM of APTES over the SiO_2 substrate (Si 95 eV, C 294 eV and O 473, 490, 512 eV peaks, due to the low amount of N it is difficult to detect). In Sample 2, both the additional detection of

Ni (717, 783, 851 eV), Cr (531 eV) and Cs (562, 574 eV) and N (385 eV) peaks along with an increased amount of C (272 eV), derived from the presence of the CN groups, clearly evidence the presence of the PBA-NPs.[29]
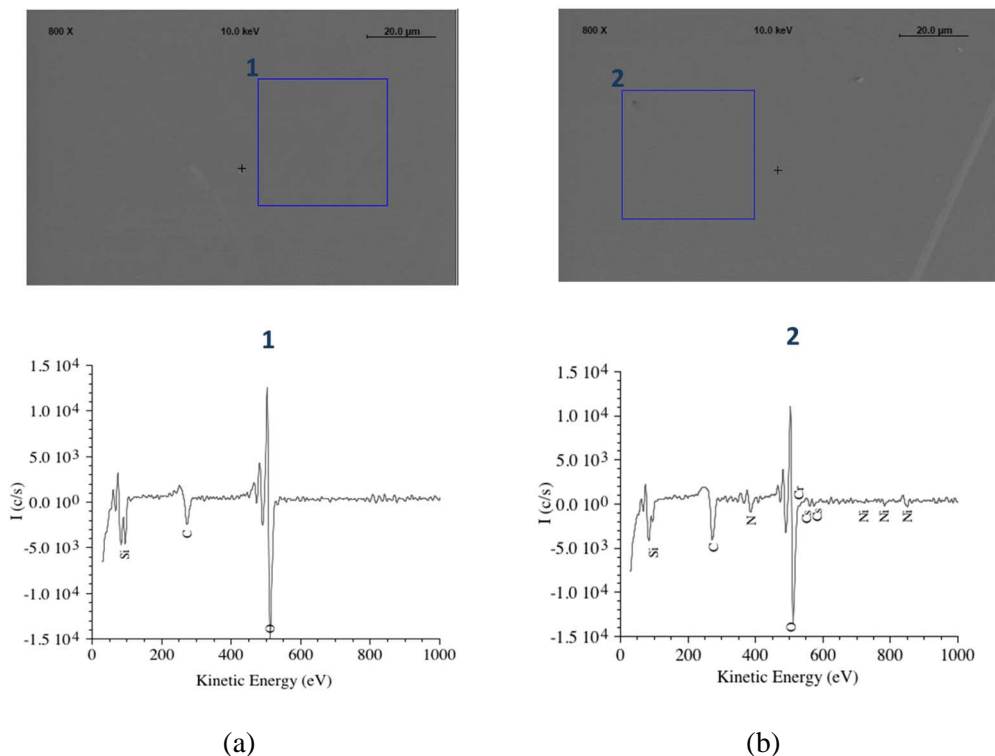
Figure 9. (a) Sample 1: SEM image and Auger electron spectra of functionalized Si substrate with protonated APTES without NPs. (b) Sample 2: SEM image and Auger electron spectra of CsNiCr NPs on functionalized Si substrate with protonated APTES.

Magnetic properties of the deposited nanoparticles were studied using a superconducting quantum interference device (SQUID) magnetometer. In order to overcome the problem of the low amount of magnetic sample (a sub-monolayer of PBA-NPs) on a large amount of diamagnetic material (silicon wafer with an APTES monolayer) a setup similar to the one proposed by B. Fleury et al.[19] was prepared (see 3.3 section). In this setup, the contribution to the overall signal of the silicon wafer is

minimized during the measurement and only the magnetic signal from the PBA-NPs is directly recorded. Field-cooled (FC) and Zero-field-cooled (ZFC) magnetization measurements of CsNiCr NPs were performed under 100 Oe applied magnetic field. As can be seen in figure 6, the two curves diverge below T = 14 K and the maximum of the ZFC is observed at 9 K (slightly higher than the NPs blocking temperature in a polymer matrix).[19,21] This blocking temperature corresponds to magnetically nearly isolated particles. Notice that the high NPs density on the surface prevents the completely isolated behavior. This limitation could be easily overcome by preparing samples with lower density PBA-NPs on the surface (for example by decreasing the protonation ratio of APTES monolayer or by lowering the deposition times). Still, the resulting decrease in the amount of magnetic material will sharply reduce signal intensity and will make the experimental measurements very difficult to perform (Figure 10).
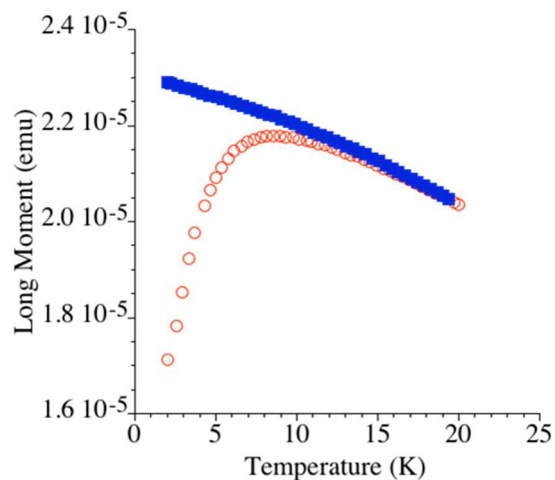

Figure 10. Field cooled (empty circles) and zero-field cooled (full squares) magnetization measurements for the CsNiCr NPs grafted on a silicon wafer previously functionalized with a protonated APTES monolayer.

3.2.2.3 Patterning experiments

General procedure

By combining the LON with the functionalization of SiO_2 with SAMs of OTS and APTES, we were able to position PBA-NPs with nanometric precision over Si surfaces. In Figure 11 it is shown the followed protocol. First, silicon substrates with markers were freshly cleaned in H_2O_2:NH_4OH:H_2O (1:1:2) solution (see section 3.3 for details). Next, they were functionalized with an OTS monolayer (i). OTS-functionalized substrates were patterned by means of LON with features of different shapes and heights (ii). The patterned substrates were then functionalized with APTES that reacts specifically with the freshly prepared LON-SiO_2 marks (iii). At this point, a good quality OTS monolayer is indispensable to prevent the APTES grafting outside the lithographed zones. After APTES functionalization the substrates were immersed in a diluted pH = 1 acid solution and sonicated for at least 7 min. (iv). During this step, amino groups got protonated and therefore the SiO_2 marks covered with APTES got positively charged. Without rinsing, a ~50 µL drop of a solution 1 mM in Ni of PBA-NPs was deposited on top of the substrate for 1 min. (v); afterwards, the sample was rinsed with Mili-Q water and dried under a N_2 stream (vi). Occasionally, as a last cleaning step, sonication in water for few minutes was required.
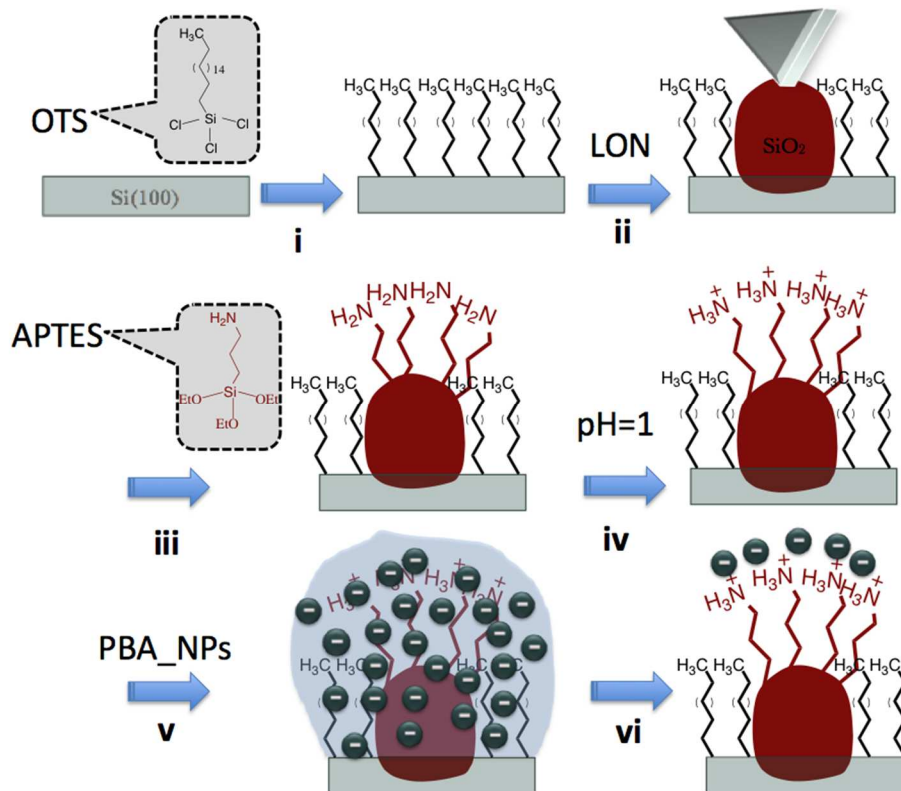
Figure 11. Steps: i) OTS monolayer formation, ii) LON pattern by means of a specific applied voltage, iii) APTES monolayer formation on top of the bare LON pattern, iv) immersion and sonication of the sample in pH =1 aqueous solution, v) deposition of PBA-NPs by drop casting the solution on top of the substrate and vi) last sample is rinsed with water and dried under a N_2 stream.

CsNiCr NPs deposition

CsNiCr NPs were successfully deposited by the procedure above described. Figure 12 shows an APTES-LON modified substrate before (Figure 12a) and after (Figure 12b) NPs deposition. In Figure 12b one can observe the high preferentiality and nanoparticle density obtained during the deposition process. In some rare cases CsNiCr NPs could be removed from the patterned marks by sonication in the same acid solution used to protonate the APTES molecules (Figure 12c). The reason why they were not always removed under these conditions is still unclear for us. In any

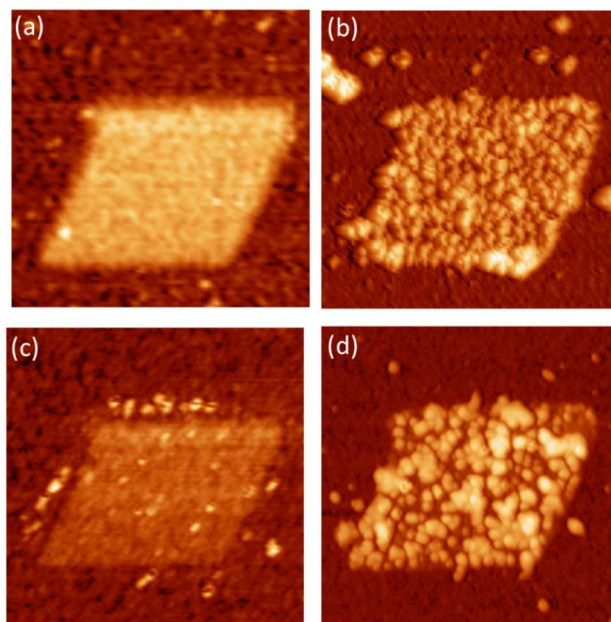case, whenever particles were removed from the surface, deposition process could be repeated (Figure 12d).

Figure 12. AFM topography images (images size: 660 nm x 660 nm) representation of different steps of the CsNiCr NPs deposition process on nanolithographed patterns. (a) OTS-functionalized substrate was patterned by LON and then marks were modified with protonated APTES. (b) PBA-NPs solution was deposited on the substrate and a clear preference for the modified nanolithographed pattern was shown. (c) Deposited CsNiCr NPs were removed by sonication in acid solution. (d) The deposition process was successfully repeated.

To further highlight the importance of electrostatic interactions between the PBA-NPs and APTES in our grafting protocol (Figure 13) in a first experiment an OTS functionalized substrate was patterned with LON-SiO$_2$ marks (Figure 13a), immersed into ethanol (without APTES molecules), sonicated in aqueous pH = 1 solution and dried under N$_2$. Then, CsNiCr NPs were deposited on this substrate by drop casting. In this case, AFM measurements show that a very low number of NPs got attached to the surface either inside or outside the mark (Figure 13b), in full agreement with our previous observation (Figure 6). In a second experiment the same sample was immersed in an APTES solution to functionalize the mark and then sonicated in

diluted HCl (pH = 1). Then PBA-NPs deposition was repeated and the mark was imaged again. In this case, the mark appeared covered with NPs (Figure 13c) while the rest of the surface remained free of them. This is a clear proof of the essential role played by APTES during the deposition of PBA-NPs. In spite of the fact that in some cases the precise number of NPs attached to the functionalized oxide mark was very difficult to quantify, the accurate measurements in z direction confirmed that the NPs were not piled up on top of the lithographed patterns.

As discussed in the previous section (3.2.2.2), electrostatic driving forces seem to control the clear preferential deposition of the negatively charged PBA-NPs on the cationic APTES surface. This preferentiality was achieved regardless of the shape of the marks which includes large strips ~400 nm x 400 nm (Figure 13a), lines ~70 nm x 400 nm (Figure 13d) or even dots of less than 75 nm in diameter (Figure 13e). Such a result proves the very precise control achieved on the organization of these negatively charged nanoparticles on surfaces at length scales ranging from hundreds to tens of nanometers.
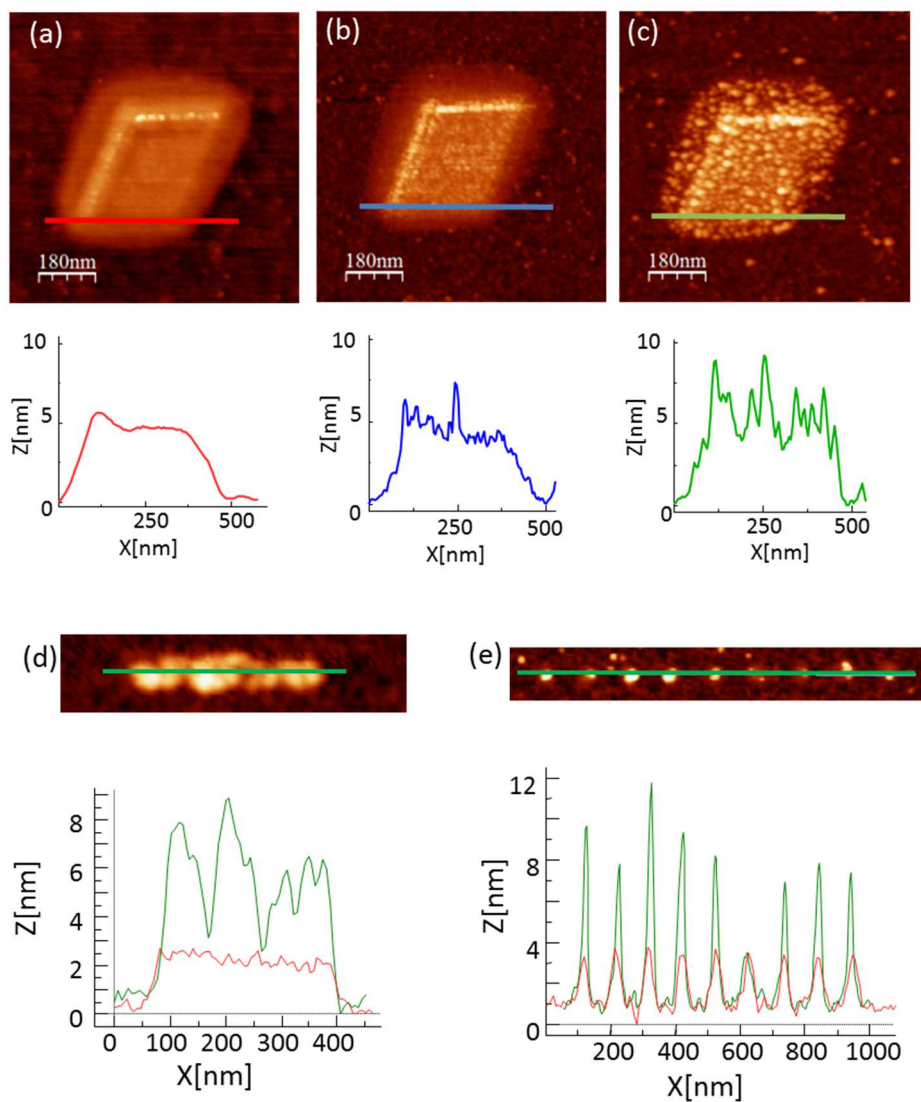
Figure 13. AFM topography images and profiles of: (a) LON-SiO$_2$ mark patterned on a silicon wafer previously covered with a OTS monolayer (red profile); (b) the same mark after deposition of CsNiCr NPs. The substrate was treated with ethanol and diluted HCl but without APTES (blue profile); (c) the same mark after functionalization with APTES and diluted HCl and deposition of same CsNiCr NPs (green profile); (d) and (e) deposition experiment on APTES modified LON-SiO$_2$ marks with different shapes and sizes (red profile: before NPs deposition, green profile: after NPs deposition).

KNiCr NPs deposition

To demonstrate the possibility of extending this precise electrostatic organization procedure to PBA-NPs of different sizes and chemical compositions PBA-NPs, the larger KNiCr NPs (approx. 25 nm) were used. Next, the same deposition protocol was applied. As can be seen in (Figure 14), high preferentiality and precision were maintained in this case too.
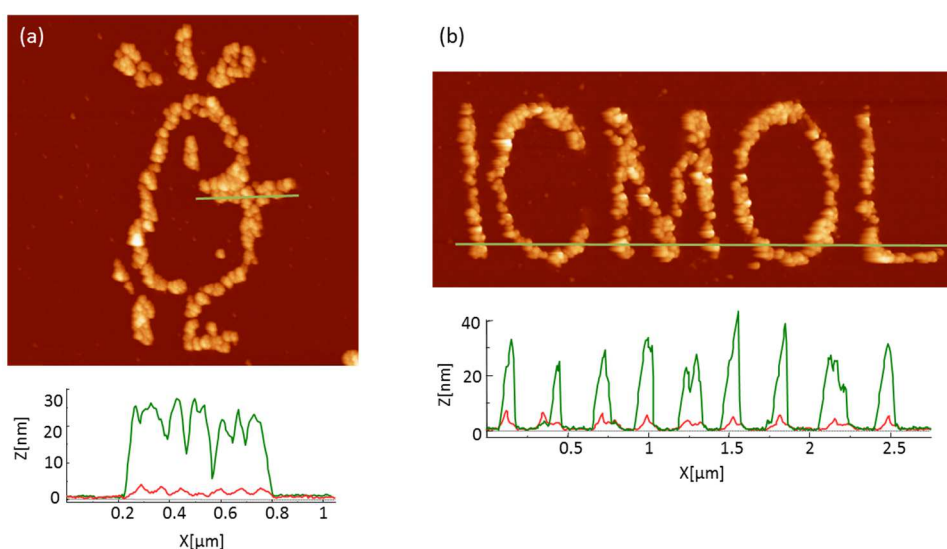
Figure 14. AFM topography images of different nanolithographed patterns on a OTS monolayer with KNiCr NPs on top with their corresponding height profiles (red: before NPs deposition; green: after NPs deposition). Marks were functionalized as usual with protonated APTES before NPs deposition. (a) image size: 2.7 µm x 2.7 µm; (b) image size: 3.1 µm x 1.3 µm).

3.2.2.4 Preferentiality of the PBA-NPs with the LON size

Interestingly, we realized that the 25 nm KNiCr NPs showed a selective preferentiality for the larger marks (Figure 15), so we decided to study it in more detail. Such a result was not observed with the smaller 6 nm CsNiCr NPs. In this case, single NPs were trapped in marks of about 30 nm width (1.5 nm height, in Figure 15a, Figure 15b). However, the minimum mark size needed to attach a 25 nm NP was larger. In fact,

marks of around 100 nm in diameter (3 nm height) were necessary to trap these NPs. Moreover, at least 4 or 5 NPs were usually found on a single mark (Figure 15c). So it seems that it is more difficult to find single NPs onto a unique LON mark when they exceed a certain size.
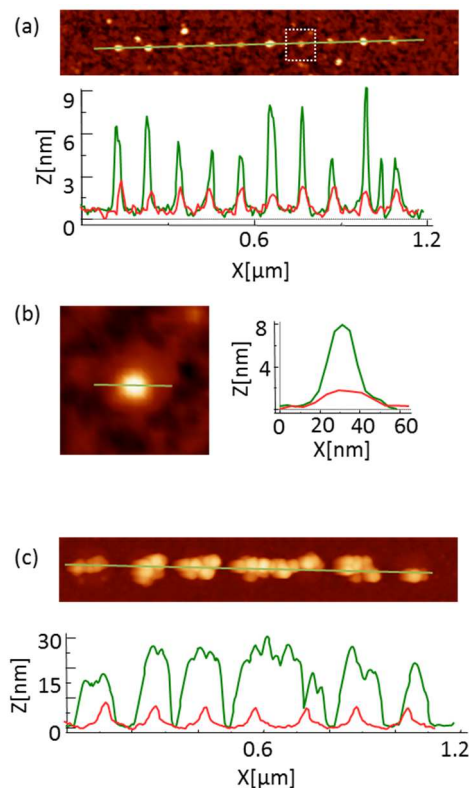
Figure 15. AFM topography images of: (a) CsNiCr NPs (image size: 1.40 µm x 0.23 µm); (b) zoom image and profile of 7th dot in (a), where one single NP has been attached (image size: 90 nm x 90 nm); (c) KNiCr NPs on nanolithographed dots (image size: 1.40 µm x 0.23 µm). Below/next each image, the corresponding superposition of height profiles before (red) and after (green) NPs deposition are shown.

The interdependence between oxide motives size and NPs size would open the door to the selective deposition of nanoparticles of specific sizes and to the hierarchical organization of NPs of different sizes on the same substrate. For a more detailed study about this particular point, a LON pattern of dots with different sizes was performed

(Figure 16a and Figure 16b). Then, KNiCr NPs (~25 nm) were deposited and we found again that the large NPs were preferentially attached onto the larger dots. A zoom in of topography AFM images of the functionalized LON marks without and with KNiCr NPs was performed (Figure 16c and d) and it can be seen that the marks presenting larger surface areas were completely full of NPs. However, as can be seen in the profile (Figure 16e), at the smallest oxide dots there were no particles attached. Although in some cases, some KNiCr NPs presenting smaller sizes always present in some degree in the NPs solution, got attached.[1] Therefore, it seems that there is selective attachment of the larger NPs onto the larger LON patterns and the smaller NPs onto the smaller patterns.
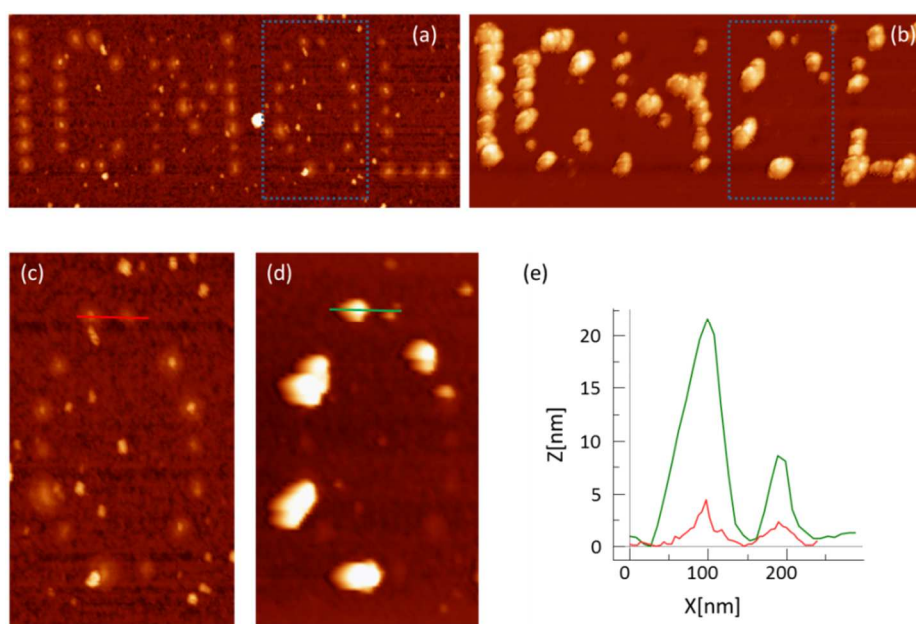
Figure 16. (a) AFM topography image of SiO_2 nanopattern on OTS functionalized silicon surface. Oxide dots have different size (width and heigh). Images size: 2.4 µm x 1.0 µm. (b) Topography image of KNiCr NPson top of protonated APTES functionalized nanopattern showed in (a). (c) and (d).Zoom in of the dotted areas of topography images (a) and (b). Images size: 600 nmx 900 nm.

[1] The thorough control of reaction parameters of the PBA-NPs synthesis (time, temperature, stirring velocity and concentrations of reactants) does not always allow narrowing down the size distribution of the NPs. Therefore it is always possible to get a certain number of NPs with smaller sizes; even the great majority have the proper size.

The next experiment was performed to check if two different kind of NPs, CsNiCr NPs (~ 6 nm) and KNiCr NPs (~ 25 nm), could be preferentially organized on a LON patterned substrate by controlling the sizes of the marks. If the above explained condition is fulfilled, the KNiCr NPs would attach onto the largest marks and the CsNiCr NPs onto the smallest. The topography image (Figure 17a) shows 5 lithographed dots with different sizes onto a Si substrate functionalized with OTS: dot 1 (150 nm x 10 nm), dot 2 (45 nm x 2 nm), dot 3 (45 nm x 1.5 nm), dot 4 (50 nm x 1.5 nm) and dot 5 (170 nm x 5 nm). Then, the sample was functionalized with APTES and sonicated (7 min) in a solution of HCl to protonate the SAM.

As the smallest NPs seemed to attach whatever the size of the oxide dot, the NPs deposition was done in two steps to avoid that all the oxide dots were filled by the smallest NPs at once. First, a drop of KNiCr NPs solution was deposited by drop casting (2 min), rinsed with mili-Q water and dried under N_2 gas. The topography and phase image of this step is shown in Figure 17b and can be clearly seen that the biggest KNiCr NPs are preferentially attached onto the dots number 1 and 5, and small KNiCr NPs present in the solution got attached onto the smallest dots, numbers 2 and 3. Second, the sample was sonicated again in HCl (2 min) to assure the attachment of the anionic NPs, and a drop of CsNiCr NPs solution was deposited by drop casting (2 min), rinse with mili Q water and dried under N_2 gas. The topography and phase image of this step is shown in Figure 17c. As can be seen in both images, the 5 dots are fully covered with the NPs, but unfortunately by checking the profiles (Figure 17d) we can conclude that large KNiCr NPs were removed and all the NPs attached are CsNiCr type (or small KNiCr NPs). Two different explanations could justify this result. The first one could be that with the sonication in the acidic solution the KNiCr NPs were detached as happened before with the CsNiCr NPs explained in section 3.2.2.3 (Figure 12). However, as was also previously mentioned, our experience with several samples indicates that it is not so easy to remove the attached NPs by sonication, and actually it usually does not occur. A second explanation would be that

in the presence of CsNiCr NPs, they displace the KNiCr NPs from the oxide dots and cover all the marks.
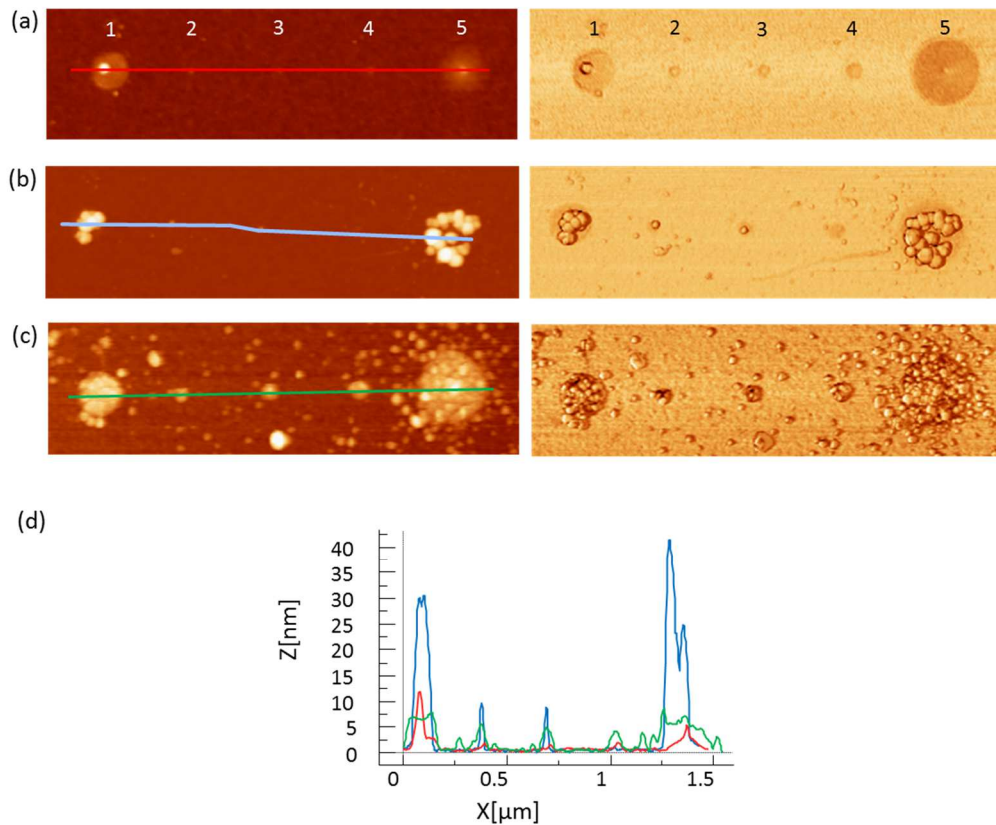
Figure 17. (a) Topography and phase images of the 5 dots oxidized by LON on a Si substrate functionalized with OTS. The 5 dots are labelled with the corresponding numbers. (b) Topography and phase images of the KNiCr NPs attached onto the lithographed dots previously functionalized with protonated APTES. (c) Topography and phase images of the CsNiCr NPs attached onto the lithographed dots. (d) Height profiles of images (a), (b) and (c).

Taking a close look on the deposited NPs, it appears that the highest central part of the patterns are always decorated with one single NP, so it looks like the deposition is very sensitive to the height of the lithographed mark. The rest of the NPs fulfil the remaining pattern and it happens for the KNiCr NPs as well as for the CsNiCr NPs.

As we are working with NPs of different composition and size, it could happen that the preferentiality of the NP deposition would be related to its surface charge instead of its size. As was mentioned in the introduction, the PBA-NPs are anionic, and depending on the chemical composition and size, their negative charge may change. To check this possibility, we decided to work with bigger CsNiCr NPs with mean sizes of ~20 nm (Figure 18) that were synthesized in the group of Dr. L. Catala. As these NPs maintain exactly the same composition as the small CsNiCr NPs that we prepared (6 nm), they should have exactly the same charge surface, although the global charge per particle is larger in the big ones.

		Size (d.n...	% Number:	St Dev (d.n...
Z-Average (d.nm): 31.27	Peak 1:	21.62	100.0	5.662
Pdl: 0.084	Peak 2:	0.000	0.0	0.000
Intercept: 0.863	Peak 3:	0.000	0.0	0.000
Result quality Good				
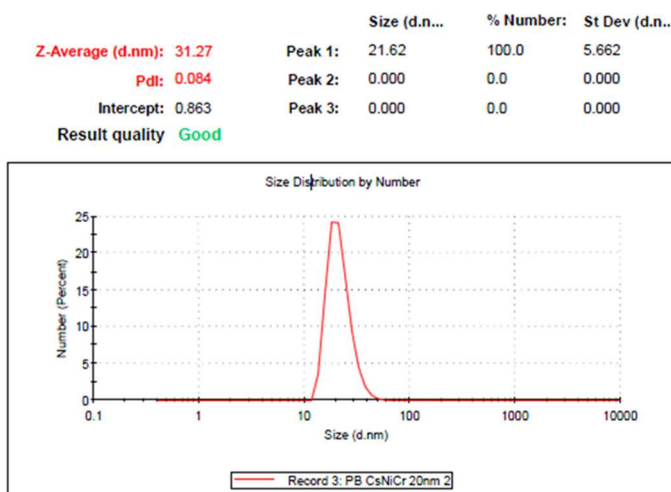
Figure 18. DLS measurements of large CsNiCr NPs.

They were deposited by drop casting onto a patterned sample that was prepared as in the previous experiments. Five dots with different sizes were lithographed: dot 1 (40 nm x 1 nm), dot 2 (40 nm x 0.5 nm), dot 3 (80 nm x 1.4 nm), dot 4 (90 nm x 1.2 nm) and dot 5 (105 nm x 1.2 nm).). As can be seen in Figure 19, again only the largest NPs got attached to the largest functionalized oxide dots (dots number 3, 4 and 5), while some small NPs, always present in the NP solution, were deposited preferentially onto

the smallest dots (number 1 and 2). In this last experiment the height of the dots were lower than in the previous one and the patterns were smoother, so the CsNiCr NPs got attached covering homogeneously the dots forming groups of NPs in the largest dots (3, 4 and 5), two small NPs in dot no. 2 and one small NP in dot no.1.

If only the surface charge were the reason of the preferentiality with the patterns size, the big CsNiCr NPs (20 nm) should have attached also to the smallest patterns (until balance the charge of the cationic pattern), as the small CsNiCr NPs (6 nm) did. By analysing again the former results with 25 nm KNiCr NPs and although the electrostatic interactions are the driving forces to anchor the NPs on the functionalized patterns (as has been proved in the previous sections), we could conclude that the NPs attachment depends on the sizes of NP and pattern. However, this is a complicated subject where several factors can influence, and more experiments would be needed to get final conclusions.
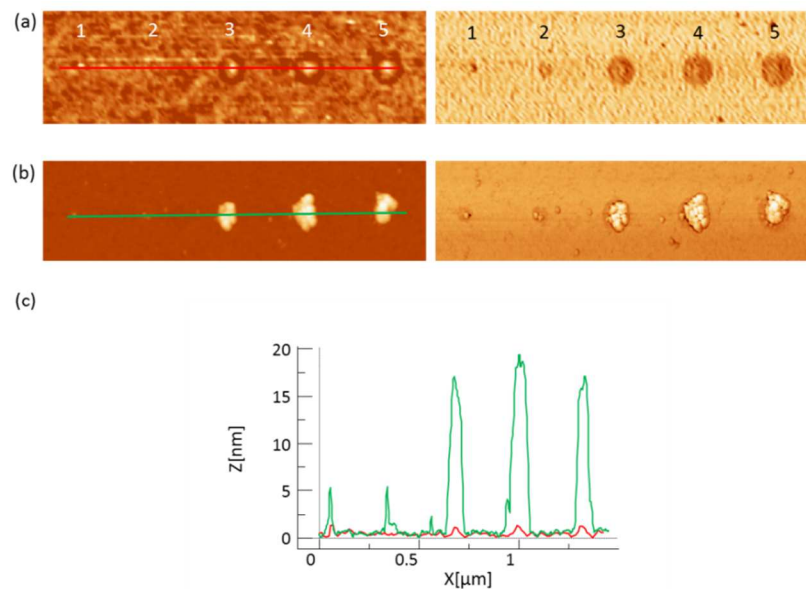

Figure 19. (a) Topography and phase images of the 5 dots oxidized by LON on a Si substrate functionalized with OTS. The 5 dots are labelled with the corresponding numbers. (b) Topography and phase images of the CsNiCr NPs attached onto the lithographed dots previously functionalized with protonated APTES. (c) Height profiles of images (a) and (b).

3.2.2.5 Chemical characterization of the PBA-NPs deposited on the marks

The chemical characterization of PBA-NPs deposited on marks patterned on a silicon wafer covered by an OTS monolayer is a challenge due to the small size of the patterns and the small amount of material to analyze. These limitations make impossible the use of ATR-IRRAS. Instead, the scanning AES technique, that is especially suited for investigation of small surface features, was used for the chemical analysis. This technique provides the possibility to simultaneously produce physical images and element distribution maps of the surface by combining Scanning Electron Microcopy imaging and AES analysis capabilities.

We have performed AES on top and outside the LON patterns (Figure 20). Compared with the experiments on full substrates (section 3.2.2.2), longer exposition times and a special care to avoid degradation of the sample were required in this case in order to get enough amount of signal. Inside the LON patterns, apart from the C (275 eV), O (473, 491, 512 eV) and Si (96 eV) peaks coming from the APTES SAM and the substrate, Ni (720, 778, 783, 849 eV), Cs (559, 574 eV), and N (386 eV) Auger peaks were detected. This result proves the presence of the PBA-NPs on the functionalized nanopatterned marks (Figure 21c-1). Outside the marks, the Auger peaks coming from OTS and the substrate were measured (C (276 eV), O (475, 492, 513 eV), and Si (95 eV). Traces of N (386 eV), but no Ni peaks were also detected (Figure 22c-2) further proving the preferentiality of our deposition protocol.[29]

The presence of N traces could come from some grade of contamination due to the contact with different nitrogen containing impurities in the solvents during sample preparation or to the presence of a small amount of APTES defects inserted in between the SAM of OTS.
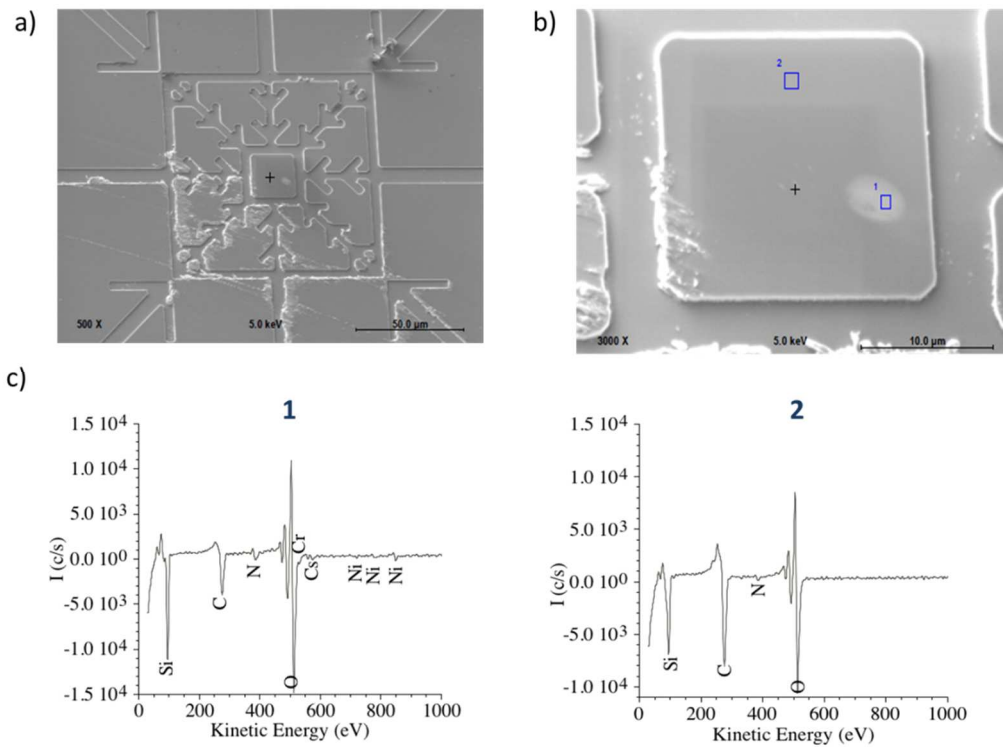
Figure 22. (a) and (b) SEM images of a Si marked substrate. (c)Auger electron spectra of : (1) PBA-NPs on top of a LON-SiO$_2$ mark modified with protonated APTES; (2) a region of the surface far from the nanolithographed mark.

In Table 1 are summarized the most important Auger peaks of the spectra showed in Figure 23 (NPs layer), Figure 22c-1 (NPs on LON mark), Figure 22c-2 (outside LON mark) and compared with the values found in literature (Reference [29]).

Element	Peak position			
	Reference 29	NPs layer	NPs on LON mark	Outside LON mark
Si	96	96	96	95
C	275	272	275	276
N	389	385	386	386
O	473/489/510	474/490/512	473/491/512	475/492/513
Cr	531	531	530	--
Cs	559/572	562/574	559/574	--
Ni	718/777/785/849	717/--/783/851	720/78/783/849	--

Table 1. Summary of Auger peaks positions.

3.2.2.6 Study on the evolution of LON nanolithographed SiO$_2$ patterns under sonication

During our studies we tracked the height profile of the marks in close detail to check the effect of the different steps during the deposition process, especially for prolonged times of sonication used for the APTES SAM preparation and sonication. For this propose we prepared LON marks and measured accurately their height profile; afterwards, we followed the procedure commonly used to grow the APTES SAM, but before the sonications steps in ethanol (cleaning steps) we measured the height profile again (Figure 24a and b). In a different experiment we prepared the LON patterns and measured the topography image, then we attached the APTES SAMs (including sonication in ethanol for cleaning proposes), and measured again. Finally we sonicated the sample in acid solution for 30 minutes and measured the final height (Figure 24c and d). All the height profiles correspond to AFM topography images performed for each step of the experiment (not shown).

The study of this effect in different solvents and conditions led us to conclude that although the effect is general, no easy correlation between height decrease and sonication time can be established. But it was clearly observed that a prolonged sonication in acidic solutions produced a decrease in the height of the mark. This fact moved us to progressively reduce sonication times in diluted HCl for the APTES protonation until a compromise was achieved. Sonicating the samples in diluted HCl for 7 minutes slightly affects the height of the marks while still assures an effective protonation of the APTES monolayer and therefore, high NPs deposition densities (see Section 3.2.2.1). A decrease in the height of the mark may wrongly indicate that during the sonication process at pH = 1 the APTES monolayer has been removed along with part of the SiO_2. In this scenario the protonation of the SiO_2 mark and the presence of trapped ionic species [30] would be the ones that induce the electrostatic attachment of the PBA-NPs onto the surface making unnecessary the APTES monolayer. Still, it has been previously shown (section 3.2.2.1, Figure 5 and section 3.2.2.3 Figure 12) that the presence of APTES is crucial for the attachment of the NPs. From our point of view, we can assume that even if some APTES molecules are removed from the surface during the sonication steps, they may be trapped again in the remaining SiO_2. Moreover, the non-stoichiometric and porous character of the fabricated oxide[30] can favor such a trapping.
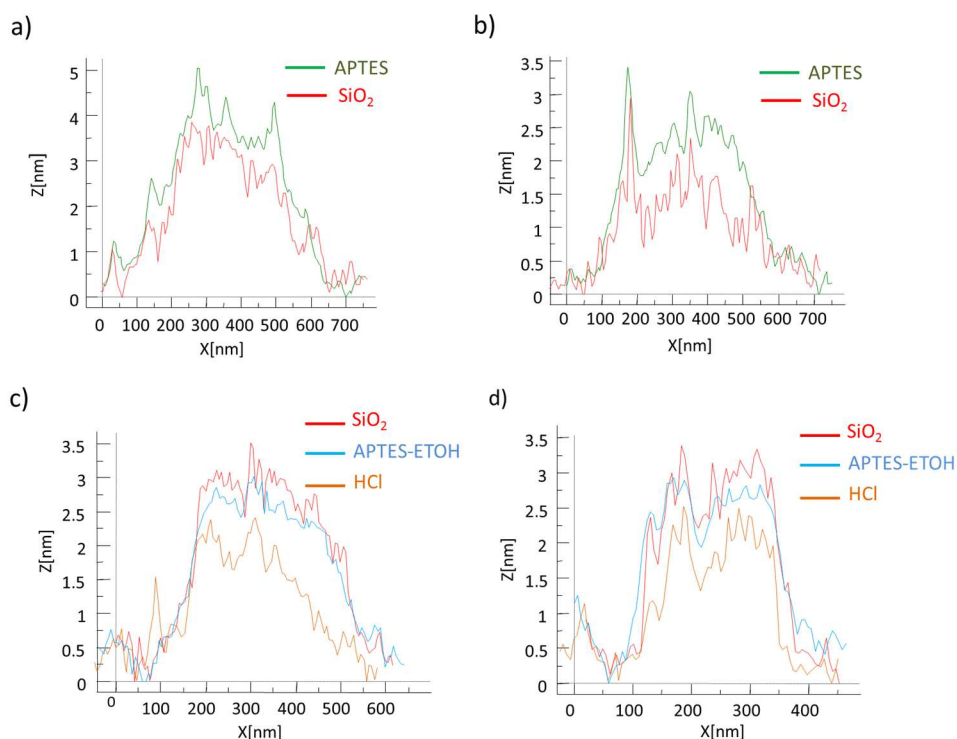
Figure 24. Height profiles of four LON-SiO$_2$ marks after different treatments: (a) and (b) red: freshly prepared mark; green: after immersion in ethanolic APTES solution, rinsed with ethanol and blow dried with N$_2$. (c) and (d) red: freshly prepared mark; blue: after immersion in ethanolic APTES solution, sonication in ethanol (twice 5 minutes) and blow dried with N$_2$; yellow: SiO$_2$ mark treated with APTES, sonication in ethanol and sonication 30 minute in diluted HCl.

3.2.3 PBA-NPs organized by DPN

As done in the so-called dip-pen nanolithography (DPN) technique, the organization of the PBA-NPs was carried out by coating an AFM probe (tip functionalization) with a solution containing the NPs, commonly referred as "ink solution". As introduced in chapter 1, in the non-direct method, the ink (molecules to form a SAM) is used as a carrier system for the later deposition of the NPs. In our case, we use the direct method where the deposition is made in one single step as the ink is formed by the PBA-NPs that is directly deposited onto the target surface (direct patterning). In most

cases, the transport of ink molecules from the tip to the substrate is mediated by a water meniscus which is formed through capillary condensation. Under typical DPN conditions, water is always present in the tip–substrate gap, and its impact on pattern formation is closely related to the solubility of ink materials in water. In our case, the NPs (our "ink") are transferred by scanning the functionalized AFM tip in contact with the surface. As the PBA-NPs are dispersed in water, the formation of the water meniscus at the nanoscale tip-sample junction would facilitate the deposition of the NPs from the tip to the surface.

While the functionalization of AFM tips may seem quite easy, it quickly becomes clear that a lot of chemical skills are needed to bind the right species to the right place with the desired amount.[31] In our case, the functionalization of the probe was done taking advantage of the knowledge acquired in the previous section (3.2.2) based on the bottom-up self-assembled method. It was successfully achieved by creating a SAM of protonated APTES on a Si tip to further form a layer of anionic PBA-NPs that got attached to it driven by electrostatic forces. The selected probes were MSNL tips from Bruker, where a Silicon (Si) tip is mounted on a Silicon Nitride (SiNi) cantilever (specifications detailed in section 3.3). These tips were selected for two reasons: First, to perform the functionalization only in the tip side of the probe (Si) and not on the cantilever side (SiNi), and second, to use soft cantilevers to be able to apply low forces (as it will be discussed below). Usually, the commercially available soft probes are all made by SiNi (lever and tip), but the tip functionalization depends on the tip composition and a Si surface is needed for the APTES assembling.

The functionalization by coating the tip with the KNiCr NPs, was made in four consecutive steps summarized in Figure 25a: In step (i), the tip was gently dipped 30 min in APTES solution, then (step (ii)) it was slowly removed from the APTES solution and directly immersed in absolute ethanol for 5 minutes. Then, in step (iii), the tip was carefully immersed into a diluted HCl solution (pH=1) for 7 minutes. The tip was removed from the acidic solution and left dried in ambient conditions. At this

point of the process, the tip was already functionalized with a protonated layer of APTES. Finally, in step (iv), the tip was immersed for 2 minutes in a KNiCr NPs solution and after removal from the NPs solution, it was left it dried under ambient conditions. The probe obtained was a Si tip functionalized with a layer of KNiCr NPs mounted on a SiNi cantilever not covered by any NP (Figure 25).

(a)

(b)
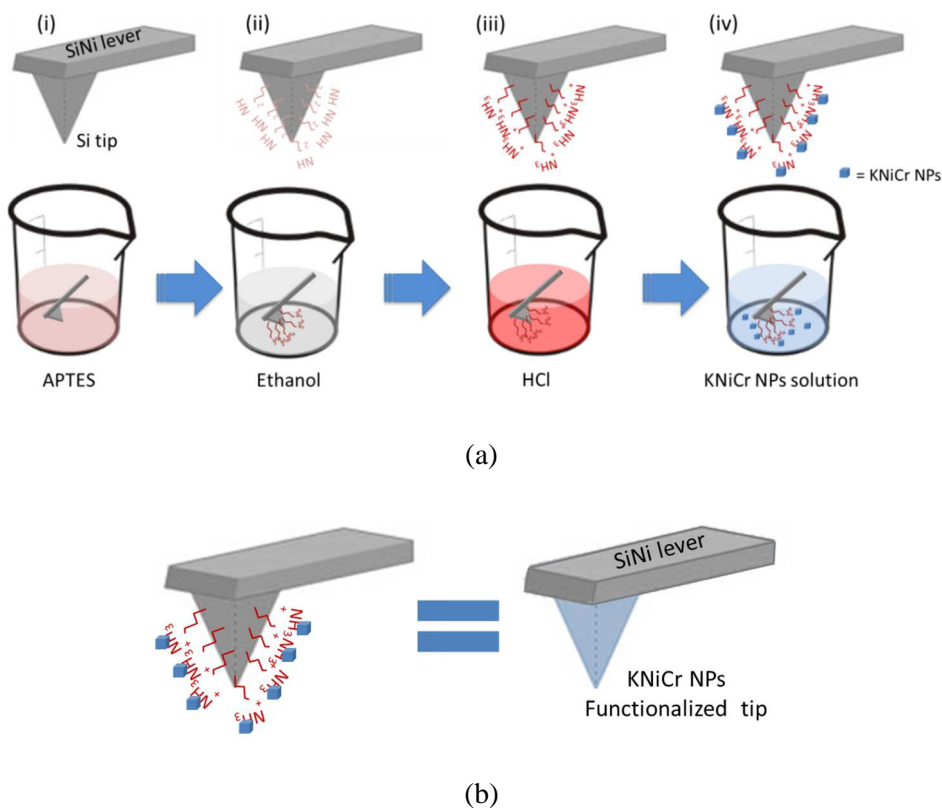
Figure 25. (a) Cartoon that represents the consecutive steps of the functionalization of the Si tip. (b) The resultant probe is a SiNi cantilever with a Si tip functionalized with a layer of KNiCr NPs.

The direct patterning was made by combining contact and dynamic modes of the AFM. The deposition of KNiCr NPs is summarized in Figure 26. The selection and characterization of the surface was made in dynamic mode while the combination of

both modes permitted the organization of the NPs in specific positions on the surface. A clean surface of previously functionalized Si substrate with protonated APTES was scanned in dynamic mode (step (i)) then, a smaller area was selected for the NP deposition and the system was brought to work in contact mode (step (ii)). The ink (KNiCr NPs) was delivered in direct contact with the surface while the tip scanned the area (previously selected) applying a certain force (step (iii)). Finally, the tip scanned over the surface in dynamic mode to characterize the deposition. All the experiment, deposition and characterization, was made with the same tip.
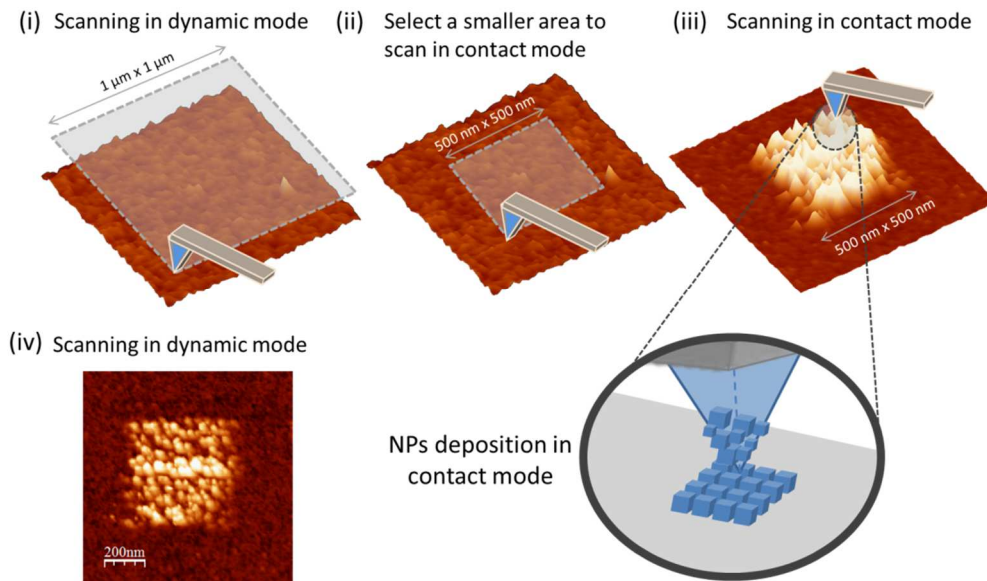
Figure 26. Different steps of the process of NPs deposition by DPN.

Some experimental parameters were studied in order to improve the deposition of the PBA-NPs by DPN. Considering the AFM cantilever like a spring that responds to a normal force F_N, according to the Hooke's law, $F_N = k \cdot \Delta z$, where k is the cantilever force constant and Δz the deflection of the cantilever (see Apendix). By measuring the cantilever deflection it is possible to measure the force on the cantilever, and therefore, it is possible to study the deposition of the NPs with respect to the force

applied while scanning in contact mode. Different cantilevers would exert different forces because the force is directly related to the cantilever force constant, so softer cantilevers (low values of k) would produce lower forces.

DPN with a soft tip (k = 0.1 N/m)

The first experiments were performed with a very soft tip (SiNi lever and Si tip), with resonance frequency f_0 = 38 KHz and k = 0.1 N/m, data provided by the manufacturer. The tip was functionalized with KNiCr NPs with a mean size of ~25 nm that were deposited on a Si substrate functionalized with protonated APTES to facilitate the anchoring to the surface.[32] Two different parameters were studied, the force applied during the contact scan and the speed of the scan. The experimental values of f_0 and k were found to be 36.58 KHz and 0.09826 N/m, respectively, the last one calculated by the method developed by Sader et al.[33] The tip displacement (Δz), measured by the AFM photodiode is given by the set point parameter in the AFM, which is an input value given in volts. The force applied is then directly related to the set point, so the higher the value of the set point, the more force is being applied to the tip.

The results are shown Figure 27 (a, b and c) where the topography images acquired in dynamic mode with the same functionalized tip are shown with the corresponding values of the deposition process: set point (SP) and scan speed (v). Below it is shown a height profile of each case. The scan was made from top to down in case (a) and from down to top in cases (b) and (c). In all cases, each scan line was performed twice (forward and backward).

Figure 27. a), (b) and (c): Topography images (top) of deposited KNiCr NPs with their values of deposition: set point (SP) and scan speed (v), and the corresponding height profiles (down). Images size: 2 µm x 650 nm.

From Figure 27a to Figure 27b both parameters, set point (force applied) and scan speed, were increased. It can be seen that the NPs deposited in Figure 27a and Figure 27b present more or less the same sizes and similar coverage. Nonetheless the heights of the NPs are not the expected for the KNiCr NPs (expected to be around 25 nm), then it could happen that the NPs would be broken or degraded. From Figure 27b to Figure 27c, the force applied in the deposition is the same but the scanning speed was increased from 2Hz to 3Hz. It can be seen that the coverage is much higher when the speed is increased (Figure 27c) although it looks like the KNiCr NPs did not withstand the high speeds and degraded or broke even more than the previous cases, showing lower values on the NPs height profiles.

DPN with a harder tip (k = 0.5 N/m)

This time, the experiments were performed with a harder tip (SiNi lever and Si tip), with resonance frequency f_0 = 125 KHz and k = 0.6 N/m, both data provided by the manufacturer. The tip was functionalized with the same KNiCr NPs and the substrate was again Si functionalized with protonated APTES. The experimental values of f_0 and k were found to be 113.86 KHz and 0.5664 N/m. The force applied to the tip in this experiment will be larger than the previous one because the cantilever force constant is 5 times larger (0.5 N/m) than the previous one (0.1 N/m).

The results are shown in Figure 28. Topography images acquired in dynamic mode are shown from Figure 28a to Figure 28d, with the corresponding deposition parameters and height profiles. From 20a to 20c, it is shown three lines of NPs deposited at the same speed (1Hz) but with increasing set points (applied forces). As can be seen in the height profiles, applying more force, only a slight increment in the heights profile were observed. These lines were done by scanning 500 nm x 40 nm several times from top to down, and vice versa, to get more coverage of deposited NPs. However, the low values of the height profiles suggest that scanning several times in the same line produce a high coverage but destroy the NPs. The next deposition was made by scanning very small areas (5 consecutive dots of 50 nm x 50 nm) from top to down, only one scan, at low speed (1Hz) and the higher value of the force applied (SP = 1.5 V). As can be seen in Figure 28d, five consecutive areas with few KNiCr NPs were successfully deposited showing the expected height values for the KNiCr NPs.
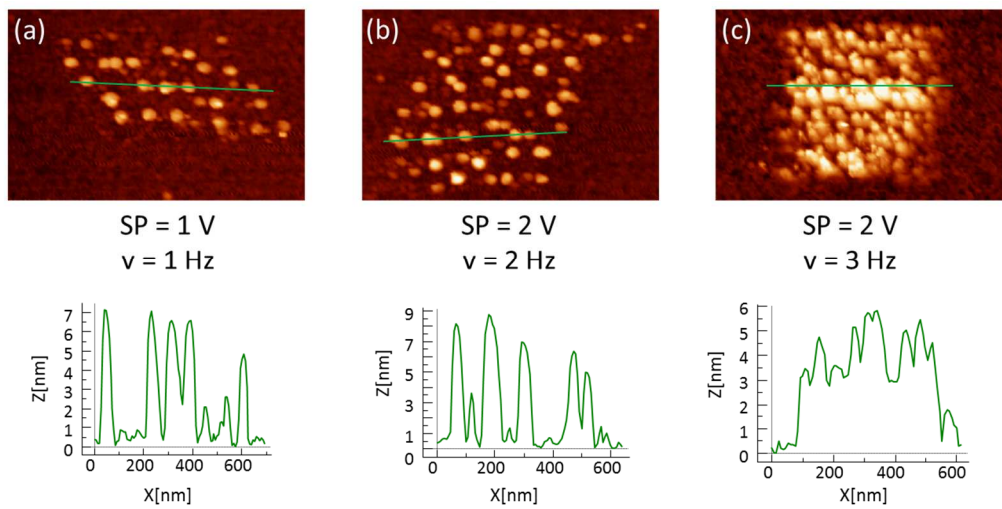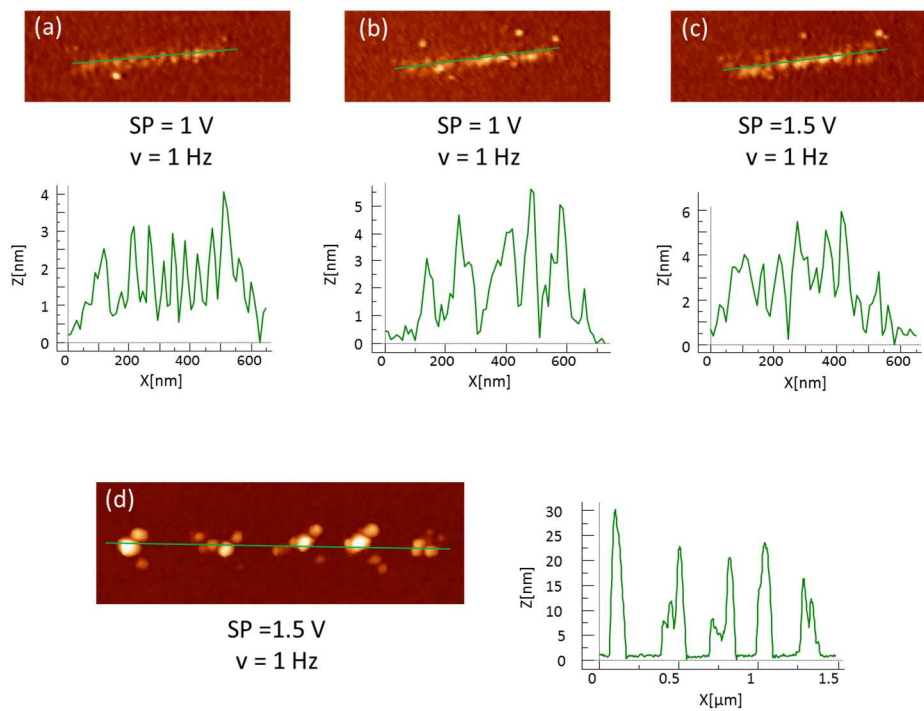
Figure 28. (a), (b) and (c): Topography images (top) of deposited KNiCr NPs forming lines with their values of deposition, set point (SP), scan speed (v) and the corresponding height profiles (down). Image size: 1 µm x 350 nm. (d) Topography image (top) of deposited KNiCr NPs in 5 dots of 50 nm x 50 nm, with the corresponding parameters of deposition and the corresponding height profile (down). Image size: 2 µm x 500 nm.

Finally, force-distance curves of the hardest tips (k ≈ 0.5 N/m) with and without functionalization were performed on a clean Si substrate (Figure 29). An AFM force-distance curve is a plot of tip-sample interaction forces vs. tip-sample distance. The difference between the approach and the withdrawal contact lines is called "loading-unloading hysteresis".[34] Once the tip has contacted the surface, it is pushed against the surface with some force in which case, the viscoelastic properties of the sample can be investigated. When the tip is pulled away from the surface, adhesion forces can be measured. If we compare the two force-distance curves (Figure 29a and b), different values of adhesion forces could be measured: the functionalized tip presents more

adhesion (102.7 nN) than the non-functionalized tip (20.4 nN). This would indicate the presence of the KNiCr NPs on the functionalized tip that causes the increment in the adhesion between the tip and the substrate.

(a)   (b)
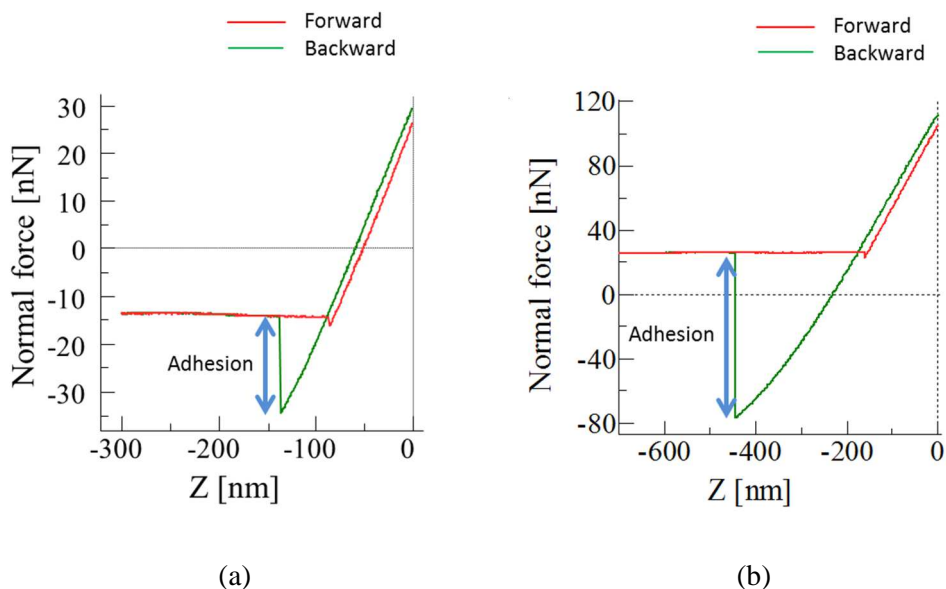
Figure 29. (a) Force-distance curve for a non-functionalized Si tip with k ≈ 0.5 N/m on a Si substrate. (b) Force-distance curve for a functionalized Si tip with KNiCr NPs on a Si substrate.

Our results suggest that by employing the known functionalization procedures for flat substrates, we are now able to attach KNiCr NPs to the tip surface, thus providing numerous possibilities for the further attachment of a wide variety of different anionic NPs. This NP-functionalized tips can be used later for the organization of the NPs on specific regions surfaces for their characterization or their integration on sensors and devices.[35]

3.2.4 PBA-NPs organized by soft lithography

The two methods described in sections 3.2.2 (LON) and 3.2.3 (DPN) for the organization of the PBA-NPs on surfaces were demonstrated to be very accurate and efficient although they are serial methods that only permits the controlled deposition

of the NPs in very small areas of the sample. It is certainly very useful because it allows the study of the NPs at the individual (or small number) level and also would permit their integration in devices, where the NPs have to be deposited in specific areas. But for many other applications, large-area patternings are required to form structures with features that range from nanometers to micrometers in size to incorporate them as active parts of micro or nanoelectronic circuits, for example.

To be able to scale up the process of the PBA-NPs organization all over the surface (up to areas of cm^2), three different routes based on soft lithography stamp-assisted methods have been used. The first method was based on the direct microcontact printing (µCP) approach. The second one was a modification of the well-known Lithographically Controlled Wetting (LCW) and the third one was an indirect method also based on stamps. A real AFM topography image of a polydimethylsiloxane (PDMS) stamp and its schematic representation, as well as the crystal structure of PBA-NPs and its schematic representation, are shown in Figure 30.

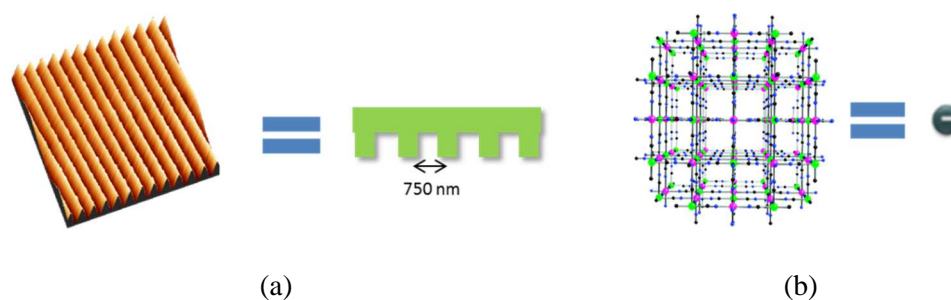(a)   (b)

Figure 30. Schematic representations of PDMS stamp and PBA-NPs. (a) AFM topography image of a PDMS stamp and its schematic representation. (b) Structure of PBA- NPs and its schematic representation.

For all the methodologies, PDMS stamps were used (stamp preparation described in section 3.3). This type of stamps presents regularly spaced parallel lines separated

around 750 nm (Figure 30a), so the features transferred will be in all cases parallel lines of PBA-NPs.

3.2.4.1 Method 1

Method 1 is based on the use of soft stamps that are inked in a NPs solution and then, the NPs are transferred from the stamp to a substrate by pressing the stamp against the substrate. This standard method was successfully used for example, by R.V. Martínez and coworkers for the organization of ferritine molecules on a functionalized Si substrate.[36] The deposition process (by method 1) of the PBA-NPs is summarized in Figure 31. The stamps were slightly pressed against a sheet paper impregnated with CsNiCr NPs solution for several seconds (step (i)) and then, the inked stamp was pressed against a silicon surface functionalized with protonated APTES. Both stamp and substrate were mounted on the nanopress system described in chapter 2 (section 2.2.1) to be able to exert a known pressure (step (ii)). A pressure of 0.16 N was applied during 1 minute (step (iii)) and then the stamp was removed from the Si surface. The patternings obtained were parallel lines of PBA-NPs (step (iv)).
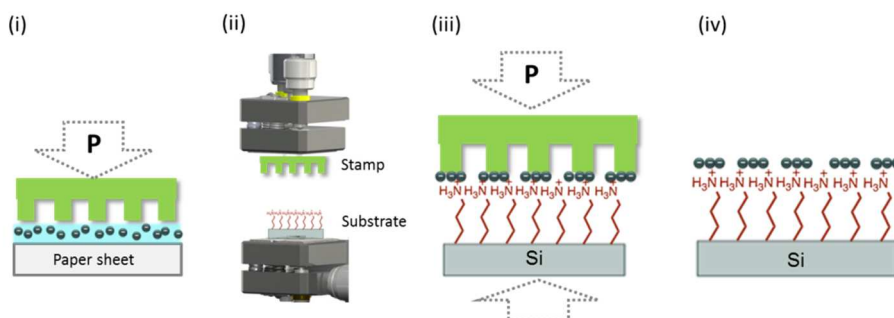

Figure 31. Different steps of the process of NPs deposition by stamp assisted method number 1.

The results of the patterning of CsNiCr NPs are shown in Figure 32. Well defined parallel lines of CsNiCr NPs were obtained although it was also found some empty areas and areas with aggregates of NPs.

(a)   (b)
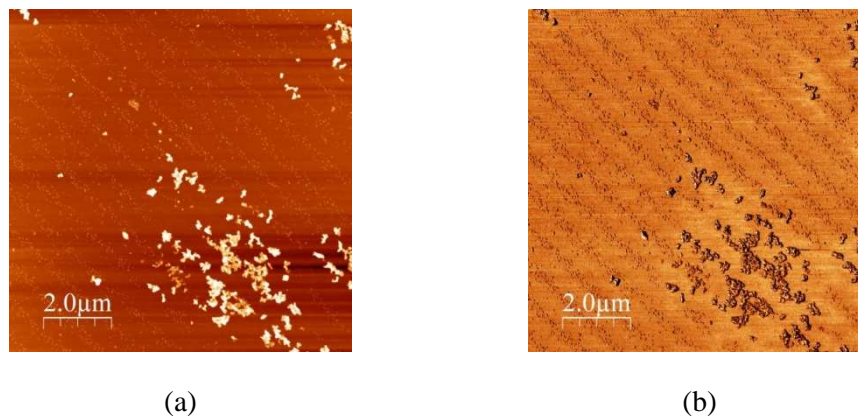
Figure 32. (a) Topography image of the CsNiCr NPs transferred to a functionalized Si substrate by the method number 1. (b) Phase image corresponding to (a). Images size: 10 µm x 10 µm.

This methodology was found to be little reproducible and the lines were not fully covered with the NPs.

3.2.4.2 Method 2

The second method is an adaptation of LCW reported by Cavallini et al.[37] LCW is based on a stamp-assisted deposition of a soluble material from a solution. As the stamp is placed in contact with a liquid thin film spread on a surface, the capillary forces drive the liquid to distribute only under the protrusions of the stamp producing an array of menisci. The stamp is then removed and, as the solvent evaporates, the deposited solute forms a pattern on the surface with the same length scale of the stamp. The concentration of the solution, the affinity between stamp/solution/substrate, the pressure between stamp and surface, are different parameters that can be modified to originate different patterns of the same compound without modifying the stamp features.

The method 2 is summarized in Figure 33: The KNiCr NPs aqueous solution (1mM in Ni) were spread directly on a Si substrate previously functionalized with protonated

APTES (step (i)), letting it dry with a PDMS stamp strongly placed on top. To assure the contact the substrate/drop/stamp system was pressed between two magnets (step (ii)). After the time needed for water to evaporate, the stamp was removed and non-uniform NPs stripes were formed over the surface (step (iii)).
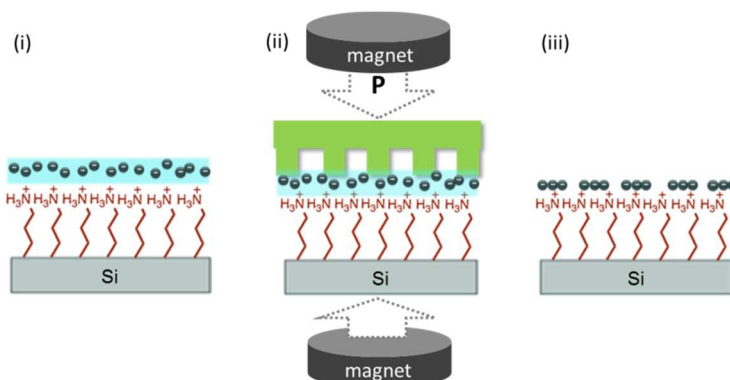
Figure 33. Different steps of the process of NPs deposition by stamp assisted method number 2.

The results for the organization of KNiCr NPs in lines by method 2 are shown in the next figure (Figure 34). The AFM topography images show that the height profiles never exceed sizes of 30 nm, which means that the NPs were not piled up. This could be justified by the high pressure between the stamp and surface and due also to the dilution of the solution.
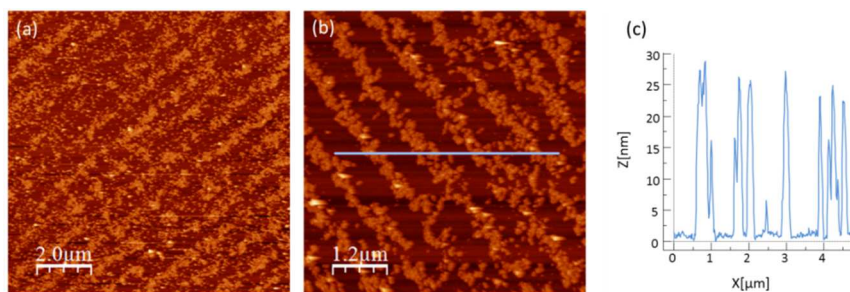
Figure 34. (a) and (b) topography images of the KNiCr NPs organized by the method number 2. Image sizes: 10 µm x 10 µm and 6 µm x 6 µm respectively (c) Corresponding height profile of the topography image shown in (b).

Due to the close contact between the stamp and the substrate forced by the pressure produced by the magnets, one can image a different picture for the solution behavior, closer to the micro-injection molding in capillaries (MIMIC) method (a well-known unconventional lithographic method), than to the LCW method. In MIMIC the grooves between the protrusions in contact with the surface form microcavities, which once in contact with the substrate delimit the sub-micrometric channels (μ-channels). When the solution is deposited at the open end of the stamp, the liquid spontaneously fills the μ-channels under the effect of capillary forces. After the complete evaporation of the solvent the stamp is gently removed. The self-organization of the solute enters into play at the later stages of shrinking, when the solution reaches supersaturation. Following our strategy, the solution could fill the cavities instead of forming a meniscus under the stamp protrusions. The final result is parallel lines although they are irregular and not completely filled with NPs.

3.2.4.3 Method 3

To improve the organization of the NPs we finally followed an indirect method based on the formation of aluminum oxide stripes all over the surface and the direct attachment of the PBA NPs on top of the aluminum lines taking advantage of the high preferentiality of these NPs that electrostatically interact with the aluminum oxide better with the native silicon oxide.

In order to prepare the aluminum oxide (Al_2O_3) lines, wet lithography was also used. The same approach followed for the direct organization of NPs (method 2) was used to form polymethyl metacrylate (PMMA) lines all over the surface. Afterwards, a thin layer of Al was evaporated and once exposed to air the oxide was formed. After a lift off process in acetone, well defined aluminium oxide stripes covered the surface, and the direct contact between the patterned surface with a diluted aqueous solution of the NPs gave rise to well organized NPs bands all over the substrate.

The method 3 is described in detail in Figure 35. PMDS stamps were prepared as in previous methods. Then, a diluted solution of PMMA (from Aldrich, Mw 350000) in acetone (1.25% in weigth) was spread over a clean silicon substrate and the polymeric stamp was placed on top. In step (i) it is shown the silicon/PMMA solution/stamp sandwich that was pressed between to magnets during the drying time (few minutes). Next, the magnets were removed and the stamp was carefully taken off from the substrate. Parallel lines of PMMA were then formed on the silicon surface (step (ii)). A thin layer of aluminium (1-2 nm) was evaporated right after (step (iii)) and a lift-off process was achieved by sonicating the samples in acetone solution for 5-10 minutes. At this step, parallel aluminium lines were formed on the silicon (step (iv)). Then, a drop of KNiCr NPs aqueous solution (1mM in Ni) was placed on the patterned surface for 1 minute (step (v)) and finally, it was rinsed with water and dried under a N_2 stream (step (vi)). Perfect lines of PBA-NPs were obtained on top of the aluminium stripes.
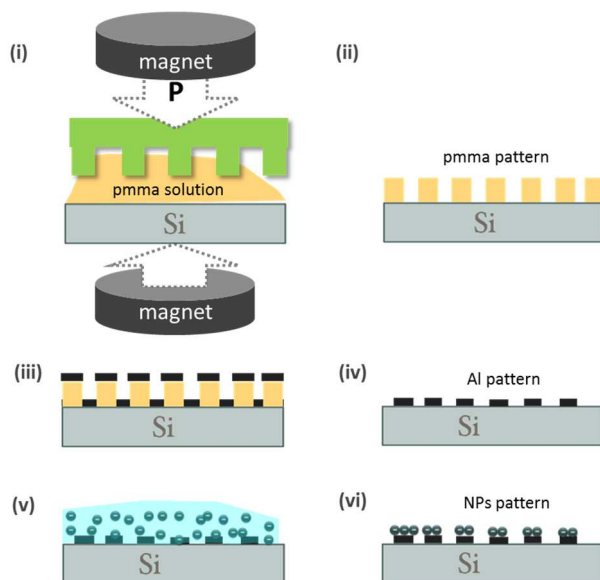
Figure 35. Different steps of the process of NPs deposition by stamp assisted method number 3.

The results for the organization of KNiCr NPs in lines by the method number 3 are shown in Figure 36.
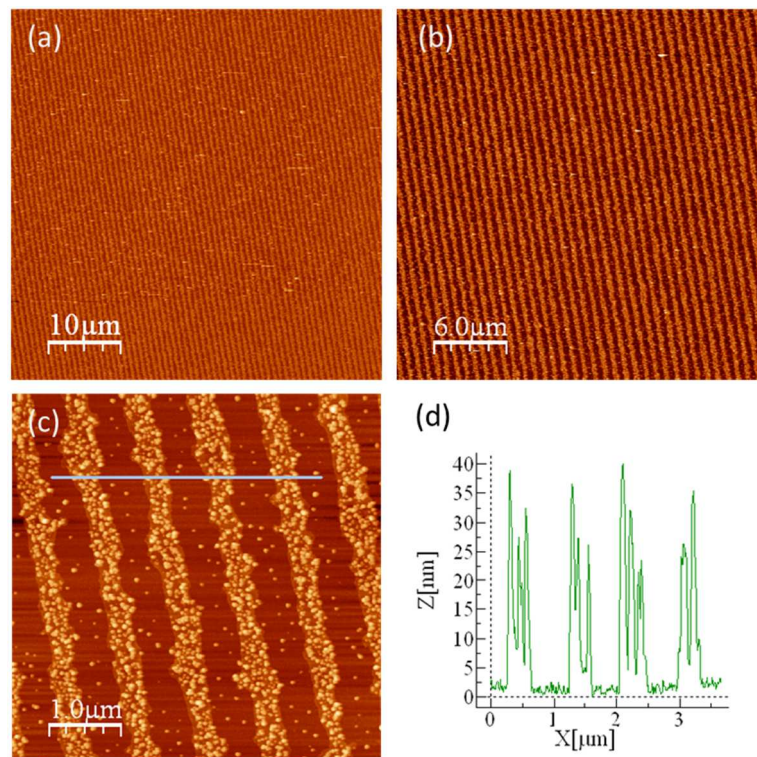
Figure 36. (a-c) AFM topographic images of KNiCr NPs lines on modified silicon surface by indirect method. (b) and (c) large areas of 50 µm x 50 µm and 30 µm x 30 µm respectively; (d) 5µm x 5 µm scan area with its corresponding profile (e).

Regularly spaced parallel lines with a high coverage of nanoparticles were found. Checking the height profile, it can be deduced that the KNiCr NPs were not piled up, forming a homogeneous layer all over the lines.

This method was successfully used also to organize the CsNiCr NPs of the two sizes, the smallest ones (6 nm) shown in Figure 37a and b, as well as the biggest ones (20 nm), shown in images Figure 37c and d.
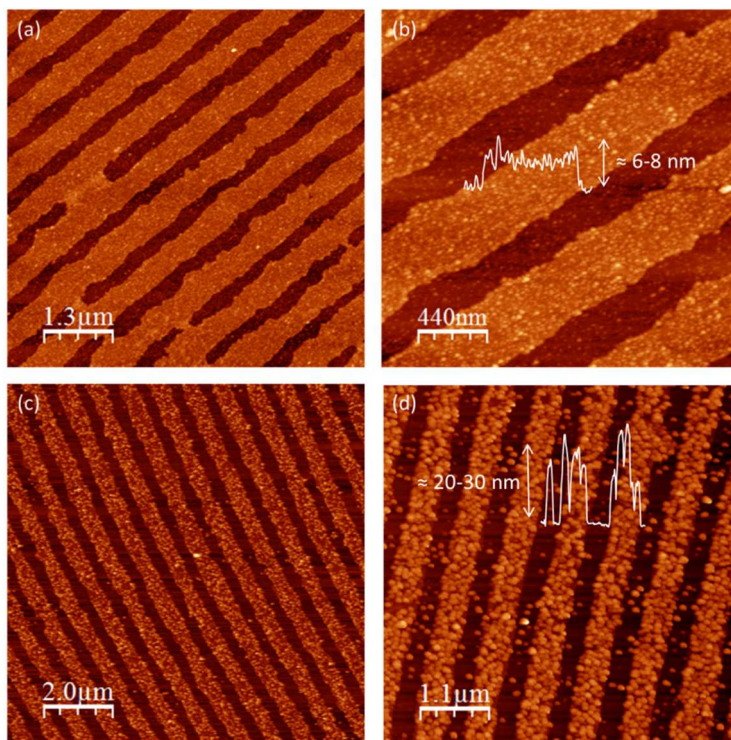
Figure 37. (a) and (b) topography image of CsNiCr NPs (6 nm) organized in lines by method 3. Image sizes: 6.7 µm x 6.7 µm and 2.2 µm x 2.2 µm respectively. Inset in (b): height profile (c) and (d) Topography image of CsNiCr NPs (20 nm) organized in lines by method 3. Image sizes: 10 µm x 10 µm and 5.5 µm x 5.5 µm respectively . Inset in (d): height profile.

The results evidence that between native silicon oxide and native aluminium oxide the KNiCr NPs, show a high preferentiality for the second one. This can be demonstrated by simply putting in contact both kinds of surfaces with a solution of the anionic KNiCr NPs, the Al_2O_3 surface get completely covered with NPs while on the SiO_2 surface only few NPs are found. These tests are shown in Figure 34 with an aluminium surface and in previous Figure 38, section 3.2.2.1 with silicon substrates.
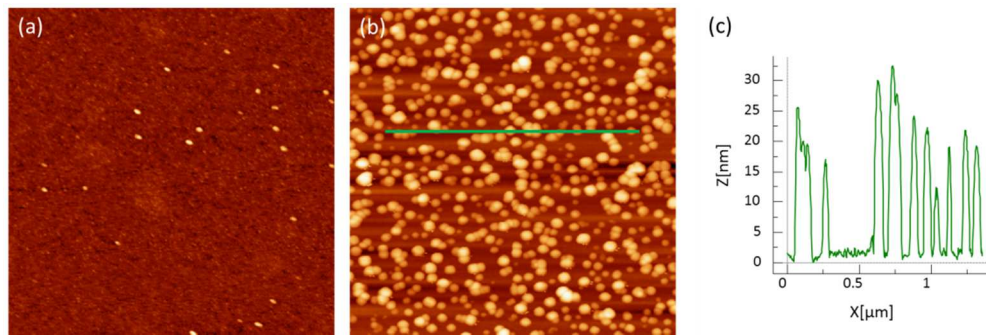
Figure 39. Preferentiality of PBA- NPs on the Al_2O_3 surface. (a) Si substrate with 2nm of Al evaporated. The Al_2O_3 is formed naturally by exposure to ambient conditions (native oxide layer). (b) KNiCr NPs deposited onto the Al_2O_3 surface by drop casting

Even though the nature of the stabilizing forces between NPs and oxide surface should be electrostatic, we have not any explanation for the preferentiality between both oxides; however, as has been demonstrated, one can take advantage of this difference and use it to organize the NPs in perfect stripes all over the surface.

3.3 MATERIALS AND METHODS

Synthesis of PBA-NPs

A solution of $Cs_{0.7}$ $Ni[Cr(CN)_6]_{0.9}$ nanoparticles was prepared on base of the synthetic procedure previously described by L.Catala et al.[15c] 50 mL 2.10^{-3} M aqueous solution of $K_3Cr(CN)_6$ was quickly added to 50 mL of 2.10^{-3} M $NiCl_2.6H_2O$ and 4.10^{-3} M CsCl aqueous solution. The suspension was stirred for at least 1 hour at room temperature before using it. KNiCr nanoparticles suspension was prepared following exactly the same procedure except for the CsCl salt, that was not included in the reaction mixture.

Substrates

The substrates used for the NPs deposition on LON-SiO_2 marks were silicon wafers (p-type) with a marker code made by means of optical lithography, in this way it was possible to localize exactly the same position on the sample (Figure 40).
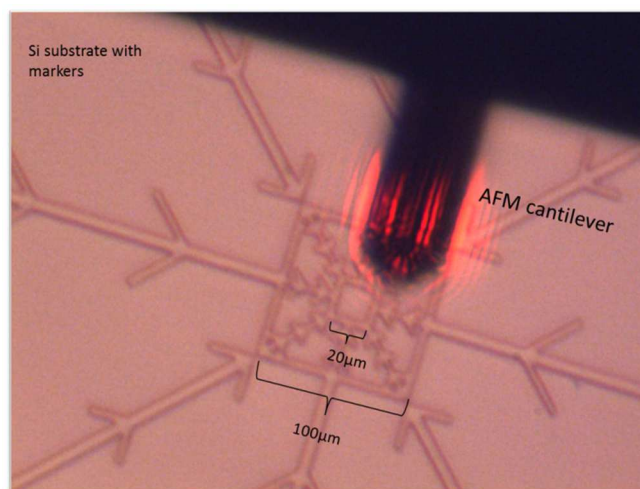
Figure 40. Top view optical image of the SiO_2 marked sustrate.

These substrates were prepared by optical lithography in the Instituto de Microelectrónica de Barcelona. For experiments where localization of specific positions was not required, common silicon wafers (p-type<100>from DXL enterprises, INC) were used.

Substrates cleaning process

Silicon wafers with or without photolithographed marked code were cleaned always just before any experiment was performed. Samples were sonicated 10 minutes in freshly prepared H_2O_2:NH_4OH:H_2O (1:1:2) solution three times. Then they were rinsed with mili-Q water, sonicated 5 minutes in mili-Q water twice and dried under a N_2 stream. Substrates with the photolithographed code were briefly sonicated in organic solvents before the cleaning process with the oxidant mixture to assure the elimination of any photoresistor residue.

Ultrasonic cleaner

A BRANASONIC MTH-5510 ultrasonic cleaner (power 185 W) was used. During different experiments we monitored the temperature of the sonication bath, but no significant change in temperature was observed for sonication times below 15 minutes (approx. +15 min. +1ºC).

Self-assemble monolayer (SAMs) preparation

OTS (90+%), APTES (99%) molecules and solvents were purchased from Aldrich and used without previous purification. Once OTS and APTES bottles were opened, they were kept always under N_2 atmosphere to avoid any degradation. OTS monolayers were prepared inside a glove box. Clean silicon substrates were dipped in 2.8 mM OTS in toluene (puriss, over molecular sieve) and kept in solution for three days, then

they were rinsed with toluene and sonicated in toluene, chloroform and 2-propanol to remove any physisorbed material/molecules and dried under N_2 stream. The quality of the SAMs was evaluated by Advancing-Receding Contact Angle measurements in a Ramé-hart automatized goniometer and by AFM imaging. APTES SAMs were prepared by dipping the substrates in 1 mM APTES in ethanol (absolute, reagent grade) for 45 minutes, then rinsed with ethanol and sonicated twice in this solvent for 5 minutes. Finally, substrates were dried under N_2 stream.

Atomic force microscopes (AFM) and local oxidation nanolithography (LON) equipment

For all the experiments, two different microscopes were utilized, a Nanoscope IIIa AFM (Veeco) with a home-made voltage amplifier for the development of LON and a Nanotec Cervantes Full Mode AFM (Nanotec Electrónica S.L.). Sharp silicon probes without coating (dynamic mode, k ~42 N/m, f_0 ~320kHz) were purchased from two different suppliers: TESP probes (Veeco) and PPP-NCH (Nanosensors). Lab humidity was increased by means of a humidifier for household use. All AFM images were processed with WSxM software from Nanotec Electrónica S.L.[38]

Superconducting quantum interference device (SQUID) measurements

Magnetic data were collected with a Quantum Design MPMS XL-5 susceptometer equipped with a SQUID sensor. In order to avoid the diamagnetic contribution of silicon surface, three pieces of Si were introduced in the SQUID measurement cannula. Bottom part: 4 cm x 0.8 cm piece of clean Si, middle: 0.8 cm x 0.8 cm piece of functionalized silicon with a monolayer of PBA-NPs and top: 4 cm x 0.8 cm piece of clean Si. DC Field-cooled and Zero-field-cooled magnetization measurements were performed under 100 Oe applied magnetic field.

Dynamic light scattering (DLS) measurements

Size distribution of the NPs samples was determined by DLS of 1 mM in Ni PBA-NPs solution with a Marlvern Zetasizer instrument.

PBA-NPs deposition

Nanolithographed patterns were drawn on silicon substrates covered with a good quality OTS monolayer (which removed OTS molecules on the patterned area). The substrates were immersed in 1 mM APTES ethanol solution and all the steps for the growing of an APTES self-assembled monolayer were followed. Next, they were sonicated between 7 and 30 minutes in diluted HCl solution (pH approx. 1). Then the substrates were dried under a N_2 stream and covered with a drop of PBA-NPs solution (1 mM in Ni) (approx. 50 µL) for 1 minute. Afterwards, the nanoparticles solution was removed by rinsing the substrate with mili-Q water and dried with N_2. When a more precise cleaning procedure was needed, the substrates were sonicated in mili-Q water (between 1 and 5 minutes) and dried once more under N_2.

Scanning transmision electron microscopy (STEM)

The shape of the NPs was evaluated by scanning transmission electron microscopy with a multi-user 200 kV instrument Tecnai G2 F20 S-TWIN (FEI Company) with a point resolution of 0.24 nm. The sample was prepared by drop casting of PBA-NPs solution (1 mM in Ni) onto a grid.

Attenuated total reflection infrared spectroscopy (ATR-IRRAS) measurements

A VeeMax II sampling stage (Pike Technologies) equipped with a 60º germanium (Ge) ATR crystal and a high-pressure clamp was placed in the sample compartment of

a NICOLET 5700 Transformation-Infrared Spectrometer. A high-pressure swivel clamp (diameter 7.8 mm) was used to apply even and constant pressure to the sample during FTIR data acquisition. The angle of incident infrared was set ~60º with respect to the surface normal of Ge crystal. Silicon substrates with APTES and a PBA-NPs monolayer film were placed (face down) between the Ge crystal and the tip of the high-pressure clamp. Each FTIR spectrum represents the average of 120 scans at 4 cm^{-1} resolution. A p-polarized infrared beam (by means of a manual polarizer ZnSe) was used and the output signal was collected with a refrigerated MCT/A detector.

Auger analysis (AES) measurements

The Auger analysis was carried out using a Physical Electronic PHI 680 Auger Nanoprobe with a Schottky emission cathode and multi-channel plate detector. The beam voltage acceleration was 10 kV, the beam current 10 nA and the incident angle 30 degrees. For short beam exposition times, these conditions allowed the analysis of single oxide motives without substantial degradation of the organometallic.

Preparation of stamps

PMDS stamps were prepared by replica molding of a CVD used as master. Thus, the protruding equidistant 750 nm width lines in the CVD become parallel grooves in the replica.

The PDMS stamps fabrication was done employing the kit named: "Kit Silicon Elastomer Sylgard 184" (Down Corning GMBH). Sylgard 184 is a bicomponent system for the fabrication of silicone stamps that is formed by a base and a curling agent. The fabrication of the PDMS stamps was made in several steps:

1. In a disposable glass, 2.5 g of curling agent was added to 25 g of base.

2. The resulting elastomer compound was vigorously stirred to assure a good mixture. At this step, multiple air bubbles were formed into it.

3. The created air bubbles were removed by degasification sonicating 20 minutes on an ultrasonic cleaner. This process allowed obtaining a complete degased and transparent elastomer mixture.

4. A commercial DVD was opened and was generously cleaned with ethanol and acetone. Then, the prepared mixture was carefully poured onto the DVD, to avoid the formation of new air bubbles.

5. Then it was introduced on an oven at 90°C during 45 minutes to harden the elastomer mixture. Then the PDMS is created.

6. PDMS stamps were prepared by cutting small pieces, depending on the experimental requirements. The resulting stamps have acquired the same sub-micrometric patterns of the DVD.

Tips used for dip-pen nanolithography (DPN)

MSNL probes are multi-tip chips with six types of cantilevers with different geometries and spring constants (see Figure 41).
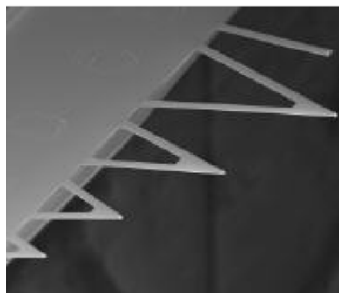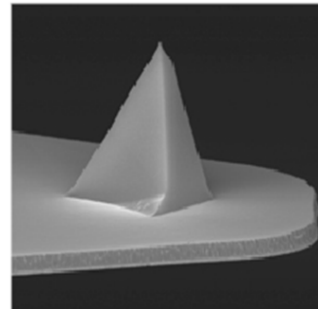
(a)   (b)

Figure 41. (a) Silicon Nitride cantilevers mounted on a chip. (b) Triangular Silicon tip mounted on a Silicon Nitride cantilever.

The MSNL cantilever multi-tip has the "A" cantilevers on one side of the probe, and "B," "C," "D," "E," and "F" cantilevers on the other side of the probe. Each cantilever has different specifications, summarized in the next figure:

Shape	Resonant Freq. kHz			Spring Const. N/m			Length μm			Width μm		
	Nom.	Min.	Max.	Nom.	Min.	Max.	Nom.	Min.	Max.	Nom.	Min.	Max.
A Triangular	22	15	30	0.07	0.025	0.14	175	180	170	22	17	27
B Rectangular	15	10	20	0.02	0.005	0.04	210	205	215	20	15	25
C Triangular	7	4	10	0.01	0.005	0.02	310	305	315	20	15	25
D Triangular	15	10	20	0.03	0.01	0.06	225	220	230	20	15	25
E Triangular	38	26	50	0.1	0.05	0.2	140	135	145	18	13	23
F Triangular	125	90	160	0.6	0.3	1.4	85	80	90	18	13	23

Figure 42. Table with cantilevers specidications.

3.4. CONCLUSIONS

In this chapter, three different lithography methods have been successfully used for the organization of PBA nanoparticles on functionalized surfaces.

The first lithography method, the local oxidation nanolithography (**LON**), allowed the selective deposition and accurate organization of PBA nanoparticles into very specific positions of a native silicon surface with submicrometric precision. In fact, one single PBA-NP has been anchored onto a LON nanometric mark of SiO_2 for the first time. This method combines a top-down approach (LON) with a bottom-up approach based on the functionalization of a silicon surface with SAMs of neutral OTS and cationic APTES selectively deposited onto the LON-SiO_2 marks. A deep study of the preferential deposition of PBA-NPs onto different functionalized substrates has been presented. Compared with the reported general methods for positioning NPs by LON, the method developed in this thesis has introduced the following improvements:

i) An increase of the electrostatic interaction through sonication in acidic solution of the sample, leading to an enhancement in the protonation of the SAM of APTES, has been achieved. This step has shown to be crucial to selectively attach the PBA-NPs onto the oxide patterns; moreover, one single nanoparticle on a ~30 nm LON-SiO_2 mark has been achieved.

ii) The influence of the combination of applied oxide voltage, oxidation time and sonication has been highlighted. The first two parameters are useful in order to control the size of the SiO_2 mark,[39] while we have observed that the sonication time is important for the final size of the SiO_2 pattern functionalized with APTES. In this context, we have shown that, even after strong sonication the APTES molecules, originally assembled onto the SiO_2 mark, prevail in the oxide motifs maintaining their recognition properties. It has been also shown the decrease of the oxide patterned during each step of the LON experiment.

iii) Thanks to the possibility of tuning nanoparticles diameter we have demonstrated a relevant interdependence between nanoparticles size vs oxide pattern size. A detailed study with three different PBA-NPs has been presented.

iv) The electrostatic nature of the method grants the electronic decoupling from the surface of the PBA-NPs, assuring the prevalence of the physical and chemical properties of the particles as demonstrated by magnetometry, ATR-IRRAS (on bulk) and AES (on a single mark).

The second lithography method used, the dip-pen nanolithography (**DPN**), allowed for a rapid and easy organization of PBA-NPs with a very high accuracy. By applying the expertise acquired by the study of the PBA-NPs preferentiality on different functionalized surfaces, the deposition experiment could be carried out without the need of specific DPN instrumentation. It was performed by the direct deposition of the PBA-NPs onto the surfaces by scanning in AFM contact mode with NP-functionalized commercial tips. The posterior characterization of the deposited NPs can be done *in situ* with the same functionalized tip, probing that the method is efficient and simple. A detailed description of the tip functionalization has been presented as well as a study of the experimental parameters that influence the correct deposition of the KNiCr NPs.

Finally, three possible approaches of **soft lithography** have been presented for the organization of PBA-NPs on large surface areas. All of them have been described in detail although only the last one has been proved to be a reliable and reproducible method. Although this indirect method involves various steps, the three types of PBA-NPs used in this thesis were successfully organized forming nanometric parallel lines over surface areas of cm^2 with homogeneous topographies confirmed and analyzed by AFM. In particular, the possibility of the formation of arrays of these magnetic NPs will be decisive for their magnetic characterization by means of low temperature magnetic force microscopy that will be presented in detail in chapter 6.

Unprecedented results for the accurate organization of PBA-NPs have been presented, from the precise positioning of one single particle by means of LON, to the possibility of upscaling their organization over large surface areas by the smart use of soft lithography. The direct and fast methodology developed by DPN permits the positioning of the nanoparticles in specific positions of the surface without the need of additional instrumentation. All of them represent practical routes that could allow the integration on PBA-NPs in devices.

3.5 BIBLIOGRAPHY

[1] a) Gubin S. P.; Koksharov Y. A.; Khomutov G. B.; Yurkov G. Yu. *Russian Chemical Reviews* **2005**, *74*, 489 - 520 ; b) Hao R.; Xing R.; Xu Z.; Hou Y.; Gao S.; Sun S. *Adv. Mater.* **2010**, *22*, 2729–2742.

[2] a) Puntes, V. F.; Gorostiza, P.; Aruguete, D. M.; Bastus, N. G.; Alivisatos, A. P. *Nature Materials* **2004**, *3(4)*, 263– 268; b) Varón M.; Beleggia M.; Kasama T.; Harrison R. J.; Dunin-Borkowski R. E.; Puntes V. F.; Frandsen C *Scientific Reports* **2004**, *3:1234,* DOI: 10.1038/srep01234c

[3] Ross C. A. *Annu. Rev. Mater. Res.* **2001**, *31*, 203–235

[4] Imre A.; Csaba G.; Ji L.; Orlov A.; Bernstein G. H.; Porod W.; *Science* **2006**, 311 205-208

[5] *Nanostructured Materials for Magnetoelectronics.* Aktas B.; Mikailzade F. **2013**, Springer Series in Materials Science, *175*, ISBN 978-3-642-34958-4

[6] *Magnetic Nanoparticles*. Gubin S. P. **2009**, Wiley-VCN, ISBN: 978-3-527-62757-8

[7] a) Singamaneni S.; Bliznyuk V.N.; Binekc C.; Tsymbal E.Y. *J. Mater. Chem.* **2011**, *21*, 16819-16845. b) Weddemann A.; Ennen I.; Regtmeier A.; Albon C.; Wolff A.; Eckstädt K.; Mill N., Peter M. K.-H.; Mattay J.;, Plattner C.; Sewald N.; Hütten A.; *Beilstein J. Nanotechnol.* **2010**, 1, 75–93.

[8] Bellido E.; Domingo N.; Ojea-Jiménez I.; Ruiz-Molina D. *Small* **2012**, *8*, 1465–1491

[9] a) Hernando A.; Crespo P.; García M.A. *The Scientific World JOURNAL* **2005**, *5*, 972–1001; b) Tran P. H.-L.; Tran T. T.-D.; Vo T. V.; Lee B.-J. *Arch Pharm Res* **2012**, *35*, 2045-2061, 2012; c) *OMICS: Biomedical Perspectives and Applications; Chapter 7. Magnetic Nanoparticles in Biomedical Applications* **2012**, Publisher: (CRC Press, Boca Raton, Fla) CODEN:69PUJB, 199-139, ISBN: 978-1-4398-5008-4

[10] a) Vaucher S.; Li M.; Mann S.; *Angew. Chem., Int. Ed.* **2000**, *39,* 1793-1796; b) Fouché, O.; Degert, J.; Daro, N.; Forestier, T.; Deplanche, C.; Létard, J. F.; Freysz, E. *presented at European Conference on Molecular Magnetism, Tomar, Portugal,* **October 2006** c) Létard, J.-F.; Guionneau, P.; Goux-Capes, L. *Top. Curr. Chem.* **2004**, *235*, 221-249; d) Coronado, E.; Galán-Mascarós, J. R.; Monrabal-Capilla, M.; García-Martínez, J.; Pardo-Ibáñez, P. *Adv. Mater.* **2007**, *19*, 1359-1361; e) Neville S. M, Etrillard C, Asthana S, Letard JF, *Eur. J. Inorg. Chem.* **2010**, *2*, 282-288

[11] a) Catala, L.; Gacoin, T.; Boilot, J. P.; Rivière, E.; Paulsen, C.; Lhotel, E.; and Mallah, T.; *Adv. Mat.* **2003**, *15* , 826-829; b) Catala L.; Volatron F.; Brinzei D.; Mallah T. *Inorg. Chem.* **2009**, *48*, 3360-3370; c) Catala, L.; Brinzei D.; Prado Y.; Gloter A.; StØphan O.; Rogez G.; T. Mallah T. *Angew. Chem.* **2008**, *121*, 189-193; *Angew. Chem. Int. Ed.* **2009**, *48*, 183-187

[12] Kaye S. S.; Choi H.J.; Long J.R. *J. Am. Chem. Soc.* **2008**, *130*, 16921–16925.

[13] *Magnetism : Molecules to Materials V; Chapter 9; Magnetic Prussian Blue Analogs* Verdaguer M.; Girolami G. Edited by Miller J. S.; Drillon M.; **2004**, WILEY-VCH Verlag GmbH & Co. KGaA, Weinheim, ISBN : 3-527-30665-X.

[14] a) Culp J. T.; Park, J.-H.; Frye, F.; Huh Y.-D.; Meisel M. W.; Talham D. R. *Coord. Chem. Rev.* **2005**, *249*, 2642-2648; b) Lepoutre S.; Grosso D.; Sanchez C.; Fornasieri G.; Rivière E.; Bleuzen A. *Adv. Mater.* **2010**, *22*, 3992–3996

[15] a) Vaucher S.; Li M.; Mann S.; *Angew. Chem.* **2000**, *112*, 1863-1866; *Angew. Chem. Int. Ed.* **2000**, *39*, 1793-1796; b) Vaucher S.; Fielden J.; Li M.; Durjardin E.; Mann S. *Nano Lett.* **2002**, *2*, 225-229; c) Brinzei D.; Catala L.; Louvain N.; Rogez G.; Stéphan O.; Gloter A. *J. Mater. Chem.* **2006**, *16*, 2593-2599; d) Clavel G.; Larionova J.; Guari Y.; Guerin C. *Chem.–Eur. J.* **2006**, *12*, 3798-3804; e) Guari Y.; Larionova J.; Molvinger K.; Folch B.; Guerin, C. *Chem. Commun.* **2006**, 2613-2615

[16] Prado Y.; Lisnard L.; Heurtaux D.; Rogez G.; Gloter A.; Stéphan O.; Dia N.; Rivière E.; Catala L.; Mallah T. *Chem. Commun.* **2011**, *47*, 1051–1053

[17] Song, Y. Y.; Jia, W. Z.; Li, Y.; Xia, X. H.; Wang, Q. J.; Zhao, J. W.; Yan, Y. D. *Adv. Funct. Mater.* **2007**, *17*, 2808–2814.

[18] a) Clemente-León M.; Coronado E.; López-Muñoz Á.; Repetto D.; Mingotaud C.; Brinzei D.; Catala L.; Mallah T.; *Chem. Mater.* **2008**, *20*, 4642–4652; b) Clemente-León, M.; Coronado, E.; López-Muñoz, A.; Repetto, D.; Catala, L.; Mallah, T. *Langmuir* **2012**, *28*, 4525–4533

[19] Fleury, B.; Volantron F.; Catala L.; Brinzei D.; Rivière E.; Huc V.; David C.; Miserque F.; Rogez G.; Baraton L.; Palacin S.; Mallah T. *Inorg. Chem.* **2008**, *47*, 1898-1900

[20] Ghirri A.; Candini A.; Evangelisti M.; Gazzadi G.-C.; Volatron F.; Fleury B.; Catala L.; David C.; Mallah T.; Affronte M. *Small* **2008**, *12*, 2240-2246.

[21] Laure Catala, Alexandre Gloter, Odile Stephan, Guillaume Rogez and Talal Mallah. Chem. Commun., 2006, 1018–1020.

[22] Martínez R. V.; García F.; García R.; Coronado, E.; Forment-Aliaga, A.; Romero, F. M.; Tatay S. *Adv. Mater.* **2007**, *19*, 291–295.

[23] a) Martínez, R. V.; Martínez, J.; Chiesa M.; García R.; Coronado E.; Pinilla-Cienfuegos E.; Tatay S. *Adv. Mater.* **2010**, *22*, 588-591; b) Yoshinobu, T.; Suzuki, J.; Kurooka, H.; Moon, W. C. ; Iwasaki, H. *Electrochim. Acta* **2003**, *48*, 3131-3135.

[24] Zheng, J.; Zhu, Z.; Chen, H.; Liu, A.; *Langmuir* **2000**, *16*, 4409-4412.

[25] a) Hoeppener, S.; Maoz, R.; Coen, S. R.; Chi, L.; Fuchs, H.; Sagiv J. *Adv. Mater.* **2002**, *14*, 1036-1041; b) Liu, S. Maoz, R.; Sagiv J. *Nano Lett.* **2004**, *4*, 845-851.

[26] Shyue, J.-J.; De Guire M. R.; Nakanishi, T.; Masuda, Y.; Koumoto, K.; Sukenik, C. N. *Langmuir* **2004**, *20*, 8693-8698

[27] a) Wallwork M.L.; Smith, D.A.; Zhang, J.; Kirkham, J; Robinson C. *Langmuir* **2001**, *17*, 1126–1131; b) Vezenov, D.V.; Noy, A.; Rozsnyai, L.F.; Lieber, C.M. *J. Am. Chem. Soc.* **1997**,

119, 2006–2015; c) Van Der Vegte, E.W.; Hadziioannou, G. *J. Phys. Chem. B* **1997,** *101*, 9563–9569.

[28]*Comprehensive Analytical Chemistry,* in *Non-Destructive microanalysis of cultural heritage materials,* Wilson, *Vol. XLII* (Eds.: K. Janssens and R. Van Grieken) Elsevier, Belgium, **2004**

[29] *Handbook of Auger Electron Spectroscopy.* Childs, K.D; Carlson, B.A.; LaVanier, L.A.; Moulder, J.F.; Paul, D.F.; Stickle, W.F.; Watson D.G. 3rd edition, (Ed: C.L. Hedberg) Physiscal Electronics, USA, **1995**.

[30] Dagata, J. A.; Inoue, T.; Itoh, J.; Matsumoto, K.; Yokoyama, H. *J. Appl. Phys.* **1998**, *84*, 6891-6900

[31]*Functionalization of Probe Tips and Supports for Single-Molecule Recognition Force Microscopy. In: Samorì P, editor. STM and AFM Studies on (Bio)molecular Systems: Unravelling the Nanoworld:* Ebner, A.; Wildling, L.; Zhu, R.; Rankl, C.; Haselgrübler, T.; Hinterdorfer, P.; et al. Springer Berlin / Heidelberg; 20082976

[32] Ding L., Li Y., Chu H., Li X., Liu J., *J. Phys. Chem. B.* **2005**, *109*, 22337.

[33] Sader J.E.. *J. Appl. Phys.* **1998**, *84*, 64.

[34] Cappella B., Dietler G.. *Surface Science Reports.* **1999**, *34* , 1-104.

[35] Bellido E., Domingo N., Ojea-Jiménez I., Ruiz-Molina D. *Small.* **2012**, *8* (10), 1465–1491.

[36] Martínez R. V., Chiesa M., García R., *Small* **2011**, *7*, 2914-2920.

[37] Cavallini M., Albonetti C., Biscarini F., *Adv. Mater.* **2009**, *21* 1043-1053. (b) Cavallini M., Biscarini F., *Nano Lett.* **2003,** 31269.

[38] Horcas I., Fernández R., Gómez-Rodríguez J.M., Colchero J., Gómez-Herrero J., Baro A. M., *Rev. Sci. Instrum.* **2007**, *78*, 013705.

[39] a) R. García, M. Calleja, F. Pérez-Murano, *Appl. Phys. Let*. **1998**, *72*, 2295-2297. b) García R., Martínez R. V., Martínez J., *Chem. Soc. Rev*. **2006**, *35*, 29–38.

PART II

4

INTRODUCTION TO THE MAGNETIC CHARACTERIZATION OF MOLECULAR-BASED MAGNETIC NANOPARTICLES ON SURFACES

4.1 INTRODUCTION

Due to the interesting properties of magnetic PBA-NPs presented in previous chapters and focusing in their capability for their potential application in patterned magnetic recording media for example, one can infer the use of small NPs aggregates as addressable information units or, even in the limit, the use of one NP as a single magnetic bit.[1] It has been presented already in chapter 3, different possible routes for their accurate organization onto surfaces which is a basic requirement for their application in such technologies. However, before these potential applicability become real, there are several points that have to be studied in detail like: (i) the local detection and modulation of their physical properties, (ii) the influence of the neighbouring particles which could block, enhance or slightly modify the property that we are detecting/tuning and (iii) the fact that molecular-based NPs usually have Curie/blocking temperatures below room temperature.

Whenever the physical property to be measured and modified is a magnetic signal, there are several magnetic characterization techniques that can be proposed. superconducting quantum interference devices (SQUID magnetometer) or Hall sensors traditionally used for magnetic bulk materials characterization have been miniaturized to increase their sensitivity down to a single magnetic nanoparticle (m_{NP}) moment.[2] Also techniques commonly used in surface science have been adapted for characterizing magnetic nanostructures, for example magnetic resonant techniques, from EPR or NMR using microwaves, to magnetic circular dichroism (MCD) or magneto optical Kerr effect (MOKE) using optical waves, and also X-ray magnetic circular dichroism (XMCD) studies performed with X-ray radiation obtained from synchrotron facilities.[3] Indeed, there are several experimental techniques that permit the imaging of the magnetization of nanometric objects as Lorentz microscopy,[4] electron holography,[5] X-ray microscopy,[6] spin-polarized scanning tunneling microscopy (SP-STM),[7] scanning hall probe microscopy (SHPM),[8] magnetic force

microscopy (MFM),[9] magnetic exchange force microscopy (MExFM)[10] or nitrogen-vacancy (NV) based magnetometry.[11] Among all these techniques, MFM has a strong potential to detect and tune the properties of individual MNPs, as it does not need of a previous specific positioning of the magnetic particle (as required for example in nano-SQUID measurements), it does not require the studied magnetic units to be prepared under ultra high vacuum conditions and deposited specifically on conducting/semiconducting materials (as needed in high resolution STM), or does not need synchrotron facilities as required for XMCD.

The utility of MFM to characterize high dense magnetic recording systems in a non-invasive manner has been already highlighted.[12] To probe the possibilities of this technique in the detection and modification of PBA-NPs, and in order to characterize their magnetic behavior after being anchored onto a surface, we have chosen KNiCr NPs among this family of PBA-NPs. These particular NPs were selected for some important reasons: they can be prepared by a very simple synthetic procedure, they present electrostatic stabilization leading to almost perfect cubic MNPs with sizes of ~20-25 nm and they are water-soluble nanoparticles with no capping layer. In this range of sizes, a very rich variety of magnetic states are coexisting within the sample: from curling (single domain NPs with non-homogeneous magnetization) to multi domain behaviors. The smallest CsNiCr NPs already introduced in chapter 3, would be more difficult to detect due to the decrease of their magnetic moment, which would generate a too weak magnetic signal to be detected with the MFM. Moreover, the magnetization reversibility in very small MNPs sometimes can be impeded due to the related increase of the surface effects.[13]

For this study, envisioning the possibilities of using one single NP or well defined NPs aggregates as information units, both situations have been simulated transferring the NPs to a surface by two different approaches: well-organized in controlled stripes by means of soft-lithography,[14] (NPs uniform aggregates) and randomly dispersed by drop casting (isolated particle) . For the first time, the detection and magnetic

characterization of individual PBA-NPs, will be carried out by means of a commercial Low Temperature MFM (LT-MFM).

4.1.1 Magnetic force microscopy

Magnetic force microscopy[15] is an imaging technique based on atomic force microscopy (AFM),[16] in which magnetic forces or force gradients are measured to image the magnetic structure of a sample. In the MFM, a cantilever with a magnetic tip is used to measure the interaction produced by the magnetic stray field from the sample. As soon as the magnetic tip interacts with the surface, generally at distances between 10 to 100 nm, the cantilever state changes caused by magnetostatic interactions which can be optically detected by an interferometer (Figure 1).
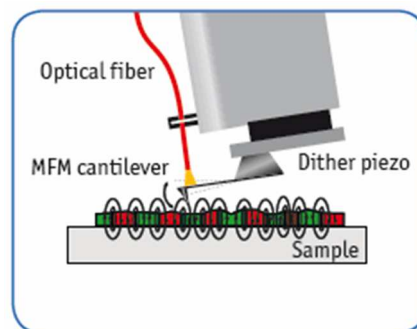
Figure 1. Schematics of the MFM tip-sample interaction detection with an optical fiber.

The MFM is a very powerful tool to study a wide variety of magnetic structures such as ferromagnetic domain patterns (Figure 2),[17] domain walls, [18] magnetic nanoparticles (MNPs)[19] and magnetic vortices,[20] as well as flux lines in superconductors.[21] Although the majority of MFM experiments are performed in zero or rather small magnetic fields, there are some MFM configurations that can be operated in variable external applied field (B). That permits to study the B-dependence of domain patterns in

ferromagnetic thin films, [22] single nanowires[23,24], nanoparticles[25] as well as the B-dependence of static and dynamic flux-line configurations in high-temperature superconductors,[26] for example.
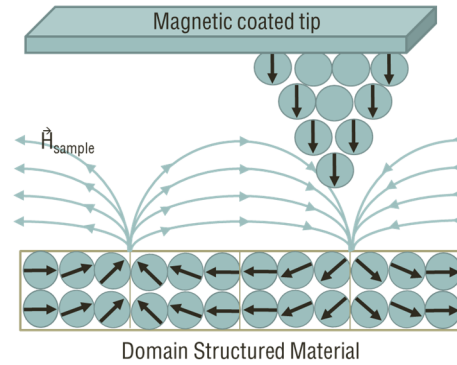

Figure 2. Schematic representation of the magnetic coated tip with a sample structured in domains. The magnetic tip senses the stray field emanating from the sample.

Although room temperature (RT) measurements are the most common, the development of more sophisticated MFM which are now commercially available allowed the measurements at low temperature (LT) and variable field.[27] Low temperature MFM (LT-MFM) is an important extension of MFM which local magnetic characterization at liquid helium temperatures down to the miliKelvin regime. The advantages of operating the MFM at low temperature are related not only to the improved sensitivity and stability, but also to the possibility of studying quantum mechanical effects, e.g., in magnetic materials and superconductors.[28] Among the magnetosensitive low temperature scanning probe techniques such as scanning Hall probe microscopy[29], spin polarized STM (SP-STM) 7 and scanning superconducting quantum interference device microscopy,[30] LT-MFM reveals a very high lateral resolution which ranges between 10 and 100 nm,[31] only surpassed by SP-STM.

The principles of operation of the MFM at LT are the same than at RT but some considerations have to be taken into account like the behavior of the magnetic tips at LT or the magnetic properties of the sample, that will be deeply discussed in chapter 5. In the present chapter, a brief introduction of the MFM modes of operation and the magnetic contrast formation will be presented (an overview of the LT-MFM instrument is included in Apendix).

4.1.2 MFM principle

If we consider the MFM cantilever like a spring that responds to a force F according to Hooke's law (Figure 3), then $z = F/k$, where k is the spring constant of the cantilever, and z is the deflection at the end of the lever. By measuring the cantilever deflection it is possible to measure the force on the cantilever, which can then be related to properties of the sample under study. This is a broadly applicable measurement technique and is used to measure atomic, electrostatic, or in the case of this thesis, magnetic forces.
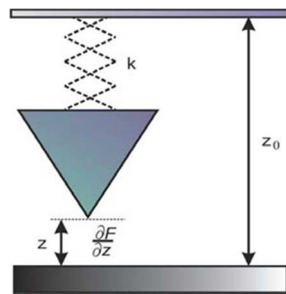

Figure 3. Modelled tip-sample interaction, where k denotes cantilever constant and the force derivative $\partial F / \partial z$ is schematically depicted here as an additive force interaction constant.

But cantilevers can also be used to measure force gradients. A cantilever driven by a sinusoidal force F_{ex} [t] follows the equation of motion for a damped harmonic oscillator:

$$m\frac{d^2y}{dt^2} + \gamma\frac{dz}{dt} + k(z - z_0) = F_{ex}[t] + F_{ts}[z] \qquad \text{(Eq. 4.1)}$$

where m is the mass of the cantilever, γ is the damping coefficient, and z_0 is the cantilever position in the absence of an external force F_{ex}. $F_{ts}[z]$ is the force between the cantilever and the sample under study at a cantilever deflection z. The force must be integrated over the total cantilever volume, but the force is likely to vary a lot over that volume. In general the force on a small region at the cantilever tip dominates the signal. A Taylor expansion of the force gives:

$$m\frac{d^2y}{dt^2} + \gamma\frac{dz}{dt} + k(z - z_0) = F_{ex}[t] + F_{ts}[z = z_0] + \frac{dFts}{dz}\bigg|_{z=z_0} \qquad \text{(Eq. 4.2)}$$

And an effective spring constant k_{eff} can be defined as:

$$m\frac{d^2y}{dt^2} + \gamma\frac{dz}{dt} + \left(k - \frac{dFts}{dz}\bigg|_{z=z_0}\right)(z - z_0) = F_{ex}[t] + F_{ts}[z = z_0]$$

$$m\frac{d^2y}{dt^2} + \gamma\frac{dz}{dt} + k_{eff}(z - z_0) = F_{ex}[t] + F_{ts}[z = z_0]$$

$$\text{(Eq. 4.3)}$$

where $k_{eff} = k - dF_{ts}/dz$. The cantilever resonant frequency in the presence of a force gradient is given by $\omega_0{}'$:

$$\omega_0{'} = \sqrt{\frac{k_{eff}}{m}} = \sqrt{\frac{k - dFts/dz}{m}} \qquad\qquad (Eq.\ 4.4)$$

The right hand side of Equation (4.4) can be Taylor expanded for $dF_{ts}/dz \ll k$. The cantilever frequency shift $\Delta\omega = \omega_0{'} - \omega_0$ is then:

$$\frac{\Delta\omega}{\omega_0} = \frac{-1}{2k}\frac{dF_{ts}}{dz} \rightarrow \frac{dF_{ts}}{dz} = \frac{\Delta f}{f_0}2k \qquad\qquad (Eq.\ 4.5)$$

where $\omega_0 = 2\pi \cdot f_0$, f_0 is the natural resonant frequency of the cantilever, and $\Delta f = f - f_0$.

However, equation 4.5 is true only under three conditions: first, the damping of the cantilever oscillation is constant throughout the image, second, the oscillation amplitude of the cantilever is small compared to the average tip-to-sample distance and third, the tip-to-sample distance is constant. The amplitudes (A_{osc}) used in this thesis rarely full the small amplitude approximation because at our measuring conditions (low temperature and low pressure), it was found that snap to contact phenomenon started to appear at small values of the A_{osc}. This phenomenon can cause severe damages on the tip, so, it was avoided by using large amplitudes. For large amplitudes, in the case of an exponentially decaying force, such as a magnetic force, the equation can be inverted analytically. In the large amplitude regime, the frequency shift is dominated by the strong variation of the force near the point of closest approach and is inversely proportional to $A_{osc}^{3/2}$. In order to be able to compare interaction forces without converting the frequency shift to force, the normalized frequency shift first introduced by Giessibl, [32] can be used:

$$\Gamma = \frac{\Delta f \cdot k \cdot A_{osc}^{3/2}}{f_0} \qquad\qquad (Eq.\ 4.6)$$

4.1.3 MFM modes of operation

One of the key points that make the MFM a powerful imaging technique is that it can relate the topographic characteristics of a specimen to its magnetic structure. The MFM is basically an AFM that performs two scans: a first one to acquire the topography image and a second one to acquire the magnetic image (Figure 4).
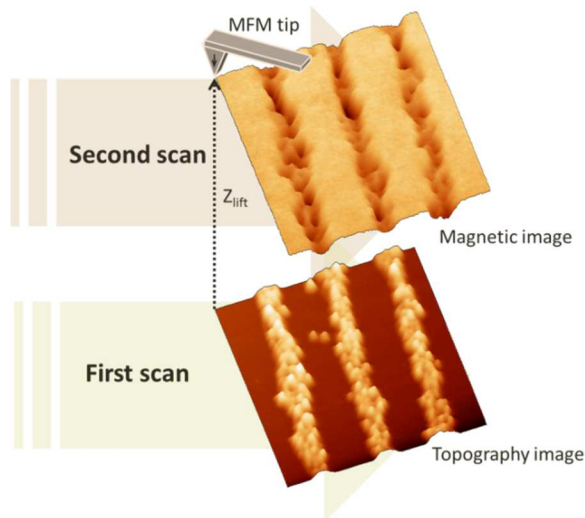

Figure 4. In this figure it is shown the MFM experiment: At the first scan, the topography image is acquired, then the tip and the sample are separated a constant distance, Z_{lift}, and the magnetic image is recorded in the second scan.

There are two distinct modes of operation for an MFM, namely constant height mode and dual pass mode. In **constant height mode**, the tip is scanned across the sample at a certain distance, (Z_{lift}) with the z-feedback switched off. In this mode, the scanning plane and the surface plane need to be aligned parallel using an electronic tilt correction beforehand. During the scan, the MFM is typically (but not necessarily) operated in amplitude mode (AM), i.e. the cantilever is excited with constant frequency f_0 and amplitude a_0. The phase-shift measured between excitation source and cantilever then reflects the magnetic field gradient. Constant height mode is

restricted to cases where the roughness of the sample surface is small compared to the tip-sample separation. For non-flat surfaces the dual-pass mode is more suitable than the constant height mode.

In **dual-pass mode**, the tip is first scanned over the surface in close proximity to get the topography image and then retracted by a predefined distance (Z_{lift}). In a second scan, the tip follows the recorded surface topography at constant separation and the phase/frequency shift due to magnetic interaction forces is recorded. To avoid problems associated with drift, dual-pass mode is executed in a line-by-line fashion. This mode is slower that the constant height mode.

Either in constant height mode or dual-pass, the MFM senses the interaction between the tip and the sample (F_{ts}) and this magnetic interaction can be recorded by the instrument as variations in amplitude (**amplitude modulation detection**, AM), or frequency of the cantilever oscillation (**frequency modulation detection**, FM). The amplitude detection technique measures force gradients by measuring changes in the cantilever's amplitude and/or phase. The cantilever is driven at a frequency slightly off resonance, and as changes in the force gradient shift the resonant frequency, the cantilever amplitude and phase change. The frequency modulation technique uses positive feedback to oscillate the cantilever at its resonant frequency, by phase shifting the cantilever vibration signal by 90º and driving the cantilever with the resultant waveform. Thus the resonant frequency can be measured directly and related to the force gradient by Equation (4.5) or (4.6) for the large amplitude regime.

Both modes can be operated in combination with a phase-locked loop (PLL). In this case, the cantilever is always excited at resonance, i.e. 90° phase shifted with respect to its detected phase at any time. Due to this fixed-phase condition, a frequency shift Δf is then observed (and recorded) whenever the tip is scanned over the surface at the corresponding separation, Z_{lift}. This technique is most frequently used at high vacuum conditions where the Q-factor of the MFM cantilever is high and will be the mode used in all MFM measurements presented in this thesis. Cantilevers with a high

stiffness (k ≥ 2 N/m) and high values of the amplitude oscillations (A ≈ 90 nm) will be used to avoid the problem of unwanted jump-to-contact phenomenon (stop of the oscillation).

The distance between the magnetic tip and the sample surface (Z_{lift}) plays important role. If the tip is brought to the region of short-ranged forces, the resulting image would be a topographic relic mainly because there is none or minimum magnetic interaction. The origin of forces acting between the tip and the sample would be then van der Waals interactions, capillary or quantum mechanical forces. On the other hand, if this distance is too large, the sensitivity and the resolution of the measurement decrease.

4.1.4. Magnetic contrast formation in MFM.

When attempting to record an MFM image, a field is applied to the sample by the tip and viceversa. This can in principle lead to different situations. There can be negligible modification of both the tip and the sample, there can be reversible modification of the tip, or the sample, or both; or there can be hysteretic or irreversible modification of the tip or the sample or both.[33] To obtain a reliable MFM image, the first case is desirable. It is also important to know how to exclude a possible modification of either the tip or the sample from the images obtained. If no mutual modification occurs, the force acting on the tip is given by the interaction of a dipole.

The stray field emanating from the sample generates a force on the magnetic force microscope tip. The magnetic force F_{ts}, responsible of the tip-sample interaction is given by the gradient of the magnetic energy:

$$F_{ts} = \nabla(\vec{m}\cdot\vec{B}) \qquad \text{(Eq. 4.9)}$$

where generally $\vec{m}$ is taken to be the magnetic moment of the cantilever tip and $\vec{B}$ the stray field from the sample. Taking $\vec{m}$ as the magnetic moment of the sample and $\vec{B}$ as the stray field from the tip is equally valid.[34]

The component actually measured is the component normal to the surface of the cantilever, $F = F_z$, where F_z is the perpendicular component of the force.
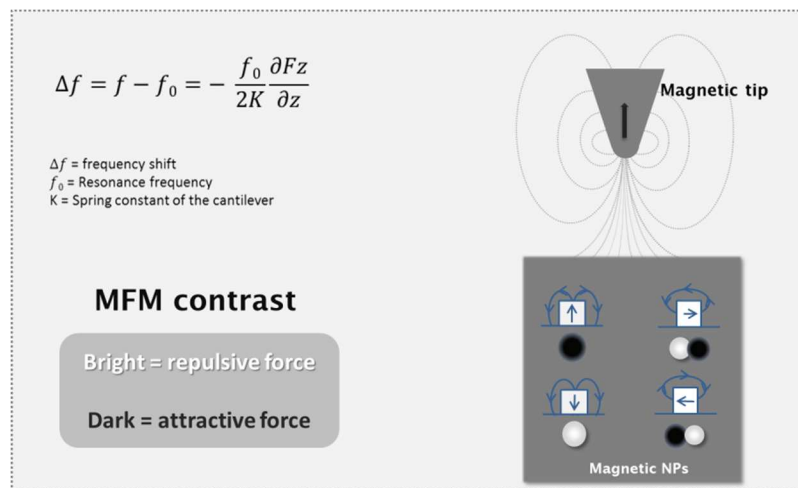
Figure 5. Schematic representation of the magnetic contrast formation in MFM.

In constant height mode at a fixed Z_{lift}, the frequency shift, $\Delta f = f - f_0$, is tracked by the PLL. It can be negative or positive depending on the tip-sample interaction (Figure 5). Considering the equation (4.5), a negative frequency shift will always indicate an attractive tip-sample interaction ($\Delta f < 0$, dark contrast) while a positive frequency shift will indicate a repulsive tip-sample interaction ($\Delta f > 0$, bright contrast). So far, the orientation of the magnetic moment of the sample (the NPs) can be distinguished.

4.2 BIBLIOGRAPHY

[1] Cavallini,M., Gomez-Segura,J., Ruiz-Molina,D., Massi,M., Albonetti,C., Rovira,C., Veciana,J., BiscariniF. *Angew. Chem. Int. Ed*. **2005**, *44*, 888 – 892.

[2] (a) Jamet, M., Wernsdorfer, W. C. Thirion, Mailly, D., Dupuis, V., Mélinon, P, Pérez, A., *Phys. Rev. Lett.*, **2001**, *86*, 4676–4679. (b) Martínez-Pérez, M. J., Bellido, E. Miguel, R. D, Sese A. Lostao J., Gómez-Moreno C., Drung, D, Schurig, T., Ruiz-Molina, D. Luis, F, *Appl. Phys. Lett*., **2011**, *99*, 032504. (c).Granata,C.,Esposito,E.,Vettoliere,A.,Petti,L.,Russo M., *Nanotechnology*, **2008**, *19*, 275501. (d) Hao L., Assmann C, Gallop, J. C, Cox, D., Ruede, F., Kazakova, O., Josephs-Franks, P., Drung D., Schurig, T, *Appl. Phys. Lett*., **2011**, *98*, 092504.

[3] Domingo,N., Bellido,E. Ruiz-Molina,D., *Chem. Soc. Rev*., **2012**, *41*, 258–302.

[4] Majetich, S. A., Jin, Y. *Science*, **1999**, *284*, 470.

[5] a) Tripp, S. L, Dunin-Borkowski,R. E, Wei Alexander. *Angew. Chem. Int. Ed*. **2003**, *42*, 5591 –5593. b) Midgley, P. A, Dunin-Borkowski, R. E., *Nature Materials*, **2009**, *8*. c) Varon, M., Beleggia. M, Kasama. T., Harrison. R., J. Dunin-Borkowski, R. E., Puntes, V. F, Frandsen C. *Scientific Reports* ,*3*,1234 | DOI: 10.1038/srep01234.

[6] a) Chen C. T. et al., *Phys. Rev. B*,**1993**,*48*, 642 b) Choe, S.-B., Acremann, Y., Scholl, A., Bauer, A, Doran, A., Stohr, J., Padmore, H. A. *Science* ,**2004**,*304*, 420.

[7] a) Wulfhekel, W., Kirschner, J. *Annu. Rev. Mater. Res*. **2007**. *37*, 69–91. b) Romming, S. K., Hanneken, C., Menzel, M., Bickel J, E., Wolter. B, Von Bergmann, K., Kubetzka, A., Wiesendanger. R., *Science*, **2013***, 341*, 636.

[8] Chang, A. M., Hallen, H. D, Harriott. L., Hess, H. F., Kao, H. L., Kwo, J., Miller R. E., Wolfe. R, Van der Zielb, J., Chang, T. Y. *Appl. Phys. Lett*. **1992***, 16,* 61.

[9] Martin, Y., Wickramasinghe, H. K., *Appl. Phys. Lett*., **1987**, *50*, 1455.

[10] Kaiser, U., Schwarz, A. Wiesendanger. *Nature*,**2007**, *446* doi:10.1038/nature05617

[11] a) Maze, J. R.,Stanwix, P. L., Hodges, J. S, Hong, S., Taylor, J. M, Cappellaro, P, Jiang, L., Gurudev Dutt, M. V., Togan, E., Zibrov, A.S, Yacoby, A., Walsworth, R. L., Lukin, M. D., *Nature* **2008,** *455*, 644-647. b) Rondin, L., Tetienne, J. P., Rohart, S., Thiaville, A., Hingant, T., Spinicelli, P., Roch, J.-F., Jacques V. *Nature Communications*, **2013**, *4*, 2279.

[12] a) Rugar, D., Mamin, H. J., Guethner, P., Lambert, S. E.,Stern, J. E., McFadyen, I., Yogi, T. *J. Appl. Phys*. **1990**,*68*, 1169. b) Moser, A., Bonhote,C., Dai Q., Do H., Knigge B., Ikeda Y., Q., Lengsfield, B., MacDonald, S., Li J., Nayak, V., Payne R., Schabes, M., Smith, N., Takano, K., Tsang, C., Van der Heijden P., Weresin, W., Williams, M., Xiao, M., *Journal of Magnetism and Magnetic Materials***, 2006,** *303*, 271–275.

[13] Krone, P., Makarov, D., Cattoni, A., Faini, G., Haghiri-Gosnet, A. M., Knittel. I., Hartmann, U., Schrefl, T., Albrecht, M., *J Nanopart Res*, **2011**, *13*, 5587–5593.

[14] Gentili, D.,Cavallini, M.,*Coord.Chem.Rev*.**2013**, http://dx.doi.org/10.1016/j.ccr.2012.12.009.

[15] Martin,Y., Wickramasinghe, H. K., *Appl. Phys. Lett*., **1987**, *50*, 1455.

[16] Binnig, G., Quate, C. F., Gerber, Ch., *Phys. Rev. Lett.*, **1986**, *56*, 930.

[17] Kleiber, M., Kümmerlen, F., Löhndorf, M, Wadas, A., Weiss, D., Wiesendanger, R., *Appl. Phys. Lett.* **1994**, *64*, 1156.

[18] a) Löhndor, M., Wadas, A., Van den Berg, H. A. M, Wiesendanger, R., *Appl. Phys. Lett.* **1996**, *68*, 3635. b) Pfeiffer, M., Schneider, M., Manne, S., Hansma, P. K, Drake, B., Maivald, P., Boles, C., Gurley, J., Elings, V., *J. Appl. Phys.* **1996**,*79*, 8578.

[19] Proksch, R. B, Moskowitz, B. Dan Dahlberg, M. E., Schaeffer, T., Bazylinski, D. A., Frankel. R. B., *Appl. Phys. Lett.* **1995**, *66*, 2582–2584.

[20] Shinjo, T., Okuno, T., Hassdorf, R., Shigeto, K., Ono, T., *Scienc*e, **2000**, *289*, 930.

[21] a) Moser, A., Hug, H. J, Parashikov, I., Stiefel, B., Fritz, O., Thomas, H., Baratoff, A., Guntherodt, H. J., Chaudhari, P., *Phys. Rev. Lett.* **1995**, *74*, 1847. b) Volodin, A., Temst, K., Van Haesendonck,C., Bruynseraede Y.,*Appl. Phys. Lett.*, **1998**, *73*, 1134.

[22] a) Schwarz, A., et al., *Phys. Rev. Lett.* **2004**, *92*, 077206. b) Liebmann, M., et al., *Phys. Rev. B*, **2005**, *71*, 104431.

[23] Wang, T., Wang, Y., Fu, Y., Hasegawa, T., Li, F. S., Saito, H., Ishio, S., *Nanotechnology*, **2009**, *20*, 105707.

[24] Jaafar, M., Gómez-Herrero, J., Gil, A., Ares, P., Vázquez, M., Asenjo. A. *Ultramicroscopy*, **2009,** *109*, 693–699.

[25] Diebel,C.E, Proksch,R.,. Greenk C.R, Neilson,P. Walker,M.M ,Nature, **2000**,*406*.

[26] a) Schwarz, A., Pi, U. H, Liebmann, M., Wiesendanger, R., *Appl. Phys. Lett.*, **2006**, *88,* 012507. b) Pi, U. H., et al., *Phys. Rev. B*, **2006**, *73*, 144505.

[27] Straver Thesis. 2004.

[28] Straver, E.W. J., Hoffman J. E., Auslaender O.M., Rugar D., Moler A.K., *Applied Physics Letters*, **2008**, *93*, 17, 172514.

[29] Oral. A, Bending. S. J, Henini. M., *Appl. Phys. Lett.* **1996**, *69*, 1324.

[30] Tsuei, C. C, Kirtley, J. R, Chi, C. C, Yu-Jahnes, L. S, Gupta, A., Shaw, T., Sun, J. S., Ketchen, M. B, *Phys. Rev. Lett.* **1994**, *73*, 593.

[31] Volodin, A., Temst, K., Van Haesendonck, C., Bruynseraede, Y. *Rev. Sci. Instrum.*, **2000,** *71*, No. 12.

[32] Giessibl, F. J, *Phys. Rev. B*, **1997**, *56*, 16010-16015.

[33] Hubert, A., Schafer, R., *Magnetic Domains*. The Analysis of Magnetic Domain Structures (Springer-Verlag, Berlin, Heidelberg, **1998**.

[34] Wright C. D, Hill E. W, *Appl. Phys.Lett.* **1995,** *67*, 433-435.

5

LT-MFM Characterization Of Single And Isolated Molecular-based Magnetic Nanoparticles

5.1 INTRODUCTION

The magnetization reversal is one of the most important fundamental processes in magnetism. It has been studied from the bulk to the nanoscale where it was theoretically predicted and described more than 60 years ago.[1] In nanomagnetism, magnetic nanoparticles (MNPs) represent an important class of nanostructured materials and the understanding of its magnetic structure and spin dynamics is essential not only from a fundamental point of view but also in order to design them for specific applications (Figure 1).[2]
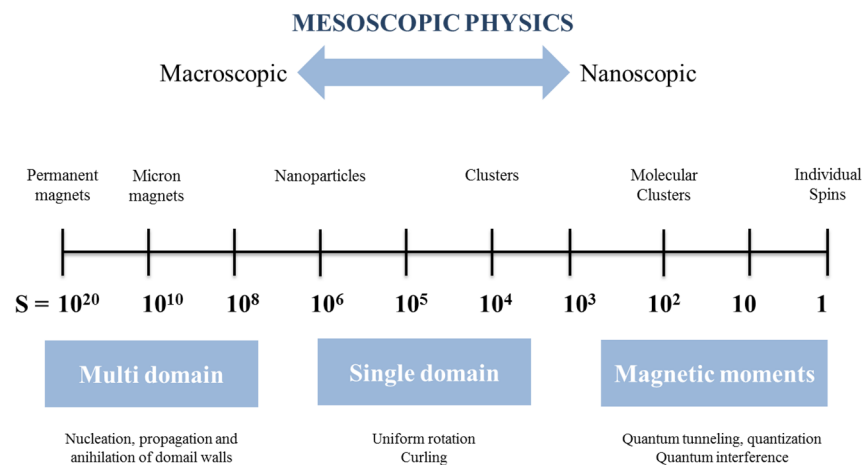

Figure 1. Scale from macroscopic to nanoscopic sizes. The unit of the scale is the number of magnetic moments in a magnetic system (roughly corresponding to the number of atoms).

The magnetization reversal mechanism of the MNPs (with same shape and anisotropy) is known to be size dependent: the smallest NPs become single domain and the magnetization reversal takes place by coherent rotation, classically described by the Stoner–Wohlfarth model,[3] while increasing the size, more complex reversal mechanisms start to appear provoking non-coherent rotation like curling.[4] When the size particle exceeds a certain limit, they become multi-domain and the magnetization rotation takes place via domain-wall motion. But aside these basic mechanisms, there

are others like pinning, localized nucleation, vortices and many combinations of them that may arise from the real-structure dependence of the magnetic materials.[5]

5.1.1 Magnetic properties of small NPs (structure and mechanisms)

The magnetic properties of small MNPs are dominated by the fact that below a certain critical size (the single domain limit, l_{SD}), the MNP contains only one domain and presents high coercivity. This critical size defines the frontier between multi and single domain MNPs and is dependent on their crystalline structure. But it is important to note that the critical single domain size is an equilibrium property, involving the energies of single- and multi domain states, but independent of the energy barriers separating the states. So, the domain structure of a magnetic material is a result of minimizing the total free energy (or micromagnetic free energy), and it reflects either a local or an absolute energy minimum.

There is a relative contribution of the different magnetic energy terms to the free energy of any magnetic structure (ε_{tot}), namely, exchange (ε_{ex}), magnetostatic (ε_m), magnetic anisotropy (ε_a) and the Zeeman energy (ε_Z, if there is an external field); however, for magnetic small objects, the effects of boundaries cannot be neglected and the shape of the element changes dramatically the relative importance of the different energy terms.

$$\varepsilon_{tot} = \varepsilon_{ex} + \varepsilon_m + \varepsilon_a + \varepsilon_Z \; ^{[1]} \qquad\qquad \text{(Eq. 5.1)}$$

---

[1] ε_{ex}: It is at the origin of ferromagnetic order. Its microscopic origin is related to combination of the Pauli exclusion principle and Coloumb repulsion between ions. It is minimum when all spins are aligned parallel to each other, so uniform magnetization states are the lowest in energy. ε_m:Classical interaction energy between magnetic dipoles. It is responsible for the existence of magnetic domains, and therefore, competes directly with the exchange energy term. ε_m: it refers to variations in the magnetic energy with the special orientation of the magnetization. ε_Z: it corresponds to the dipole interaction with an external applied magnetic field.

The term *single domain* does not require a necessary uniform magnetization throughout the whole particle, but only implies the absence of domain walls. Figure 2 shows a schematic of the variation in coercivity of small particles with particle size. As the size of the NP is reduced from the bulk, the coercivity initially increases as single-domain particles are formed.
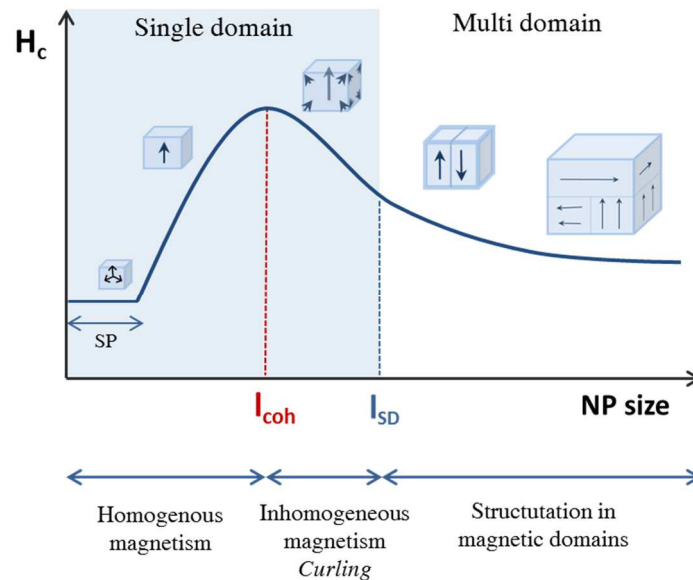

Figure 2. Sketch of the dependence of the magnetization hysteresis loop coercive field (Hc) with the NP size. Below a critical size, a particle contains only one domain. This limit is usually called the single domain limit (l_{SD}). In the region of the single domain, another limit appears and this is the size at which the NP rotates its magnetization by coherent rotation. It is then, the coherent rotation limit (l_{coh}).

The fact that the large coercivity of small particles is the result of single domains was first demonstrated in by Kittel et al in the 1950s.[6] Below the critical size, however, the coercivity decreases and eventually drops to zero. The drop in the coercivity for very small NPs is the result of a corresponding reduction in anisotropy energy with size. The anisotropy energy, E_a, holds the magnetization along an easy direction. It is given by $E_a = K \cdot V$, where K is the anisotropy constant and V is the volume of the NP. As

the volume is reduced, KV becomes comparable to the thermal energy, $k_B T$. As a result, thermal energy can overcome the anisotropy force and then, the magnetization of a particle spontaneously reverses from one easy direction to the other, even in the absence of an applied field. This phenomenon is called superparamagnetism (SP).

Magnetic domains are caused by strongly geometry and size- dependent magnetostatic self-interaction and the width of a domain wall depends on the balance between the exchange energy (which prefers a wide wall) and the magnetic anisotropy energy (which prefers a narrow wall). When the MNP become multidomain, they present lower magnetostatic energy but higher exchange energy, so above a certain size, it can be found that a two-domain state is more favorable than the single domain state (Figure 3).
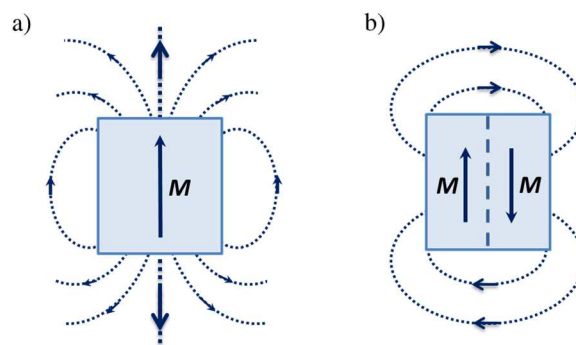

Figure 3.(a) Magnetic field lines for a NP as single domain. (b) Magnetic field lines for a two-domain NP, that have been formed due to high magnetostatic energy.

Typical domain-wall widths are much smaller than the domains themselves (from about 1 nm in extremely hard materials to several 100 nm in very soft materials), so when the size of a particle is smaller than the domain wall width, as encountered for example in soft magnetic nanodots, then the distinction between domains and domain wall blurs, and the determination of the micromagnetic spin structure requires additional considerations as for example, the curling-type flux-closure (Figure 4).
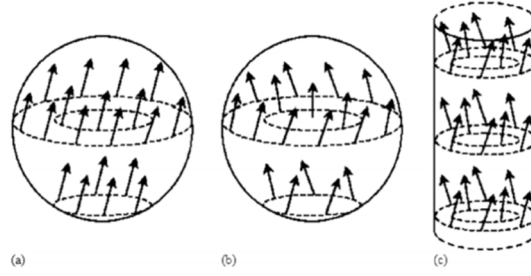
Figure 4. Nucleation modes in homogeneous magnets: (a) coherent rotation in a sphere, (b) curling in a sphere and (c) curling in a cylinder. From Skomski J. Phys.: Condens. Matter 15 R841 (2003)

The transition from coherent to curling state, takes place at a certain MNP size: the coherent length (l_{coh} in Figure 2). For MNPs with sizes below the coherent length, $l < l_{coh}$, the exchange energy dominates and the magnetization reversal of these MNPs is realized by coherent rotation, whereas for MNPs with $l > l_{coh}$ the magnetization reversal is dominated by flux closure and it is realized by curling.

The coherent length is related to the exchange length which is defined as[2]

$$l_{ex} = \sqrt{\frac{A}{\mu_0 M_s^2}} \qquad \text{(Eq. 5.2)}$$

where A is the exchange constant, μ_0 is the permeability of free space and M_s is the saturation magnetization of the MNP.

Typical values of l_{ex} vary from 2.4 nm for Fe to 4.9 nm for Fe_3O_4 and define the shortest scale on which the magnetization can be twisted in order to minimize the dipolar interaction. The transition from coherent rotation to curling occurs at $l_{coh} \approx$ 3.655 l_{ex}, in spheres and at $l_{coh} \approx$ 5.099 l_{ex}, for wires.5 Note that l_{coh} is anisotropy-independent, in contrast to the critical single domain size l_{SD}. Since $l_{coh} \ll l_{SD}$ in hard magnets, there is a broad region $l_{coh} \approx$ 10 nm and $l_{SD} \approx$ 1 μm, where single-domain

---

[2] Other definitions of exchange length can be found in the literature, such as $\sqrt{(2A/\mu_0 Ms^2)}$ or $\sqrt{(A/Keff)}$, where *Keff* is an effective anisotropy constant.

particles can demagnetize incoherently. On the other hand, l_{coh}, is directly related to A, which is temperature dependent in the form: $A = (k_B\ T_c)/2a_0$, where k_B is the Boltzmann contact, T_c is the Curie temperature and a_0 is the lattice parameter of the MNP.

Typically, in the regime below the maximum single domain particle size ($l < l_{SD}$) there are no domain walls. The magnetization reversal of MNPs, therefore, occurs by rotation of the magnetization upon application of a magnetic field. Before application of an external field, the magnetization of a single-domain MNP lies along an easy direction which is determined by the shape and magnetocrystalline anisotropies. When an external field is applied in the opposite direction, the particle is unable to respond by domain-wall motion, and instead, the magnetization must rotate through the hard direction to the new easy direction. The anisotropy forces which hold the magnetization in an easy direction are strong, and so the coercivity is large. This mechanism is known as coherent rotation described by Stoner and Wohlfarth in 1948. They theoretically determined that the coercivity, (H_c), of these particles along the anisotropy axis should follow the relationship:

$$H_c = \frac{2K_u}{M_s} \qquad\qquad \text{(Eq. 5.3)}$$

where K_u is the uniaxial constant anisotropy and M_s is the saturation magnetization. Even when a nanoparticle has a defect-free crystal structure, the different local environments of atoms at the particle boundary and inside the particle result in a non-uniform magnetization in the particle and distortion of the perfect collinear magnetic structure. Under the action of an external magnetic field, the spins of the atoms forming the MNP can rotate not only coherently but also in a more complex manner via curling rotation.[7] Curling rotation is more favorable from the point of view of magnetostatic self-interaction, because it forms a flux closure, although it costs some exchange energy, because $\nabla M \neq 0$, and takes place for MNPs with $l > l_{coh}$, as discussed before.

The magnetization reversal via domain nucleation and growth is the most common mechanism in ferromagnetic materials and takes place in MNP with $l > l_{SD}$. But real materials are inhomogeneous to some extent and they have a surface. The magnetization reversal can be initiated in a small nucleation volume around a surface defect. Surface defects are sources of strong local demagnetizing fields and often act as nucleation centers. Once a small nucleus of volume $V \approx \delta_w^3$ has been formed,[3] the wall may propagate outwards, growing from the nucleation volume until the reversibility is reached by annihilation of the domain walls. It can also happen that the wall propagation may be blocked by one of these defects, which is known as *pinning*. The domain wall gets trapped in the pinning center (defect) and the reversibility of the MNP does not take place (Figure 5).
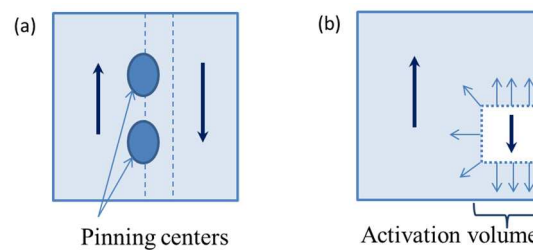

Figure 5. Pinning and nucleation. a) A scheme of a MNP with two defects on the surface (pinning centers) that impede the domain-wall motion. b) A scheme of a MNP with an activation volume that has reversed its magnetization.

5.1.2 Magnetization mechanisms on cubic NPs

The orientation of the magnetization inside a cubic shaped magnetic nanoparticle is determined as in the general case by the minimization of its total magnetic free energy stored inside. As mentioned before, the most significant contributions to the total energy of the ferromagnetic materials are the self-demagnetizing energy, the exchange energy, the magnetocrystalline anisotropy energy and the external field energy and there are many possible strategies for magnetic particles to reduce self-energy. If the

---

[3] $\delta_w = \sqrt{(A/K_u)}$ where A is the exchange constant and K_u is the uniaxial constant anisotropy.

MNP parameters and the shape of the MNP are given, then the minimum energy configuration only depends on the size of the particle.[8] Micromagnetism simulations allow studying the state of magnetization inside magnetic nanoparticles and the study of the size dependence of the magnetic ground state in cubic MNPs became a standard problem (µMAG Standard Problem No.3) started up by the µMAG group at NIST in order to obtain reliable tests of numerical algorithms reported by independent groups.[9] In 2002, R. Hertel and H. Kromüller presented a deep study on the calculations on the single domain limit of a ferromagnetic cube, providing a comparison with other groups.[8] Important definitions as flower state, twisted flower state and vortex state were described (Figure 6).
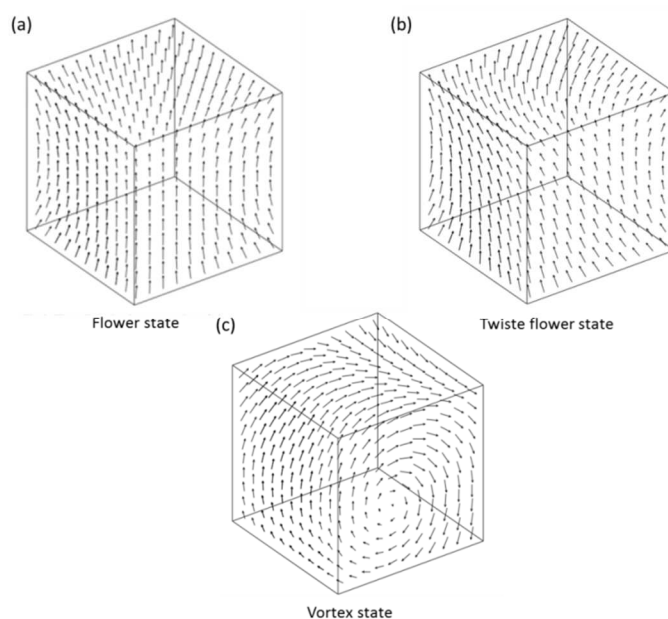

Figure 6. (a) Three-dimensional representation of the flower state in a cubic-shaped magnetic nanoparticle. The magnetization is mainly homogeneous and oriented parallel to the easy axis. (b) Three-dimensional representation of the magnetic structure for the twisted flower state in a cubic-shaped magnetic nanoparticle. (c) Three-dimensional representation for a vortex state in a cubic-shaped magnetic nanoparticle. This vortex is represented twisted from the vortex axis, which is perpendicular to the easy axis. Figures extracted from reference [8]

But much before, in 1998, W. Rave et al. had already provided a description of the magnetic states of small cubic particles with uniaxial anisotropy.[10] Although the dynamics of the magnetization reversal is not studied in these two reports as they only model the zero field states, they serve as a guide to follow the more energetically favored magnetic states of cubic MNPs with increasing the particle size (Figure 7). There are other groups that have reported on the micromagnetic modeling of the dynamics of cubic pseudo-single domain particles of magnetite which is very interesting in the fields of paleoclimatic measurements and geophysics that also agrees with the previous mentioned studies and serves us to support our experimental results.[11]
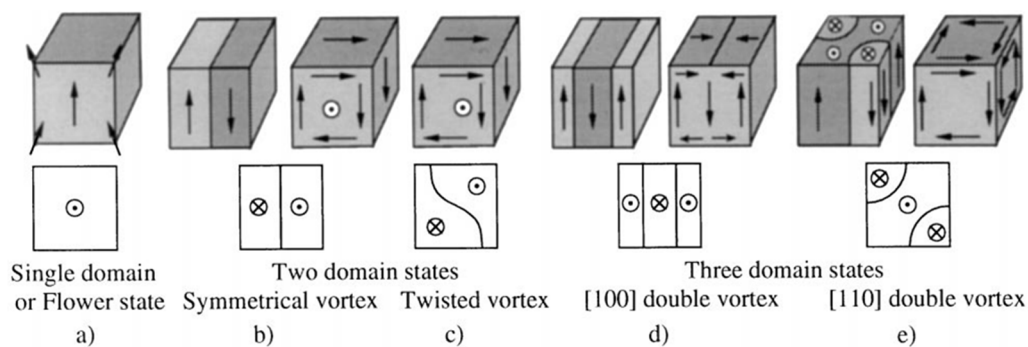

Figure 7. The energetically favored one, two and three-domain states: (a) flower state, (b, c) two-domain states for high and low anisotropy, (d, e) three-domain states for high and low anisotropy. The sketches in the second row always show the central slice in the z-direction indicating the walls and domains. Figure taken from reference [10].

More recently, in 2010, P. Krone et al. presented micromagnetic simulations of the magnetization reversal mechanism of individual cubic nanomagnets studying them as bits for the application of bit patterned media.[12]

From all these theoretical studies for cubic MNPs it can be summarized the different possible magnetic states of the KNiCr PBA-NPs studied in practise by LT-MFM in this thesis (Figure 8).
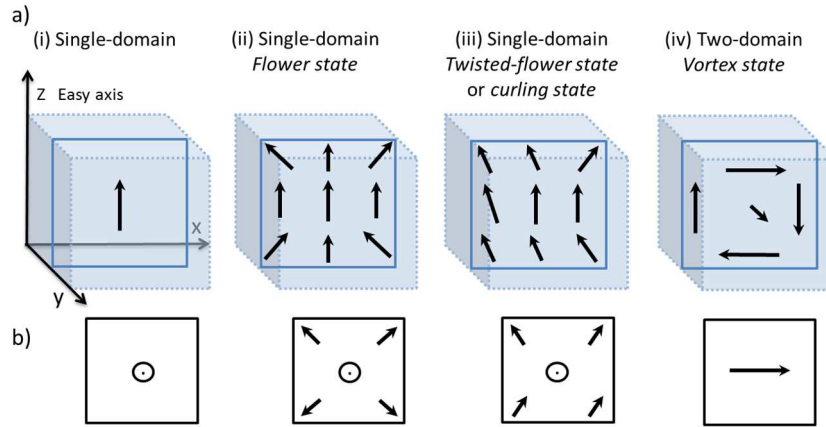
Figure 8. a) Sketches of the more energetically favored states of cubic nanoparticles with uniaxial anisotropy with easy axis in the z direction. (b) Top view of the XY plane representation of each case. From ref [14].

For the smallest MNPs magnetized along the easy axis, uniformly magnetized state prevails, conforming the single domain or flower state (Figure 8a, cases i and ii) that carries only little anisotropy energy. With increasing nanoparticle size, inhomogeneous states become energetically favorable and twisted flower or curling state appears (Figure 8a, case iii) near the limit of the single domain. For larger sizes, two magnetic domains become more energetically favored and the so-called vortex state appears (Figure 8a, case iv).

Regarding the dynamics, it is important to introduce the switching field that is defined as the applied field at which the magnetization reverses. The switching takes place via coherent rotation for the single domain NPs and will be non-coherent for the rest of the cases presented in Figure 8. The twisted flower state aligned with the field applied (aligned with the MNP easy axis) reverses its magnetization to a similar antiparallel structure via curling. When the two domain state is energetically favored, the magnetization reversal mechanism will take place by vortex formation and annihilation. As the MNPs can have real-structure defects at the core or at the surface, it can also induce inhomogeneous reversal mechanisms as localized nucleation or

domain wall pinning.[13] The localized nucleation is produced when the magnetization reversal starts from a very small activation volume at a certain value of the field (switching field) which has reversed its magnetization while the rest of the particle remains at the initial state. This small reversed area propagates when the external field is increased until the whole NP is reversed completely. On the other hand, the domain-wall pinning is produced by strong structure defects or *pinning centers* at the surface of the MNP that blocks the domain-wall motion while increasing the external applied field.

5.1.3 Experimental measurements of magnetization reversal of MNPs

The first clear demonstration of uniform (or coherent) magnetic reversal mode of a single NP was found by the group of Prof. Wernsdorfer in Cobalt NPs[14] and BaFeO NPs[15] measured with a micro-SQUID. The same group also reported on the experimental evidence of magnetization reversal by curling on isolated nanoscale wires with a diameter smaller than 100 nm[16] and some years later, they were capable to measure the switching of magnetization of a Cobalt cluster of 3 nm[17] and on a single 20 nm Cobalt NP,[18] by nor linear resonance. Although the micro-SQUID is a powerful tool that can resolve the angular dependence of the switching field or its dependence with the temperature down to the miliKelvin range, it does not allow the imaging of the magnetization reversal process within the nanoparticle. Other techniques as Mössbauer spectroscopy,[19] also allows the characterization of the magnetization reversal at the nanoscale but again, it is an indirect measurement not capable to image the process. The magnetization reversal mechanism of individual and isolated nanoscale systems have been mainly described and modeled by micromagnetic simulations.[20]

There are several experimental techniques for the imaging of the magnetization of nanometric objects already mentioned in 5.1. However, most of them require highly

complex sample and/or tip preparation. The improvement of the resolution of these magnetic techniques has been challenging and goes on nowadays. The results of all of them have confirmed fundamental concepts in nanoscience such as the single-domain state, superparamagnetism, magnetic vortices or the spin polarized tunneling among others, but still the imaging of the magnetization reversal mechanisms inside a single, small (< 50 nm) and isolated MNP has not been performed.

Among these magnetic imaging techniques, the more extended and well-known tool for the magnetic mapping at the nanoscale is the magnetic force microscope (MFM) that can record the magnetic stray field generated by a magnetic sample without any specific sample preparation. [21] During the last years, major efforts have been focused on the magnetization reversal studies by MFM on lithographed structures of permalloy [22], Niquel [23] or Cobalt, [12b,24] but not in synthesized MNPs. Some examples of the detection of MNPs by MFM in ambient conditions can be found in the literature. For example the magnetic imaging of agglomerates of iron oxide superparamagnetic nanoparticles[25] or NPs clusters embedded in a silica matrix have been successfully performed,[26] although no MFM signal (in ambient conditions) of an individual iron oxide NP was observed for particles smaller than 15 nm.[27] The detection of a 5 nm ferritin molecule was possible working in liquids[28] and the imaging and magnetic moment estimation of single domain MNPs within a magnetotactic bacterium has been also achieved.[29] Only a few works present the switch of the magnetization of small, single and isolated nanoparticles: C.E. Diebel et al. showed the switch of the magnetization induced by an in-plane variable external field on a single domain 50 nm crystal of magnetite[30] and T.M. Nocera et al. detected FeO superparamagnetic NPs of 20 nm in different remanent states by applying an out-of-plane external field produced by a permanent magnet.[31] However, none of these works show the dynamic processes of the magnetization reversal of small, single and isolated nanoparticles.

From all these works it can be deduced that the MFM is a suitable technique to detect MNPs, although the lateral resolution of the MFM in ambient conditions is not enough

to resolve the magnetic configuration within small NPs. In ambient conditions, the MFM resolution depends on the tip-sample separation and the effective probe size. While the tip-sample distance can be easily set in every measurement, the size of the magnetic tip is a technical problem more difficult to resolve. Trying to overcome this limit, many groups have reported on the use of carbon nanotubes as a MFM probe: Magnetically coated carbon nanotubes[32], iron-filled carbon nanotubes which can be used for the quantitative MFM measurements independently of the sample stray field geometry,[33] or magnetic coated CNT by sputtering a magnetic layer onto it and then mounted on a Si cantilever. In these cases, the diameter of the resulting magnetic tip is about 40 nm and the lateral resolution was found to be 10–20 nm.[34] Also, magnetic Ni nanowires of 40 nm have been used for the lateral improvement of the MFM imaging.[35] Other nano-objects as spherical magnetic particles,[36] or cubic Co clusters,[37] obtained tips from 50 nm to 240 nm. High aspect ratio tips fabricated by ion focus beam can reach a resolution of 10 nm.[38] More recently, Cambel et al. have fabricated low momentum and low-coercive switching magnetization-magnetic force microscopy (SM-MFM) probes with triangular magnetic element in single-domain magnetic state suitable for imaging flat surfaces operating in SM-MFM.[39] Resolution of sub-10 nm range was also obtained by controlling the multidomain state of a nanomagnetic probe.[40] But note that all these tips have been tested using a magnetic recording tape, taking the magnetic domains as patterns to calculate the best resolution. Then, more complex magnetic structures or nanoparticles have not been inspected with this kind of tips. Just few groups have reported on the use of special tips to resolve MNPs. For example Wiesendanger et al. obtained single-domain tips with a lateral resolution of 10 nm by only coating the side face perpendicular to the surface and they were capable to image isolated circular out-of-plane polarized magnetic domains.[41] Also, ferritin molecules with a magnetic core have been used to functionalize an AFM tip to reach a resolution up to 10 nm. However, the functionalization implies a complex process with the use of DNA sequences for the ferritin immobilization on a substrate.[42]

Developments of functionalized tips thus improve the MFM resolution although it implies dedicated tip preparation.

Further improvements of the lateral resolution of the MFM may lead to measurements under typical low-noise conditions involving high vacuum (or low pressure) and low temperatures that would enhance the sensitivity and permit the detection of very small gradient forces, even working with commercial tips.

Although it is known that the MFM tip can interfere in the magnetic states of the sample, choosing carefully the measurements conditions this effect can be minimized and the resolution can be enhanced. [43] This is possible thanks to the use of a low temperature MFM working in low pressure and relatively high tip-sample distances, which has been successfully used to measure magnetic vortices in superconducting layers, for example.[44] These features make LT-MFM a very promising technique for the characterization of MNPs.

So, we can conclude that the current state of the art shows that experimentally, it is possible to detect small magnetic nanoparticles and their magnetic moment directions, describe their reversibility and even distinguish among the different magnetic reversal mechanisms through many techniques. However, the reality is that the imaging of the process of the magnetization reversal within a single small MNP (< 50 nm) predicted more than 60 years ago, has not been performed so far.

In this chapter, it will be presented high resolution magnetic imaging by LT-MFM of the magnetic switching driven by an out-of-plane external field of a collection of small molecular-based PBA-NPs ($\leq$ 25 nm) exhibiting different magnetization reversal mechanisms. The chosen NPs are KNiCr NPs with a small dispersion of sizes, which present a very rich variety of magnetic states coexisting within the same sample: from single domain and curling, to multi domain behaviors. Temperature dependence measurements will be presented as well as magnetization reversal imaging in individual and isolated NPs. Among the different possible reversibility processes, it

will be shown the image sequence of the formation and evolution of the curling state in a 19 nm NP and the image sequence of the creation and annihilation of a vortex in a 25 nm NP with the change of the polarization of its core. Finally, the in-situ functionalization of the MFM tip has allowed us to detect the magnetization direction of the individual and isolated PBA-NPs.

5.2. RESULTS AND DISCUSSION

5.2.1 Magnetic Characterization of the KNiCr NPs in a Polymeric Matrix

KNiCr NPs present a magnetic moment intermediate between that of the largest molecules and of the smallest oxide or metallic particles because of the low metal density due to their coordination nature. Typical values of S are:[45]

Single-molecule magnet (Mn$_{12}$ acetate)	S = 10
Cyanide-bridged Nanoparticles (2 nm $\leq$ NP size $\leq$ 5 nm)	100 < S < 1000
Metallic particles (NP size $\geq$ 3 nm)	S $\geq$ 1000

Table 1. Values of S for different materials of similar size.

Taking into consideration the ratio Ni:Cr 1:0.74 per unit formula obtained from the elemental analysis, the size of the cubic NPs, the spin ground states $S_{Ni(II)}$=1, $S_{Cr(III)}$=1.5, and assuming $g_{Cr(III)}$=1.9 and g_{Ni}=2.2 g values for Ni(II) and Cr(III) cations, the maximum magnetic moment of NPs between 20 to 25 nm side will lie in the $1.4 \cdot 10^{-18}$-$2.7 \cdot 10^{-18}$ A·m^2 range by spin-only approximation.

AC susceptibility measurements were performed in a zero applied dc field at different frequencies. A frequency dependence of the in-phase χ' and of the out-of-phase χ'' magnetic susceptibilities was observed which shows the characteristic behavior of MNPs. Even at the highest dilution ratios in PVP polymer, two families of broad peaks were observed. From the ZFC/FC dc measurements an estimation about the Curie temperature can be extracted, Tc ~ 40 K, which cannot be considered with high precision due to the broadness of the ZFC maximum. Curie temperatures between 60

and 90 K have been reported in bulk samples for different derivatives of $A_xNi[Cr(CN)_6]_y$ (Figure 9).

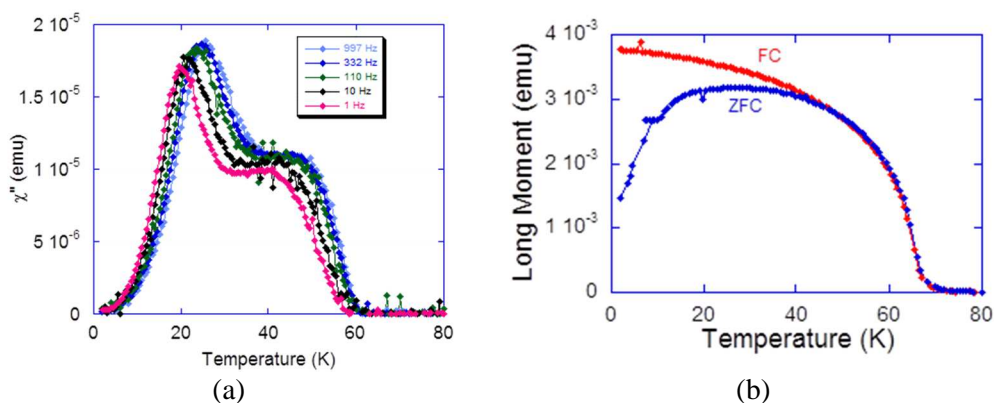(a)   (b)

Figure 9. (a) SQUID measurements of thermal variation of the out of phase ac susceptibility for KNiCr NPs in a PVP matrix at different frequencies; (b) SQUID zero field cool-field cool (ZFC-FC) measurements of KNiCr NPs diluted in a PVP matrix.

The magnetization hysteresis loops performed between ±5 T at 5 K showed values of coercive field of ~135 Oe. This value is more sensitive to the sample than to the amount of PVP inside the matrix, and changes a bit from sample to sample (Figure 10).
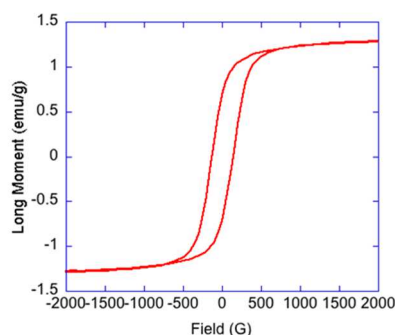

Figure 10. Magnetization hysteresis measurements of KNiCr MNPs diluted in a polymer matrix (300 eq), at 5K.

This bulk magnetic characterization of diluted KNiCr NPs points out the presence of different magnetic contributions. First, interparticles interactions cannot be avoided even at high dilutions. There are two families of peaks observed in *ac* measurements centered at 20 K and 40 K approximately (figure 1a), and as DLS and SEM rule out the presence of two populations within the samples (DLS and SEM measurements shown in chapter 3, section 3.2.1), the two peaks can be attributed to presence of nearly-isolated particles and closer interacting particles within the samples, even highly diluted samples.

The precise single domain critical size for KNiCr NPs is not known, however, it has been recently published a detailed study about the size dependent magnetic behavior of the CsNiCr NPs (NPs size ~ 25 nm), that in spite of some structural differences, is the closest system to KNiCr NPs.[46] In this paper it is shown that 12 nm size is the frontier between single and multidomain behavior and from 12 to16 nm, NPs with single domain or curling may be encountered.

A brief approximation about the reversal magnetization nature can be interpreted applying the Néel–Brown thermal activated model where an estimation of the attempt time τ_0 value and the Mydosh parameter Φ can be performed. This study can help us to evaluate if there are single- or multidomain isolated NPs or interacting with each other.[47] The τ_0 and Φ values, that can be calculated from the frequency dependence of the out of phase susceptibility maxima with temperature (family of peaks at lower temperature), indicate a non-uniform magnetization due to curling effects or to a multidomain situation combined with the incomplete cancellation of the dipolar interactions.

The values of τ_0 and Φ for different KNiCr NPs dilutions are summarized in the next table:

Table 2. τ_0 and Φ estimated values for two different NPs dilutions.

	3000 eq	6000 eq
τ_0	$6.5 \cdot 10^{-17}$s	$1.2 \cdot 10^{-15}$s
Φ	0.065	0.071

Taking into consideration that τ_0 expected value for single domain NPs lies in the 10^{-9}-10^{-13} s range and Φ is supposed to be higher than 0.1, one can assume that our samples are not pure single domain and present a non-uniform magnetization. Comparing to the previous mentioned study on CsNiCr NPs, the KNiCr NPs show τ_0 and Φ values similar to the corresponding values of CsNiCr NPs of similar sizes.[4] We could expect then, that the single domain critical size for the KNiCr NPs would lie around a similar value obtained for the CsNiCr NPs (12 nm), and curling and multidomain behaviors may coexist within the sample.

Obviously, in a bulk magnetometric measurement this variety of behaviors cannot be distinguished. Hence, it is mandatory to perform local measurements if one wants to detect the magnetic response of each NP individually.

5.2.2 Randomly dispersed KNiCr NPs on a silicon surface

KNiCr NPs were randomly dispersed on the surface by drop casting using a method based on the formation of a protonated amminopropyl triethoxysilane (APTES) self-assembled monolayer (SAM) on a passivized silicon surface, before putting it in contact briefly with the aqueous NPs solution (described in detail in section 5.4). As discussed in chapter 3, the modification of the native silicon oxide by a protonated

---

[4] τ_0 and Φ values for our maximum dilution sampleof KNiCr NPs, mach the values for 18 nm CsNiCr NPs, then we could expect single domain critical sizes a bit larger than 12 nm for KNiCr NPs. However, we must be careful when comparing close but different PBA derivatives.

amino-SAM was proved to be very efficient for the stabilization of anionic Prussian blue analogue NPs.

To perform local LT-MFM measurements of isolated NPs it is necessary to reach an appropriate coverage over the substrate: not fully covered and enough dispersed. For that purpose, the NPs solution concentration and the period of time for the substrate to be in contact with the NPs solution can be decreased. As can be seen in Figure 11, the topography image of dispersed KNiCr NPs shows isolated particles as well as small aggregates that probably were formed in the solution or during the deposition process.
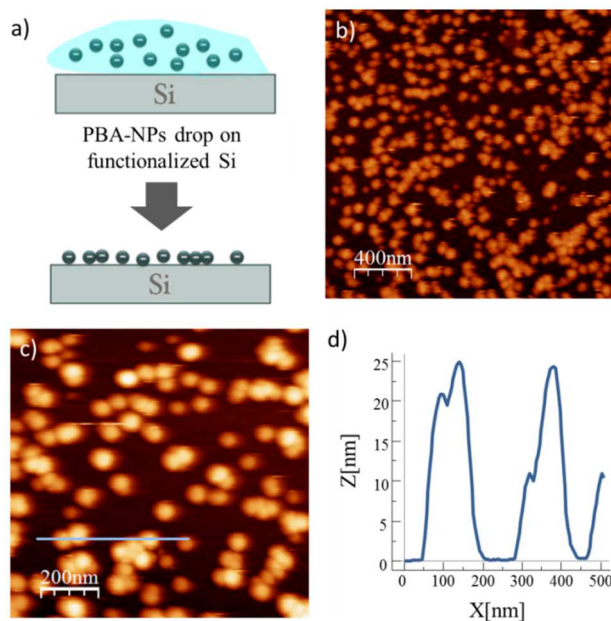

Figure 11. (a) Schematic representation of drop casting for the deposition of randomly dispersed NPs on a functionalized silicon surface. (b) Topography image (2µm x 2µm) of randomly dispersed KNiCr-NPs (c) Topography image (1µm x 1µm) and the corresponding height profile (d).

5.2.3 LT- measurements of randomly dispersed KNiCr NPs

The magnetic characterization of the KNiCr NPs was done with a LT-MFM (Attocube) working at 4.2 K in a He gas environment at a very low pressure (30 mbar at RT) with a commercial magnetic-coated cantilever (MFMR Nanosensors, ≈75 KHz

resonant frequency and ≈3 N/m force constant). In these conditions, the quality factor of the cantilever dramatically increases up to 5000, which enhances the sensitivity of the technique allowing the detection of very small gradient forces.[43] The instrument senses the dipolar interaction between the tip and the sample and this magnetic response can be recorded either as variations in amplitude, phase, or frequency of the cantilever oscillation. Because of magnetostatic tip-sample interactions, the free resonant frequency of the cantilever f_0 is shifted by Δf, where $\Delta f = f - f_0$. In our case, the frequency shift (Δf) is tracked by a Phase Locked Loop (PLL), which feedback parameters have to be set for every measurement and are extremely sensitive to the environment conditions. A negative frequency shift indicates an attractive tip-sample interaction ($\Delta f < 0$, dark contrast) while a positive frequency shift indicates a repulsive tip-sample interaction ($\Delta f > 0$, bright contrast), as introduced in chapter 4. Whenever an external magnetic field $\mathbf{B_{ext}}$ is applied, it is important to consider that the total magnetic field $\mathbf{B}$ that the scanned sample feels is the resultant of the magnetic field produced by the tip plus the external field applied, $\mathbf{B} = \mathbf{B_{tip}} \pm \mathbf{B_{ext}}$. So both fields are added when they point in the same orientation and partially/totally compensated when they are opposite. For the same magnitude of external fields in opposite orientations, the stray field of the tip will cause dark contrast always to be more intense than bright one.

Previously any magnetic characterization, the sample was scanned in dynamic mode to acquire the topography and compensate the tilt. Due to the relatively large tip-radius of the magnetic-coated tip ($r \leq 50$ nm) it is not possible to resolve the cubic shape of the PBA-NPs. Although the height of isolated nanoparticles can be accurately characterized with the tip of the MFM, the apparent lateral dimensions of the NPs whose size are comparable or even smaller than the tip radius curvature, are substantially increased by the well-known tip-sample convolution effect.[48] From now on we will consider the real size of the cubic KNiCr NPs, the measurement of the

height with an error of ±11 % coming from considering the maximum value of the aspect ratio, which is aprox. 1.1.

To record the MFM data, we worked in *constant height mode* where the sample is retracted at a constant distance (Z_{lift}) from the tip. At this distance, the tip scans a plane over the sample obtaining a magnetic map of the scanned area given by the Δf caused by the tip-sample magnetostatic interactions. *Constant height mode* was chosen because it has the best signal to noise ratio (no feedback noise) and the potential of increased scan speeds. All the images were taken from down to top and forward/backward scans were performed and recorded in every line of the scan.

At such distances (Z_{lift}), long-range forces can be detected by the tip; not only the magnetic interactions but also the electrostatic ones that could be mixed with the magnetic signal and even hide it. In our case, an external field $\mathbf{B_{ext}}$ is applied perpendicular (out-of-plane, see Figure 12) to the sample, and the magnetic response is recorded by varying the intensity and orientation of $\mathbf{B_{ext}}$. ($\mathbf{B_{ext}} = B_{ext}\ \mathbf{u_z}$) so the magnetic contribution can be clearly distinguished.
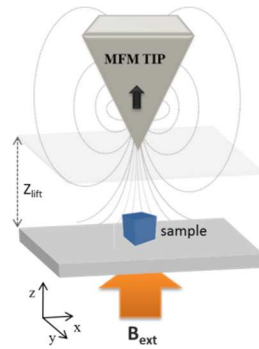

Figure 12. Scheme of relative position of sample and the MFM tip. The external applied field is applied perpendicular to the sample.

5.2.4 Calibration of the magnetic tip at low temperature

MFM images depend on the magnetic interaction between the magnetic-coated tip, the magnetic sample and the external magnetic field applied. The magnetization reversal of the sample may be detected with the MFM via changes in the image contrast resulting from the reorientation of the direction of magnetization of the sample with respect to the magnetization of the tip. However, the interpretation of the image contrast may be ambiguous, since the applied magnetic field may also affect the magnetization direction of the MFM tip to some unknown extent. Thus, in order to differentiate the contributions arising from the reorientation of magnetization of both, tip and sample (the KNiCr NPs in this case), detailed knowledge of the magnetization reversal of the tip is needed. Moreover, all the measurements (NPs characterization as well as the calibration of the MFM tip) need to be done at the same value of the temperature to ensure a correct interpretation of MFM images.

A commercial MFMR-Nanosensor tip with a CrCo coating of 40 nm was used, but all the technical data provided by the company were at room temperature (coercivity of app. 300 Oe, remanence magnetization of app. 300 emu/cm^3) (Figure 13).

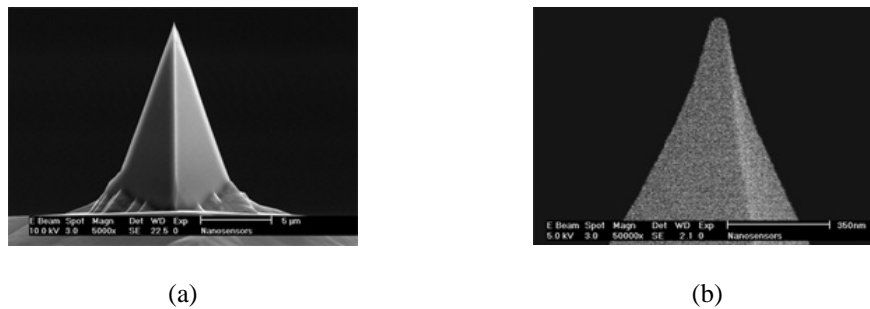<div align="center">(a)   (b)</div>

Figure 13. Technical data provided by manufacturer. (a) SEM image of a PPP-MFMR tip (side view). (b) SEM image of a PPP-MFMR tip (close-up).

As far as our measurements are performed at low temperature and it is well known that the magnetic coercivity increases when temperature decreases, a calibration at low temperature needs to be performed. The magnetic measurements were performed at 4.5 K with external applied field in-plane and out-of-plane the sample, following the procedure proposed by M. Jaafar et al[49] to calibrate the coercive field of the commercial MFM probes. Using a commercial hard disk piece as reference sample, the changes of the magnetic images contrast on the bits were measured when sweeping the B_{ext}. Due to the broad coercive field of the hard disk, the changes in the magnetic contrast give us information about the magnetization of the MFM tip since in this case, the magnetization of the tip is reoriented with the change of B_{ext} while the magnetization of the hard disk remains unmodified. From the analysis of the evolution of the MFM contrast versus magnetic field, we deduced the out and in-plane coercivity of the MFM probes.

The value obtained for the out-of-plane measurements at 4.5 K was Hc $\approx \pm$ 750 Oe. (Figure 14)
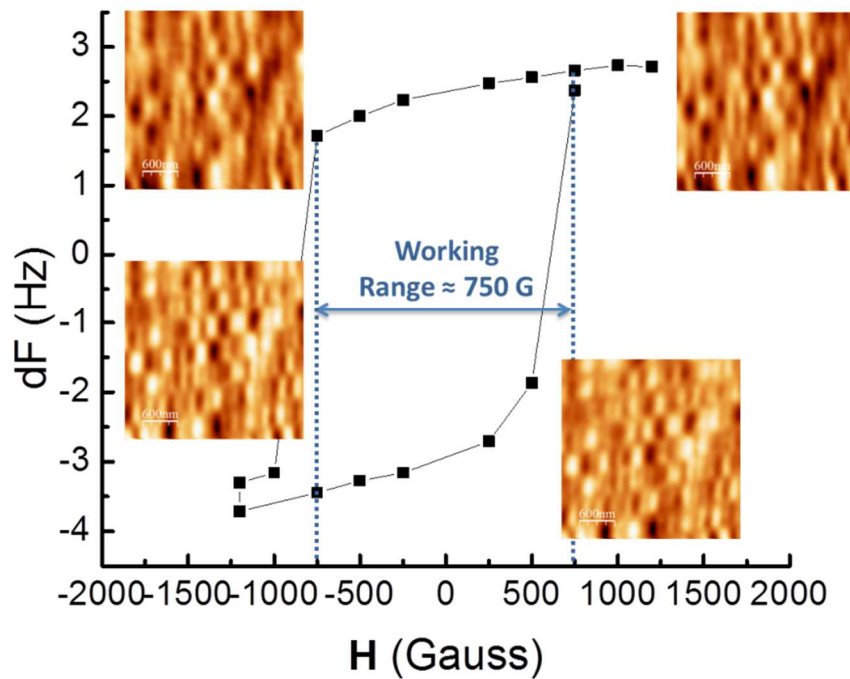
Figure 14. Magnetic calibration of MFMR Nanosensors tip with an out-of-plane applied field. Four MFM images are shown at +1000 G, -500 G, -1000 G and +500 G.

For in-plane applied fields, the magnetic contrast corresponds to the stray fields coming from magnetic walls instead of from domains.[49] No significant change in the contrast was observed while sweeping the external field, so it seems that the tip cannot be orientated by applying parallel fields.

Magnetic coercive field of Nanosensors-MFMR tips increases from 300 Oe at room temperature to 750 Oe at low temperature (4 K) which, in principle, makes them suitable for measuring the magnetic reversibility of KNiCr NPs, as will be later discussed.

5.2.5 Temperature dependence measurements in isolated KNiCr NPs

Apart from the tip used, there are several parameters that have to be optimized in order to be able to resolve the magnetic interactions from individual small particles, as for example the working temperature. The minimum detectable force gradient is temperature dependent in the form:

$$\left[\frac{df}{dz}\right]_{min} = \frac{1}{A}\sqrt{\frac{4\,k\,k_b\,BW\,T}{\omega_0\,Q}}$$ (Eq. 5.4)

where T is the working temperature, BW is the measurement bandwidth, k is the force constant of the cantilever, k_b is the Boltzman constant, ω_0 is the natural resonance frequency of the cantilever ($\omega_0 = 2\pi\,f_0$), Q is the quality factor, and A is the amplitude of oscillation of the cantilever. Taking A~ 90 nm, Q ~ 5000, f_0 ~ 7500 Hz, k ~ 2.8 N/m as typical values for our instrument and type of cantilever, the minimum detectable force measurable at 4.2 K is theoretically ~ 0.18 nN/√Hz. This would lead to a minimum detectable frequency shift of 0.025 mHz/√Hz, if only considering the thermal noise. The reduced thermal noise and the low thermal drift confer high stability of the tip–sample gap and a better signal-to-noise ratio (noise levels are discussed in detail in Appendix I).

But the working temperature is not only chosen with the aim of the best signal to noise ratio and stability. Another important aspect related with the specific properties of the sample need also to be taken into account. For example, it is very important to know that PBA materials generally present Curie temperatures (T_C) lower than 100 K. When these materials are prepared as NPs, the T_C values decrease as the NP size does, becoming blocking temperature (T_B) when a single domain size is reached and pure superparamagnetic behavior takes place. So working below the Curie temperature is crucial in order to be able to freeze the magnetic moments of the NPs to detect them by the MFM without the need of applying strong magnetic fields.

As deduced from SQUID magnetic characterization, for KNiCr NPs the T_c is around 40 K. But this value is probably a little bit overestimated due to interparticles interactions that are not completely avoided in the polymeric matrix used for SQUID measurements. As can be observed in the hysteresis loops at different temperatures (Figure 15a), with the same value of the applied field, higher magnetization values are reached by decreasing the temperature, meaning that there are more NPs with their magnetic moments oriented parallel to the external field.

A deep study about the temperature dependence with the magnetic tip-NP interactions was performed to probe that only working below the Curie temperature the remanent magnetization of the NPs can be detected with the MFM. Routine topographic images of 1 µm x 1 µm at 4.2 K were taken to characterize the dispersed NPs just prior all magnetic measurements. To acquire the MFM images the Z_{lift} was set to 100 nm in all cases and the tip was previously magnetized in +z direction. In step (1) an external out-of-plane field of +200 Oe was applied and the magnetic interactions of the tip and the NPs show dark and white contrasts (attractive and repulsive interaction) because at this value of the B_{ext} not all the NPs are oriented with it, so both contrasts are detected by the tip. Then, the temperature was increased up to 30 K (step 2) without external field applied and again, both topography and MFM images were acquired. The magnetic image at 0 Oe still shows dark-bright contrasts, although much weaker and blurry. This points out that the field applied by the tip is high enough to maintain the magnetization of the NPs because we are working below the Curie temperature. In step (3), the temperature was set to 50 K, above the Curie temperature estimated by ZFC-FC measurements. Topography and MFM images were taken then at 0 Oe. No magnetic interaction was observed in the 50 K magnetic image because the magnetic moments of the NPs are not aligned any more even considering the magnetic field from the tip. The magnetization at this temperature would give a too weak signal and no appreciable magnetic contrast can be found at 50 K. Then, an external field of +200 Oe was applied to magnetize the sample. The MFM image does not change, and no

magnetic contrast can be detected even at this field (step 4). Then, the sample was finally field cooled at +200 Oe to 4.2 K (step 5) and again, a large tip-sample magnetic interaction was observed. In this case, the contrast is only dark due to the field cooled. Thus, the NPs were aligned by the external field and got frozen when the temperature was decreased down to 4.2 K ($T < T_c$) so the magnetic moments of the NPs and the tip were parallel (+z direction) giving rise to a tip-NP attractive interaction (dark contrast). It was also measured without external field applied (step 5) and dark contrast was measured again.

It is important to point out that due to the thermal drift, it was not possible to measure exactly in the same area when the temperature was increased but, due to the high homogeneity of the sample, we can extrapolate these results to all the KNiCr NPs in the surface. All these MFM measurements are in good agreement with the data extracted from the hysteresis measurements of NPs dispersed on a PVP polymer matrix (4500 eq), measured at different temperatures by a SQUID magnetometer (Figure 15a). In general, the magnetization decreases as the temperature increases, which explains the decrease in the intensity of the magnetic signal in the MFM images without external applied field even below the T_c. From 30 K at 0 Oe (step 3) to 4 K at 0 Oe (step 6) the intensity of the magnetic signal increases a 60 %.
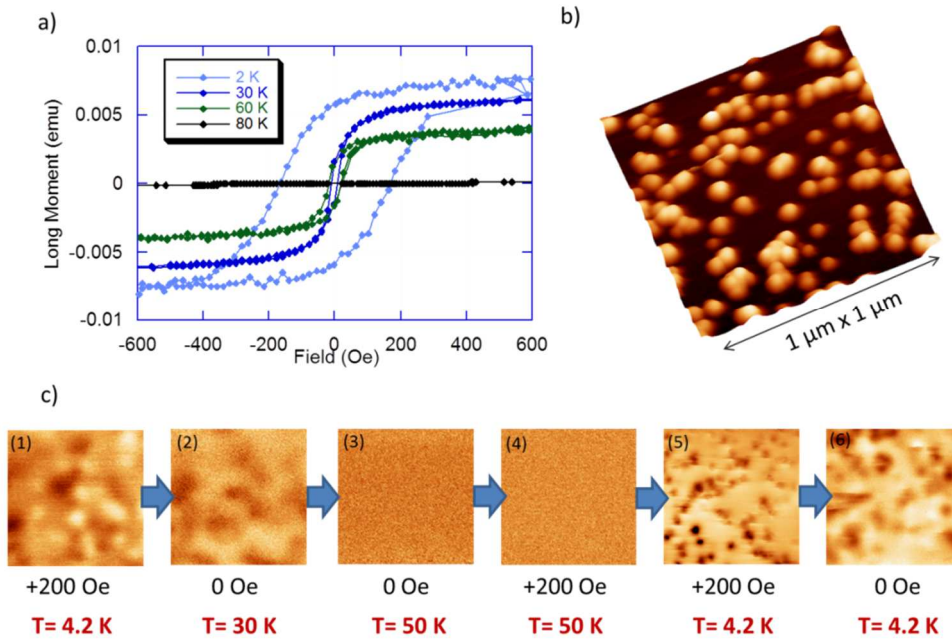
Figure 15. a) SQUID measurements of hysteresis loops at different temperatures showing how the remanent magnetization decrease while the temperature increases. (b) Topographic image of the dispersed KNiCr NPs corresponding to step (1) of the following set of MFM images. (c) A set of magnetic images of an area of 1 µm x 1 µm of randomly dispersed KNiCr NPs at different values of temperature and external applied out-of-plane field.

According to the SQUID measurements, one could think that applying high enough fields (more than +200 Oe applied for the previous measurements), it should be possible to align the magnetic moment of the nanoparticles (m_{NP}) and be able to detect them by the instrument, even above the Curie temperature at least in the range between 40 K and 80 K. The next figure corresponds to the result of MFM measurements applying a high value of out-of-plane magnetic field, 1T, at 4.2 K (Figure 16a) and 40K (Figure 16b). As can be seen in the images, at 40 K with an applied field of 1T it was possible to detect the magnetic contrast of the KNiCr NPs even at 40 K. But in this case, the intensity of the detected tip-sample interaction was 82% lower than at 4.2 K. Hence, using this order of magnitude of B_{ext}, one cannot

detect the magnetization reversal of the KNiCr NPs because the tip would have reversed its magnetization as well.
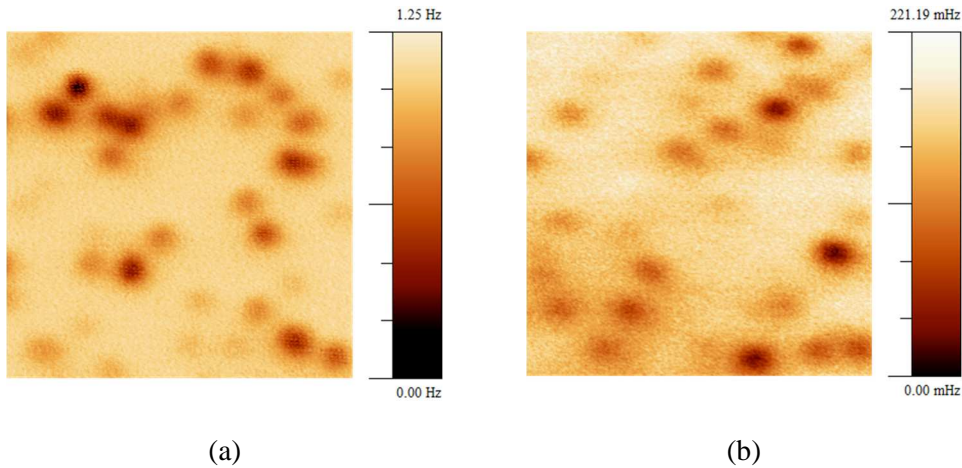

(a)   (b)

Figure 16. (a) Magnetic image of randomly dispersed KNiCr NPs taken at 1T and 4.2 K with the corresponding Z scale. b) Magnetic image of randomly dispersed KNiCr NPs taken at 1T and 40 K with the corresponding Z scale. Size of the images: 750 nm x 750 nm

5.2.6 Magnetic reversal measurements in isolated KNiCr NPs

I. Previous considerations: the B_{ext} working range

It is very important to highlight that to be able to measure the magnetic reversal of the KNiCr NPs, the condition:

$$M_s^{tip} > B_{ext} > M_s^{NP} \qquad (5)$$

has to be accomplished, being M_s^{tip} the saturation magnetization of the tip, B_{ext} the external applied field and M_s^{NP} the saturation magnetization of the KNiCr NPs. This is the real key point of this experiment. As previously mentioned, the selection of the tip is very important; otherwise, it could happen that the external applied field would change the magnetization orientation of the tip and the reversibility measured would come from the tip, not from the sample (as observed in the experiment performed with a hard disk to calibrate the tip). On the other hand, if the magnetization saturation of

the KNiCr NPs were higher than the magnetization saturation of the tip, it would be impossible to measure their reversibility. These statements leave a narrow window of possible values of the external field to measure the magnetization reversal of the KNiCr NPs. From the tip calibration measurements at 4.5 K we know that it is almost saturated at ±750 Oe then, values of B_{ext} below this limit were always employed. From the SQUID measurements of the KNiCr NPs dispersed on a polymer matrix at 2 K, we know that the NPs are almost fully saturated around ± 600 Oe. Then, applying external fields between ±750 Oe should allow us to successfully measure the magnetization reversal of the KNiCr NPs.

II. Previous considerations: real isolated NPs

As the sample is prepared by drop casting, well isolated NPs are dispersed all over the surface. However, it can be found couples of NPs or small aggregates that are not always easy to differentiate due to the small size of the KNiCr NPs compared with the size of the tip apex (~ 50 nm). To be able to study the magnetization reversibility of single and isolated KNiCr NPs one has to distinguish whether an aggregate of two closed NPs is formed, or they are real isolated MNPs. As an example, two possible cases named as **1** and **2** in Figure 17 has been chosen. The height profiles point out, that **1** is a single isolated KNiCr NP of (18.0 ± 1.8) nm height and **2** is actually formed by two different NPs. In this case, the real height of the two NPs cannot be measured with high precision because they seem to be slightly mounted but as an approximation, we can estimate two KNiCr NPs of (20.8 ± 2.1) and (22.2 ± 2.2) nm. For their magnetic characterization, the MFM tip was previously aligned in the +z direction and the magnetic moment of the NPs were fully saturated in the same direction applying an external magnetic field of + 1 T.
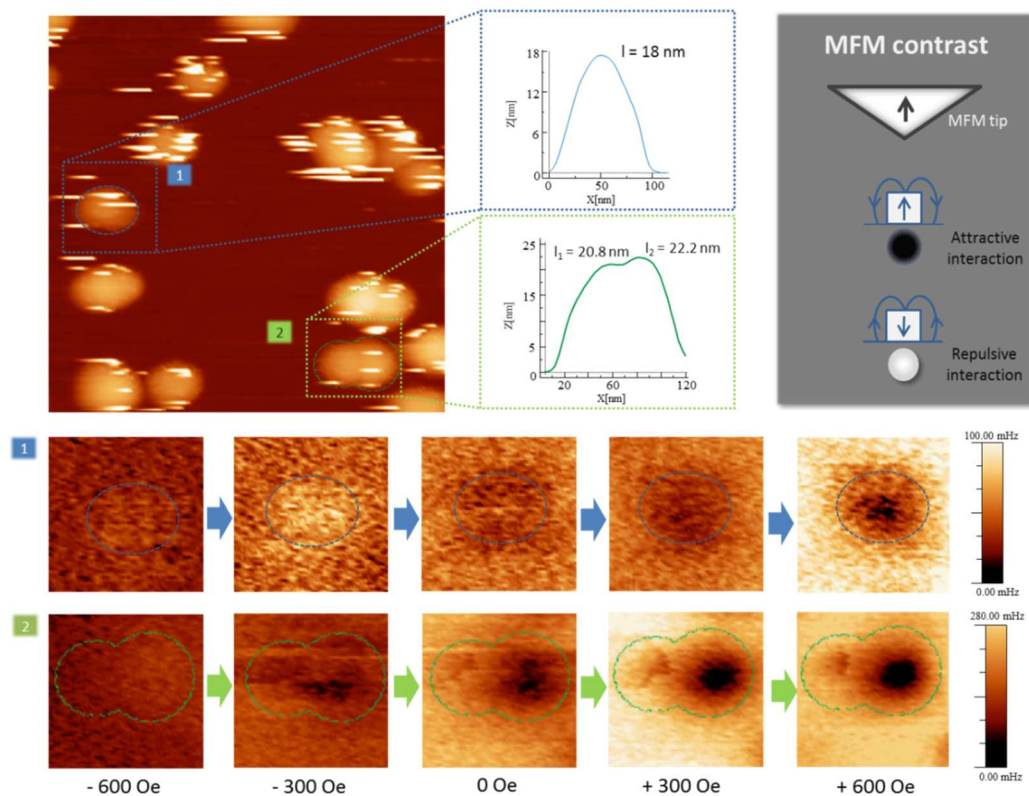
Figure 17. (a) Topography images of KNiCr NPs dispersed on modified silicon, with the height profiles of some of these particles (Image size: 500 nm x 500 nm). Blue and green dotted lines have been added as guide for the eyes. (b) Schematic representation of the magnetic contrast in MFM (c) Set of magnetic force images of 1 and 2 in (a) (Image sizes: 114 nm x 114 nm) at Bext of -600 Oe, -300 Oe, 0 Oe, +300 Oe and +600 Oe respectively.

A set of magnetic images were recorded sweeping the external magnetic field from – 600 Oe to + 600 Oe to check the reversibility of the NPs. NP **1** shows bright contrast at B_{ext} = -600 Oe reflecting magnetic repulsion between tip and NP, so the magnetization of the KNiCr NP is pointing to -z direction (opposite to the MFM tip). At B_{ext} = -300 Oe, almost the same bright contrast is observed, so the magnetization reversal of the NP has not taken place yet. Once the external field is decreased down to 0 Oe the resultant magnetic moment of the NP presents dark contrast. In this

situation the magnetic moments of tip and NP are pointing in the same direction (attractive interaction). So at a field between -300 Oe and 0 Oe, the magnetic reversal of the KNiCr NP has started because B_{ext} does not compensate the stray field of the tip (B_{tip}) anymore. The intensity of the dark contrast increases as B_{ext} reaches positives values and at B_{ext} = +600 Oe the KNiCr NP seems to be fully rotated.

The change of the magnetic moments of the two attached NPs with the external applied field presents more complexity. At B_{ext} = -600 Oe, an overall bright contrast is detected which reflects that both NPs are pointing in the same orientation (-z) and opposite to the tip (+z). However, at B_{ext} = -300 Oe, bright and dark regions appear which indicates that the magnetization reversal in the two NPs has started to take place, but not homogeneously. At 0 Oe, general dark contrast is observed but two regions can be differentiated. This is more clear at B_{ext} = +300 Oe where only a full dark contrast is reached at the biggest NP investigated (22.2 nm), which could reflect a complete reversal of its magnetic moment. The smallest NP (20.8 nm) seems to be influenced by the big one probably due to dipolar interaction, showing a less intense and inhomogeneous dark contrast. This situation that is not modified even at B_{ext} = +600 Oe. The magnetic profiles of **1** and **2** are shown in the Figure 18, where one can clearly distinguish the magnetization reversal.
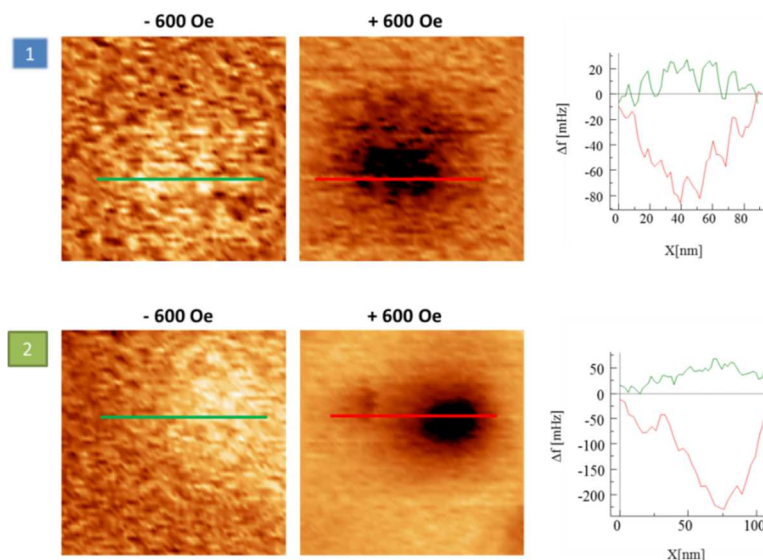
Figure 18. Case 1: Magnetization reversibility images at B$_{ext}$ $\pm$ 600 Oe and the corresponding profile. The intensity of the signal at -600 Oe is lower than at +600 Oe. Magnetic images sizes of 110 nm x 110 nm. Case 2: Magnetization reversibility images at B$_{ext}$ $\pm$ 600 Oe and the corresponding profile. Again, the intensity of the signal at -600 Oe is lower than at +600 Oe. Magnetic images sizes of 120 nm x 120 nm.

III. Previous considerations: the alignment of the magnetic moments

Finally, one more consideration is needed to understand completely the reversal mechanism of our KNiCr NPs: the alignment of the magnetic moment of the nanoparticle (m$_{NP}$) with the external field, B$_{ext}$, depends not only on the B$_{ext}$ strength but also on the angle between the easy axis of the MNP, the external field and the magnetic tip. The maximum magnetic response from the tip-NP interaction will be measured only when the m$_{NP}$ is perfectly aligned along the direction of B$_{ext}$ and the alignment of the tip (which would be the +z direction).

Deep study of the magnetization reversal mechanisms in single and isolated KNiCr NPs

Taking into account the previous considerations, a deep study of the magnetization reversal mechanism within single and isolated KNiCr NPs was performed. The inspected sample was formed by a group of dispersed NPs easily prepared by drop casting as previously mentioned, presenting a random distribution on easy magnetization directions. The KNiCr PBA-NPs are almost perfect cubic particles with an aspect ratio between 1 and 1.1 and this slight elongation induces shape anisotropy, so the easy axis of magnetization would lie on the long axis of elongation and the hard axes would be along the two directions perpendicular to the easy axis. All the magnetic measurements were performed at 4.2 K, well below their Curie temperature in such a way that the m_{NP} of all the KNiCr NPs could be frozen and driven by an external magnetic field. The measurements at 4.2 K and at very low pressure also allowed us working with the best signal to noise ratio, reaching high spatial resolution. Another important experimental aspect is the influence of the stray field of the tip on the magnetic state of the sample, which can be adjusted and minimized by the tip-sample distance.[43] In order to prevent as much as possible the effect of the stray field from the tip apex, a 100 nm tip-sample distance was set.

In general, PBA materials are soft magnetic materials[50] and so are the KNiCr NPs used in this work. From now on, we will consider our NPs as cubic particles with uniaxial anisotropy with a low relative anisotropy, treating this nanosized magnetic volume as an effective magnetic moment (m_{NP}) that is the sum of all magnetic moments of the spins of the magnetic NP.[51]

In this scenario, a field of +10000 Oe (1T, out of plane field) was applied. This way, both tip and sample were strongly magnetized and aligned in the +z direction. A topography image of 900 nm x 900 nm was first acquired that shows randomly dispersed NPs over the surface as isolated units or forming small aggregates (Figure 19a). For the study of the correlation between magnetization reversal mechanism and

the MNP size, only individual and isolated MNPs were chosen (highlighted in Figure 19b). An area of 520 nm x 520 nm was selected, where MNPs of heights from (13.2 ± 1.3) nm to (32.1 ± 3.2) nm can be distinguished.
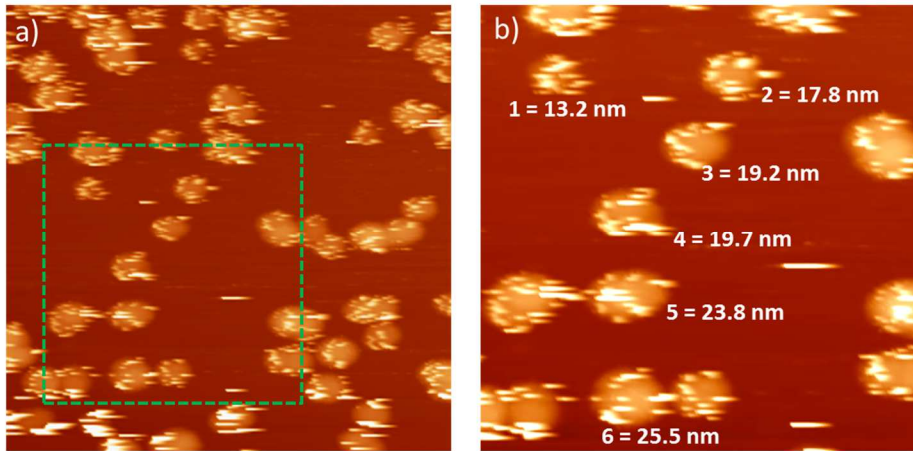

Figure 19. (a) Topography image of 900 nm x 900 nm showing the NPs deposited over the silicon surface. (b) Topography image of the selected area where only the isolated and individual NPs are labeled with number and size. Scan area: 520 nm x 520 nm.

Then the experiment was carried out by varying the out-of-plane external field (B_{ext}) from -600 Oe to +600 Oe in consecutive steps and the magnetic images were recorded at every value of the field as snapshots of the magnetization process. A general view is shown in Figure 20.
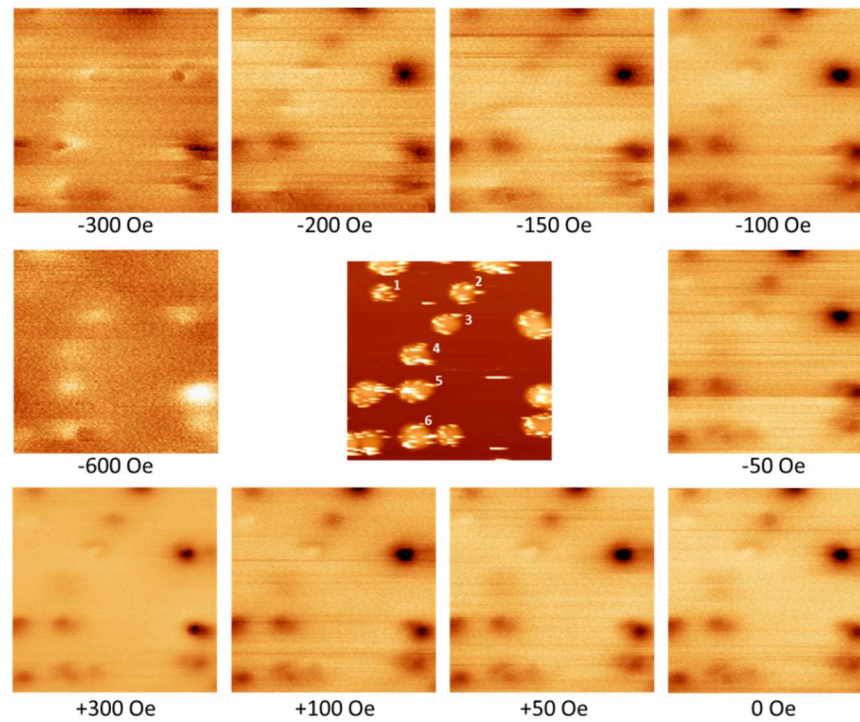
Figure 20. Set of magnetic high resolution images at different out-of-plane B_{ext}. In the center, topography image with the selected NPs labelled by numbers. Size of images: 520 nm x 520 nm.

A closer look on each individual MNP at each step of the external field can be performed and the magnetic reversal process can be tracked in more detail. Magnetic high resolution imaging was successfully achieved and we were capable to resolve the internal magnetic configuration of the nanoparticles at various steps of the magnetization reversal (Figure 21).
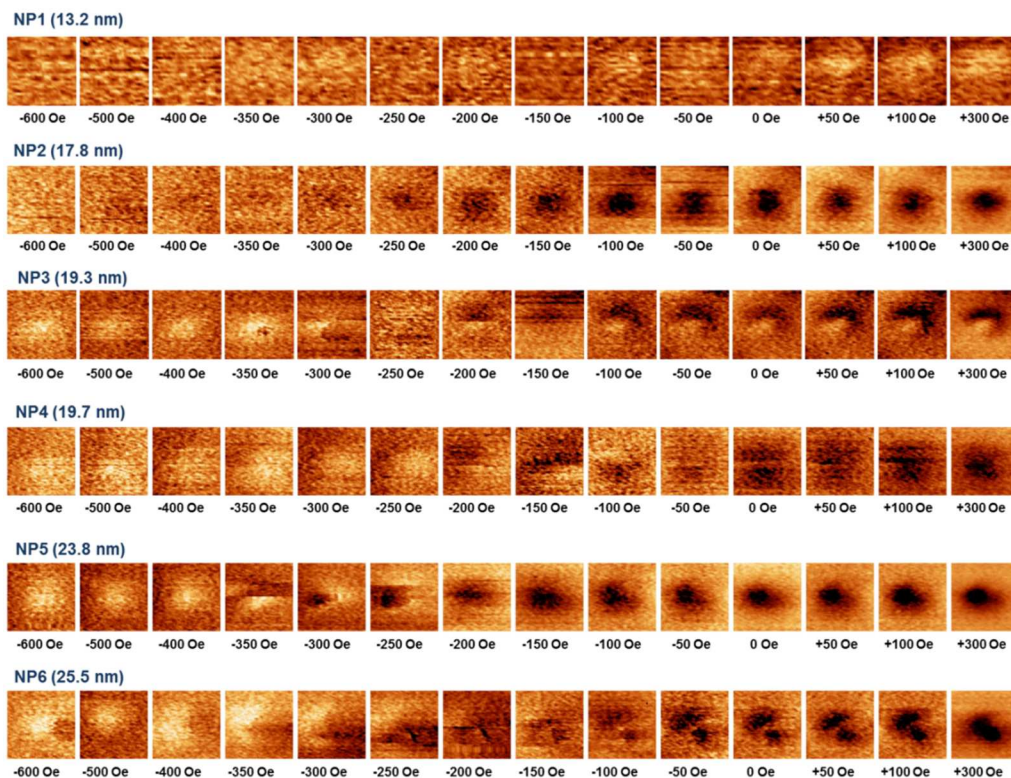
Figure 21. Sequence of high resolution magnetic images of the selected NPs at different values of the external out-of-plane applied field. Scan areas of 98 nm x 98 nm.

Different magnetic contrasts were measured in the MFM images. In the present configuration, with the tip aligned in the +z direction, a dark contrast means an attractive tip-sample interaction so the m_{NP} is oriented with the external applied field in the +z direction, while a bright contrast means a repulsive tip-sample interaction and the m_{NP} would be then pointing to the opposite orientation (-z direction). When all the spins are oriented with the external field, the magnetic contrast presents a symmetric and more confined configuration and reaches the maximum intensity. It is important to remember that the intensity of the bright signal is always lower than the intensity of the dark one at the same value of external applied field (but in opposite orientation). This can be explained by the influence of the stray field of the tip which

cannot be completely avoided. When B_{ext} is applied in the same orientation than the magnetization of the tip, both fields are added giving rise to a total field higher than B_{ext}, however when B_{ext} points to the opposite orientation, there will be a decrease in the resulting field acting over the KNiCr NPs.

The low temperature MFM images of deposited KNiCr NPs presented in this work show high resolution imaging of real examples of each one of the magnetization reversal mechanisms described in the introduction: coherent rotation, curling, pinning, localized nucleation and domain wall, domain-wall motion, and vortex formation. Following, a deep discussion of each case will be presented.
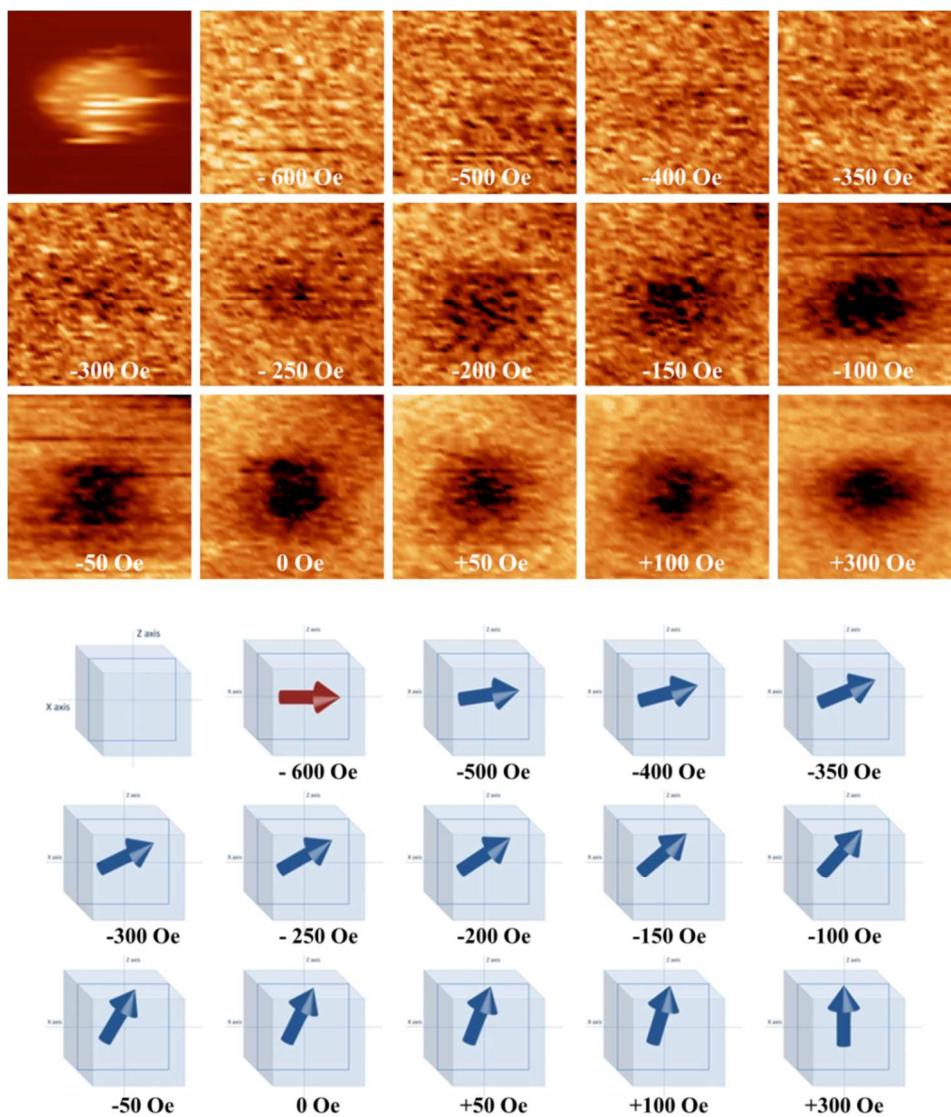
NP2

Figure 22. Nanoparticle 2, h = (17.8 ± 1.8) nm.Top: Set of images of 98 nm x 98 nm. The first image corresponds to the topography and the rest corresponds to magnetic images at consecutive values of B_{ext} at 4.2 K. Down: Schematic representation of the magnetization reversal of the MNP where the arrow simbolize the magnetic moment of the nanoparticle.

NP 2: Size (17.8 ± 1.8) nm. The magnetic reversal process starts at -600 Oe, where no magnetic contrast could be recorded (Figure 22). As discussed before, the compensation of B_{ext} with the stray field of the tip (pointing in opposite orientation, at +z direction) originates a lower negative resultant field over the NP. The resultant applied field could be, in this case, not enough to provoke the complete magnetization reversal of the NP and this is why at -600 Oe, the magnetic image does not show bright contrast. In this situation, the absence of magnetic contrast could be explained if the m_{NP} would be canted from the +z axis caused by the effect of negative B_{ext} ,not enough to reverse it but enough to have a tilted out-of-plane component too small to be detected by the magnetic tip. Then, the external field was gradually changed and at -350 Oe, a smoothed dark contrast started to appear. This means that the out-of-plane component of the m_{NP} is rotating following the external field in the YZ plane. The out-of-plane component of the m_{NP} (shown as a dark spot) was gradually aligned with the external field while it was swept from -350 Oe to +100 Oe without jumps or discontinuities. Finally, at +300 Oe, a more intense and confined dark area is shown in the magnetic image, so the m_{NP} was fully rotated and aligned with the external field.

It is known that the coherent rotation of the spins is accompanied by a substantial increase of the switching field compared to the incoherent switching mechanism.[52] On the other hand, Stoner-Wohlfarth theory predicts that the energy to rotate a single domain NP would be higher if the external applied field is aligned with the easy axis of the NP. These two facts would explain why the magnetization reversal of this MNP was not completed. This homogeneous magnetization reversibility observed by MFM points out that this is an example of **single domain NP** with a Z-easy axis and the reversal mechanism would be via **coherent rotation**. This case could be also a flower state that is mostly a homogeneous state and only at the vicinity of the corners or edges the magnetization spreads out due to the inhomogeneity of the stray field.8
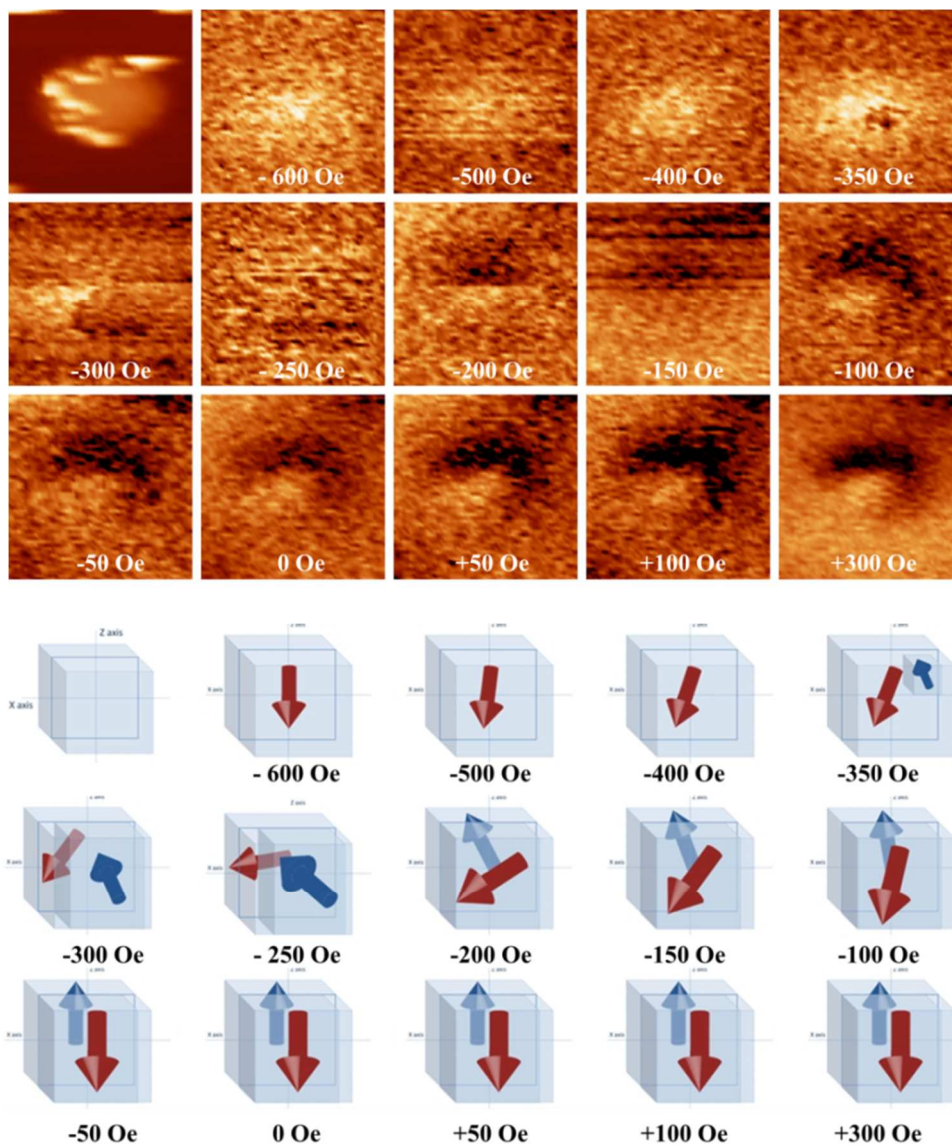
NP3

Figure 23. Nanoparticle 3, h = (19.3 ± 1.9) nm .Top: Set of images of 98 nm x 98 nm. The first image corresponds to the topography and the rest corresponds to magnetic images at consecutive values of B_{ext} at 4.2 K. Down: Schematic representation of the magnetization reversal of the MNP where the arrow simbolize the magnetic moment of the nanoparticle.

NP 3: Size (19.3 ± 1.9) nm. The starting magnetic state at -600 Oe presents bright contrast meaning that the m_{NP} is pointing down (-z direction) (Figure 23). This bright contrast decreases as the B_{ext} is gradually changed denoting that the m_{NP} is rotating. At -350 Oe, an activation volume appears, probably due to a defect at the MNP surface, and this small domain starts to reverse (showing a dark contrast). This is seen in the -350 Oe MFM image as a small dark spot that, once nucleated, tends to expand via domain-wall motion under the action of the applied field. The magnetization reversal evolves via domain-wall propagation of two opposite domains that rotate and expand by the effect of B_{ext}, as can be seen in images from -300 Oe to -200 Oe. At -200 Oe a domain-wall clearly appears showing two domains aligned in opposite orientations (dark/bright region). At -150 Oe one of the domains (bright one) continues its propagation but at -100 Oe, this expansion is blocked due to a strong defect or *pinning center* that avoids the domain-wall movement. A bright/dark contrast of the two opposite magnetic domains is clearly observed from -100 Oe to +300 Oe. Then, the magnetization reversal has not taken place completely even increasing the strength of the applied field.

From the sequence of high resolution magnetic images we conclude that the nanoparticle is a **two-domain MNP** that starts to rotate via domain **localized nucleation** on a surface defect although is not completely reversed due to **domain-wall pinning**.
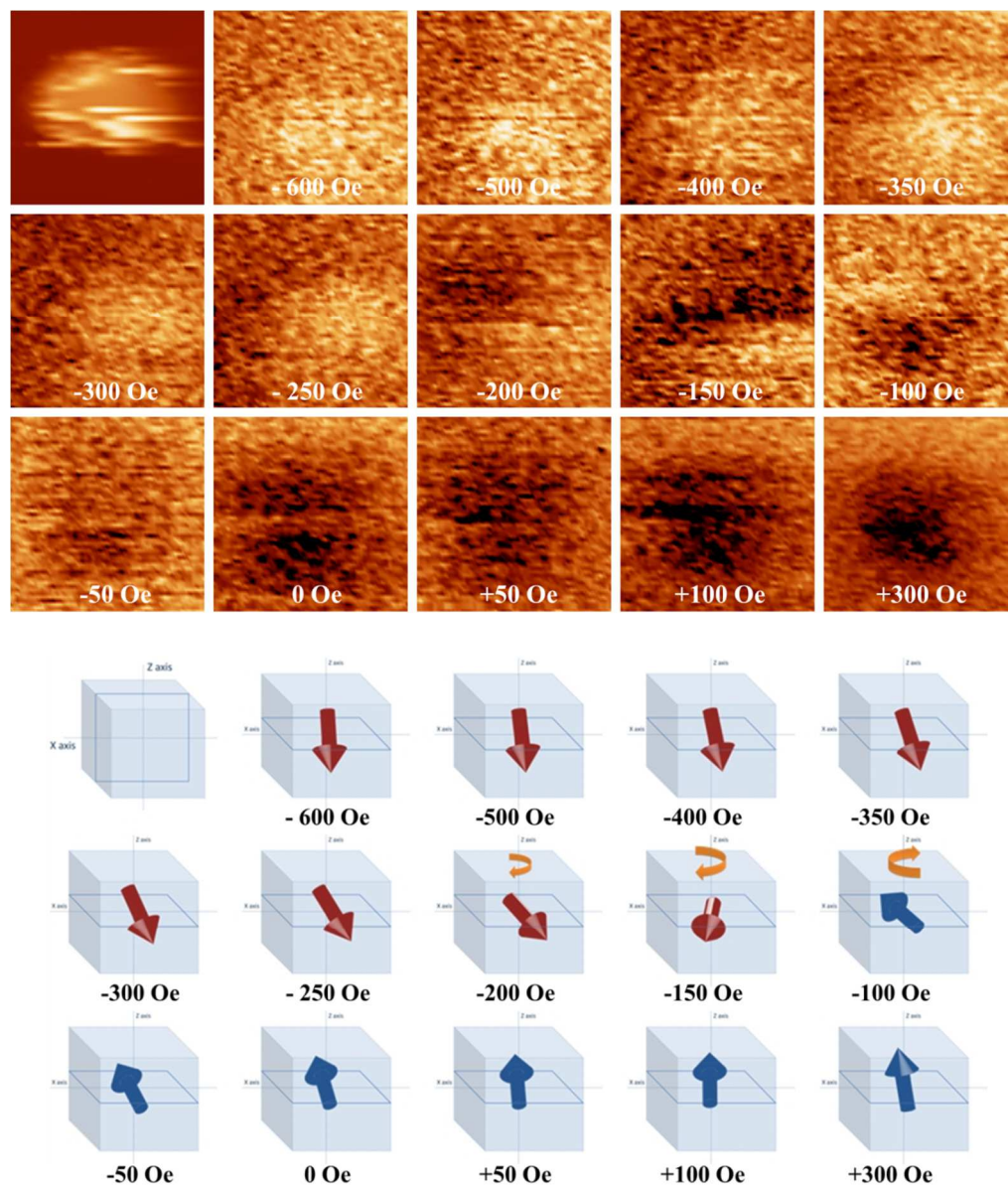
NP4

Figure 24. Nanoparticle 4, h = (19.7 ± 2.0) nm .Top: Set of images of 98 nm x 98 nm. The first image corresponds to the topography and the rest corresponds to magnetic images at consecutive values of B_{ext} at 4.2 K. Down: Schematic representation of the magnetization reversal of the MNP where the arrow simbolize the magnetic moment of the nanoparticle.

NP 4: Size (19.7 ± 2.0) nm. At the initial state at -600 Oe, the m_{NP} is pointing down although slightly tilted with respect to the z axis as can be seen in the magnetic image, where a non-symmetric bright contrast is shown (Figure 24). The bright contrast intensity gradually decreases as the external field is varied from -600 Oe to -250 Oe and this means that the out-of-plane component of the m_{NP} is rotating. At -200 Oe, the magnetic image presents a dipolar contrast (dark/bright) that would indicate an in-plane m_{NP} that will successively rotate in three steps, as can be seen in the images from -200 Oe to -100 Oe. Between -150 Oe and -100 Oe the m_{NP} rotates 180°, presenting a chiral symmetry that evolves with the external field. The m_{NP} is following the external field and tends to align with it so at -50 Oe, the m_{NP} presents an out-of-plane component, showing a smooth dark contrast. The out-of-plane component of the m_{NP} continuously rotates following the external field and showing a dark contrast more intense at each step (images from -50 Oe to +100 Oe). Finally, at +300 Oe it presents a non-symmetric dark magnetic contrast which would mean that the m_{NP} is a little bit canted with respect to the z axis.
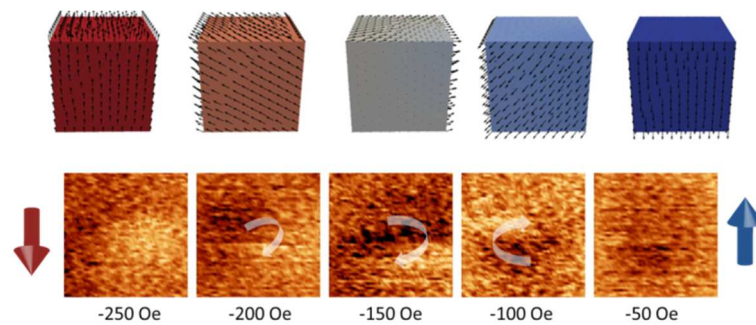

Figure 25. Top: Simulation of the different steps of magnetization reversal of a cubic NP of 10 nm x 10 nm x 10 nm by curling. Taken from reference [12b]. (b) Experimental measurements of the magnetization reversal of NP4 by curling.

If we consider the easy axis on the z direction, these images could correspond with a twisted flower state where the twist of the magnetization tends to maintain a homogeneous state parallel to the easy axis and to reduce the stray field energy by forming a structure similar to a vortex. The twisted flower state or curled state presents by definition a chiral symmetry that evolves with the external field and

finally the m_{NP} rotates completely. This nanoparticle is then a **single domain** near the single domain limit, and the magnetization reversal mechanism would be via **curling**. The magnetic reversal via quasi-coherent (curling) of a cubic nanoparticle was simulated by Krone[12b] and matches quite well with our experimental data (Figure 25).

NP 5: Size (23.8 ± 2.4) nm. The magnetic reversal of this NP (Figure 26) is very similar to NP 3. At -600 Oe, the m_{NP} is pointing down (-z direction) showing an overall bright contrast. The bright contrast decreases slightly from -600 Oe to -350 Oe, meaning that the out-of-plane component of m_{NP} is rotating only a little by the effect of the B_{ext}. At -350 Oe, a discontinuity is shown as a dark region crossing the NP. This can be explained if a defect is positioned on the surface of the NP and the tip strongly interacts with it. At -300 Oe, an activation volume has appeared as a localized area with reversed magnetization (a squared dark region that means that the spins have rotated to an orientation opposite to the initial state). This is consistent with a defect that starts to reverse as previously mentioned at NP 3, via localized nucleation. Then, the magnetization reversal evolves via domain-wall propagation that can be seen in the consecutive magnetic images from -300 Oe to -250 Oe. The reversed region becomes larger until at -200 Oe, the domain pointing down (bright contrast) is completely annihilated. From -200 Oe, only remains one domain with an out-of-plane component (dark contrast) that successively rotates trying to align with the B_{ext} while increasing it. Finally, the magnetic image at +300 Oe shows an irregular shape of the dark magnetic contrast that could be explained if the easy axis of the m_{NP} is not completely aligned with the external field.

From the magnetic images we infer that this NP is a **two-domain NP** that has reversed its magnetization by **domain-wall nucleation** caused by a defect on the MNP surface and the reversal was done via **domain-wall motion**. In comparison with NP 3, the defect on the NP surface was not so large to block the propagation of the domains and the MNP was reversed completely. In this case, the magnetization has taken place by discontinuous and continuous processes: a combination of rapid rotation of discrete regions of the particle (nucleated region) and gradual movements of domain walls regions.
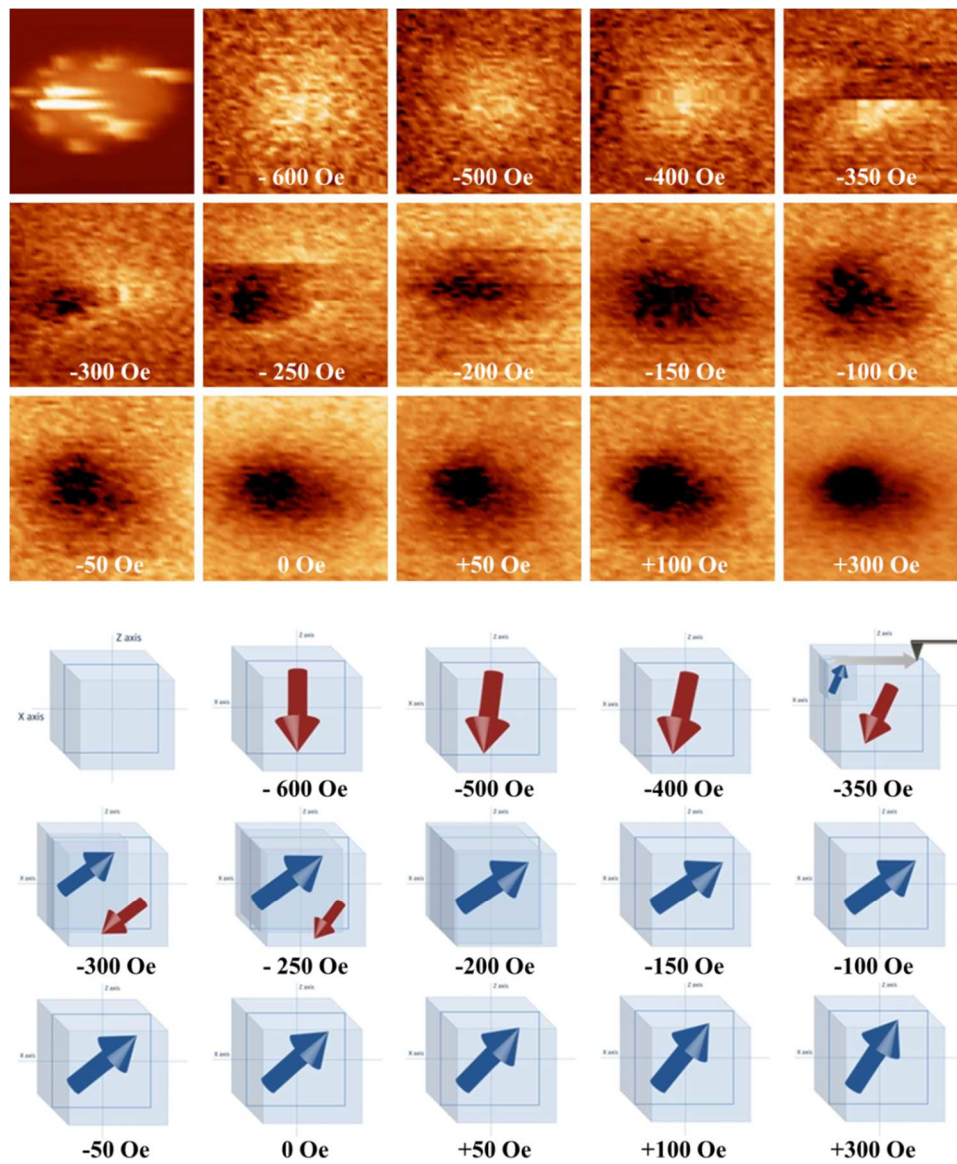
NP5

Figure 26. Nanoparticle 5, h = (23.8 ± 2.4) nm .Top: Set of images of 98 nm x 98 nm. The first image corresponds to the topography and the rest corresponds to magnetic images at consecutive values of B_{ext} at 4.2 K. Down: Schematic representation of the magnetization reversal of the MNP where the arrow simbolize the magnetic moment of the nanoparticle.

NP6

Figure 27. Nanoparticle 6, h = (25.5 ± 2.5) nm. Top: Set of images of 98 nm x 98 nm. The first image corresponds to the topography and the rest corresponds to magnetic images at consecutive values of B_{ext} at 4.2 K. Down: Schematic representation of the magnetization reversal of the MNP where the arrow simbolize the magnetic moment of the nanoparticle.
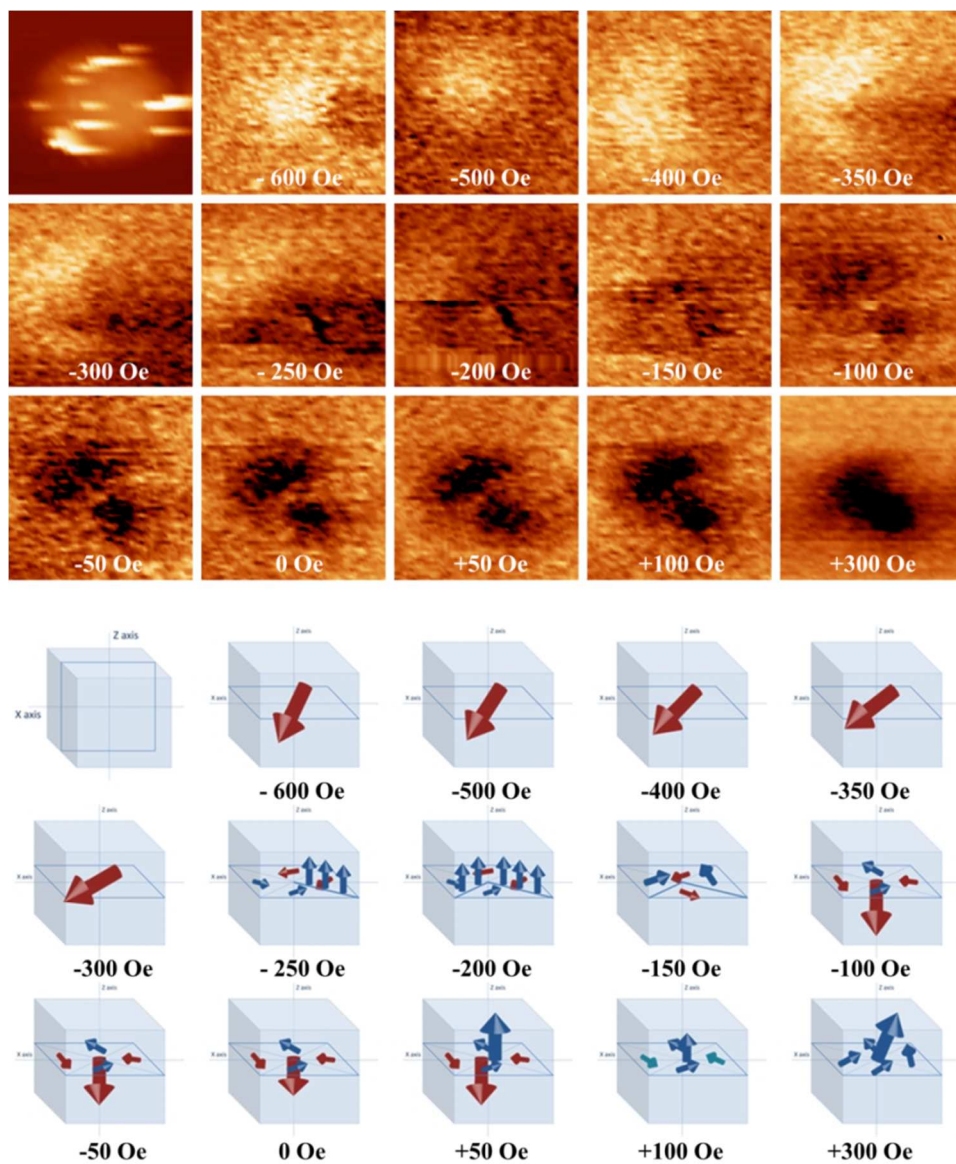
NP 6: Size (25.5 ± 2.5) nm. This NP present a bright/dark contrast at the initial state (-600 Oe), meaning that the m_{NP} is pointing down but a little bit canted from the z axis (Figure 27). It then starts to rotate as the B_{ext} is increased (from -350 Oe to -250 Oe), and the same two regions (dark/bright) are distinguished slightly modifying their contrast and shape. At -250 Oe, one domain-wall with dark contrast appears. In the next step, two domain walls pointing up are resolved at -200 Oe (two centered dark lines in the magnetic image forming a 120° angle). At -150 Oe the domain-walls have slightly rotated and at -100 Oe, the magnetic image resolves a complete vortex structure. The high resolution magnetic image shows the typical contrast of an in-plane magnetization (dark/bright regions) and at the center it is shown the core of the vortex as an out-of-plane bright central dot (○).
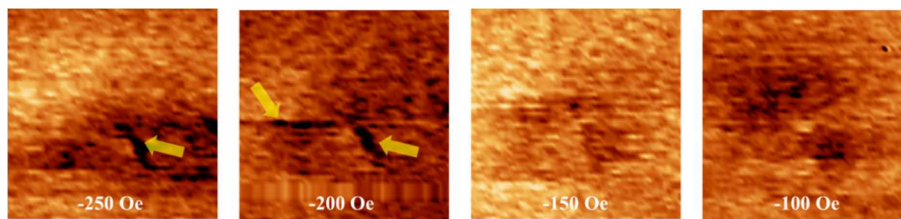

Figure 28. Magnetic images showing the first stages of the vortex formation. The formation of the domain-walls is pointed by arrows: at -250 Oe one domain-wall appears and at -200 Oe it appears two domain-walls forming a 120° angle. At -150 Oe the domain-walls blur and the domains start to appear more clearly. At -100 Oe, the magnetic vortex is completely formed with its core pointing down (bright contrast). Size of all images: 98 nm x 98 nm.

By varying the applied external field, the intensity of the core is gradually reduced (images from -100 Oe to +50 Oe). At +100 Oe, the vortex core is completely reversed presenting a dark contrast (●). Finally, the vortex state is annihilated due to the saturation of the NP presenting a non-homogeneous dark region that would indicate again that the vortex axis is not completely aligned with the B_{ext} axis. The magnetic images reveal that this NP is a two domain NP with the easy axis pointing in the X direction and the magnetization reversal takes place via **vortex formation and annihilation** (Figure 28).

A magnetic vortex is defined as an in-plane closed-flux magnetization with a central dot called the vortex core. The magnetization switching of vortices takes place via nucleation, propagation and annihilation and the reversal of its core involves complex processes widely study for the last years. The existence of vortex cores was already predicted more than 40 years ago[53] but the first experimental evidence was shown in 2000 by T. Shinjo et al. where core vortices on circular permalloy dots were observed by MFM.[54] The vortex core is known to be a nanometric structure confined in an area of few exchange length of diameter[55] and can be characterized by a polarization p = ±1, that defines if it is orientated up or down.[56,57] Together with the polarization, the in-plane circulation that can be clockwise or counterclockwise c = ±1, defines the vortex structure.[56,24a,58]
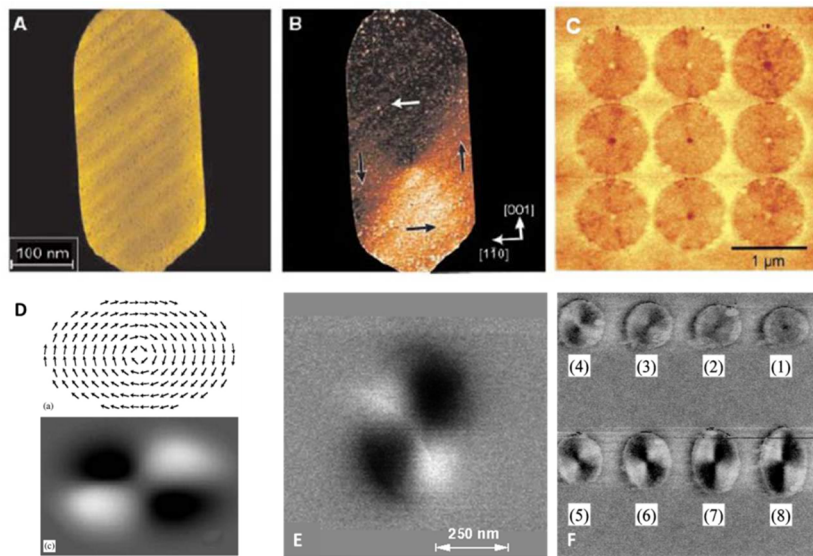

Figure 29. (a) Topography and (b) magnetic image obtained with spin-polarized scanning tunnelling microscopy of a single nanoisland of Fe. The arrows indicate the orientation of the domains. From reference [68] (c) MFM image of an array of Permalloy dots with 1 µm of diameter and 50 nm thick. The central dot in each disk shows the evidence of the vortex formation. Figure extracted from reference [67]. (d) The magnetization distribution and corresponding calculated MFM contrast of a Co elliptic dot, for c = +1. Figure adapted from reference [57]. (e) Magnetic force image of a single 18 nm thick Co dot after saturating the sample in the hard-axis direction. Figure adapted from reference [¡**Error! Marcador no definido.**]. (f) MFM image of elliptical dots, where the width is 1 mm along the short-axis and increases gradually from 1 µm (1) to 2 µm (8) along the long-axis. Figure extracted from reference [58].

The mechanism of polarity reversal generally involves the creation and annihilation of a vortex–antivortex pair, followed by the formation of a core with opposite polarity. Nowadays, this reversal process is a well-known ultrafast mechanism[59] that seems to be independent of the type of excitation and the creation of the vortex-antivortex pair determines the sense of rotation of a freely gyrating vortex.[60,56] The reversibility of the core vortex have been achieved by applying different external stimuli like pulsed magnetic fields,[59,61] alternating magnetic fields,[62] spin-polarize currents[63] and spin-waves[64] or even induced by the non-homogeneous magnetic field from the probe of a MFM.[65] It has been also probed that a field-driven switching of the vortex core polarization in circular permalloy lithographed dots is possible by applying a static magnetic field perpendicular to the vortex plane; however, this process requires high values of the field on the order of 500 mT.[66] Such large field values indicate that a high energy barrier must be overcome to switch a magnetic vortex core. Recently, it has been also demonstrated that pulsed switching requires approximately half the field strength compared with static switching and field switching scales strongly depend on the disk geometry.[67] But note that all the studies (theoretical and experimental) of the reversal of vortex cores were focused on lithographed thin-film elements of permalloy[68] or Co[57] with lateral dimension of 150 nm x 200 nm in the best case.[55] In these types of magnetic structures, there is an in-plane magnetization due to the magnetic shape anisotropy, characteristic of ferromagnetic films with thicknesses below the magnetic exchange lengths.[60] The reversal of the vortex core through the creation and annihilation of the pair vortex-antivortex in lithographed dots is a process driven by the exchange field, unlike the precessional switching typical for small magnetic NPs that is driven by the demagnetizing field. The magnitude of the exchange field is about 100 times larger than the demagnetizing field, so we could think that in principle, for vortices in magnetic NPs the field required to reverse the core should be lower than for lithographed dots.[59] In our case, the vortex core switch was achieved by applying a small value of out-of-plane external field of 50 Oe (5 mT), as shown in Figure 30, which is 100 times lower than the values reported up to

now for lithographed dots of permalloy or cobalt. From the orientation of the in-plane dark/bright regions it can be deduced that the circulation is clockwise (c=+1) and the vortex polarization has been switched from p = -1 to p = +1.[57]
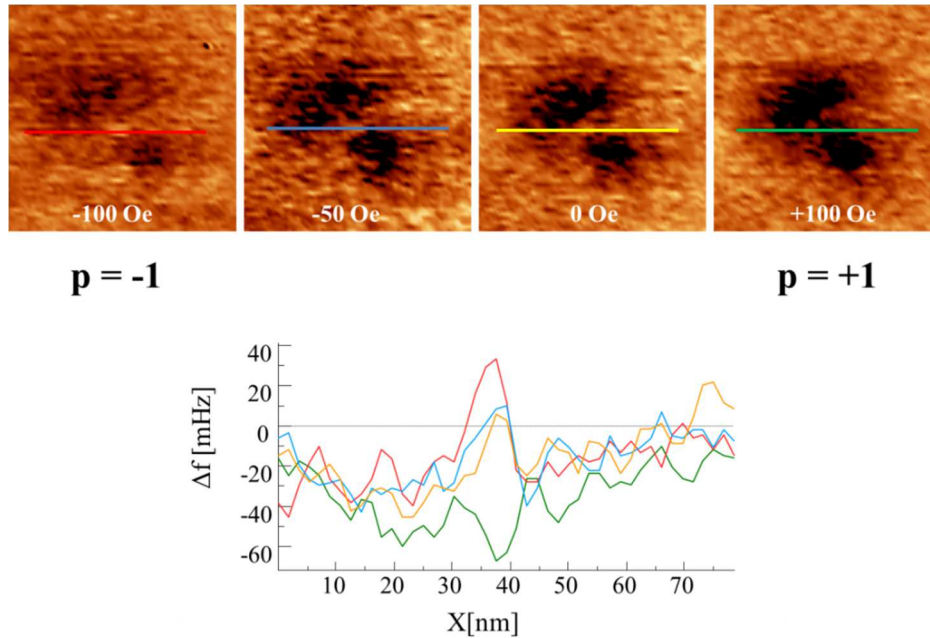

Figure 30. Top: Magnetic images of the vortex core reversal. (size of all images: 98 nm x 98 nm). Down: The gradual change of the core polarization is plotted in the graphic until at +100 Oe the polarization is completely reversed.

On the other hand, the switch of the vortex core is made through the creation of the pair vortex antivortex that has been described as an ultrafast process that takes place in the range of picoseconds (ps). Note that all these works concerning the pair vortex-antivortex formation, were performed at room temperature. In 2006, R. Wieser et al. reported on the thermodynamic behavior of nanomagnets with a vortex configuration.[69] First, the finite temperature dynamic behavior of nanomagnets with a vortex configuration was studied numerically using Langevin dynamics simulations,

putting special emphasis on the behavior of the vortex core. The simulations started from one of the ground states with the core magnetization pointing upwards. For lower temperatures the magnetization of the core was stable over a long time period before an abrupt switching event to the opposite direction occurs. For the case of single-domain nanoparticles this kind of behavior is known as superparamagnetism. In this report, analogously, the two energetically equal states of the vortex core is separated by a finite energy barrier which can be overcome by thermal fluctuations. The switching time decreases with increasing temperatures and at the same time the fluctuations of the magnetization increase. To describe this effect in more detail they investigated the mean first switching time, defined as the time between starting the simulation with up magnetization and switching to down magnetization. They were able to fit the low temperature data obtained by a straight line showing that the switching time could be described rather well by a thermal activation law. The switching time could be described then as:

$$\tau = \tau_0 e^{\Delta E_b / k_b T} \qquad \text{(Eq. 5.5)}$$

with an energy barrier E_b, and valid for T<< Tc. In the low temperature limit, the energy barrier is given by the energy difference between a vortex configuration and a transient state with the highest energy during the reversal. This way, for sufficient low temperatures, the magnetization of the core would be stable over a long time period before an abrupt switching event to the opposite direction may occur by thermal activation. This could explain why we can see and induce the switching of the vortex core even at scales of time much larger than the usual reported values (several minutes, required to acquire the MFM image).
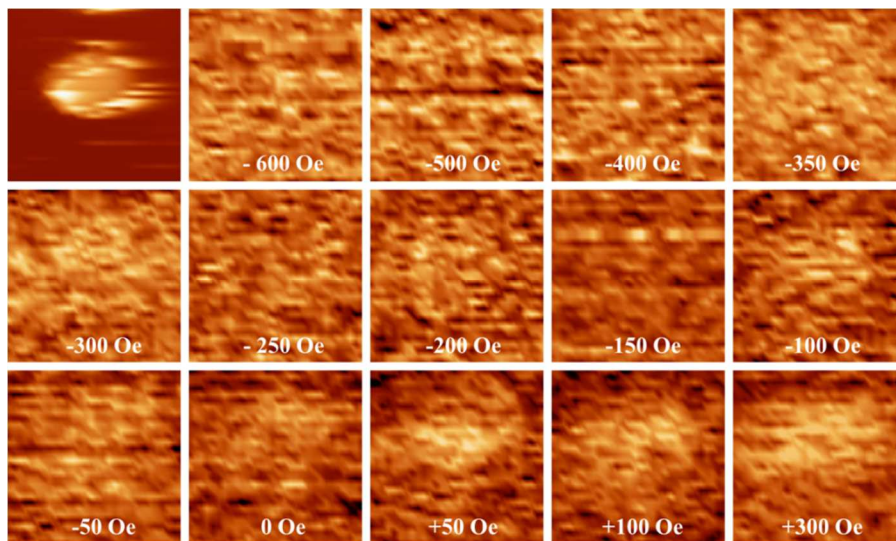
NP1

Figure 31. Nanoparticle 1, h = (13.2 ± 1.3) nm .Set of images of 98 nm x 98 nm. The first image corresponds to the topography and the rest corresponds to magnetic images at consecutive values of B_{ext} at 4.2 K

NP 1: Size (13.2 ± 1.3) nm. Finally, we present a MNP where the magnetic contrast, bright in this case, does not change so the magnetization in this NP does not reverse (Figure 31). Although the images show slight differences in the bright magnetic contrast, this is probably due to slight changes in the alignment of magnetic tip with the external field that at negative values could cause a small canting. But the fact is that this MNP shows in all magnetic images a bright contrast that means that it has not reversed at any point of the experiment. Two possible explanation of this behavior are discussed: 1- As the NP size decreases, a large percentage of all the atoms in a nanoparticle are surface atoms, which implies that surface and interface effects become more important. Then, the non-reversibility of this particular MNP would be due to the presence of surface defects that could cause high stress fields impeding the rotation of the magnetic moments and therefore an increment of the anisotropy, in both cases leading to an increase of the coercive field.8 2- Another possible

explanation is that a coherent reversal process is known to be accompanied by a substantial increase in the switching field, compared to the incoherent reversal mechanisms.[12b,52] As already discussed, the smallest sizes tend to present single domain and coherent rotation, so by considering the size of this particular NP, h = 13.2 nm, it would be in this range. To rotate the magnetization of the smallest NPs, B_{ext} much higher than ±600 Oe would be needed as shown in scheme of Figure 2.

5.2.7 Magnetic measurements with a functionalized tip

In the last part of the experiment we present the results from magnetic measurements performed with a functionalized-MFM tip. The in-situ functionalization occurred by serendipity and took place as follows: After the measurements at +300 Oe (topography and magnetic image was recorded), the B_{ext} was increased up to +600 Oe. Then at this value of the B_{ext}, and at Z_{lift} = 100 nm, the magnetic image was acquired. All the images (topography and magnetic), were always acquired from down to top, and forward and backward scans were performed in every line of the scan. When the regular MFM tip was scanning (forward) just above the two-domain pinned NP (labeled as No.3 in the previous section) at the typical lift value of 100 nm, it was "fished" by the magnetic tip. The process is shown in the Figure 32:
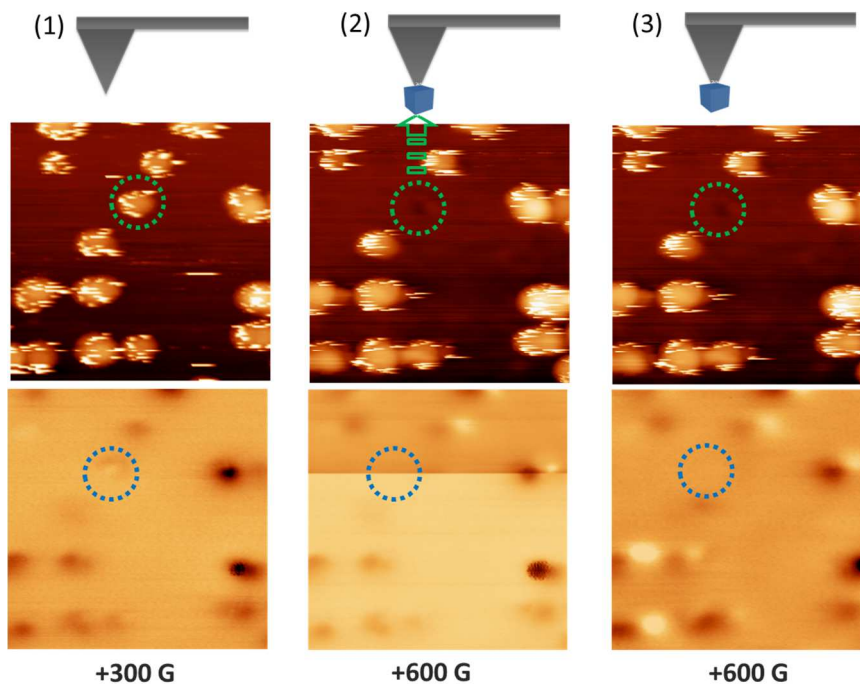
Figure 32. Three steps of the MFM tip functionalization showing the experimental topography (top) and magnetic images (down). NP3 is tagged with a green circle in the topography and a blue circle in the magnetic image. (1) Regular situation in MFM when a magnetic-coated tip scans over the sample to get the topography image and magnetic image at out-of-plane magnetic field of +300 Oe. (2) Topography image taken with the functionalized MFM tip. The image shows the empty area where the "fished" NP3 should be placed. The magnetic image at out-of-plane magnetic field of +600 Oe clearly shows the scan line where the "fishing" takes place. (3) Topography image taken with the functionalized MFM tip. The magnetic image at out-of-plane magnetic field of +600 Oe shows the new magnetic contrast. Images size: 520 nm x 520 nm.

As described before, this particular NP seemed to present a strong defect at the surface that acted as a pinning center and impeded the complete switch of its magnetization. The irregularity of NP number 3 is probably the reason why this NP and not another, got attached to the magnetic tip while it was scanning above it. The magnetic configuration of the NP3 at +300 Oe, and presumably at +600 Oe, was formed by two domains with opposite orientations. This configuration is equivalent to an in-plane effective m_{NP} as shown in Figure 33.
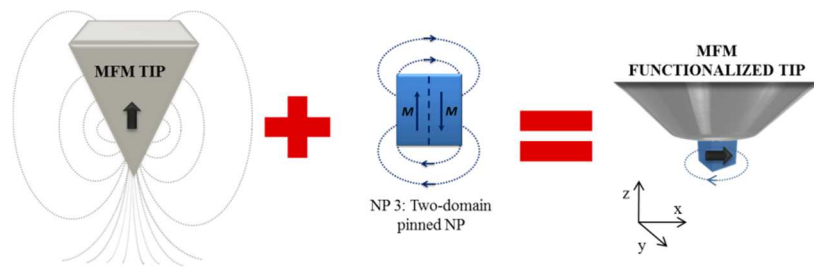
Figure 33. Schematic representation of the change of the magnetic structure of the tip. When the NP3 got attached to the regular MFM tip that was initially magnetized in the Z axis, the resulting tip is magnetized in the X axis

From then on, the magnetic configuration of the tip was completely changed and according to the experiments performed by Kleiber et al., the new contrast observed is compatible with an in-plane magnetized MFM tip.[24b] This fortuitous fact converted the ~50 nm tip into a ~19 nm functionalized-tip with an effective magnetic moment in the +x. The functionalization is displayed in the next figure (Figure 34).
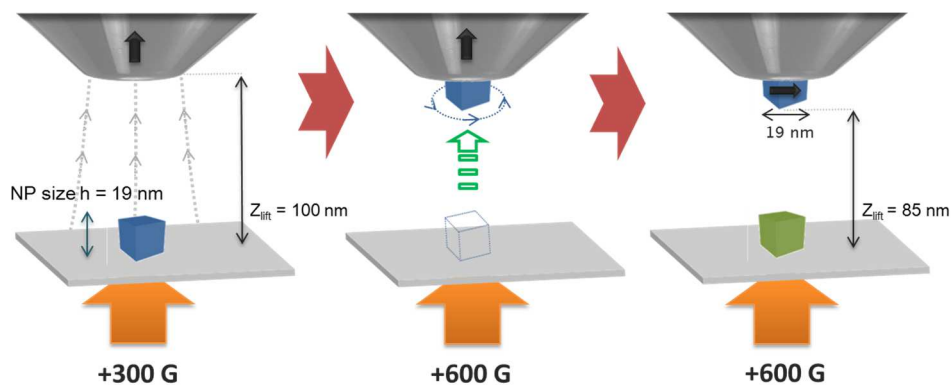
Figure 34. Schematic view of the three steps of the functionalization process. (1) The regular magnetic-coated tip of ~50 nm tip radius is scanned over the PBA-NP at a fix tip to sample distance of 100 nm. (2) The external magnetic field is increased 300 Oe up to +600 Oe, and when the tip scans this particular NP, the "fishing" takes place and the NP3 gets attached to the MFM tip. (3) A new effective tip of 19 nm radius is created, with an in-plane magnetic configuration

In the magnetic images acquired with the functionalized tip (Figure 36), each NP presents two or three alternated dark/bright lobular contrasts. According to Kleiber (see Figure 35) these features would be characteristic of the interactions of the different poles of a magnetic NP with an MFM tip magnetized in the +x direction.
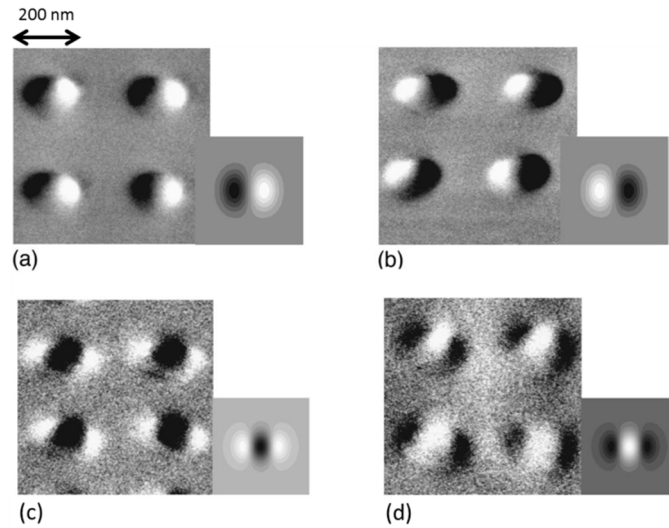

Figure 35. (a) and (b) MFM images of dots (diameter: 200 nm, thickness: 17 nm), that have been magnetized in plane (+x direction) under a strong external field ~400 kA/m outside the microscope. After scanning (a) the field has been applied in the opposite direction (-x direction). The small figures show the results of a simulation for the MFM contrast of dots magnetized in the (+x) and (-x) direction and scanned by using a tip magnetized in the z direction (perpendicular to the plane of the sample).Scan size: 1.1 µm x 1.1 µm. (c) and (d) MFM images of same dots magnetized again in plane, in oposite orientations (+x and -x) and scanned with a tip magnetized in the x direction. Attached are the results of the simulation for a tip magnetized in the x direction. Scan size: 1.1 µm x 1.1 µm. Figures extraxted from reference [74].

This lobular contrast could not be resolved before with the conventional magnetic coated tip because this tip cannot be magnetized in plane (as mentioned in section 5.2.4). Looking carefully in the MFM image (Figure 36), one can observe some NPs showing 2 lobes at the magnetic contrast. This would be the result of the interaction of the x-magnetized tip with a perpendicular magnetized NP. Taking as example NPs 1

and 2 (Figure 36) and comparing their magnetic images before and after the fishing moment, we can deduce the orientation of the magnetic moment of the fished NP.
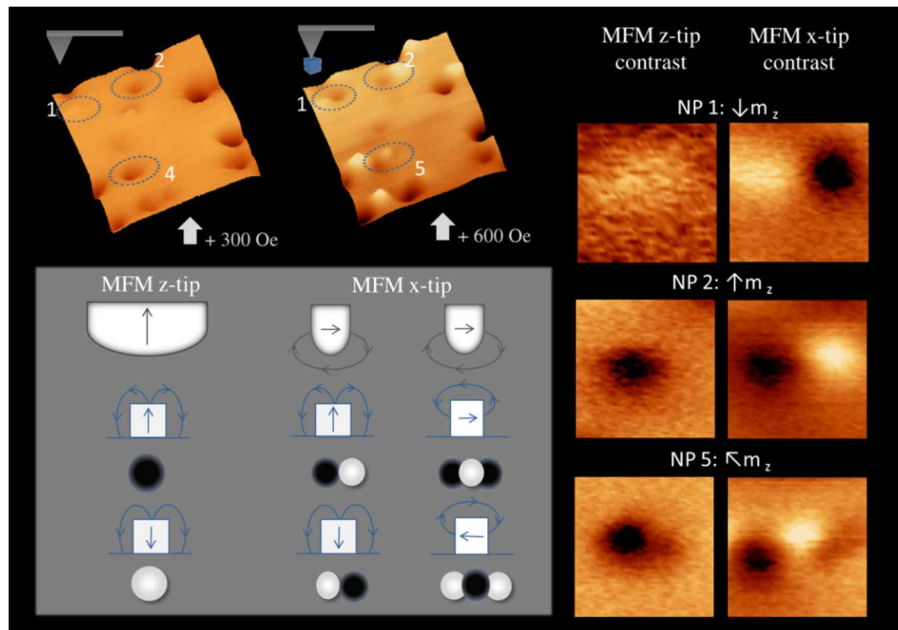

Figure 36. 3D magnetic images acquired with the regular MFM tip (left) and the functionalized-NP tip (right). Three NPs are highlighted and a zoom in of 115 nm x 115 nm show the different magnetic contrasts for each case. A schematic of the magnetic contrast for the different situations is shown for clarity.

Before fishing, the magnetic moment of the tip was undoubtedly in the z direction, so the contrast at +300 Oe of NP 1 was clearly a single bright lobe (○) and of NP 2 a single dark lobe (●). This one single lobe contrast indicates that the magnetization of NPs 1 and 2 were in the same direction of tip magnetization (but pointing in opposite orientations). After the "fishing" moment, each single lobe appears as two lobes, bright/dark for NP1 (○●) and dark/bright for NP2 (●○). Some other NPs show 3 lobes contrast, for example the NP 5. As was previously discussed, this NP would be a little bit canted with respect to the z axis that was explained because at +300 Oe the NP showed an irregular dark contrast. This canting is confirmed by the MFM image acquired with the functionalized tip that shows a contrast of three consecutive lobes

dark/bright/dark ($\bullet \circ \bullet$), with the last right lobe less intense than the left one. This indicates that the direction of the m_{NP} is in between the +z and the -x axes. When the external applied field was set to -600 Oe, the resulting magnetic contrast was the same as for +600 Oe, although less intense, this indicates that the NP of the tip was also affected by the external field. Therefore, the functionalized tip is not suitable for magnetization reversal measurements. However, the in-plane functionalized magnetic tip permitted us to assign the magnetic directions of individual and isolated NPs with more detail than with the use of an out-of-plane tip. With this criterion, it has been possible to allocate the magnetization directions at +600 Oe for all the NPs studied in this experiment, as can be seen in Figure 37. There are two NPs that present canting on their magnetization directions: NPs 5, 6. As can be seen in the topography image, these two NPs are located close to a neighboring NP. The inerparticle interactions could have affected their magnetization configurations causing the canting of their magnetization directions.
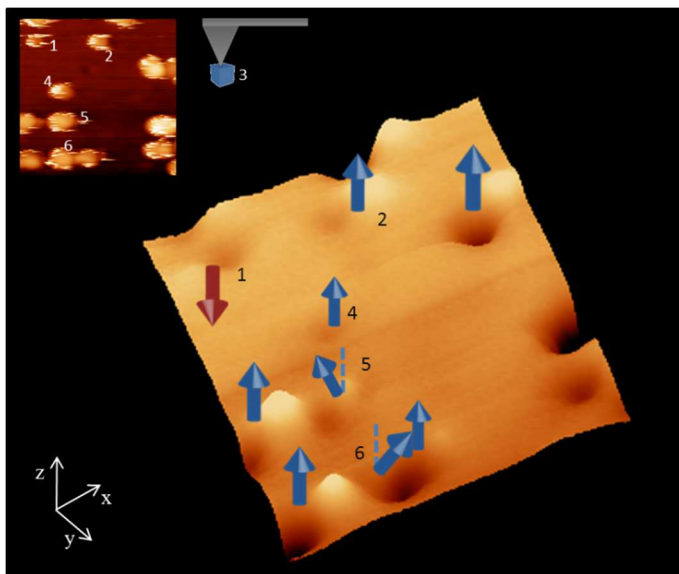

Figure 37. 3D magnetic image acquired with the functionalized-NP tip. The arrows assign the magnetization directions of the NPs. Blue means a +z magnetization direction while red means a –z magnetization direction. The inset shows the corresponding topography image. Image sizes: 520 nm x 520 nm.

Unfortunately, further inspection of the MFM functionalized tip by high resolution electron microscopy for example, was not possible because the NP was detached as the temperature was increased above the Curie temperature (for T > 40 K) and the regular magnetic-coated tip was then recovered. When the system was set again to 4.2K, the magnetic images showed the typical magnetic contrast for a MFM tip magnetized in the z axis. Due to the thermal drift the image was acquired in another location of the sample. (Figure 38)
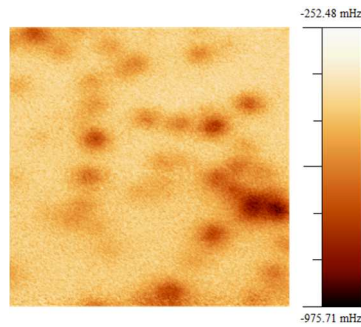

Figure 38. Magnetic image acquired at 4.2 K with the recovered MFM tip without any NP attached to it. Size: 750 nm x 750 nm.

5.3. MATERIALS AND METHODS

Low temperature magnetic force microscope (LT-MFM)

All the MFM measurements were done with a commercial low temperature magnetic force microscope, attoMFM I (Attocube Systems AG). The instrument is a cantilever based SPM with interferometric deflection detector. It permits to work in various modes and includes a PLL for working in frequency modulation. The range working temperature varies from 4.2 K to 300 K. It is equipped with two superconducting magnets that allow applying variable magnetic field in two directions: out-of-plane up to 8 T and in-plane up to 2 T. Both directions can be combined to apply a vector magnetic field up to 1.5 T.

Magnetic tips

The tips used were magnetic coated cantilevers commercially available MFMR tips with hard magnetic coating of CoCr alloy (40 nm thickness), spring constant of $k \approx 3$ N/m, and resonance frequency of $f_0 \approx 70$ KHz from Nanosensors. To avoid the unwanted jump-to-contact phenomenon and to enhance the SNR, relatively high amplitude oscillations were used ($A \approx 90$ nm).

Ramdomly dispersed KNiCr NPs on silicon

KNiCr NPs were attached to the surface by drop casting using the method described previously in chapter 3. The method is based on the formation of a protonated SAM of APTES on a silicon surface, and then a drop of aqueous KNiCr NPs solution is put in contact with the functionalized silicon surface for 10 seconds. Finally, it is rinsed with mili Q water and dried under a N_2 stream.

5.4. CONCLUSIONS

In this chapter a very detailed and dedicated study of the magnetization reversal processes of single and isolated magnetic cubic PBA-NPs has been presented. All the measurements were performed below the Curie temperature of the NPs. This feature permitted the manipulation of the magnetization direction of the individual NPs by a variable out-of-plane external magnetic field.

Previously any MFM measurement of the NPs, a complete characterization of the magnetic tip was performed to assure the correct interpretation of the results and to be able to detect the reversibility of the NPs. Some considerations about the effect of the stray field of the tip, the tip-sample distance and the cantilever amplitude oscillation were discussed as well.

Unprecedented studies of the change in the strength of magnetic signal by varying the working temperature were presented. It was found measurements at 4.2 K were needed not only to be able to manipulate the magnetic moments of the NPs, but also to achieve enough signal to detect them. Even applying high external magnetic fields the magnetic response at 40 K was found to be 80% lower that at 4.2 K.

For the first time, the reversibility of the magnetic moment of individual NPs based on molecular materials was imaged. We could go further by saying that these measurements are the first experimental results for the imaging of the different cases for the magnetization reversal mechanisms of magnetic cubic nanoparticles. As highlighted in the introduction, these important processes were already predicted more than 60 years ago and, more recently, simulated by micromagnetic modelling, but they were never seen experimentally in magnetic nanoparticles. The magnetic reversibility of NPs is a size-dependent phenomenon. The narrow size distribution of the KNiCr NPs prepared by the synthetic procedure presented in chapter 3, allowed us to select MNPs centered in the critical size limit for single domain NP. In this region, a rich phenomenology of magnetic switching behaviors was encountered, which allowed to

study for the first time, various cases of magnetization reversal in the border between the single and two domain NPs. Six of these cases have been studied in detail: (NP2) single domain NP presenting coherent rotation, (NP3) defective two-domain NP which magnetic moment rotation was pinned by structural defects, (NP4) single-domain NP with non-coherent rotation or *curling*, (NP5) two-domain NP that starts switching via localized nucleation and evolves by domain wall propagation, (NP6) two-domain NP which magnetization reversal takes place via vortex formation and annihilation and finally (NP1) single domain NP that does not reverse its magnetization.

Among them, two of these cases could be stand out: the magnetization rotation in a single-domain NP via *curling* and the magnetization rotation in a two-domain NP via vortex formation. The *curling* mechanism has been widely studied, modelled by micromagnetic simulations and experimentally measured in magnetic wires, for example, but the imaging of the process of magnetic reversal via curling presented in this thesis is unprecedented. On the other hand, the magnetic vortex formation is a well-known magnetic mechanism of reversibility that has deeply studied the last decade by many experimental techniques. However, all the results presented up to now were magnetic measurements of vortices formed in lithographed magnetic dots. For the first time, high resolution images of the vortex formation and annihilation processes has been seen in a three dimensional nanostructure, a single and isolated magnetic nanoparticle of 25 nm. The vortex-core was successfully resolved, and the change of its polarity as well as the annihilation of the vortex was induced with an unprecedented small value of the applied field, which is 100 times lower that the typical values obtained for a permalloy lithographed nanodot.

This work is relevant from the point of view of a fundamental study about reversal magnetization processes in nanoparticles and moreover increases the potential applicability of this large family of magnetic NPs in future information storage or

processing devices, which is still in its earliest studies in comparison with the large variety of NPs of this nature that has been already prepared and deeply characterized.

Finally, the in-situ functionalization of the MFM tip permitted an enhancement of the magnetic resolution of the images and it was possible to assign the magnetization directions of the individual MNPs.

5.5. BIBLIOGRAPHY

[1] a) Kittel C., *Revs. Mod. Phys*, **1949**, *21*, 541. b) Stöhr J., Siegmann H. C., *Magnetism: from fundamentals to nanoscale dynamics*, Springer Series in Solid-State Sciences *152*, Springer (Heidelberg, **2006**).

[2] a) Papaefthymiou. G. C. *Nano Today*, **2009**, *4*, 438-447. b) Bellido, E., Domingo, N., Ojea-Jiménez, I., Ruiz-Molina D. *Small* **2012**, *8*, No. 10, 1465–1491.

[3] Stoner, E. C, Wohlfarth, E. P., *Philosophical Transactions of the Royal Society of London*, Series A **,1948,** *240*,599.

[4] Aharoni, A., Shtrikman, S., *Phys. Rev*. **1958**, *109*, 1522.

[5] Skomski, R. Zhou, J. *Nanomagnetic models*, Springer **2006**.

[6] Kittel, C., Galt, J. K., Campbell, W. E. *Phys. Rev.*, **1950,** *77*, 725.

[7] Gubin, S. P., Koksharov, Y. A., Khomutov, G. B. Y., Gleb,Y.. *Russian Chemical Reviews* 74, **2005**, *6*, 489 – 520.

[8] Hertel,R., Krommüller,H., *J. Magn. Magn. Mater,* **2002**, *238*, 185-199.

[9] McMichael, R. D., Standard Problem Number 3, *Problem Specification and Reported Solutions*, http://www.ctcms.nist.gov/~rdm/mumag.html, **1998**.

[10] Rave,W., Fabian, K., Hubert, A. *J. Magn. Magn. Mater*, **1998**, *190*,332-348.

[11] a) Wiliams, W., Dunlop D. J., *J. Geophys. Res*. **1995**,*100*, 3859-3871,. b) Afremov, L. L., Lamash, B. Panov, E., *Physics of the Solid Earth*, **1998**, *34*, 927–931. c) Carvallo.C., Muxworthy A.R, Dunlop D. J., Wyn W. *Earth and Planetary Science Letters*, **2003**, *213*, 375-390.

[12] a) Krone,D., Makarov M., Albrecht,T., Schrefl,D., Suess *J. Magn. Magn. Mater*, **2010**, *322*, 3771–3776. b) Krone,P., Makarov.D., Cattoni,A., Faini,G., Haghiri-Gosnet A.-M., Knittel, I., Hartmann,U., Schrefl,T., Albrecht,M. *J Nanopart Res*,**2011,***13*,5587–5593.

[13] Skomski R, Zhou J. *Advanced Magnetic Nanostructures*. Charpter 3, **2006.**

[14] Wernsdorfer W., Orozco E. B. Hasselbach, K., Benoit, A., Barbara, B., Demoncy N., Loiseau A., Pascard H., Mailly D., *Phys. Rev. Lett.* **1997**, *78*, 179.

[15] Wernsdorfer,W., Bonet,E., Orozco,K., Hasselbach,A., Benoit,D., Mailly,O., Kubo,H., Nakano, ,Barbara.B.; *Phys. Rev. Lett.* **1997**,*79*, 4014.

[16] Wernsdorfer W., Hasselbach K., Benoit A., Barbara B., Doudin B., Meier J.,. Ansermet J.-Ph, Mailly D. *Phys. Rev. B*, **1997**, 551, *17*, 70994-11559.

[17] Jamet M., Wernsdorfer W., Thirion C., Mailly D., Dupuis V., Mélinon P., Pérez A. *Phys. Rev. Lett*. **2001,** *86*, 4676-4679.

[18] Thirion C., Wernsdorfer W., Mailly D. *Nat. Mater*., **2003**, *2*, 524–527.

[19] Helgason O.,Rasmussen H.K, Mørup S., *J. Magn. Magn. Mater*. **2006,** *302*,413.

[20] a) Xu N., Boo B.H., Lee J.K, Wang Kim J.H. *J. Phys. D: Appl. Phys.* **2000**, *33,*135-156; b) Martinho H., Rettori C., Huber D.L, Mitchell J.F, Oseroff S.B., *J. Magn. Magn. Mater s*, **2004**, *272–276*, 1736–1737. c) Hertel R., Kirschner J., *J. Magn. Magn. Mater*, **2004**, *278*, L291–L297. d) Rawlings C., Durkan C., *Nanotechnolog,* **2013**, *24*, 305705.

[21] Martin Y., Wickramasinghe H. K. *Appl. Phys. Lett.* **1987**,*50-20*,1455-1457.

[22] García J.M., Thiaville A., Miltat J., Kirk K.J, Chapman J.N. *J. Magn. Magn. Mater*, **2002**, *242-245*, 1267–1269.

[23] a) Jaafar M., Yanes,R., Asenjo ,A., Chubykalo-Fesenko,O., Vazquez,M., Gonzalez,E. M., Vicent ,J. L. *Nanotechnology,* **2008**,*19* 285717. b) Yongseok,K., Young-Soo,S., Taewan,K., Naesung,L., Yongho,S. *Solid State Communications* ,**2009**,*149*, 839 842.

[24] a) Fernandez, A., Gibbons, M. R, Wall, M. A, Cerjan, C. J. *J. Magn. Magn. Mater.* **1998**, *190*, 71-80. b) Kleiber, M., Kümmerlen, F., Löhndorf, M., Wadas, A., Weiss, D., Wiesendanger, R. *Phys. Rev. B* , **1998**, *58,9*, 5564-5567 c) Fruchart, O., Masseboeuf, A., Toussaint, J. C., Bayle-Guillemaud, P. *J. Phys.: Condens. Matter*, **2013**, *25,* 496002.

[25] a) Schreiber, S., Salva, M, Pelekhov, D. V., Iscru, D. F., Selcu, C., Hammel, P. C., Agarwal, J, C. *Small,* **2008**, *4*, 2, 270 – 278.

[26]) Bittova B., Vejpravova J. P., Mantlikova A. *IOP Conf. Ser.: Mater. Sci. Eng.* **2011,** *18*, 022019.

[27] Raşa, M., Kuipers, B. W. M., Philipse, A. P. *J. Colloid Interface Sci.* **2002**, *250*, 303–315.

[28] Dietz ,C.,Herruzo,H.T, Lozano,J. R , Garcia,R., *Nanotechnology*, **2011**, *22*, 125708.

[29] Proksch, R.B., Schaffer, T. E., Moskowitz, B.M., Dahlberg, E.D., Bazylinski, D.A., Frankel, R.B. *Appl. Phys. Lett.* **1995**, *66*, 2582–2584.

[30] Diebel,C.E., Proksch R., Green,C.R., Neilson, P., Walker, M.M. *Nature* , **2000**, *406* (20), 299-302.

[31] Nocera,T.M, Chen,J., Murray,C.B., Agarwal,G. *Nanotechnology*, **2012**,*23,* 495704.

[32] Deng,Z., Yenilmez,E., Leu,J., Hoffman,J. E, Straver ,E.W.J, Dai,H., Moler,K.A, *Appl. Phys. Lett.* **2004**,*85*, 626.

[33] Wolny,F. , Weissker ,U., Mühl ,T., Leonhardt ,A., Menzel ,S., Winkler,A., Büchner,B. *J. Appl. Phys.,* **2008**, *104*, 064908.

[34] Kuramochi,H., Uzumaki, T., Yasutake, M., Tanaka, A., Akinaga, H., Yokoyama, H., *Nanotechnology,* **2005**,*16*, 24.

[35] Yang,G., Tang,J., Kato,S., Zhang,Q., Qin,L. C., Woodson,M., Liu,J., Kim,J. W., Lillehei,P. T., Park,C. , Zhou O. *Appl. Phys. Lett.* **2005**, *87*, 229901.

[36] Arie,T, Nishijima,H., Akita,S.,Nakayama,Y., *J. Vac. Sci. Technol. B* ,**2000**,*18*, 104.

[37] Córdoba, R., Fernández-Pacheco ,R., Fernández-Pacheco ,A, Gloter ,A.,Magén ,C., Stéphan O., Ibarra ,M. R., De Teresa, J.M., *Appl. Phys. Lett.* **2002**, *80*, 4792.

[38] Koblischka, M. R, Hartmann,U., Sulzbach ,T., *J. Magn. Magn. Mater.* **2004**, *272–276*, 2138.

[39] Cambel,V., Gregušová,D., Eliáš,P., Fedor ,J., Kostič,I., Maňka,J, Ballo,P. *Journal of Electrical Engineering*. **2011**, *62*(1), 37–43.

[40] Amos,N., Ikkawi,R., Haddon,R., Litvinov,D., Khizroev,S.. *Appl. Phys. Lett.* **2008,** *93*, 203116.

[41] Schwarz,A., Wiesendanger,R. *NanoToday.* **2008,** *3*, (1-2), 28-39.

[42] Kim,D., Chung,N., Allen,S., Tendler,S. J. B., Park ,.W. *ACS Nano*, **2012**, *6* (1) 241–248.

[43] Hartmann U. *Annu. Rev. Mater. Sci.* **1999**. *29*:53–87.

[44] Straver E. W. J., Hoffman J.E., Auslaender O.M., Rugar D., Moler K.A. Applied Physics Letters, **2008**, *93*(17), 172514.

[45] Catala, L.; Gacoin, T.; Boilot, J. P.; Rivière, E.; Paulsen, C.; Lhotel, E.; and Mallah, T.; *Adv. Mat.* **2003**, *15*, 826-829.

[46] Prado,Y.; Lisnard,L.; Heurtaux,D.; Rogez,G.; Gloter,A.; Stéphan,O.; Dia,N.; Rivière,E.; Catala,L.; Mallah,T. *Chem. Commun.* **2011**, *47*, 1051–1053.

[47] Wernsdorfer,W. , Prigogine ,I., Rice,S.A.. *Advances in Chemical Physics*, **2007**, *118*, 99–190.

[48] a) Bukharaev,A. A., Ovchinnikov,D. V., Bukharaeva,A. A., *J. Appl.Phys.* **1997**, *5*(10) , b) Bukharaev,A. A., Ovchinnikov,D. V., Nurgazizov,N. I., Kukovitski,E. F., *Phys. Solid State* **1998**, *40* (7).

[49] Jaafar,M., Asenjo,A., Vázquez,M.*, IEEE Transactions on nanothechnology.***2008**, *7*(3), 245-250.

[50] Sun,H., Shi,H., Zhao,F., Qi,L., Gao,S. *Chem. Commun.*, **2005**, 4339-4341.

[51] Wernsdorfer,W. *Advances in Chemical Physics*, **2007**, *118*.

[52] a) Ishii,Y. *J.Appl.Phys.* **1991**, *70* (7), 3765-3769. b) Frei,E. H., Shtrikman,S., Treves,D. *Phys. Rev.* **1957,***106*, 446-455 c) Aharoni,A. *J.Appl.Phys.* **1997**, *82*, 1281-1288.

[53] Feldtkeller,E., Thomas,H., *Phys. Kondens. Materi.* **1965**, *4*, 8.

[54] Shinjo, T., Okuno, T., Hassdorf, R., Shigeto, K., Ono, T. *Science.* **2000**, *289*, 930–932.

[55] Wachowiak, A., Wiebe J., Bode M., Pietzsch O., Morgenstern M., Wiesendanger,R. **2002**, *298*, 577–580.

[56] Guslienko,K., Hernandez Heredero,R., Chubykalo-Fesenko,O. *Phys Rev. B*. **2010**, *82,* 014402.

[57] Mironov,V.L. , Gribkov,B.A., Fraerman,A.A., Gusev,S.A., Vdovichev,S.N., Karetnikova I.R., Nefedov,I.M., Shereshevsky,I.A.. *J. Magn. Magn. Mater.* **2007,***312*,153–157.

[58] Okuno T., Shigeto K., Ono T., Mibu K., Shinjo T.. *J. Magn. Magn. Mater.* **2002,** *240,* 1–6.

[59] Hertel, R., Gliga, S., Fahnle, M. & Schneider, C. *Phys. Rev. Lett.* **2007**, *98*, 117201.

[60] Choe,S.-B., Acremann,Y., Scholl,A., Bauer,A., Doran,A., Stöhr,J., Padmore,H. A.. *Science* **2004**, *304*, 420-422.

[61] a) Xiao,Q., Rudge,J., Choi ,B., Hong ,Y., Donohoe ,G. *Appl. Phys. Lett.* **2006**, *89*, 262507. b) Weigand, M., Van Waeyenberge,B., Vansteenkiste,A., Curcic,M., Sackmann,V., Stoll,H., Tyliszczak,T., Kaznatcheev,K., Bertwistle,D., Woltersdorf,G., Back,C.H., Schütz,G. *Phys. Rev. Lett.* **2009**,*102*, 077201.

[62] a) Van Waeyenberge,B., Puzic,A., Stoll,H., Chou,K., Tyliszczak T. W., Hertel,R., Fähnle M., Brückl,H., Rott,K., Reiss,G., Neudecker,I., Weiss,D., Back,C. H., Schütz,G. *Nature* **2006**.*444*, 461–464. b) Curcic,M., Van Waeyenberge,B., Vansteenkiste,A., Weigand,M., Sackmann ,V., Stoll,H., Fähnle ,M., Tyliszczak ,T., Woltersdorf ,G., Back ,C.H., Schütz ,G. *Phys. Rev. Lett.* **2008**,*101*, 197204. c) Lee, K., Kim, S. *Phys. Rev. B Condens. Matter Mater. Phys.* **2008**, *78*, 014405. d) De Loubens;G., Riegler;A., Pigeau,B., Lochner,F., Boust,F., Guslienko,K. Y., Hurdequint ;H., Molenkamp ;L. W., Schmidt; G., Slavin ;A. N., Tiberkevich V. S., Vukadinovic;N., Klein O. *Phys. Rev. Lett.* **2009**,*102*, 177602.

[63] a) Yamada;K., Kasai;S., Nakatani;Y., Kobayashi;K., Kohno;H., Thiaville;A., Ono;T. *Nat. Mater.* **2007**, *6*, 269–273. b) Yamada, K., Kasai, S., Nakatani, Y., Kobayashi, K., Ono, T. *Appl. Phys. Lett.* **2008**, *93*, 152502.

[64] a) Kravchuk, V., Sheka, D., Gaididei, Y. & Mertens, F. *J. App. Phys.* **2007**, *102*, 043908. b) Kammerer M., Weigand M., Curcic M., Noske M., Sproll M., Vansteenkiste A., Van Waeyenberge B., Stoll H., Woltersdorf G., Back C.H., Schuetz G. *Nat. Com.* **2011**, *2*, 279.

[65] *Electromagnetic, Magnetostatic, and Exchange-Interaction Vortices in Confined Magnetic Structures.* Chapter 8. Mironov V.L, Fraerman A.A. **2008**. Editor: E.O. Kamenetskii.

[66] a) Kikuchi, N., Okamoto,S., Kitakami,O.,Shimada,Y, Kim, S. G., Otani,Y., Fukamichi,K., *J. Appl. Phys* **2001**. *90*, 6548. b) Okuno, T., Shigetoa, K., Onob, T., Mibua, K., Shinjo,T., *J. Magn. Magn. Mater.* **2002,** *240*, 1. c) Thiaville, A.*,* Garcia, J. M., Dittrich ,R., Milta, J., Schrefl, T., *Phys. Rev. B* **2003**, *67*, 094410.

[67] Urbanek,U.M., Hladık,L., Spousta J., Im,M-Y., Fischer,P., Eibagi,N., Kan, J. J., Fullerto, E. E. , Sikola,T.. *Nat. Nanotec.* **2013**, *8*, 341.

[68] Zhu,X., Grutter ,P., Metlushko ,V., Ilic ,B. *Phys. Rev. B.* **2002**, *66,* 024423. b) Yamada N., Ohno,E., Nishiuchi,K., Akahira,N. , Takao,M.. *J.Appl. Phys*, **2002**, 91, 7340.

[69] Wieser R., Usadel K. D., Nowak U., *Physical Review B,* **2006**, *74*, 094410.

6

Lt-Mfm Characterization Of Organized Molecular-based Magnetic nanoparticles

6.1 INTRODUCTION

As discussed in chapter 3, the controlled positioning of the MNPs in specific areas of the surface is a fundamental requirement for the exploitation of their functionalities. In particular two-dimensional arrays of nanoparticles are interesting model systems for the development of future applications. For example, in ultra-high dense magnetic recording an ordered array of magnetic bits is needed,[1] which relies on a size reduction of these individual nanometric units and the distance between them. The magnetic state of the system formed by these elements depends on their magnetostatic coupling.[2] Magnetic nanoparticles are then good candidates for their use as individual bits on this type of recording media. However, with interparticle distances smaller than few nanometers, dipolar interactions are not negligible and can become a problem. The dipolar interactions may induce changes in the individual NP magnetization directions, and therefore magnetization reversal processes can be affected by the neighbouring nanoparticles.[3] Thus, it is necessary to know the minimum distance at which the MNPs should be organized to avoid these interactions or at least, to know how the magnetization directions of individual NPs are altered when they are arranged in close proximity.[4]
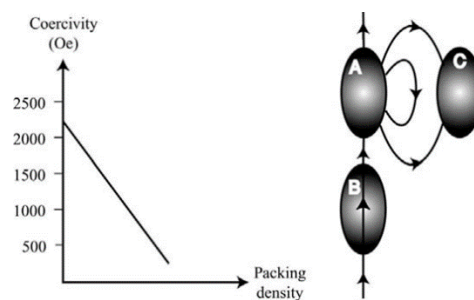

Figure 1. Inter-particle interactions in media composed of small particles. All the particles are initially magnetized in the up direction. The field which particle A exerts on particle C acts in the down direction. So when the external field is reversed and applied in the down direction, the field from particle A acting on particle C assists the applied external field, and so C reverses its magnetization at a lower applied field than it would in isolation. Overall the sample has a lower coercivity than a collection of isolated particles. Figure extracted from reference [4]

The magnetic characterization of these organized MNPs on surfaces become essential for the study of their applicability although it is a difficult task that involves several technical handicaps. In particular, as discussed in chapter 5, PBA-NPs are challenging because their characterization require measurements at low temperatures and they have relatively low magnetization. As far as we know, the closer magnetic characterization performed in organized PBA-NPs was carried out by A. Guirri et al, using Scanning Hall Probe Microscopy (SHPM).[5] The results suggested low temperature canted ferromagnetism in the anchored PBA-NPs, as had been observed previously in the bulk PBA material. But the measurement and manipulation of the magnetization of the individual NPs over the organized monolayers was not reached. In fact, these authors only show results for the large magnetic ordering within the monolayers with very poor resolution, so the intrinsic magnetic properties of the NPs were not discussed. All these technical difficulties can be overcome by using LT-MFM, as has been already probed in the previous section, and offers the appropriate scenario (with optimum resolution) to measure the magnetic properties of the organized PBA-NPs on surfaces.

Another aspect worthy to mention is the difficulty of positioning the MFM tip over the locally organized PBA-NPs. Although the regular AFM permits to position the tip in a reference area of the surface as it is mounted with a top-view optical microscope, the set-up of our LT-MFM does not allow this option, making really difficult to find the small localized areas with PBA-NPs organized by LON or DIP-PEN. This is why organized stripes of NPs have been prepared using a soft lithography method. As in chapter 5, the study has been focused in the KNiCr NPs. In the present chapter, LT-MFM characterization of these NPs arrays will be presented.

6.2 RESULTS AND DISCUSSION

6.2.1 Organization of KNiCr NPs in lines

The organization of KNiCr NPs was made by the soft lithography method already described in chapter 3, based in the formation of aluminum oxide stripes. To prepare the aluminum oxide lines, wet lithography was used to form PMMA ridges all over the surface with a PDMS stamp. Afterwards, a thin layer of Al was evaporated and once exposed to air, the native oxide was formed after the lift-off process. The direct contact between the patterned surfaces with a diluted aqueous solution of the KNiCr NPs gives rise to well organized NPs forming stripes all over the surface (Figure 2 (a), (b), (c)). The topography images show that the NPs get attached onto the aluminun oxide but they are not piled up. The height profile (Figure 2(d)) confirms the presence of only one layer of NPs on top of the lines.
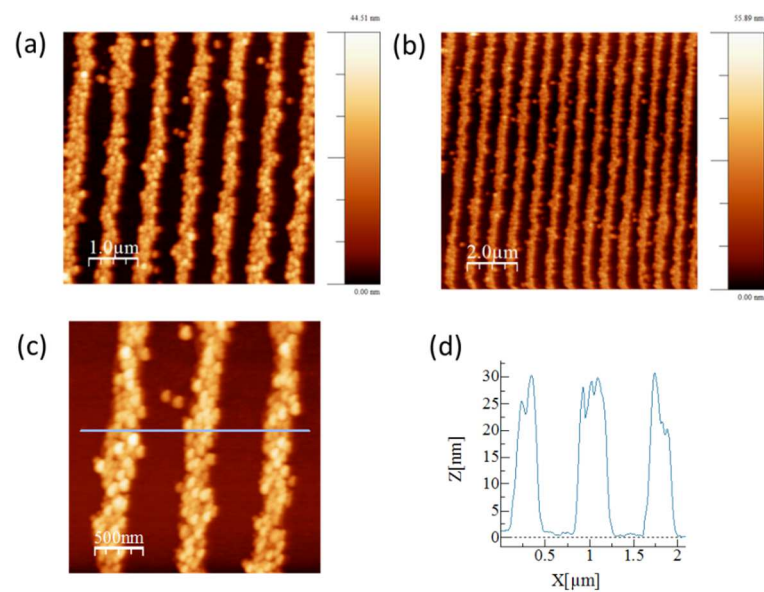

Figure 2. Images of stripes taken with an MFM tip in tapping mode. (a), (b) and (c) Topography image of 5 µm x 5 µm, 10 µm x 10 µm, 2.5 µm x 2.5 µm, respectively. (d) Height profile of image (c).

6.2.2 Height dependence measurements

For the detailed magnetic imaging of densely packed NPs in stripes, very high resolution measurements are required to be capable to resolve the individual NPs within the lines. Some considerations have to be taken into account as for example the distance at which the sample is retracted from the tip to acquire the magnetic images. It is known that the magnetostatic tip-sample interaction in MFM strongly depends on the working distance (Z_{lift}) so, for an accurate MFM measurement, the selection of the Z_{lift} is very important. Crucial information can be lost by choosing the wrong tip-sample value so a detailed study was made in order to select the appropriate Z_{lift}.

A set of magnetic images were taken at different values of Z_{lift}. First, the tip was previously magnetized and the sample was field cooled at +200 Oe. A 2.5 µm x 2.5 µm topography image was acquired to characterize the morphology of the sample and the tilt was compensated. An external applied field of -500 Oe (out-of-plane) was set and a tip-sample separation of 100 nm was fixed. This value of Z_{lift} was found to be the minimum distance where the "jump-to-contact" phenomenon disappeared, so ≈100 nm was the minimum working distance without the influence of topography in the magnetic image. Then, in the same area the MFM image was acquired at 100 nm and showed very high resolution. As can be seen in Figure 3(c), the magnetic signal of the individual NPs could be differentiated inside the lines. To check the influence on the imaging resolution the value of the Z_{lift} was varied from 100 nm to 120 nm, 140 nm and 160 nm and the corresponding magnetic images were recorded at each distance (Figure 3). The same measurements were performed at + 500 Oe and equivalent results were obtained but with the opposite contrast. At this value of the external field, the magnetic moments of the organized KNiCr NPs were completely reversed as happened with the isolated KNiCr NPs.
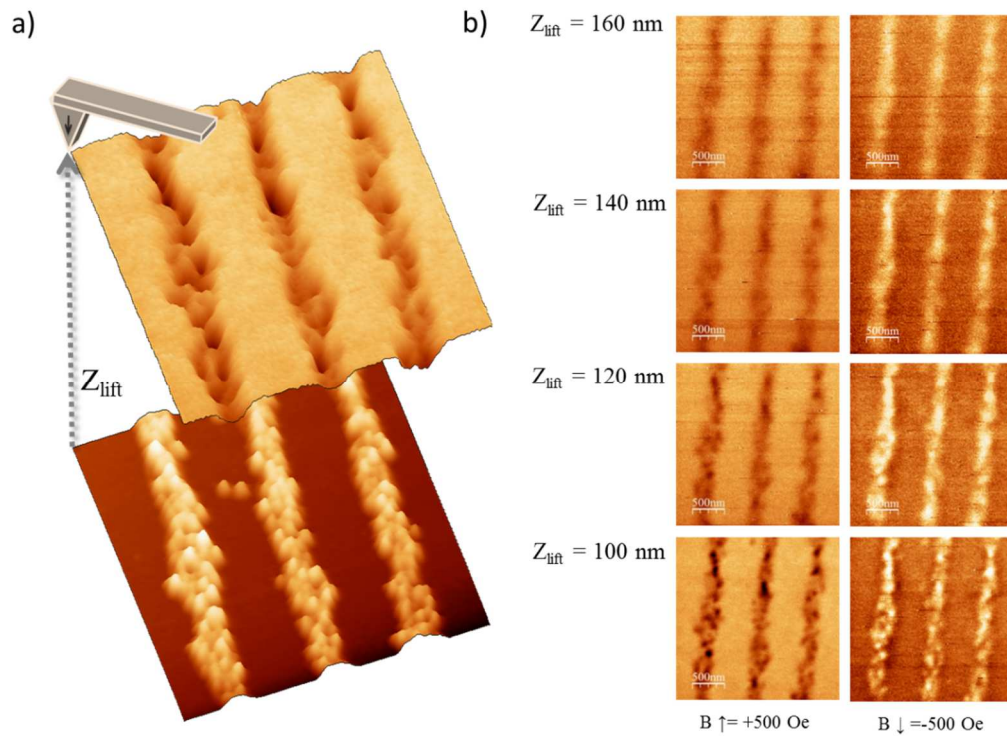
Figure 3. (a) 3D Topography and magnetic images. (b) Set of MFM images at $B_{ext} = \pm 500$ Oe using different tip-NP distances (Z_{lift}): 100 nm, 120 nm, 140 nm and 160 nm.

In Figure 3(b) it is shown the frequency shift profiles of the +500 Oe magnetic images for different lifts of 100 nm, 120 nm, 140 nm and 160 nm, on top of one of the lines. It can be clearly seen that the intensity of the signal decreases with the height as well as the confinement, probing that increasing the tip-sample distance not only the sensitivity decreases but also the resolution. If the Z_{lift} is selected close enough (but far from the topography influence), one can distinguish individual NPs or even small aggregates and it is possible to detect individual changes in the NPs while changing the external field. Scanning too high, for example at 140 nm or 160 nm, may lead to the conclusion that all the NPs show a homogeneous magnetic contrast (tip-sample interaction) at the same value of the field applied. This conclusion is far from the real

271

behavior of these NPs. It also avoids the possibility of detecting the magnetic reversibility of the NPs inside the lines at different B_{ext} as will be discussed in the next section (Figure 4).
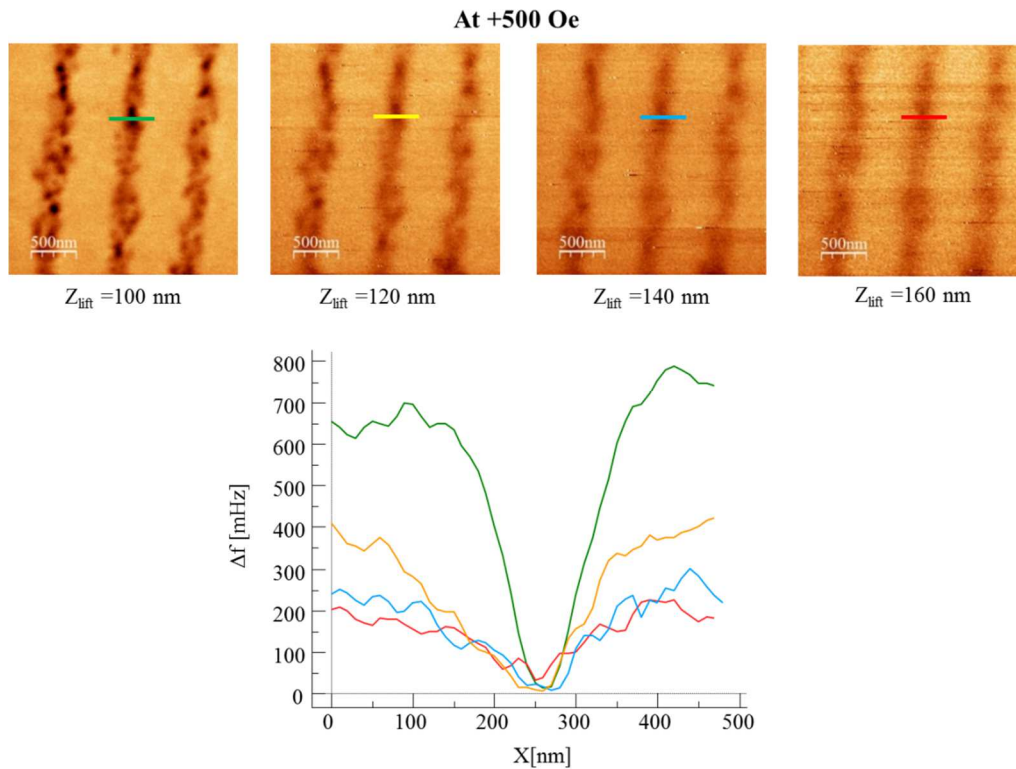

Figure 4. Set of MFM images at $B_{ext} = + 500$ Oe using different tip-NP distances (Z_{lift}). Frequency shift profiles at three different distances: 100 nm, 120 nm and 140 nm.

6.2.3 Magnetization reversal measurements

One of the challenges of this work was to ascertain if it is possible to detect the influence of the dipolar interaction between close-packed PBA NPs. Actually, quantitative data with the MFM are really difficult to perform, although some qualitative results can be extracted from the magnetic images at different values of the external field.

For the LT-MFM study of magnetic reversibility and the interparticles interactions of the close organized NPs we have to take into account some important factors:

First, the total magnetic field (B) acting over the KNiCr NPs is the resultant of the sum of the stray field of the tip and the external applied field as discussed in chapter 5. Considering that the tip was previously magnetized in the +z direction and it is not influenced by the external field (which it is not strictly truth), at positive values of B_{ext} the total field B would be $B = B_{tip} + B_{ext}$ and at negatives values of B_{ext}, the total field would be $B = B_{tip} - B_{ext}$. This effect produces that at negatives values of the B_{ext} the magnetic intensity signal (Δf) is lower than at positive values of the B_{ext}, as was already mentioned for the isolated NPs. This is shown in Figure 5 (a), where one can see MFM images at B_{ext} = -500 Oe, 0 Oe and +500 Oe of the KNiCr-NPs organized in lines. The Z_{lift} was fixed to 100 nm to get the best resolution and, as discussed before, it is possible to correlate the magnetic signal to specific NPs in the topographic image thanks to the high resolution achieved. It is also shown how at $B_{ext} = \pm 500$ Oe all the NPs change completely their magnetic contrast, achieving for each case the complete magnetization reversal. As can be observed in Figure 5 (c), the intensity of the bright signal is lower than the intensity of the dark signal at the same value of external applied field (but in opposite orientation). This can be explained taking into account the influence of the stray field of the tip.
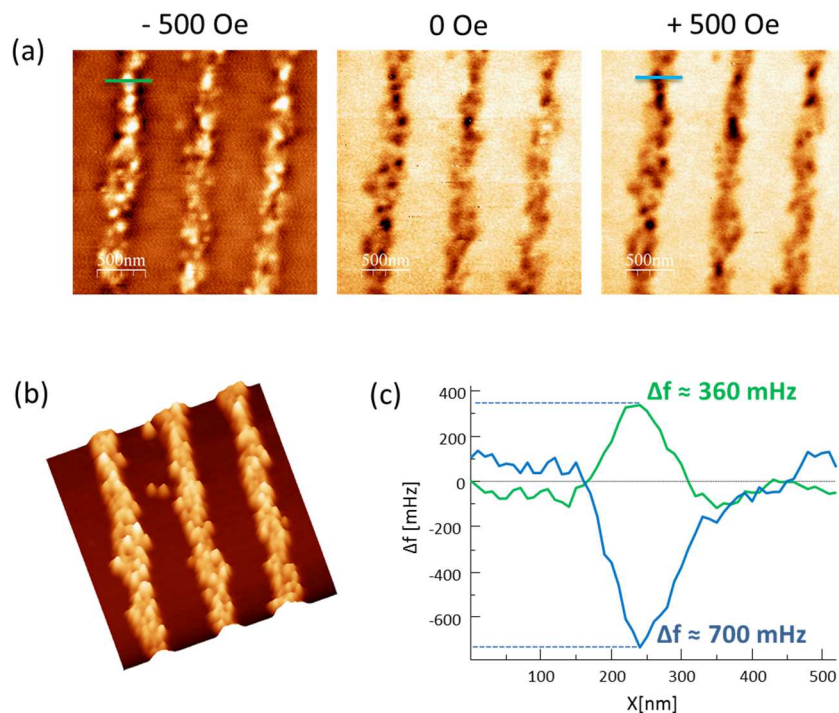
Figure 5. (a) MFM images of the lines of NPs at different external magnetic fields applied out-of-plane. (b) 3D Topography image of KNiCr NPs organized in lines by indirect stamp method (2.5 µm x 2.5 µm). (c) Frequency shift profiles at B_{ext} = +500 Oe (blue profile) and B_{ext} = -500 Oe (green profile) in one of the lines (marked in the corresponding magnetic images in (a).

Second, the magnetic reversibility process is highly influenced by the MNP size and the orientation of its easy axis, as has been deeply discussed for the dispersed NPs. To be able to deposit the KNiCr NPs with a preferencial magnetic orientation onto the surface, it would be necessary to apply a magnetic field at the moment of deposition but below the blocking temperature. This scenario is technically impossible as these nanostructures are prepared from solution. So the KNiCr NPs are organized in lines but their easy axes directions are randomly orientated. On the other hand, the preparation of the KNiCr NPs from solution, always produce a distribution of NPs with sizes of around (25 ± 5) nm (see DLS measurements in chapter 3). The

occurrence of these two factors together with the fact that the KNiCr NPs are bare NPs and very close packed in the lines, produce a wide type of magnetic responses to the external field.

The magnetic reversibility of the organized KNiCr NPs (considering them as perfect crystals) would then be governed by the influence of the tip stray field, the NPs size, their easy axis orientation, the dipolar interactions among them and finally, the external total field. All in all, it was possible to detect how the individual NPs inside the lines gradually change their magnetic moment with the external applied field.

A set of magnetic images was recorded at different values of the out-of-plane B_{ext} and the gradual change of the magnetic signal of the KNiCr NPs within the stripes was successfully measured (Figure 6). All the measurements were performed again at a fixed tip-sample distance of 100 nm at the same area of the topography image (2.5 µm x 2.5 µm).
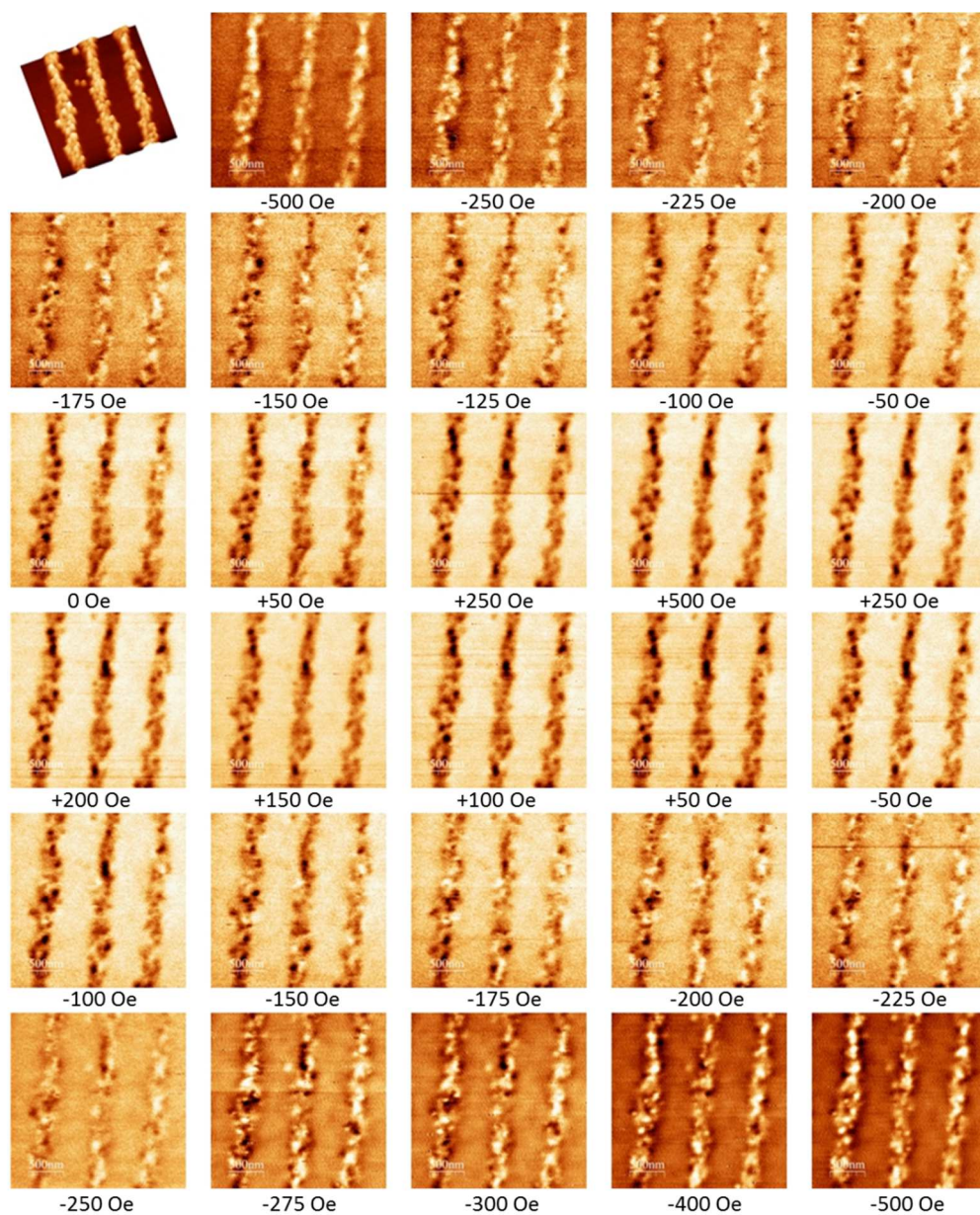
Figure 6. Set of MFM images of the NPs stripes at different external magnetic fields applied out-of-plane. Image size: 2.5 µm x 2.5 µm.

A zoom in one of the stripes is shown in next figure (Figure 7) where the magnetic response from the NPs can be better seen. It gradually changes with the external field applied from B_{ext} = +500 Oe to -500 Oe although not all the KNiCr NPs start changing their magnetization at the same value of the B_{ext}. Apart from the small dispersion of NPs sizes and the different orientations of their easy axes, the dipolar interactions of the very close-packed bare PBA NPs probably play an important role in the reverse of the NP magnetization with the influence of external field. But finally, applying high enough fields (±500 Oe) it is possible to beat the influence of the dipolar interactions and completely reverse the magnetization of all the NPs as happened with the randomly dispersed KNiCr NPs.

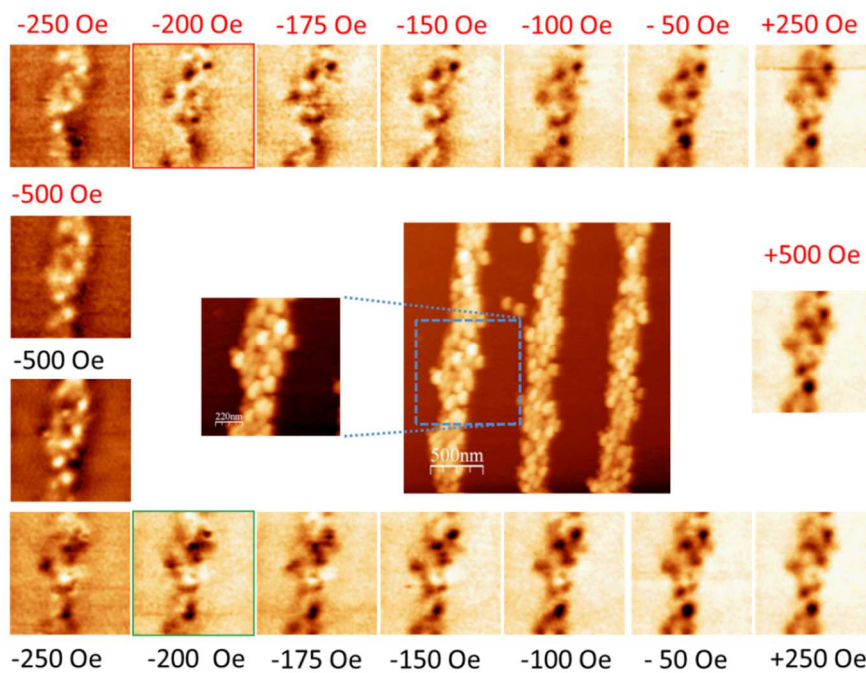Figure 7. (a) Topography image of KNiCr NPs organized in lines by indirect stamp method. Following, MFM images of the lines of NPs at different external magnetic fields applied out-of-plane. (b) In the center, topography image (2.5 µm x 2.5 µm) of the organized KNiCr NPs and a zoom on a single stripe. Set of MFM images of a single stripe at different external fields applied. Image size: 1.1 µm x 1.1 µm.

It is also important to note that for the same values of the B_{ext} we can find different magnetic configurations if we come from a negative or from a positive value of the external field applied. For example, focusing on the MFM images at –200 Oe one can see that both are different (Figure 8). The NPs that have switched their magnetization at -200 Oe coming from +500 Oe are not all exactly the same ones than the NPs reversed at -200 Oe coming from -500 Oe. This is due to the intrinsic hysteretic behavior of the KNiCr NPs at this temperature (4.2 K), besides the dipolar interactions that may be influencing the hysteretic response of the close-packed KNiCr NPs.
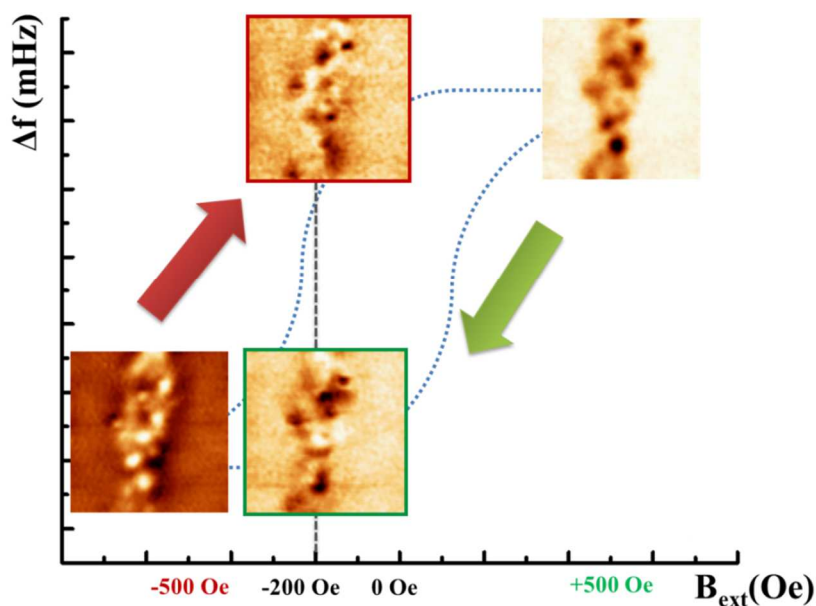

Figure 8. Histerestic behaviour of the organized KNiCr NPs. At the same value of the B_{ext}, the magnetic image shows different contrast if coming from -500 Oe or +500 Oe. The lines drawn behind the MFM images is a cartoon of an ideal hysteresys plot, included to facilitate the explanation.
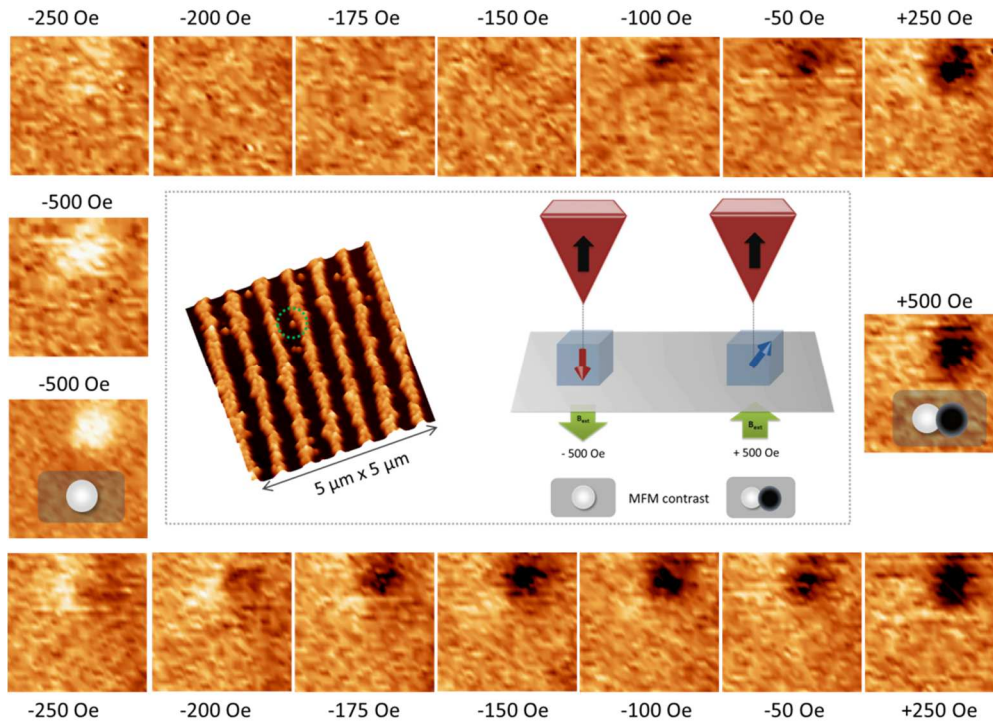
Figure 9. Set of magnetic images showing the magnetization reversal of a single NP of h = 25 nm. In the center (highlighted with a dashed green circle), the topography image and a sketch about the theoretical magnetic contrast expected with different orientations of the PBA-NP magnetic moment. Z scale of the magnetic images Δf = ±150 mHz.

In Figure 9, a closer view of an isolated PBA-NP of (25.0 ± 2.5) nm at the side of one of the stripes is presented. To measure the hysteresis of this particular NP, the external magnetic field was swept from -500 Oe to +500 Oe and set to -500 Oe again. The magnetic switch of the single NP was clearly detected as can be seen in the magnetic images. The size of this PBA-NP is above the size limit for the single domain (calculated to be around 19 nm, in chapter 5), which implies a non-uniform magnetization reversal. In a fast look one can observe a bright spot at B_{ext} = -500 Oe (magnetic moment pointing in –z direction, opposite to the tip magnetization) that changes to dark gradually by changing the intensity of the external magnetic field. In a closer look to $B_{ext} = \pm 250$ Oe magnetic images, a combined dark/bright contrast is

observed which points out an effective magnetic moment gradually switching from bright to dark, so the magnetization reversal is being recorded in every step. At +500 Oe, the magnetic contrast is not a homogeneous dark spot which would mean that the magnetization reversal was not fully completed. So the resultant magnetic moment may be canted due to a curling or non-homogeneous magnetization of the NP, to a crystallographic defect or to the anisotropy of the NP.

Finally, the influence of the neighboring stripe on the discussed NP could be discarded as the NP was separated around 120 nm from the line. As observed in chapter 5, to detect interparticle interactions they have to be placed much more closer (a few nanometers) to be affected by a neighboring NP.

6.3. MATERIALS AND METHODS

The synthesis of the KNiCr NPs as well as their organization in lines by soft lithography is explained in detail in chapter 3. The magnetic characterization was performed following the same procedure as in chapter 5 for the isolated NPs. The same magnetic tips were used in this case.

6.4. CONCLUSIONS

A detailed magnetic characterization of ordered arrays of KNiCr NPs organized by soft lithography has been presented. First, the influence of the tip-sample distance has been discussed and, as shown in the results, this is a crucial experimental parameter that has to be carefully set in order to get the best resolution images. The selection of a too large distance would lead to erroneous conclusions about the magnetic behavior of the ordered NPs.

Thanks to the high resolution achieved it was possible to detect the change of the magnetization of individual NPs inside the lines. The magnetic behavior of these NPs has been highlighted by performing a complete characterization of the NPs by varying the external field from -500 Oe to +500 Oe and coming back to -500 Oe. For intermediate values between +500 Oe and -500 Oe, a mix of contrasts within the lines was found, meaning that the NPs do not reverse equally due to the dispersion of sizes and the interparticles interactions. Moreover, a hysteretic behavior was also observed, as the magnetization states are not equivalent if one comes from +500 Oe or from -500 Oe. Finally, it was observed the magnetization reversal of a single NP placed at 120 nm of one of the lines. From this measurement, together with the measurements performed in chapter 5, we conclude that the NP is not affected by the neighboring line.

Therefore, from these results it can be inferred that in spite of the existence of strong dipolar interactions between the adjacent particles forming within the lines, ordered arrangements of small groups of KNiCr NPs, separated distances in the order of 100 nm, could be formed to be used as single bits of information that can be switched completely by an external stimulus (small values of external fields ($\pm$ 500 Oe)).

6.5 BIBLIOGRAPHY

[1] Skomski,R. *J. Phys.: Condens. Matter.* **2003,** *15*, R841–R896.

[2] a) Imre,A., Csaba,G., Ji L., Orlov,A., Bernstein,G. H., Porod,W. *Science*, **2006**, *311*, 205. b) Bisero,D., Cremon,P., Madami,M., Tacchi,S., Gubbiotti,G., Carlotti,G., Adeyeye,A. O. *IEEE Trans. Mag.*, **2012**, *4*, 48.

[3] Puntes,V. F., Gorostiza,P., Aruguete,D. M., Bastus,N.G., Alivisatos,P.A. *Nature Materials*, **2004**, *3*, 263 – 268.

[4] *Magnetic Materials*. Spalding N. Cambridge University Press. **2003**.

[5] Ghirri,A., Candini,A., Evangelisti,M., Gazzadi,G.C., Volatron,F., Fleury,B., Catala,L., David ,C., Mallah,T., Affronte,M. *Small,* **2008**, *4*, 12, 2240–2246.

Very briefly I would like to give some hints about the perspectives of our future plans to continue this work.

Taking advantage of the knowledge acquired with the soft lithography and the LON, we are currently implementing a device for parallel oxidation lithography (POL) that will allow us to perform local oxidation nanolithography over macroscopic regions. Metalized stamps will be used to oxidize the surfaces with the same procedure as the utilized for LON. The system will be integrated in the Nanopress complemented with a voltage amplifier. This lithographic technique can be very versatile as can be used to create oxide motives for the controlled positioning of nanoobjects such as NPs and/or molecules of interest. POL will also permit to perform the large patterning onto the exfoliated 2D crystals looking for the modification of the physical properties of the lithographed system and giving rise to new heterostructures.

Envisioning the great chances that offer the molecular-based materials, we would like to move to other type of NPs, like spin crossover NPs (SC-NPs) that can be switchable at room temperature. We have already performed some preliminary experiments for the controlled organization of SC-NPs of iron(II) triazole salts onto surfaces by means of soft lithography that show up the possibility to organize them.

Besides, there are some questions that remain unexplained in this thesis like the oxidation growth behavior onto TaS_2 and the NbS_2 surfaces forming concentric rings, or the nature of the cane-like exfoliated stacks of NbS_2. Currently we are collaborating with the group of Prof. Angel Rubio for finding an explanation of these unprecedented

formations. Spectroscopic and electron microscopy measurements will be performed on the NbS_2 to ascertain their chemical composition.

We would like also to perform a systematic study of the degradation of the metallic exfoliated layers of different TMDCs that seem to get oxidized, depending on the environmental conditions. Following with the TMDCs, we will like to study the formation of magnetic vortices in ultra-thin layers of $NbSe_2$ that presents a superconducting transition temperature, of 7.2 K, with the LT-MFM. We will be able to study the formation of the magnetic vortices at 4.2 K by varying the external applied field. The study of patterned $NbSe_2$ will be also performed, to measure the pinning of the vortices on the surface.

RESUMEN

El desarrollo de nuevos dispositivos multifuncionales se basa en la posibilidad de miniaturización de sus componentes así como de su ensamblado de una manera controlada. Conocer el tamaño, la forma y las propiedades de estos nanocomponentes así como poder integrarlos y combinarlos a voluntad son factores cruciales a la hora de diseñar dispositivos inteligentes que integren estas nanoestructuras con macro(nano) electrodos. El reto que se plantea tiene pues dos vertientes: por un lado la caracterización y manipulación de nuevos materiales en la nanoescala, y por otro, su organización en superficies y/o su ensamblado para crear materiales multifuncionales heteroestructurados.

En esta tesis se ha tratado de abordar estos dos problemas mediante la organización, manipulación y caracterización de dos tipos de nanomateriales: (i) cristales bidimensionales de espesor atómico y (ii) nanopartículas (NPs) magnéticas de base molecular.

(i) Desde el descubrimiento del grafeno en 2004, los **cristales bidimensionales de espesor atómico** han tenido un creciente interés por sus interesantes propiedades que los convierten en potenciales candidatos para su uso en futuras aplicaciones en campos como la microelectrónica o en sensores (tales como componentes electrónicos flexibles, electrodos transparentes o sensores químicos ultrasensibles). Por otro lado, son materiales atractivos desde el punto de vista fundamental ya que sus propiedades varían con su espesor, siendo diferentes las propiedades de una sola capa de las del material en volumen. De entre estos cristales bidimensionales, los dicalcogenuros de

los metales de transición (*transition metals dichalcogenides*, TMDCs) han sido estudiados en esta tesis.

(ii) Por otro lado, las **NPs magnéticas** de análogos de azul de Prusia (PBA) utilizadas en este trabajo son **de base molecular** y por lo tanto, comparándolas con las NPs magnéticas convencionales de metáles u óxidos metálicos (Fe, Co, Fe_3O_4, etc), presentan ventajas importantes intrínsecas a su naturaleza molecular, como baja densidad, transparencia y síntesis química sencilla y rica (originando gran cantidad de derivados de la misma familia con diferentes propiedades mediante pequeñas modificaciones). Además son solubles en agua, carecen de envoltura orgánica y son aniónicas lo que permite su inmovilización a través de interacciones electrostáticas.

El manuscrito está dividido en dos partes. En la primera parte se ha presentado la manipulación de los dos materiales mencionados, con el objetivo de transferir estos nanoobjetos de una manera eficiente y controlada. Además, para el caso de los TMDCs, se ha presentado la generación de heteroestructuras a través de la manipulación química de su superficie.

Esta primera parte está dividida a su vez, en tres capítulos. El primero es una introducción general de los tipos de micro y nanolitografías existentes, prestando especial atención a tres tipos de métodos litográficos menos convencionales: la nanolitografía por oxidación local (*local oxidation nanolithography*, LON) llevada a cabo con un microscopio de fuerzas atómicas (*atomic force microscope*, AFM), la litografía por *Dip-pen* (*Dip pen lithography*, DPN) y la litografía suave (*soft lithography*) con sellos elastoméricos.

En el capítulo 2, se ha presentado una manera viable y eficaz de fabricar heteroestructuras de capas atómicas de TMDCs metálicos, como el TaS_2, con su

correspondiente óxido, Ta_2O_5, por medio de LON. Se ha desarrollado un nuevo modo de oxidación "estático" que ha permitido producir motivos de tamaños nanométricos sobre capas de espesor atómico de TaS_2 de manera precisa y muy reproducible. Asimismo, este método se ha generalizado y ha sido utilizado para la creación de patrones de óxido nanométricos en otros TMDCs como el $TaSe_2$, NbS_2 y el $NbSe_2$. Durante el estudio de oxidación local de estos materiales con el método tradicional o "dinámico", se encontró un crecimiento del óxido anormal para el TaS_2 y NbS_2. Se observaron formaciones con forma de anillos concéntricos con una protuberancia central. Este fenómeno no se ha observado en ningún otro material oxidado con LON. Además, el NbS_2 se exfolió de dos maneras distintas, en forma de placas (que es la manera general de los TMDCs) y en forma de cañas. En las cañas también se observó un crecimiento anormal, en forma de dendritas. Sin embargo para los casos del $TaSe_2$ y el $NbSe_2$ se observó la formación de un único anillo exterior. Este fenómeno sí había sido observado en la oxidación local en silicio y en algunos polímeros. El estudio sistemático así como una explicación detallada de todos estos procesos de oxidación han sido presentados en profundidad en este capítulo. Finalmente cabe destacar que para la obtención de las capas de espesor atómico de los TMDCs se ha desarrollado una nueva tecnología que permitió la delaminación de manera controlada de los materiales expuestos en este capítulo. Esto no había sido posible hasta ahora con los procesos de exfoliación micromecánica convencionales como el conocido método de *Scotch Tape*. Este nuevo dispositivo llamado "Nanoprensa" ha sido utilizado para la exfoliación de varios dicalgogenuros metálicos así como para la obtención de grafeno. El control y la versatilidad que ofrece el aparato permitieron la deposición de varios de estos materiales sobre sustratos de distintos tipos.

En el capítulo 3 se han utilizado los tres métodos litográficos introducidos en el tema 1 para la organización de manera controlada de NPs magnéticas de base molecular sobre

superficies funcionalizadas de silicio. Estas NPs de derivados de azul de Prusia presentan propiedades magnéticas modulables a través de estímulos externos, lo que las convierte en potenciales candidatas para su integración en dispositivos electrónicos o espintrónicos. Como paso previo, se han desarrollado las técnicas litográficas necesarias para organizar estas NPs de manera muy precisa y local (con LON y DPN), así como su organización a gran escala logrando crear patrones de líneas paralelas cubriendo áreas de cm^2 (con la litografía suave). Esto fue posible aplicando una aproximación híbrida entre técnicas litográficas, conocidas como técnicas de "arriba a abajo" (*top-down*) con técnicas de autoensamblado de monocapas de moléculas, denominadas técnicas de "abajo a arriba" (*botom-up*) y aprovechando el carácter aniónico de las NPs para controlar su organización a través de interacciones electrostáticas. El estudio detallado así como los resultados de todos los casos se han presentado de manera ordenada y sistemática. También se ha hecho un estudio detallado de las propiedades químicas de las nanopartículas una vez depositadas y ordenadas en la superficie demostrando que no se ven alteradas a pesar de su manipulación previa.

Por otro lado, no hay que olvidar que para poder integrar estas NPs en dispositivos funcionales, sus propiedades magnéticas también se tienen que ver inalteradas una vez ordenadas en superficie y a su vez, estas propiedades han de poder detectarse con claridad y modularse externamente. Para ello se ha hecho un estudio en profundidad de las posibilidades del uso a bajas temperaturas de un microscopio de fuerzas magnéticas de campo variable para la detección, manipulación y caracterización de las propiedades magnéticas de las NPs de PBA fijadas en una superficie. Este estudio se desarrolla en la segunda parte del manuscrito que está también dividida en tres capítulos.

El cuarto capítulo (primero de esta segunda parte), es una introducción general sobre la caracterización de nanopartículas magnéticas sobre superficies. En él, se han introducido la variedad de técnicas que existen para dicha caracterización en general, y en particular, con microscopia de fuerzas atómicas.

En el capítulo 5, se ha presentado el estudio detallado de la caracterización magnética de NPs individuales y aisladas. Primero se ha presentado un estudio sobre cómo varía la señal magnética de las NPs con la temperatura, que es un parámetro crucial ya que el momento magnético de éstas NPs se puede fijar por debajo de su temperatura de Curie. Se encontró que únicamente trabajando a bajas temperaturas (4.2 K) se obtiene una señal óptima para poder detectar las NPs de manera individual. Una vez analizados todos los parámetros para obtener imágenes de alta resolución, se llevaron a cabo experimentos de reversibilidad magnética en una serie de NPs aisladas de distintos tamaños. Es sabido que los mecanismos de reversibilidad magnética dependen del tamaño de las NPs. Seis tipos de reversibilidad se pudieron distinguir y medir entre los cuales caben destacar la reversibilidad vía *curling* y por formación de vórtices. El *curling* es un proceso muy estudiado y que ha sido predicho teóricamente (en nanotubos de materiales magnéticos, por ejemplo), aunque esta es la primera vez donde se ha presentado su creación y evolución en imágenes de alta resolución. Por otro lado, la formación de vórtices se ha visto para microestructuras y nanostructuras magnéticas (no más pequeñas de 100 nm) litografiadas pero nunca en NPs preparadas desde disolución. La formación de vórtices en NPs cúbicas magnéticas también fue predicha teóricamente y ha sido simulada mediante simulaciones micromagnéticas, sin embargo, hasta ahora nadie había presentado evidencia experimental en imagen sobre su formación y aniquilación. En este trabajo se han presentado con éxito estas dos formaciones magnéticas en NPs de tamaños 20 nm y 25 nm, respectivamente. Finalmente, gracias a la funcionalización *in situ* de la punta magnética con una sola

NP, se pudieron obtener imágenes de alta resolución que permitieron asignar las direcciones de los momentos magnéticos de varias NPs depositadas en superficie y manipuladas con un campo externo.

En el capítulo 6 se ha presentado las medidas de caracterización magnética con microscopia de fuerzas a bajas temperaturas y campo variable en NPs organizadas en líneas con litografía suave. Se hizo un estudio detallado de cómo afecta la distancia entre la punta magnética y la muestra para poder optimizar los parámetros experimentales y obtener imágenes de alta resolución. Gracias a la alta resolución obtenida se pudo identificar la señal magnética de NPs individuales dentro de las líneas. También se ha mostrado la evolución de los momentos magnéticos de las NPs individuales dentro de las líneas variando el campo externo aplicado. A valores de ± 500 Oe se observó la reversibilidad total de todas las NPs que formaban las franjas, mientras que a valores intermedios se observaron diferentes contrastes debidos a la dispersión de tamaños de las NPs que formaban las líneas y las interacciones dipolares entre las mismas. Finalmente, se ha analizado una sola NP que se encontraba a 120 nm separada de una de las líneas. Con estas medidas y junto con los resultados obtenidos en el capítulo 5, se concluye que las NPs de base molecular se podrían ordenar en pequeños grupos de NPs separados unos 100 nm entre ellos y cuya reversibilidad magnética se conseguiría aplicando campos magnéticos suaves (± 500 Oe).

Como conclusión final podríamos destacar que durante el desarrollo de esta tesis se han utilizado metodologías convencionales (tanto métodos de litografía como de exfoliación micromecánica) que han sido modificadas y mejoradas para su optimización para la organización y manipulación de nanomateriales tan novedosos como las capas monoatómicas de cristales bidimensionales o nanopartículas magnéticas de base molecular. También se ha hecho un estudio sistemático y detallado de su caracterización con microscopia de campo cercano, destacando en particular la

caracterización magnética de las NPs llevada a cabo con microscopia de fuerzas magnéticas a bajas temperaturas. En ese aspecto se ha hecho un estudio a nivel fundamental de la reversibilidad magnética de éstas NPs que fue predicho hace más de 60 años y que hasta ahora, no se había presentado de forma experimental.

APPENDIX

I.1 Introduction to Scanning Probe Microscopy (SPM)

Scanning probe microscopes (SPM) are a family of tools that represents a set of experimental methods developed to study surface properties up to the atomic resolution as well as obtaining 3D topographic images. The SPM family has become essential tool in almost all laboratories around the world dedicated to nanoscience as well as for industrial fabrication. The scanning probe microscopes use a physical probe with a very sharp tip that scans the sample used not only to image the surfaces of solids and their characteristics but also to manipulate single atoms or molecules and hence it is possible to create heterostructures at the atomic-nanometric scale (for example by performing local oxidation nanolithography (LON)). By modifying the tip it is possible to measure a wide variety of tip-sample interactions as for example electric (CT-AFM: conductive tip atomic force microscopy) and magnetic properties (MFM: magnetic force microscopy), and also to perform various types of spectroscopies (Figure 1).
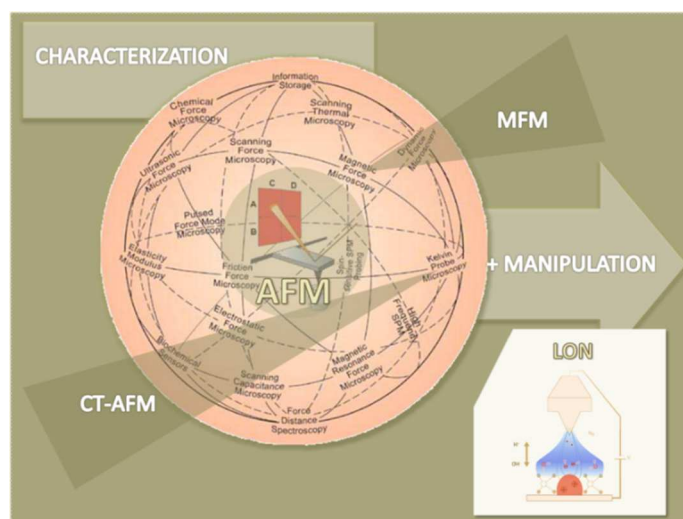

Figure 1. Global image of the SPM family: The atomic force microscopy (AFM) in the center has inspired a variety of other scanning probe techniques that are not only used to image the topography of surfaces.

The Scanning Tunneling Microscope (STM)

The starting point of SPM was the invention of the scanning tunneling microscope (STM). After the very first successful tunneling experiment with an externally and reproducibly adjustable vacuum gap invented by Binnig, Rohrer et al. in 1981,[1] the robust development connected to SPM techniques has been noted. In 1982 the STM was presented for the first time.[2] The principle of STM is based on the electron tunneling between the metal tip and the conductive sample separated by insulating layer (vacuum, gas) where a potential barrier is generated. The tunneling current is the responsible for the STM image and depends on the distance between the tip apex (~ 1 nm) and the sample surface in the form:

$$I_t \sim V_{Bias} e^{-cS}$$

Where I_t is the tunneling current, V_{Bias} is the constant bias voltage applied between the tip and the sample, c is a constant and S is the tip-sample distance. As a consequence of this invention, Binnig and Rohrer were awarded with the Nobel Prize in 1986.

In a standard STM experiment, a metallic tip is moved in the three dimensions by piezoelectric scanners. The tip-sample distance is set to a constant tunneling current controlled by an electronic unit which is connected to a computer that records the distance as a function of the lateral movement of the tip. This is then displayed as a topographic image (Figure 2).
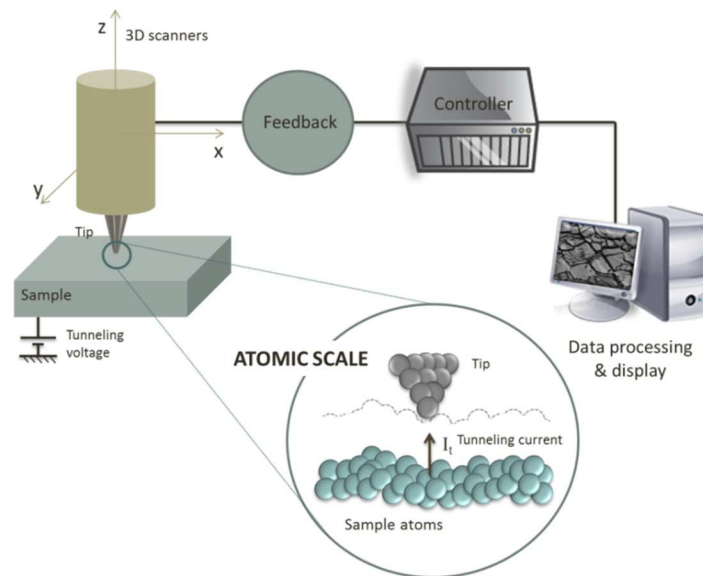
Figure 2. Schematic representation of a STM with the basic elements of the experiment.

With this example, all the basic elements of the SPM have been introduced: A short tip-sample interaction which is sensed with the local probe, the scanners to move the probe on the three dimensions that permits the 3D imaging at the atomic-nanoscale and the electronic controller and computer (software) that records, controls and process all the information acquired in the previous steps. The experiment needs a rigid construction and very high mechanical stability in order to allow reproducible and accurate results on the atomic scale.

The Atomic Force Microscope (AFM)

The family of the SPM is formed by several techniques depending on the tip-sample interaction. The main one is the atomic force microscope (AFM) which is the first and most important extension of the STM and was invented by Binning, Quate and Gerber in 1986. [3] Unlike the STM is limited to measure conducting or semiconducting samples, the AFM permits to measure also insulating materials. Its working principle

is the measurement of the interactive force between a tip and the sample surface. The tip is now mounted on a cantilever and the tip-sample interaction in recorded by measuring the cantilever deflection caused by this interaction (Figure 3).
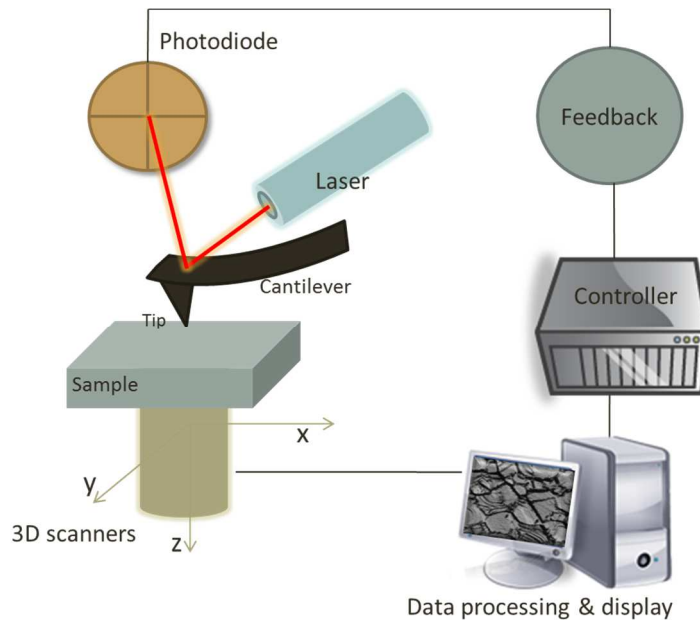

Figure 3. Schematic representation of an AFM with the basic elements of the experiment.

AFM cantilevers are microfabricated from silicon or silicon nitride using photolithographic techniques. Typical lateral dimensions are on the order of 100 μm, with thicknesses on the order of 1 μm. The force on the tip due to its interaction with the sample is sensed by detecting the deflection of the compliant lever with a known spring constant.

The tip-surface interactions measured by the cantilever deflection are dependent on the tip-sample distance and three regions can be differentiated: (1) Repulsion regime. At very small tip-sample distances (a few angstroms) a very strong repulsive force appears between the tip and sample atoms. Its origin is the so-called exchange

interactions due to the overlap of the electronic orbitals at atomic distances. When this repulsive force is predominant, the tip and sample are considered to be in contact. (2) Attraction regime (Van der Waals): An instantaneous polarization of an atom induces a polarization in nearby atoms and therefore an attractive interaction. (3) Far away from the surface long range interactions are the responsible of the cantilever deflection: electrostatic and magnetic forces. The electrostatic interaction is caused by both the localized charges and the polarization of the substrate due to the potential difference between the tip and the sample. Magnetic interaction is caused by magnetic dipoles both on the tip and the sample (Figure 4). The force measured by the tip-sample interaction is ultrasmall, typically in the order of nanoNewtons.
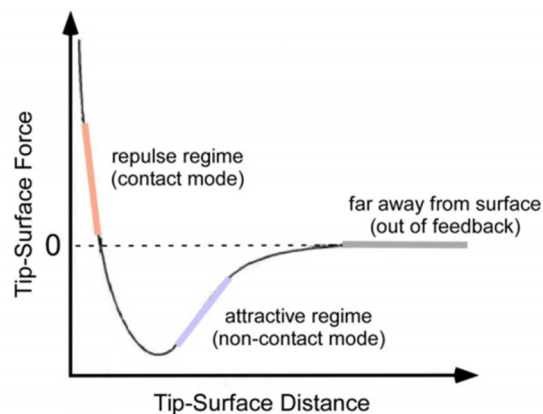

Figure 4. Dependence of the tip-surace force with the distance between the tip and the sample.

The AFM can be used either in the static or the dynamic mode. In the **static mode**, also referred to as the repulsive or contact mode, a sharp tip at the end of the cantilever is brought into contact with the surface of the sample. During initial contact, the atoms at the end of the tip experience a very weak repulsive force due to electronic orbital overlap with the atoms in the surface of the sample. The force acting on the tip causes the cantilever to deflect, which is usually measured by optical detectors. This

interaction force between tip and sample is measured by monitoring the cantilever deflection.

In the **dynamic mode** of operation, also referred to as attractive force imaging or noncontact imaging mode, the tip is brought into close proximity to (typical few nanometers), but not in contact with the sample. The cantilever is deliberately vibrated in either amplitude modulation (AM) mode or frequency modulation (FM) mode. Very weak van der Waals attractive forces are present at the tip–sample interface. The surface topography is measured by laterally scanning the sample under the tip while simultaneously measuring the separation-dependent force gradient (derivative) between the tip and the surface. The force gradient is obtained by vibrating the cantilever and measuring the shift in the resonant frequency of the cantilever. But the most used working mode in AFM is the so-called *tapping* mode (intermittent contact mode). In the tapping mode, during the surface scan, the cantilever/tip assembly is sinusoidally vibrated by a piezo mounted above it, and the oscillating tip slightly taps the surface at the resonant frequency of the cantilever (70–400 kHz) with a constant (20–100 nm) amplitude of vertical oscillation, and a feedback loop keeps the average normal force constant. The oscillating amplitude is kept large enough that the tip does not get stuck to the sample due to adhesive attraction ("snap to contact" phenomenon). The tapping mode is used in topography measurements to minimize the effects of friction and other lateral forces to measure the topography of soft surfaces.

To obtain topographic information, the interaction force is either recorded directly, or used as a control parameter for a feedback circuit that maintains the force or force derivative at a constant value. Using an AFM operated in the contact mode, topographic images with a vertical resolution of less than 0.1 nm (as low as 0.01 nm) and a lateral resolution of about 0.2 nm have been obtained. Forces of 10 nN to 1 pN are measurable with a displacement sensitivity of 0.01 nm.[4]

There is a third mode- the **force calibration mode-** that can be used to study interactions between the cantilever and the sample surface. In the force calibration

mode, the force–distance curve, a plot of the cantilever tip deflection signal as a function of the voltage applied to the piezo tube, is obtained (Figure 5). As the piezo extends, it approaches the tip, which is in mid-air at this point and hence shows no deflection. This is indicated by the flat portion of the curve. As the tip approaches the sample to within a few nanometers (point 1), an attractive force kicks in between the atoms of the tip surface and the atoms of the surface of the sample. The tip is pulled towards the sample and contact occurs at point 2 on the graph. From this point on, the tip is in contact with the surface, and as the piezo extends further, the tip gets deflected further. This is represented by the sloped portion of the curve (point 3). As the piezo retracts, the tip moves beyond the zero deflection (point 4) due to attractive forces (van der Waals forces and long-range meniscus forces), into the adhesive regime. At point 5 in the graph, the tip snaps free of the adhesive forces, and is again in free air. The horizontal distance between points 2 and 5 along the retrace line gives the distance moved by the tip in the adhesive regime. Multiplying this distance by the stiffness of the cantilever gives the adhesive force. Incidentally, the horizontal shift between the loading and unloading curves results from the hysteresis in the piezotube scanner.
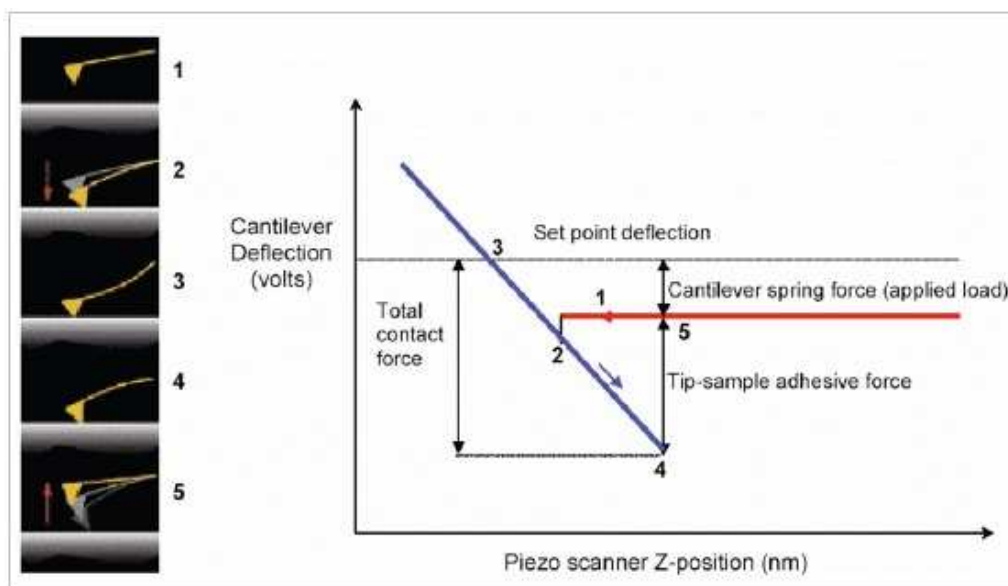
Figure 5. Force distance curve. The approach (red) and withdraw (blue) curves are shown on the right. Note that the total contact force is dependent on the adhesion as well as the applied load.

Almost all SPMs use piezo translators to scan the sample, or alternatively to scan the tip. The tube scanners are the most used in AFMs which provide sample scanning range with a small size. Electronic control systems for AFMs are based on either analog or digital feedback, although Digital feedback circuits are better suited for ultralow noise operation. Images from the AFMs need to be processed. An ideal AFM is a noise-free device that images a sample with perfect tips of known shape and has a perfectly linear scanning piezo. In reality, scanning devices are affected by distortions and these distortions must be corrected. In spite of the high resolution on the vertical direction, AFM images are usually affected by artefacts decreasing its lateral resolution. The AFM data require special processing for eliminating such undesired effects, which result from very different sources like the intrinsic non-linearity of the scanner, an improper tip-sample feedback, electrical noise or the tip convolution effects (artefacts). AFM manufacturers have gained much experience in eliminating

most of them with the improvement of software, hardware and control electronics. An example of powerful and user-friendly sotware for treating SPM images is WSxM software (Nanotec), which contains many innovative features suggested by SPM users world-wide as it is compatible with almost all SPM instruments commercially available.[5]

Among the large family of SPM, two derivatives of AFM are used in this thesis: the conductive-tip AFM (CT-AFM) and the low temperature magnetic force microscope (LT- MFM).

I.2. CONDUCTIVE TIP ATOMIC FORCE MICROSCOPY (CT-AFM)

Very briefly, the CT-AFM is a secondary imaging mode derived from contact mode AFM that characterizes conductivity variations across medium from conducting to low-conducting and semiconducting materials. It is used to measure and map current in the 2 pA to 1 µA range while simultaneously collecting topographic information.
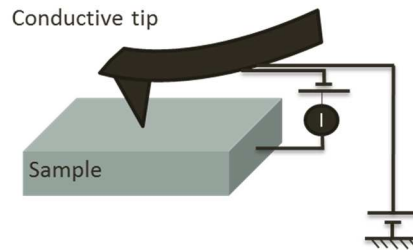
Figure 6. Schematic representation of the CT-AFM.

The conductive tip is scanned in contact with the sample surface while a voltage is applied between the tip and the sample, generating a current image (Figure 6). At the same time, a topographic image is also generated. Both, the current and the topographic images are taken from the same area of the sample, which allows the identification of features on the surface conducting more or less current. While the topography is acquired using the deflection signal of the cantilever, the electric conductivity is measured through an electric current amplifier.

I.3 LOW TEMPERATURE MAGNETIC FORCE MICROSCOPY (LT-MFM)

The Magnetic force microscopy (MFM)[6] already presented in chapter 4, is an imaging technique in which magnetic forces or force gradients are measured to image the magnetic structure of a sample. A magnetic coated tip is used to measure the interaction produced by the magnetic stray field from the sample. The magnetic tip-interaction produces a deflection in the cantilever that can be detected by different detections systems (an optical interferometer in the Attocube system).

The MFM is a very powerful tool to study a wide variety of magnetic structures. Despite room temperature (RT) measurements are the most common, the development of more sophisticated MFM allowed the measurements at low temperature (LT) and variable field.[7] Low temperature MFM (LT-MFM) is an important extension of MFM which allows locally measuring the magnetic properties at liquid helium temperatures down to the milliKelvin regime. The advantages of operating the MFM at low temperature are related not only to the improved sensitivity and stability, but also to the possibility to study quantum mechanical effects in magnetic materials and superconductors.[8] Among the magnetosensitive low temperature scanning probe techniques (Figure 7) such as scanning Hall probe microscopy,[9] scanning superconducting quantum interference device microscopy,[10] spin polarized STM (SP-STM) and reveals a very high lateral resolution which ranges between 10 and 100 nm, only surpassed by SP-STM.[11]
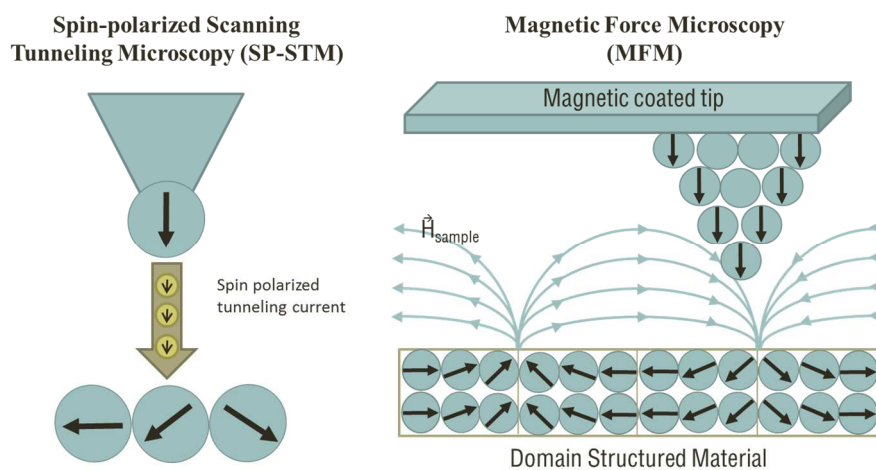
Figure 7. Sketches of SP-STM and MFM.

As the general principles and modes of operation of the MFM at LT were discussed in chapter 4, in this appendix some details of the working operation in Attocube LT-MFM system used in this thesis will be described.

I.4 MFM MEASUREMENTS WITH THE ATTOCUBE SYSTEM

System overview

As with all low temperature scanning microscopes, the Attocube LT-MFM is a fairly complicated instrument. It incorporates a high vacuum chamber, cryogenics, vibration isolation, superconducting magnets, temperature controller, a fiber optic sensor, MFM electronics and control software.

To perform low temperature microscopy, the Attocube LT-MFM is cooled by a controlled exchange gas atmosphere in a liquid Helium bath cryostat. Alternatively, the MFM head, mounted in a long rod, is inserted in a tube that can be pumped to operate under vacuum conditions. In Figure 8, the main parts of the system are shown:

1: LT and HV compatible feedthroughs, 2: vacuum window, 3: microscope insert, 4: superconducting magnets, 5: liquid He dewar, 6: Titanium housing for the MFM head and scanners, 7: xyz coarse positioners, 8 xyz scanners, 9 sample heater and sample stage, 10: optical fiber for interferometric deflection detection, 11: cantilever.
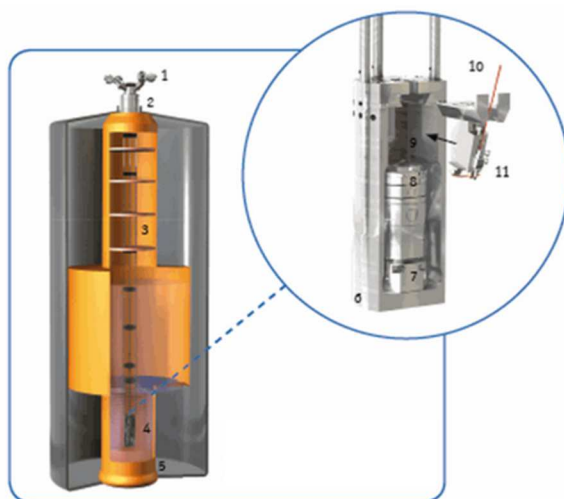

Figure 8. Scheme of a cryogenic LT-MFM insert including cryostat, superconducting magnets and the MFM head. Figure taken from Attocube.

There are two superconducting magnets that allow applying variable magnetic field in two directions: out-of-plane up to 8 T and in-plane up to 2 T. Both directions can be combined to apply a vector magnetic field up to 1.5 T. The temperature working range of the system is 4.2 K to 300 K.

The tip is mounted on a cantilever holder that can be moved in and out of a precision positioning sample stage (Figure 9a). The cantilever is aligned with the fiber and it is place just above the sample (Figure 9b). The correct alignment of the infrared light onto the tip is crucial in order to get good results. The get better performance, the system was complemented with a digital optical microscope that allowed a direct view of the ferrule and the cantilever.

The instrument works by scanning the sample below a fixed magnetic cantilever. The sample is usually glued with silver paste on a sample holder that is placed just on top of a sample heater. The sample holder and heater are located on top of the scanners (Figure 9c).
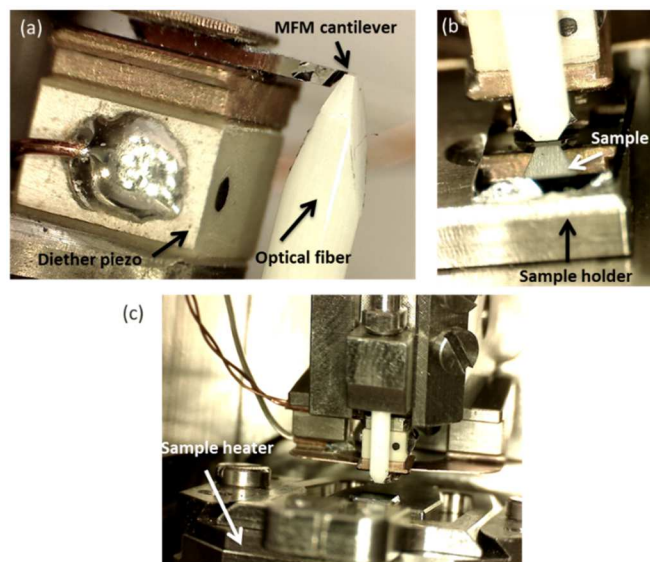

Figure 9. (a) Real picture of the tip mounting of the MFM. The MFM is mounted on the stage just above the diether piezo and aligned with the optical fiber. (b) The tip and fiber on top of the sample. (c) General view of the MFM head and sample holder.

There are many important issues concerning to the cooling process like making the vaccum and filling the tanks in the correct order. We used to insert the sample into the dewar (for its operation at low temperature) in the afternoon and wait over the night to stabilize the system. Concerning to the variable temperature measurements, one have to take into account that the response of the piezo scanners is temperature-dependent. A complete calibration of the Attocube system was performed at various temperatures with a grid because the system was only calibrated for RT and 4.2 K.

Modes of operation

All the LT-MFM measurements presented in this thesis were performed working in dynamic mode, amplitude modulation (AM) and for recording the magnetic signal, the constant height mode was chosen. This way, the topography was acquired by performing the feedback on the amplitude value (AM) and the magnetic response was recorded by measuring the frequency shifts (Δf) operating in combination with a phase-locked loop (PLL). Sometimes, the PLL was also enabled to track the topography which conferred more stability to the topographic measurements.

In amplitude modulation mode the cantilever is excited at its resonance frequency by an AC voltage. Correspondingly, the photo-detected AC signal at the resonance frequency reflects the oscillation amplitude of the cantilever. As the cantilever approaches the sample, this vibration amplitude decreases rapidly with diminishing tip-sample distance. This signal serves as the input to a feed-back loop which maintains the cantilever oscillation amplitude at a so called "set level", which corresponds to a given force between the sample and the cantilever. The vibration amplitude of the cantilever (A) serves as the input to a feedback loop, which maintains the cantilever oscillation at the set level by adjusting the voltage on the z-scanner (amplitude feedback). Alternatively, the amplitude and the phase of the oscillation resonance can be kept constant (phase feedback). During the scan, the output signal of

the feedback loop is recorded (z piezo voltage), providing the topographic information. The error signal is the oscillation amplitude of the cantilever.

We usually used magnetic coated cantilevers with stiffness constant of $k \approx 3$ N/m and high values of the amplitude oscillations ($A \approx 90$ nm) to avoid the problem of unwanted jump-to-contact phenomenon. Figure 10 illustrates the interference signal measured by an interferometric deflection detection system. The output signal is largest if the cantilever vibrates around the point of maximum slope of the interference signal (working point). The working point is set by applying an offset DC voltage to the dither piezo which is the responsible of the cantilever oscillation.
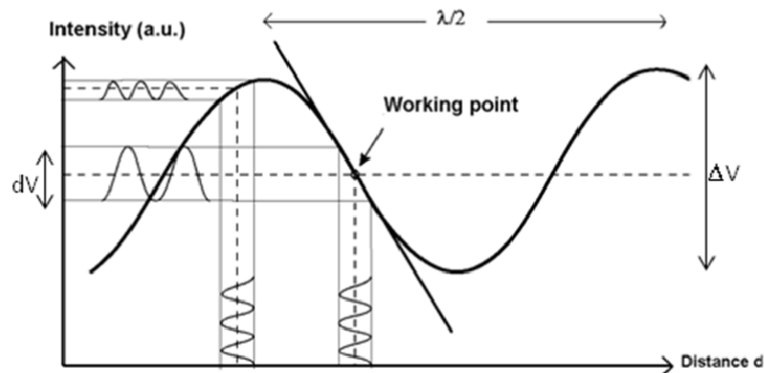

Figure 10. Schematic drawing of the interference signal. Figure taken from Attocube.

In AM, the tip-fiber cavity has to be adjusted to the point of highest interference sensitivity, i.e. at which the change in the tip-fiber distance gives the largest (linear) change in the interferometric signal. After the cavity has been adjusted to this point, the cantilever must be excited at its resonance frequency (f_0) and the photo-detected AC voltage signal, which is the A_{osc}, will be used as measuring signal for the feedback loop (Figure 11).
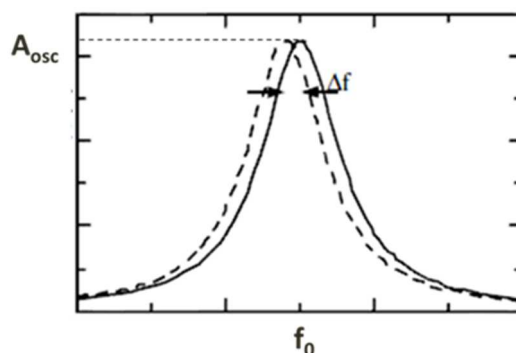
Figure 11. Resonance curve of a cantilever. The change in resonance frequency, Δf, is induced by the interaction with the surface. Figure from Attocube.

It is possible to extract the real oscillation amplitude, A in nm, of the cantilever from the resonance curve with the help of the calibration of the interference signal (Figure 10):

$$A = \frac{\lambda}{2\pi} \cdot \frac{V}{\Delta V} \approx 246 \text{ nm} \cdot \frac{V}{\Delta V}$$

where λ = 1,545 nm is a given parameter from the interferometer, V is the photo detector signal at resonance and ΔV is the peak-peak amplitude of the interference signal. The amplitude A is typically chosen to be within 80 nm to 100 nm, depending on the working conditions.

Besides the oscillation frequency of the resonance (f_0), the Full Width at Half Maximum (FWHM) can also be deduced from the resonance curve which allows calculating the cantilever's Q factor, $Q = f_0$ / FWHM. Typical values of Q, between 5000 and 40,000 are obtained at low temperature and high vacuum.

Apart from AM mode, constant height can be operated in combination with a phase-locked loop (PLL). In this case, the cantilever is always excited at resonance, i.e. 90° phase shifted with respect to its detected phase at any time. Due to this fixed-phase condition, a frequency shift Δf is then observed (and recorded) whenever the tip is scanned over the surface at the corresponding separation, Z_{lift}. This technique is most frequently used at high vacuum conditions where the Q-factor of the MFM cantilever is high.

The distance between the magnetic tip and the sample surface (Z_{lift}) plays an important role in the MFM. The Z_{lift} is a value that is set by the user for every measurement. In practice, the Z_{lift} value given to the Attocube MFM is the real Z_{lift} only in contact mode when no force is exerted to the tip (step ii in Figure 12). Working in non-contact and constant height mode (step iv in Figure 12), the real Z_{lift} value can be calculated from the following approximation:

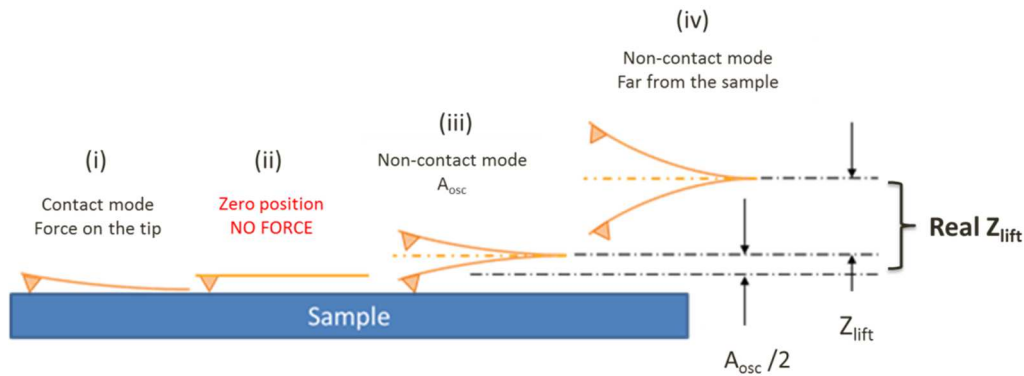$$\text{Real } Z_{lift} \approx \frac{A_{ocs}}{2} + Z_{lift}$$

Figure 12. Schematic representation of the MFM tip at various steps of the scan. Contact position is shown in step i. The zero position is defined when the tip is in contact with the sample but no cantilever deflection is detected (zero force, step ii). When the tip is brought to non-contact mode, the MFM is

operating in AM and the cantilever is oscillating away from the sample at a certain distance that is approximately $A_{ocs}/2$ (step iii). In step iv, the sample is retracted a certain distance, Z_{lift}, from the step iii.

Noise levels

The system frequency noise level δf_T is due to the contributions from noise in the PLL detector δf_{det}, cantilever thermal noise δf_{th}, and interferometer noise δf_{int}:

$$\delta f_T = \sqrt{(\delta f_{int})^2 + (\delta f_{th})^2 + (\delta f_{det})^2}$$

In our case, for the Attocube system, the interferometer noise is 0.78 pm/$\sqrt{Hz}$.

The minimum detectable force gradient for thermally limited measurements is:[12]

$$\delta f_{th} = \left[\frac{df}{dz}\right]_{min} = \frac{1}{A}\sqrt{\frac{4\,k\,k_b\,BW\,T}{\omega_0\,Q}}$$

where T is the working temperature, BW is the measurement bandwidth, k is the force constant of the cantilever, k_b is the Boltzman constant, ω_0 is the natural resonance frequency of the cantilever $\omega_0 = 2\pi\,f_0$, Q is the quality factor and A is the amplitude of oscillation of the cantilever.

For cantilevers with high quality factors at low T, noise from the deflection sensor will likely dominate the measurement. Let $n_{\Delta x}$ be the cantilever deflection sensor noise density, which yields a minimum detectable force gradient of:

$$\delta f_{det} = \left[\frac{df}{dz}\right]_{min} = \frac{2k}{\sqrt{3}\omega_0}\frac{n_{\Delta x}}{A}\,BW^{3/2}$$

Note that in both limits: thermodinamical and detector noise, increasing the oscillation amplitude A and using softer cantilever (smaller k) will improve the detection sensitivity. However, as the spring constant is reduced, the tip-sample separation at which the cantilever will jump into contact with the sample surface (snap-in) increases. So it is needed to reach a compromise between k and A to select the appropriate cantilever and working conditions to get the better signal to noise ratio.

All the magnetic measurements presented in this thesis were performed at low temperature and high vacuum operating in AM working with the PLL to track the Δf, and at constant height mode. The tips used were magnetic coated cantilevers commercially available MFMR tips with hard magnetic coating of CoCr alloy (40 nm thickness), spring constant of $k \approx 3$ N/m, and resonance frequency of $f_0 \approx 70$ kHz from Nanosensors. To avoid the unwanted jump-to-contact phenomenon and to enhance the signal to noise ratio, relatively high amplitude oscillations were used ($A \approx 90$ nm). With these conditions, the total RMS δf noise of the instrument is around 2 mHz (RMS value).

BIBLIOGRAPHY

[1] Binnig,G., Rohrer,H., Gerber,Ch., Weibel,E., *Appl. Phys. Lett*., **1982**, *40*, 178.

[2] Binnig,G., Rohrer,H., Gerber,Ch., Weibel,E., *Phys. Rev. Lett*., **1982,** *49*, 57.

[3] Binnig,G., Quate,C. F., Gerber,Ch., *Phys. Rev. Lett*., **1986**, *56*, 930.

[4] *Handbook of Nanotechnology*. Bhushan, B. Springer. **2006**.

[5] Horcas,I., Fernandez,R., Gomez-Rodriguez,J.M., Colchero,J., Gomez-Herrero,J., Baro,A. M., *Rev. Sci. Instrum.* **2007**, *78*, 013705.

[6] Martin,Y., Wickramasinghe,H. K., *Appl. Phys. Lett*., **1987,** *50*, 1455.

[7] Straver,E.W.J. PhD Thesis. **2004**.

[8] Straver,E. W. J., Hoffman,J.E., Auslaender,O.M., Rugar,D., Moler,K.A. *Applied Physics Letters,* **2008**, *93*(17), 172514.

[9] Oral,A., Bending,S. J., Henini,M., *Appl. Phys. Lett*. 69, **1996**, 1324.

[10] Tsuei,C. C., Kirtley,J. R., Chi,C. C., Yu-Jahnes,L. S., Gupta,A., Shaw,T., Sun,J. S., Ketchen, M. B. *Phys. Rev. Lett*. **1994,** *73*, 593.

[11] Volodin,A., Temst,K., Haesendonck,C. V, Bruynseraede,Y.. *Rev. Sci. Instrum*., **2000**, 71.

[12] Albrecht,T., Grutter,P., Horne,D., Rugar,D., *J. Appl. Phys*. **1991**, *69*, 668.